بِسْمِ اللَّهِ الرَّحْمَٰنِ الرَّحِيمِ

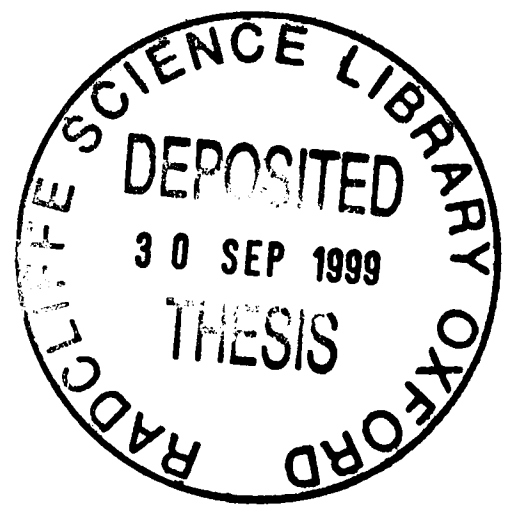
Dedicated to the memory of my father, Haji Hukam Dad Chaudhry, a man whom I have felt I have known more than through just the words of others, and for whom I have the deepest of respect and admiration.

Vertical Transport through *n*-InAs/*p*-GaSb Heterojunctions at High Pressures and Magnetic Fields

Wahid Chaudhry

A thesis submitted for the degree of
Doctor of Philosophy

Hertford College
Oxford
Trinity Term 1999



Vertical Transport through *n*-InAs/*p*-GaSb Heterojunctions at High Pressures and Magnetic Fields

Wahid Chaudhry

A thesis submitted for the degree of Doctor of Philosophy
Hertford College, Oxford
Trinity Term, 1999

ABSTRACT

The conduction band of InAs lies lower in energy than the GaSb valence band. In order to preserve continuity of the Fermi level across the interface, charge transfer takes place resulting in a confined quasi two dimensional electron gas (2DEG) in the InAs and a confined quasi two dimensional hole gas (2DHG) in the GaSb.

This study is an investigation into the vertical transport in an *n*-InAs/*p*-GaSb single heterojunction (SHET). Application of a forward bias (InAs negative with respect to GaSb) increases the 2DEG and 2DHG concentrations and, therefore, their confinement energies. Eventually a critical bias is reached where the electron confinement energy moves above the hole confinement energy (the theoretical voltage induced semimetal/semiconductor transition V_c). Any subsequent increase in voltage is expected to result in a current decrease, and a region of negative differential resistance (NDR) should occur.

The SHET can be grown with two distinct interface types, 'InSb-like' and 'GaAs-like'. This in turn affects the vertical transport characteristics of each type. Experimental IV traces at various pressures are compared with the corresponding results from sophisticated self-consistent band profile calculations taking into account band mixing effects for the first time through a **k.p** theory framework. Experimental IV traces of the SHETs under a magnetic field parallel to the interface are also compared with results from calculations that take into account the coupling of the growth and in-plane electron and heavy hole motions. Both sets of analysis support earlier conclusions that NDR occurs after V_c for both interfaces, and that each interface supports a different conduction mechanism.

Evidence of multiple phonon processes occurring in both sample types is observed for the first time and is proposed to reconcile the above experimental observations with theory. This data is found to offer explanations for a number of other observations.

Field perpendicular to the interface leads to the observation of features beyond the NDR region in both sample types. In samples with an 'InSb-like' interface, applying additional hydrostatic pressure leads to very strong features beyond the main NDR. Through a complex self-consistent decoupled model taking into account electrons and heavy holes, all these features are proposed to be due to a filling of an integer number of Landau levels. The band profile is predicted to alter dramatically at this point. The same model explains the observation of weaker features at 1 bar at high fields (~ 40T).

A variation of NDR position is found with a rotation of an-plane field.

ACKNOWLEDGEMENTS

There are many people to whom I am grateful for over the past few years for the help and support in completing this work (and in some cases for much more). But without any doubt, my greatest thanks are reserved to those who have sheltered me and have supported me unconditionally throughout all my endeavours, academic and non-academic. First, my mother, Karamat Bibi, whose love, trust and patience I am grateful for. Consistently steadfast throughout the years, she has been a tremendous role model. To my sister, Imtiaz Akhtar and her husband, Shoukat Hussain, I express heartfelt thanks for their unwavering support, materially and emotionally. It wouldn't be an exaggeration to say that I owe it all to them. I sincerely hope that in years to come I shall be able to repay at least some of their kindness. To Naheed Akhtar and Khalid Mahmood, who had the misfortune of putting up with me for so many years, thanks for rescuing me from many a time of boredom back home!

Here at Oxford, I would first of all like to thank my supervisor, Philip Klipstein, particularly for his scrutiny during the final months. I would of course also like to thank the extended family that makes up the so-called Spectroscopy Group, a funny name I've always thought. It is only during these final days that I realise how privileged I have been in working with such a highly talented group of individuals. They and the atmosphere they generated will be missed. First and foremost, I am indebted to Hyunsik Im. Without his experimental expertise and all-round physics knowledge, I suspect I would be busy fixing diffusion pumps somewhere in the transport laboratory, and without his wife, Ini, ensuring a steady supply of dinners, I would not have appreciated the full delights of Korean cuisine. To Georg Rau, for introducing me to my first 8×8s and his way of life – doing everything in the comfort of an office while listening to some obscure classical piece, as well as for the many discussions at silly hours of the night (which thankfully didn't always revolve around physics). To Sergey Lyapin, whom I thank, like so many others have before me, for his computer wizardry; to Jason Smith, Thane Gilmour and Andrew Glanfield, all who left me with invaluable advice about dealing with the problems that crop up when one writes up; to Yun-Chul Chung, a cool Dr if I ever met one; to Hyun-jin

Choi, whom I shall remember as spending more time smoking cigarettes outside the Clarendon than doing experiments inside (though understandably); to Tobias 'Dude' Reker, epitome of all that is Oxford Rowing and Football; to Matthew Roberts, another rowing fanatic, partially redeemed though by his continuation of antimonide research; to Guy Towlson, who I shall remember as a bit of a Muffin baking genius; and finally to Laura Bremme and Ruth Child, who have had a good knack of reminding me how comparatively unproductive my first year was. Beyond the Group but still in the Clarendon, I would also like to thank Andrew Poulter and Javed Rehman of the Nicholas Empire, who are still yet to convince me that the odd deranged night out is healthy, but there's plenty of time ahead!

I would also like to thank the many other friends at College and beyond that have made life during the D.Phil. especially enriching. For lack of space, I cannot name all of them here, but I particularly thank Farukh 'Jungle Boogie' Malik for his cynicism; Adil Khan for his level-headedness; Luis Pillich for the long soulful discussions on the merits of Investment Banking; Sajid Gulzar and Ikram Mohammed whom I can only describe as 'best friends'; and finally, Julia Aguilar (*pour qui la lutte valait la peine*). Oxford has been a wonderful experience. It has been challenging, and I shall look back at this work, the days as an undergraduate at Lincoln and a postgraduate at Hertford with great fondness.

'Give me a place to stand, and I *shall* move the Earth'

Archimedes

CONTENTS

1. INTRODUCTION AND BACKGROUND 1

1.1 Introduction 2
1.2 III-V Bulk Semiconductor Material Properties 3
1.2.1 The Brillouin Zone 5
1.3 Heterostructures 6
1.3.1 Structure Types 8
1.4 The Esaki Tunnel Diode 9
1.5 The InAs/GaSb System 10
1.5.1 Resonant Conduction 12
1.5.2 The SHET Interface 16
1.6 Applications of Antimonide Based Materials 17
1.6.1 Infra-red Lasers 17
1.6.2 Microwave diodes 18
1.6.3 Transistors 19
1.7 Outline of Thesis 19
1.8 References 21

2. EXPERIMENTAL TECHNIQUES 24

2.1 Introduction 25
2.2 A Brief Overview of Sample Growth and Processing 25
2.3 Vertical Transport IV Data Acquisition 27
2.3.1 The High Pressure Russian Cell 29
2.3.2 Continuous and Pulsed Magnetic Fields 31
2.4 References 32

3. K.P THEORY AND THE ENVELOPE FUNCTION APPROXIMATION 34

3.1 Introduction 35
3.2 Symmetries of the Zinc-Blende Structure 36
3.3 **k.p** Theory for Bulk Semiconductors 38
3.3.1 Nondegenerate Perturbative Approach 38
3.3.2 Degenerate Bands - The Kane Model 40
3.3.3 Far Band Considerations: Löwdin Perturbation Theory 44
3.4 Heterostructures and The Envelope Function Approximation 46
3.5 Computational Details and Approximations 50
3.5.1 Calculating the Hamiltonian at finite $k_{||}$ 50
3.5.2 The Axial Approximation 51
3.5.3 Time Reversal Symmetry and Kramers Degeneracy 51
3.6 Summary 52
3.7 References 52

4. ZERO FIELD K.P SELF-CONSISTENT BAND PROFILE CALCULATIONS 55

4.1 Introduction 56

4.2 Self-Consistent Calculations 57
4.2.1 Method of Calculation 57
4.3 Interface Type and the Band Overlap 69
4.4 Presenting Experimental and Theoretical Results 71
4.4.1 Dependence of NDR on Hydrostatic Pressure 71
4.5 Phonon Processes in InAs/GaSb Structures 81
4.5.1 A Detour into Raman Spectroscopy 81
4.5.2 Observed Phonon Cascades 83
4.6 Band Gaps, Wavefunctions and In-Plane Dispersion Curves 86
4.7 Summary 91
4.8 References 91

5. MAGNETIC FIELD PERPENDICULAR TO THE SHET INTERFACE 95

5.1 Introduction 96
5.2 'InSb - like' Interface Experimental Results 97
5.2.1 1 bar Results 97
5.2.2 Results at Higher Pressures 99
5.3 Semiclassical Dynamics of Electrons in Magnetic Fields 103
5.4 Quantum Mechanical Approach to Electrons in a Magnetic Field 105
5.5 The SHET under a Perpendicular Field 106
5.5.1 Method of Calculation 108
5.6 Calculated Results and Discussion 116
5.7 General Behaviour 116
5.7.1 Analysis at High Pressure 118
5.7.2 Analysis at 1 bar 124
5.8 'GaAs - like' Interface 129
5.9 Summary 133
5.10 References 135

6. MAGNETIC FIELD PARALLEL TO THE SHET INTERFACE 136

6.1 Introduction 137
6.2 Experimental Results 138
6.2.1 'InSb-like' Interface 138
6.2.2 'GaAs-like' Interface 141
6.3 The SHET in an in-Plane Magnetic Field 142
6.3.1 Perturbative Method 143
6.3.2 Fully Self-Consistent Calculations 144
6.3.3 Results 148
6.4 Comparison with Experiment 153
6.5 Angle-Resolved Magnetotunnelling 158
6.6 Summary 163
6.7 References 165

7. CONCLUDING REMARKS 167

7.1 Summary 167
7.2 Future Development 171

7.3 References..... 172

1. Introduction and Background

1.1 Introduction 2

1.2 III-V Bulk Semiconductor Material Properties.....3

1.2.1 The Brillouin Zone.....5

1.3 Heterostructures.....6

1.3.1 Structure Types 8

1.4 The Esaki Tunnel Diode.....9

1.5 The InAs/GaSb System 10

1.5.1 Resonant Conduction.....12

1.5.2 The SHET Interface 16

1.6 Applications of Antimonide Based Materials.....17

1.6.1 Infra-red Lasers.....17

1.6.2 Microwave diodes.....18

1.6.3 Transistors.....19

1.7 Outline of Thesis 19

1.8 References 21

1.1 Introduction

Solid state electronics is undergoing rapid changes driven by heteroepitaxy, lithography, and new device concepts. The advent of semiconductor lasers and integrated electronic circuits has led to a flurry of activities in compound semiconductors, bringing into the mainstream the III-V family of semiconductors with the notable examples of GaAs, AlAs and InGaAs. Remarkable advances in thin film epitaxy have allowed active semiconductor devices with sub 3-dimensional properties and built in biaxial strain due to lattice mismatch, providing a tremendous playground for the semiconductor physicist, experimental and theoretical alike. Instead of working with a fixed set of material parameters, one now has a tailorable array of parameters which can be chosen for optimum device response. As the 21st century approaches, semiconductor physics is far from being exhausted. It will continue to provide a plethora of subject matter for the study of fundamental quantum physics as well as being a fertile ground for further technological innovation.

The work here specifically is related to an effect proposed and demonstrated by Esaki [1, 2]: that of negative differential resistivity (NDR). This is a regime of decreasing current under increasing bias voltage. His work initially was based around heavily doped Ge and Si leading to his proposal, and later demonstration of, NDR in the tunnel diode in the late 50s (section 1.4). Later collaborative research with Tsu focused on the tunnelling characteristics of multiple barrier structures and superlattices, which again yielded them the experimental observation of their predicted NDR. This ultimately led Esaki to be awarded the Nobel Prize in 1973.

As a consequence of its peculiar electronic band structure, the InAs/GaSb single heterojunction (SHET) is one such system that exhibits strong NDR. In-house growth developments allowing precision fabrication of this and related structures has yielded rich results over the past decade [3, 4, 5, 25, amongst others]. Following the initial work of Austing *et al* [4] and more recently (and more relevantly) that of Khan-Cheema *et al* [5], the study here further explores the SHET's transport properties to yield information about the nature of tunnelling, band structure and any interface dependent processes.

The aim of this chapter is to provide a background for the research carried out. Sections 1.2 and 1.3 introduce some general solid-state physics concepts which aid in the understanding of specific semiconductor phenomena. Section 1.4 provides an overview of the historical back-drop of semiconductor research with particular emphasis on the Esaki Tunnel Diode. After a discussion of this first case of Negative Differential Resistance (NDR), the InAs/GaSb SHET is introduced with a brief discussion of its resonant conduction mechanism. This is followed by a discussion of the rich variety of possible optical and electrical devices that the antimonide heterostructure family may yield. The chapter finishes with a thesis outline, mapping out the new observations made during the research and their possible implications.

1.2 III-V Bulk Semiconductor Material Properties

The behaviour of electrons in a crystal as they move under the influence of the atomic cores might at first sight appear to be impossible to calculate. However, it turns out that the electrons move through the crystal as if they were free and even the simplest free electron model allows one to appreciate concepts such as bandgaps and effective masses [6]. However, instructive as it is, it is not a clear description of electron behaviour in real semiconductors. More advanced treatments such as the tight binding and pseudopotential methods can describe the entire valence and conduction bands while perturbative methods such as **k.p** theory accurately describe band structures very close to a high symmetry point [7]. It is the latter of these theories which is used in chapters 3 and 4 to calculate the band structure of the InAs/GaSb heterojunction.

Before continuing the discussion, it will be useful to examine the atomic structure of some of the elements which make up the various III-V semiconductors. Consider, for example Ga and As,

Ga $1s^2 2s^2 2p^6 3s^2 3p^6 3d^{10} \mathbf{4s^2 4p^1}$

As $1s^2 2s^2 2p^6 3s^2 3p^6 3d^{10} \mathbf{4s^2 4p^3}$

The outermost electrons are *s* or *p* type and in fact it is found that even in the crystalline semiconductor, the electrons in the valence and conduction bands will retain this type of character, even though they are 'free' Bloch electrons. The outer *s*-levels will depopulate, donating their electrons to the empty *p*-states and will form covalent bonds. After hybridising into bonding and antibonding orbitals and, because of the large number of interacting unit cells, they are broadened into bands. The deeply bound s^2 antibonding orbitals form the conduction band, with the p^6 bonding orbitals forming the valence band. The resulting tetrahedral atomic arrangement provides the crystal with a zincblende structure consisting of two inter-linked face centred cubic Bravais lattices with offset of $(ai+aj+ak)/4$ where a is the lattice constant (Figure 1.1).

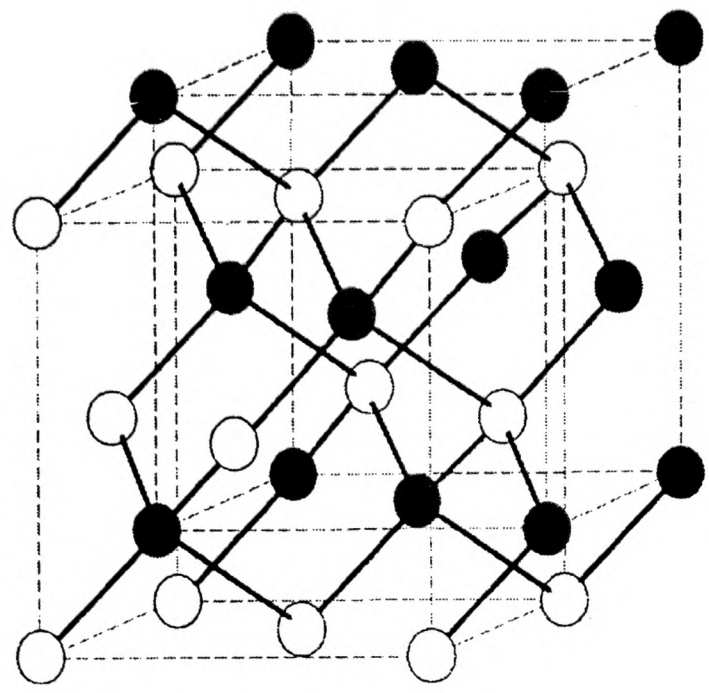


Figure 1.1. Conventional unit cell for the zincblende structure. It consists of a face centred cubic lattice with a basis of two elements, where each is offset in real space by (¼*l*, ¼*l*, ¼*l*) from the other where *l* is the lattice constant.

The six occupied *p*-states (valence band) are nominally degenerate in energy at $\mathbf{k} = 0$, but split due to interaction of the angular momenta of the valence band states with the crystal potential (the spin-orbit interaction). This results in a four-fold degeneracy at the band edge and a two-fold degeneracy lying lower in energy (the spin split-off band). For $\mathbf{k} \neq 0$, the four-fold degeneracy splits, forming the light and heavy holes (calculated dispersions of the electron and hole states in bulk InAs and GaSb are presented in chapter 3, Figure 3.1). The relevant examples of band structure for bulk InAs and GaSb are given in Figure 1.2. Note that both the conduction and valence band have extrema at the Γ point separated by an energy gap, a characteristic feature of all III-V semiconductors. Free electrons are thus likely to populate the conduction band in the region of the Γ point and similarly free holes will populate the Γ point valence bands. This important detail is necessary when trying to model the system using for example **k.p** theory which only lends itself to regions in **k**-space that are close to a high symmetry point. The semiconducting

behaviour of III-V materials then occurs because this gap may be small (as in the case of InSb) or it can contain doping levels within ~k_BT of either band (as in GaAs).

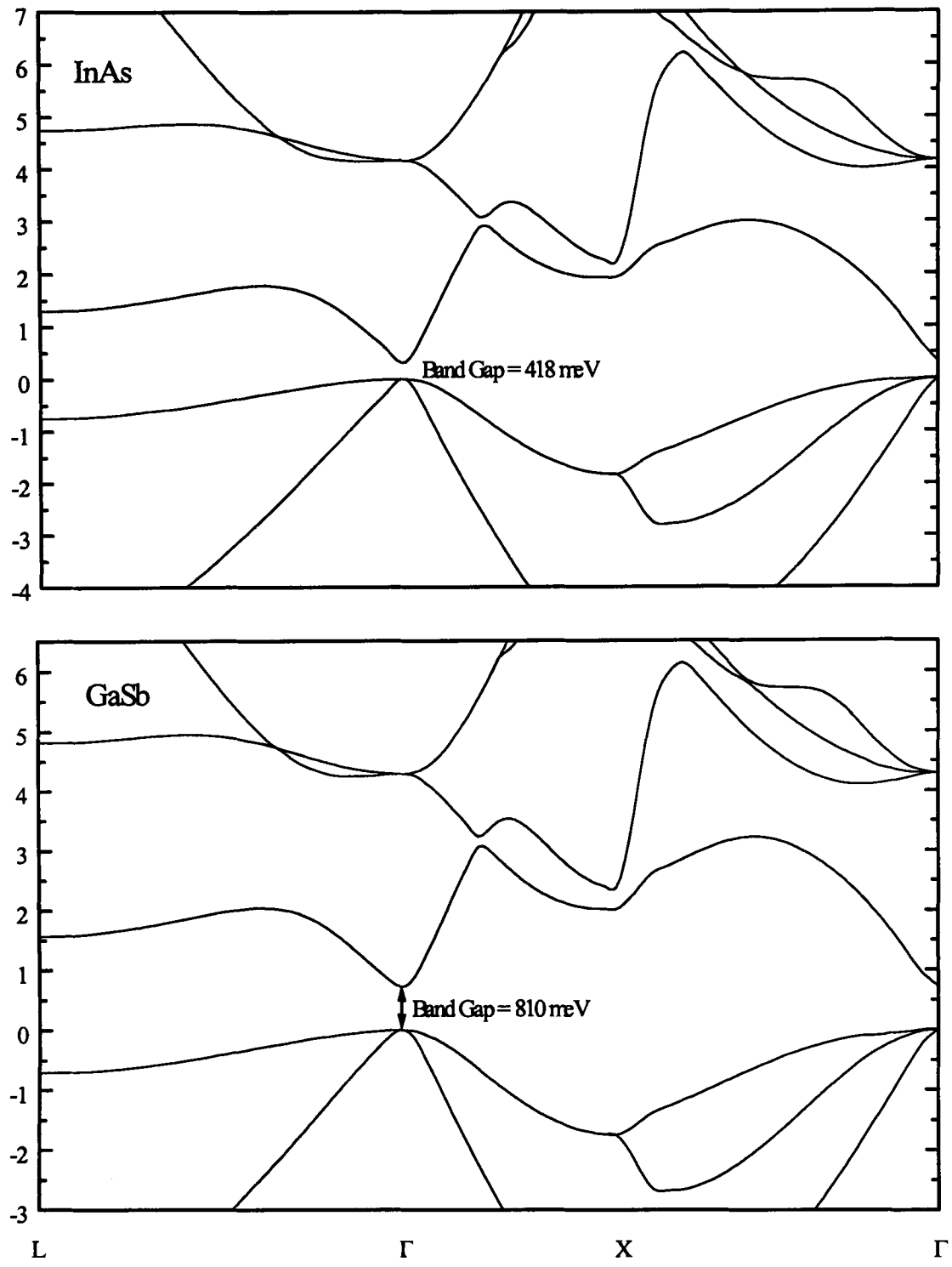


Figure 1.2. The electronic bandstructure of bulk InAs and GaSb between various points of symmetry, as calculated from the pseudopotential technique of ref. [8]. The valence band maximum has been taken as the zero of the energy scale (the Γ-point).

1.2.1 The Brillouin Zone

The reciprocal lattice of a crystal lattice is that described by the set of vectors **G** such that

$$e^{i\mathbf{G}.\mathbf{T}} = 1 \qquad (1.1)$$

where **T** is the set of real space vectors which describe the Bravais lattice of the crystal. For an fcc Bravais lattice, it can be shown that the reciprocal lattice is body-centred cubic with a primitive cell volume of $4(2\pi/a)^3$. The Brillouin zone is then defined as a primitive cell in the reciprocal lattice and is the smallest volume entirely closed by the planes that are the perpendicular bisectors of the reciprocal lattice vectors drawn from the origin. Within the first BZ there are points which have higher degrees of symmetry and will therefore feature more strongly in any observed physical process. They are labelled in Figure 1.3. The work in this thesis is concerned with the BZ centre at $\mathbf{k} = 0$ which is labelled as the Γ point. In describing the transport characteristics of the SHET under varying pressure (chapter 3), states further away from this point are shown to have a small effect, and further work when the SHET is under magnetic field (chapters 5 and 6) is consequently interpreted as occurring between carriers only at this point.

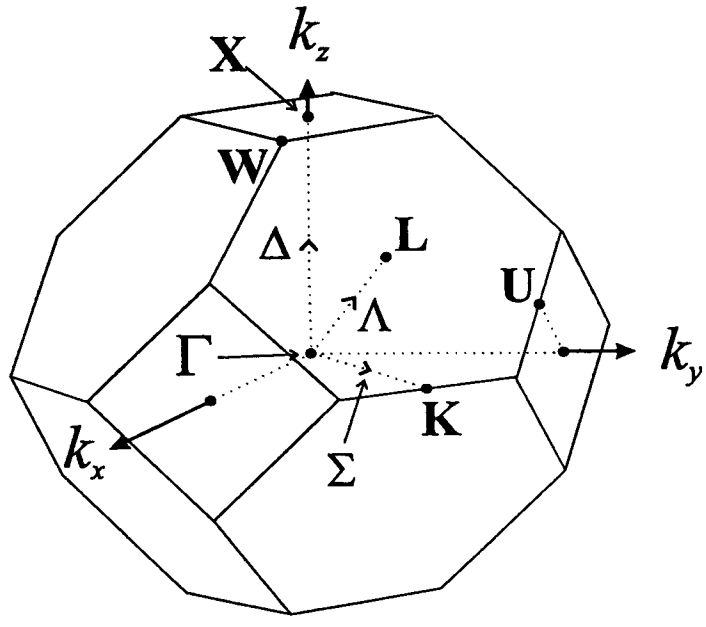


Figure 1.3. First Brillouin zone of the zincblende crystal lattice

1.3 Heterostructures

Since essentially all the electronic and optical properties of semiconductor devices are dependent upon the bandstructure, the ability to tailor it is obviously a powerful tool offering the possibility of designing novel devices with superior performance. This can be achieved by alloying two or more semiconductors, use of built-in strain via lattice mismatched epitaxy and the use of heterostructures to cause quantum confinement. The latter of these has been realised through the advent and improvement of controllable growth techniques such as Metal Organic Vapour Phase Epitaxy (MOVPE) and more recently that of Molecular Beam Epitaxy (MBE). While earlier growth methods could grow high quality single crystals, it was difficult for these techniques to abruptly change semiconductors during growth. MOVPE and MBE techniques, however, make it possible to 'grow' very pure and well ordered

semiconductors on top of each other with the unprecedented precision of one atomic layer. This leads to new optical and electrical devices whose properties are determined by the quantum confinement of electrons and holes throughout the entire heterostructure[1]. As an example, consider the $Al_xGa_{1-x}As$-GaAs-$Al_xGa_{1-x}As$ quantum well (Figure 1.4) where the band line-up confines the carriers in the z direction so that essentially a 2D electron system[2] forms with a free electron dispersion in the x-y plane. Thus, the electron energy can be written as,

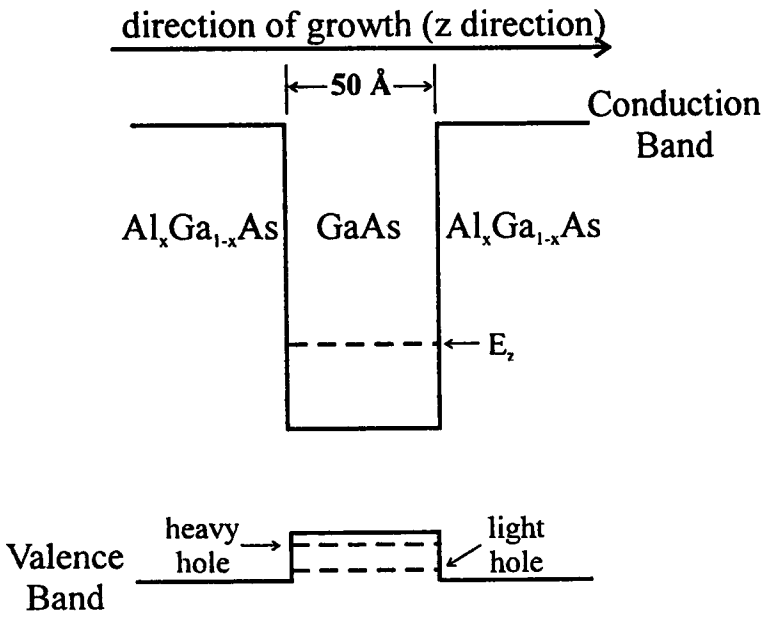


Figure 1.4. Schematic representation of the band structure of a GaAs/$Al_xGa_{1-x}As$ quantum well neglecting any band bending, showing confinement of electrons and holes in GaAs in the direction of growth with an indication of a typical well width L.

$$E = E_z + \frac{\hbar^2}{2m_{\parallel}^*}\left(k_x^2 + k_y^2\right) \qquad \textbf{(1.2)}$$

where E_z is the energy of the carriers in the z direction and $m_{\parallel}^*$ is their effective mass in the plane perpendicular to the interface. Similarly, 2D hole systems form in the valence band. For a simple infinite quantum well, the electron confinement energy is given by,

$$E_z = \frac{n^2\pi^2\hbar^2}{m_{\perp}^* L^2} \qquad \textbf{(1.3)}$$

For a more realistic quantum well, of the type shown in Figure 1.4, E_z will similarly depend on the well width L. The energy separation between states of differing index number n therefore is roughly inversely proportional to the square of the well width – by varying this value the energy levels within the heterostructure can be tuned enabling the design of opto-electronic devices over a wide wavelength range.

---

[1] Confinement is not restricted to one dimension. Continuing efforts in advanced epitaxial techniques are being dedicated to realizing confinement in two dimensions (quantum wires) and all three dimensions (quantum dots).

[2] The system is more accurately described as being *quasi* 2D as the confinement potential acts over a finite length. In this case the 2D DOS is slightly modified by the profile of the 3D DOS (shown in Figure 1.5).

The filling of the subbands themselves is determined by considering the density of states (DOS). For parabolic bands in the (x, y) directions, the 2-dimensional DOS is found to be independent of energy [9],

$$\rho_1 = \frac{m_{\|}^*}{\pi\hbar^2} \tag{1.4}$$

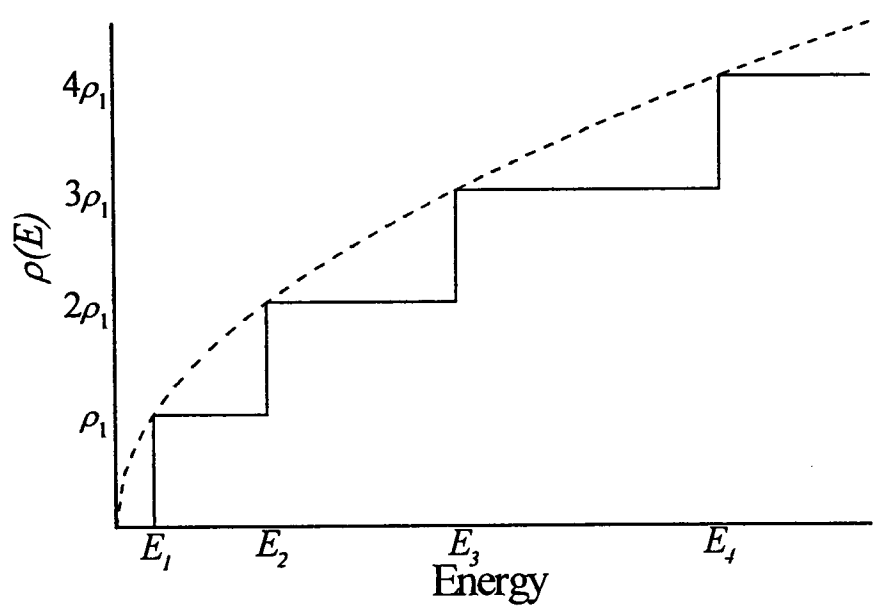


Figure 1.5. The density of states for a quasi 2D quantum well are integral multiples of (1.4). E_1, E_2,... are the bound state energies for the potential confining the electrons. The broken curve shows the square root energy dependence of the density of states for the 3D electrons in a film of large thickness.

Adding together the densities associated with all the bound states gives the total density shown in Figure 1.5. As the well width increases, the bound state energies become more closely spaced so that the steps in the DOS become more difficult to observe. The DOS then approaches the smooth form appropriate to 3D free electrons indicated by the broken curve in Figure 1.5.

In the absence of band coupling, bound states in triangular potentials also produce free 2D systems in the (x, y) plane. The 2D DOS is then similarly step-like. In the presence of coupling however, the problem becomes more difficult. I return to this point in chapter 4.

1.3.1 Structure Types

The $Al_xGa_{1-x}As$-GaAs-$Al_xGa_{1-x}As$ system above is an example of a 'type I' system, i.e. the quantum wells for the holes and electrons appear in the same material. Other heterostructures can be engineered with the band lineups such that the electron and hole quantum wells are in different materials. They are termed 'type II' with two distinct types: staggered (InAs/AlSb) or broken gap (InAs/GaSb, and studied here). Figure 1.6 summarises these three distinct ways in which the conduction and valence

bands can line up at the interface between two semiconductors. Further charge transfer and/or doping effects will alter the band profiles from their straight line bulk case and make them bend (section 1.5). The heterostructure can then quantum mechanically confine electrons and holes near the interface where the band bending occurs as well as in any well or barrier. In the case of the InAs/GaSb SHET, the carriers will only be confined in the resulting triangular potential well near the interface.

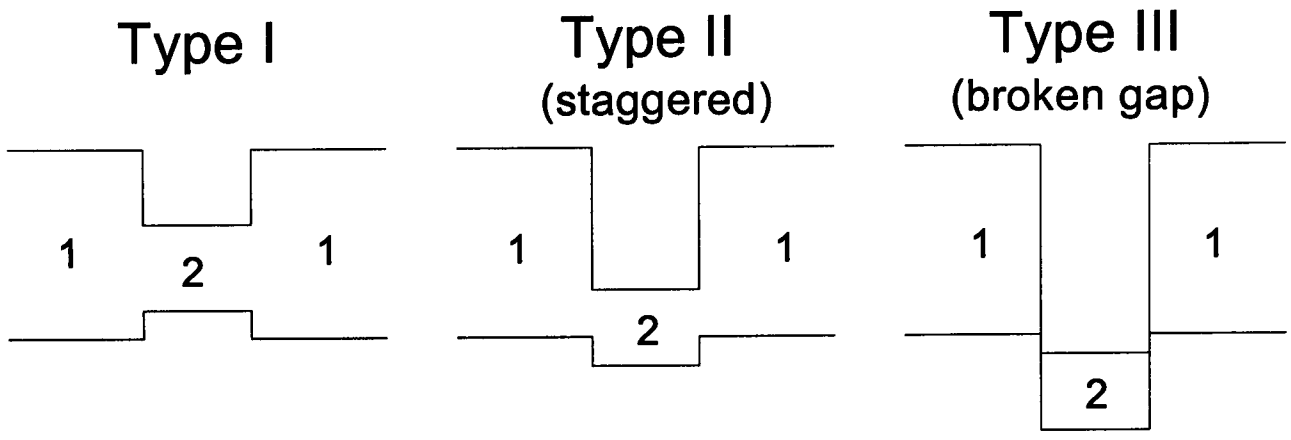


Figure 1.6. Schematic of the three distinct ways in which the conduction band valence bands can line up at the interface between two semiconductors.

1.4 The Esaki Tunnel Diode

At this point it would be instructive to introduce the 'Esaki Tunnel Diode', a device with transport behaviour similar to that of the structure under investigation in this thesis - the InAs/GaSb SHET. Such a device, proposed and demonstrated in 1958 [1] is basically a heavily doped (10^{19} - 10^{20} impurities cm^{-3}) *p-n* junction and was predicted to show Negative Differential Resistance (NDR), i.e. a regime of decreasing current under increasing bias voltage

With such high doping concentrations the valence band of the *p*-type part is degenerate in energy with the conduction band of the *n*-type region at zero bias (Figure 1.7(1)). The uppermost occupied state is at the Fermi energy E_F, so that there are empty levels at the top of the valence band on the *p*-type side, and occupied levels in the conduction band on the *n*-type side. When the junction is biased (Figure 1.7(2)), electrons tunnel across the narrow junction to fill the empty levels in the valence band on the right. The current rises with applied voltage until it reaches a peak. Any further increase in bias reduces the number of crossing electron and hole

states available for tunnelling and the current begins to grow weaker (Figure 1.7(3) and (4)). By point (4), there are no available electron and hole states a the same energy and so any tunnel current is blocked by the band gap. At higher bias still (Figure 1.7(5)), the increasing current is due to the increasing thermal current. The high doping means that the junction is very narrow (~100Å). Since the time of flight of the tunnelling electrons is proportional to the length of the electron path, the tunnel diode can be used as a fast switch. The most remarkable property of tunnel diodes is the negative slope of the current-voltage curve - this means that the system has negative differential resistance in that region that can also be technologically exploited. Not only does the InAs/GaSb SHET exhibit NDR, but the mechanism is similar to that operating in the Esaki Tunnel diode. This is elaborated upon in more detail in the following section.

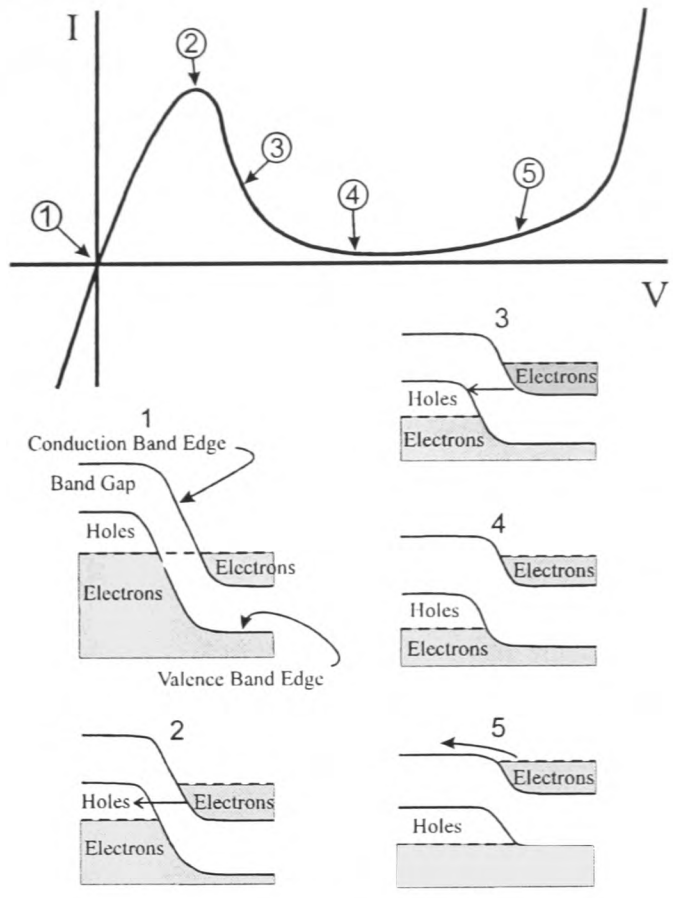


Figure 1.7. Schematic IV characteristic of an Esaki Tunnel diode exhibiting NDR with representations of the band structure at various positions on the curve.

1.5 The InAs/GaSb System

Heterostructure research has primarily been centred around the nearly lattice matched GaAs/$Al_xGa_{1-x}As$ system. Its uses were realized long ago in the early seventies [10] and, in comparison, with the first proposal of the InAs/GaSb nearly lattice matched system during the late 70s by Sai-Halasz [11], the antimonide family of heterostructures is relatively new.

Figure 1.8 shows the band line-ups of both InAs and GaSb. As the valence band of GaSb lies well above the conduction band of InAs, the SHET is described as being extreme type II in nature. It is exactly the result of this type of band line-up between

the two materials which gives the InAs/GaSb SHET its unique and unusual properties. When brought together to form the heterostructure, charge is transferred across the interface in a process of 'internal compensation' preserving the continuity of the Fermi level across the structure. Electrons leave the GaSb band and flow into the InAs conduction band, leaving behind holes. An electric field is set up causing the bending of the conduction and valence bands in accordance with Poisson's equation. The triangular potentials near the interface will now be able to confine charge in the *z* direction resulting in a two dimensional electron gas in the InAs coexisting back to back with a two dimensional hole gas in the GaSb.

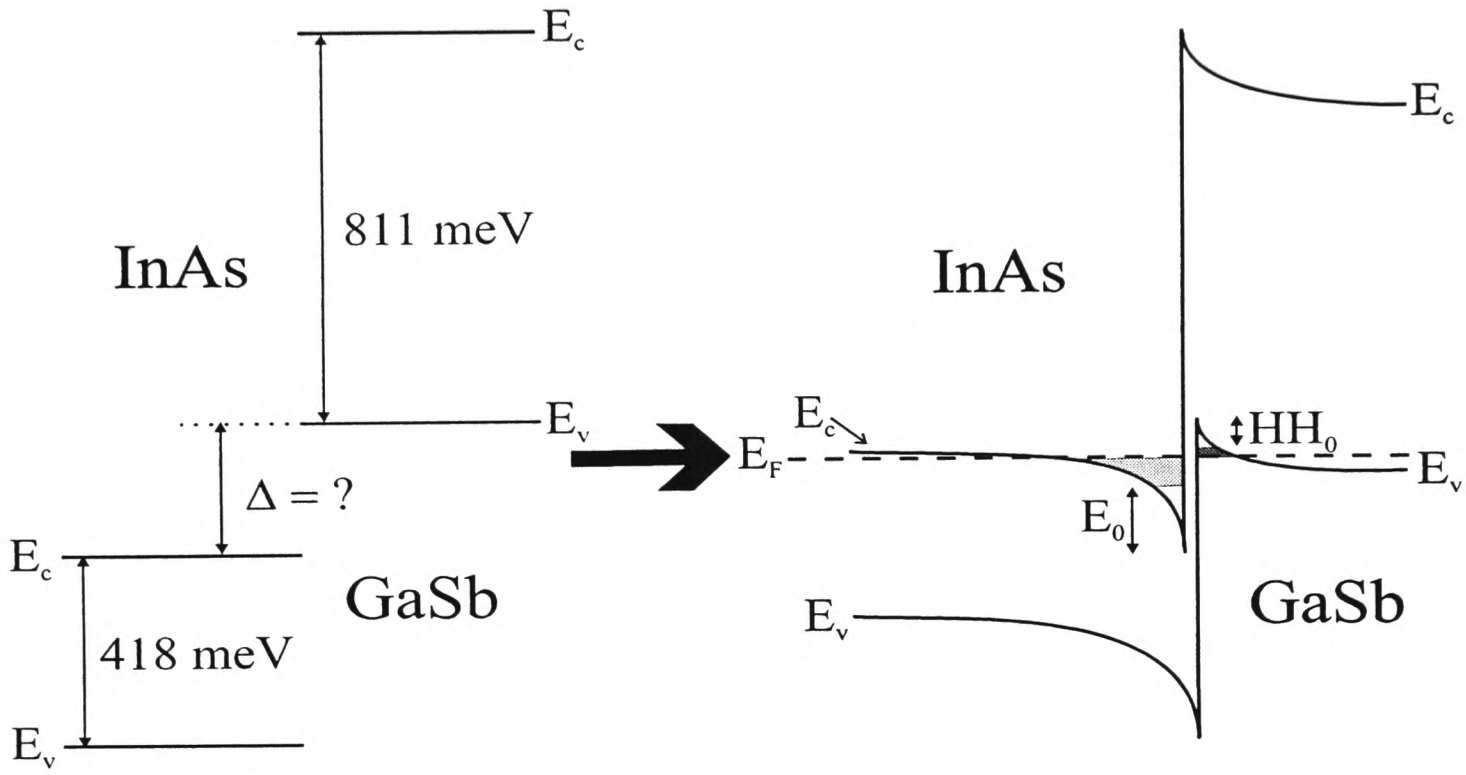


Figure 1.8. The left hand side shows the relative energies of the conduction and valence band extrema at 0K with the value of the band overlap, Δ, as yet unknown (approximately 100-200 meV). The right hand side shows a schematic SHET band profile at 0K, where a charge transfer process results in the back to back confinement of quasi 2-dimensional electron and hole gasses at the interface.

The charge transfer process therefore yields very high intrinsic 2D mobile charge concentrations of very high quality without the need for potentially performance degrading doping. Consequently, these conduction devices result in high peak current densities. With the added possibility of including the nearly lattice matched barrier material AlSb in the epitaxial growth sequence, the possibility exists for further improvements to antimonide based transport or optical devices (section 1.6 and references 12, 13, 14, 15, 16, 17, 18, 19).

1.5.1 Resonant Conduction

Figure 1.9 shows a sample result of the IV characteristic of an InAs/GaSb SHET at 4K. A number of features can be immediately seen: *i)* a linear reverse bias trace, *ii)* a zero bias kink after which is *iii)* a linear increase in current with bias, *iv)* an NDR region and finally *v)* a region after the NDR valley again where the current increases with bias (but now non-linearly). This section aims to detail the nature of the conduction mechanism in the SHET (in the absence of magnetic field) and thus it will include an explanation of each of the above, though not necessarily in the given order.

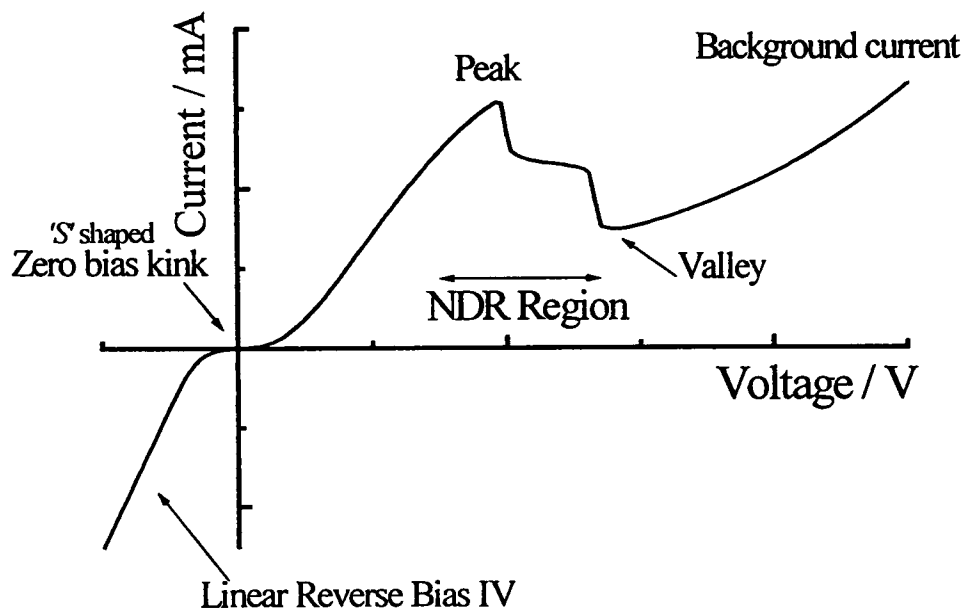


Figure 1.9. IV trace for an 'InSb-like' interface sample at 4K showing the main feature in the trace. Circuit oscillations lead to a 'step' in the NDR region [4, 20, 21].

The transport mechanism itself can be appreciated by utilising a very simplified two subband picture of the SHET in which conduction is assumed to occur through electron and heavy holes only. It assumes that there is no interaction between the electrons and the holes and they therefore are completely free to move in the *xy* plane. With their motion confined in the *z*-direction, their motion is governed by equation (1.2). Thus, we have a free 2D electron gas in the InAs existing in the energy range between the first confined level and the Fermi energy. In the GaSb exists a free 2D heavy hole gas between the Fermi energy and the first confined hole state. Under zero applied bias, the Fermi energy is continuous throughout the interface (Figure 1.10a).

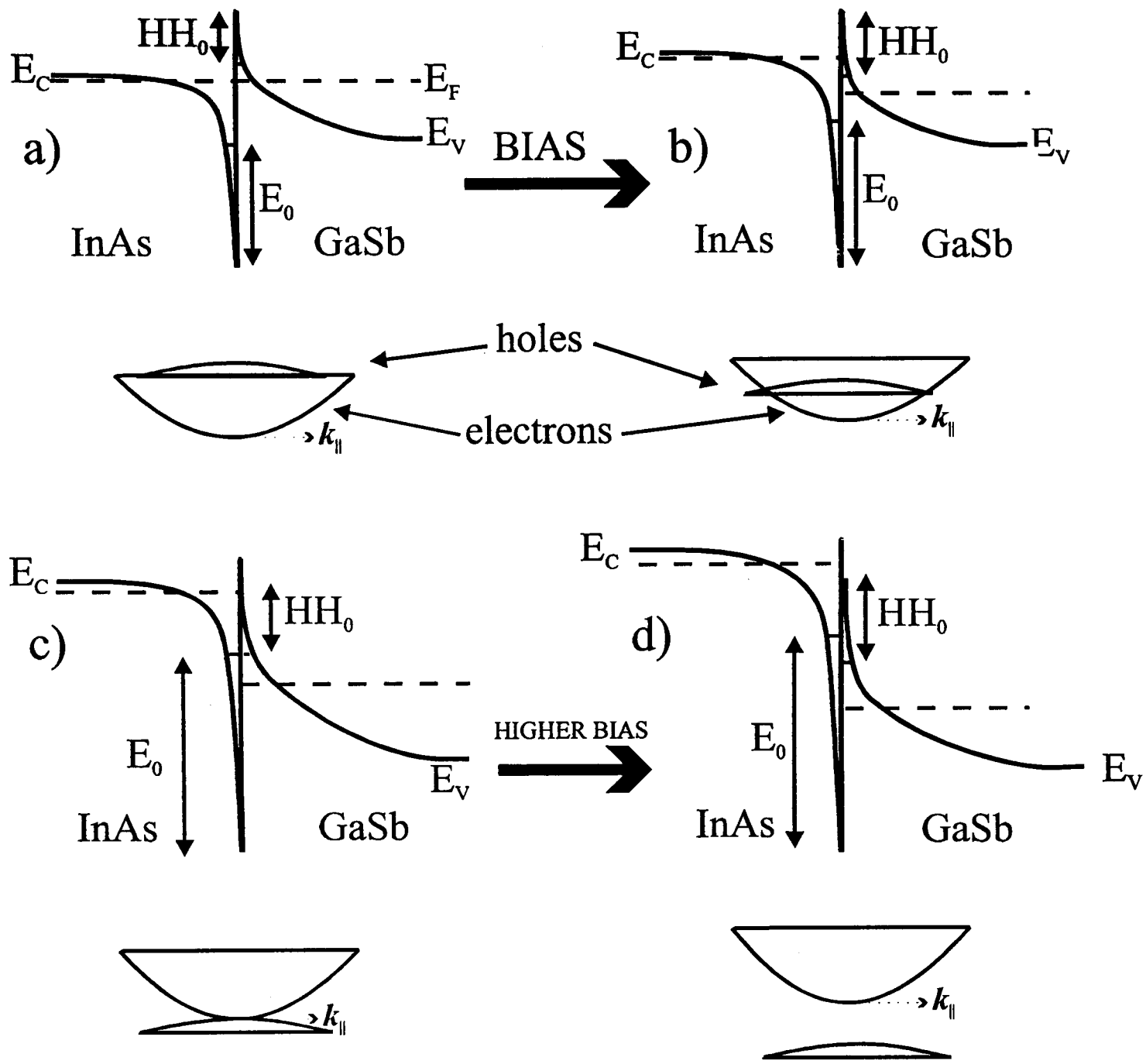


Figure 1.10. a) Shows the zero bias, zero temperature SHET band edge profile in the vicinity of the Fermi energy. Application of forward bias (InAs negative with respect to GaSb) increases the electron (hole) concentration which increases the band bending, resulting in an increase in E_0 (HH_0) which is shown in the remaining diagrams. Also shown are the relative positions of the in-plane dispersions for electrons and heavy holes for both cases (light and split-off hole dispersions are not shown for clarity) .

When a small forward bias is applied, the electron concentration will rise thereby increasing the band bending and raising both the electron confinement energy and the quasi electron Fermi level. Similarly, the hole confinement energy and quasi hole Fermi level will fall. Though there is an energy overlap between the electrons and holes, tunnelling is not possible if parallel momentum $k_{||}$ is to be conserved [22], since the maximum parallel momentum of the holes is significantly less than the parallel momentum of electrons with the same total energy. With a further increase in (small) bias, tunnelling is still prevented until holes at the quasi Fermi level have the same energy as electrons with the hole Fermi wave vector. Thus, up until this bias, the

tunnelling current will be zero so accounting for the so-formed 'S' shaped kink near zero bias. From then on however, hole states can tunnel through electron states (Figure 1.10b). The current increases monotonically with increasing voltage as the number of hole states increases. The point at which the maximum tunnel current can be thought of as being reached when the quasi hole Fermi level is aligned with the bottom of the electron subband. Any subsequent increase in voltage leads to a monotonic reduction of the current (NDR) until it vanishes at a bias V_c when the hole confinement energy reaches the electron confinement energy and no electron and hole states have the same energy (Figure 1.10c).

This rather simplistic picture neglects a few important effects which alter the conduction mechanism. Firstly, phonons may allow electrons to scatter into hole states. This can occur at any value of $k_{||}$ and is capable of providing a significant current beyond V_c (Figure 1.10d). A major part of this work is in fact to determine if at all such phonon processes occur and if they are interface dependent. The actual details of these results are left until chapters 4 to 6 as the aim of this section is to provide a short insight into conduction in the SHET. Another important effect that the above discussion neglects is electron-hole and heavy hole-light hole coupling. Band mixing effects between electrons and holes can be successfully neglected in GaAs/AlGaAs systems because the separation between conduction and valence band states is large. In the InAs/GaSb SHET, band mixing introduces large band non-parabolicites so that the in-plane free electron/hole dispersion picture is in fact a significant approximation [23]. Chapters 3 and 4 detail the **k.p** method applied to the InAs/GaSb SHET which for the first time to take into account these non-parabolic effects caused by band mixing.

Various conduction mechanisms have been suggested [5] to explain the variation of the current beyond the NDR region, termed the background current. These are summarised below,

- One step tunnelling of electrons from the InAs to GaSb conduction band or holes from GaSb to InAs valence band. However, according to previous calculations [5] this is unlikely as the GaSb conduction band remains well above the InAs conduction band (and similarly for the valence bands) at high biases. In addition

as the bands will have uncrossed at such high bias, states at finite $k_{||}$ will be restricted to existing on one side of the interface: those in InAs predominantly electron-like and those in GaSb hole-like. Thus band mixing is also unlikely to be a significant background current source.

- Thermal excitation of electrons from the conduction band in InAs into the GaSb conduction band (and similarly excitations of holes into the InAs valence band). However the lack of any fit between high bias currents and the thermionic emission theory (via the Richard-Dushman equation), the temperature insensitivity of the valley and the fact that large background currents even at 1K are observed suggest that the role of thermal contribution is small [5]. Note that Shen [24], in contrast, has been able to prove that the unexpected large background current in the InAs/AlSb/GaSb/AlSb/InAs system is partly due to this thermal contribution.

- The role of impurities aiding thermal or tunnelling conduction remains unclear. A low background doping and consequently a low impurity density of states would be unlikely to provide any significant contribution to the background current.

- Again the possibility exists for phonon mediated tunnelling contributing to the background current. These may allow electrons (holes) to tunnel into local impurity levels located in the band gap and then lose (gain) energy through phonon emission into the GaSb valence (InAs conduction) band.

This perhaps is the least well understood part of the IV trace of the SHET. With studies focused more on the NDR region, it seems that the study of the background current is relegated to a secondary position, though with the various possible conduction mechanisms (or combinations of) suggested above, there is clearly a rich amount to be learnt through resolving its component sources.

In reverse bias, the SHET exhibits an altogether different IV curve - with bulk GaSb valence band states and bulk InAs conduction band states overlapping, a current

proportional to the voltage flows, rather like reverse bias in an Esaki tunnel diode but without the barrier.

This introduction into the operation of the SHET lays the foundations to understanding its IV characteristics. In reality however, band mixing, inelastic processes and interface effects all affect the conduction mechanism and it is the aim of this work to determine which processes are responsible for tunnelling and in what proportion. The conclusions will be discussed in detail in later chapters.

1.5.2 The SHET Interface

The lack of any common element in the bulk materials of the InAs/GaSb heterojunction allows structures to be grown that are nominally identical except for the monolayer at the interface. Two possibilities exist. Either an 'InSb-like' or - 'GaAs-like' interface may be grown (Figure 1.11). This monolayer in turn determines the band overlap Δ (measurements by Daly *et al* [25] show it to be 155±5 meV and 125±5 meV respectively), and the diode vertical transport characteristics [26]. It is not unreasonable to assume that the different responses of the two sample types could be explained by the difference of 30 meV. However, this is found not to be the case. Pressure and field measurements presented (here and earlier in [5]) show the two interface types support very different conduction mechanisms, with the 'InSb-like' samples behaving more predictably than the 'GaAs-like' samples. With the added **k.p** analysis taking into account band mixing effects as well as decoupled models taking into account the effect of magnetic field, this thesis will provide further clues to aid in discovering the underlying reasons (or additional processes) responsible for the difference. These are presented in the remainder of the thesis and a more detailed discussion on Δ is reserved until section 4.3.

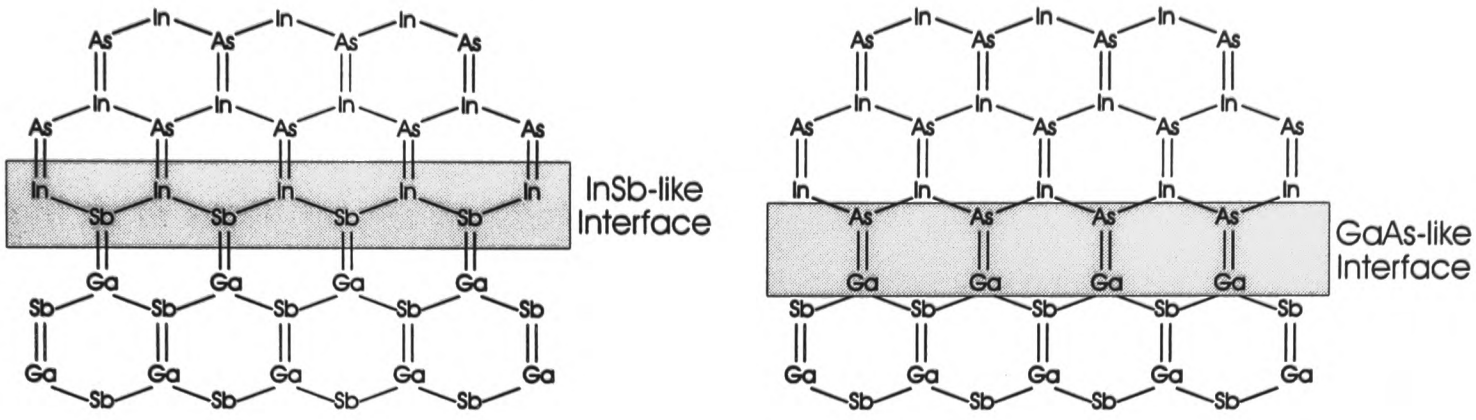


Figure 1.11. [110] projections of the SHET with an 'InSb-like' interface and a 'GaAs-like' interface. Single lines are bonds in the plane of the paper and the double lines are projected up from or down through it.

1.6 Applications of Antimonide Based Materials

The nearly lattice matched InAs and GaSb (along with AlSb) offer a large range of possible band alignments which can be used to fabricate a wide array of structures for transport and optical use. The applications of antimonide based materials are therefore tremendous and include devices for infra-red gas detectors, laser technology and long haul communications. The following section, as a representative cross-section lists some antimonide based devices under development.

1.6.1 Infra-red Lasers

Recent developments exploiting the novel band gap alignment between InAs and GaSb have led to a realisation of type II quantum cascade (QC) lasers for high power mid and long wavelength IR source applications. The basic unit in a type II QC laser structure comprises two coupled QWs residing in conduction and valence bands respectively, with the valence band edge in one QW higher in energy than the conduction band edge of the other QW. The approach, utilising intersubband transitions is determined, not by the band gap, but by the small energy separation of conduction subbands arising from quantum confinement in QW structures based on wider band-gap semiconductor materials. A bias is applied to the structure so that the hole level in the GaSb layer becomes resonant with the lower electron bound state in the InAs well. Electrons will therefore tunnel out of the lower confined state very quickly. They cannot tunnel out of the upper state because this lies in the forbidden gap of the layers to its right and a population inversion is therefore created. The

electrons in the upper state must undergo a radiative transition to the lower state before tunnelling out of the InAs well. A significant advantage of such a device over others is that the lasing wavelength can be tailored over a wide spectral range from mid IR to submillimetre by changing either the composition or thickness of the QW layer. Yang *et al* have provided an analysis and demonstration of such lasers [27] with verification by Hasenberg *et al* [28]. With the emission wavelength of current semiconducting lasers mainly in the near IR, such antimonide based lasers producing light in the atmospheric IR transmission windows (3-5 and 8-12 μm) would be of tremendous benefit. Their potential applications would be widespread and could, as examples, be used in atmospheric pollution monitoring, medical diagnostics and communications.

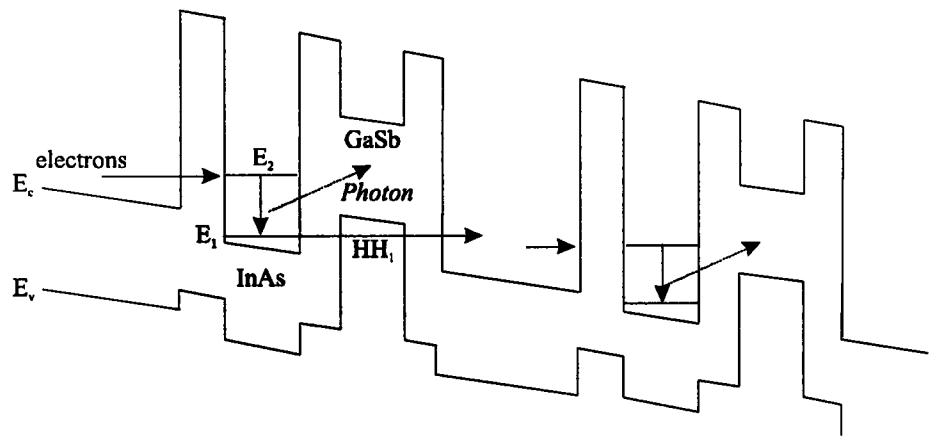


Figure 1.12. A section of a Quantum Cascade Layer based on intersubband transitions in an InAs/AlSb/GaSb type II quantum well structure. By varying the composition and thickness of each layer, the laser energy can be fine tuned. Note also the possibility of direct transitions between electron and hole states ($E_1 - HH_1$ for example) giving another mechanism to produce light.

The optical applications of antimonide based materials do not limit themselves to lasers. High efficiency LEDs based on GaInAsSb/GaSb and GaInAsSb/GaAlAsSb structures [29] have been fabricated in addition to high performance superfast GaInAsSb/GaAlAsSb photodiodes [29, 30], etc. and indicate the established use of antimonides in modern optoelectronics.

1.6.2 Microwave diodes

An obvious, yet very important application of devices exhibiting NDR is their use as oscillators extending into the microwave frequency band. At biases near the NDR the diodes can be inserted in a resonant circuit or cavity generating oscillations at the resonant frequency. Recently, Brown *et al* [31] have reported oscillations at

frequencies between 100 to 712 GHz using an InAs/AlSb double barrier structure. Not only did their device yield frequencies in excess of those produced by the GaAs/AlAs material system, but the measured power density at the resonant frequency was considerably larger. Clearly, such antimonide based devices exhibiting NDR might be used as microwave sources for communications and radar.

1.6.3 Transistors

One of the earliest applications of the InAs/GaSb material systems, exploiting the novel energy band line ups was in transistor technology [32]. As early as the late 80s, the hot-electron transistor [33] was fabricated by Chiu *et al* who used AlSb, InAs and GaSb as the emitter, base and collector respectively. At around this period, the bipolar [34] and field effect transistors (FETs) [35] were also developed, again utilising InAs and GaSb as well as Al based materials. More recently, Tehrani *et al.* [36] designed a three terminal resonant interband tunnelling FET, based on the InAs/AlSb/GaSb resonant tunnelling diode integrated into the drain or source region of an InGaAs/AlGaAs/GaAs FET. Their device demonstrates the possibility of combining the best tunnelling diode structure with the best of FET technology to achieve the highest peak to valley ratios and gain. The same group were also responsible for the Stark effect transistor, a device which made use of Stark shifts of energy levels in a quantum well to exhibit transistor action at room temperature. Such devices have the potential to be used in the fabrication of high speed and high frequency circuits.

1.7 Outline of Thesis

This section provides a brief outline of the contents of the subsequent chapters.

Chapter 2 provides a summary of the experimental methods used in collecting the data for this thesis as well as briefly reviewing the work of Mason *et al*, who instigated the programme of growth and development that ultimately has lead to experimentally accessible samples. Detail in these chapters for both sections is deliberately avoided as it has been well documented in previous work [5].

The next three chapters present experimental results and the results of theoretical models used to aid the understanding of the conduction mechanism in the SHET. They therefore represent the central chapters of this work. Chapter 3 and 4 collectively present a study of the SHET under pressure using a full **k.p** Schrödinger-Poisson model taking into account band mixing effects. As a substantial improvement to the decoupled model employed in [5], the results of this chapter are crucial to corroborating their conclusions, namely that resonance tunnelling in 'InSb-like' interface samples is consistent with the mechanism outlined in section 1.5.1, though inconsistent for tunnelling in 'GaAs-like' samples.

Chapter 5 provides a detailed account of the effect of magnetic field perpendicular to the interface on the IV trace of the SHET. Pressure is used as a further parameter in investigating various features that are field induced and analysed using a decoupled model. Evidence for Landau levels in the samples is presented and perhaps unsurprisingly, interface dependent features revealing strong evidence for inelastic processes in both sample types (and especially strong in the 'GaAs-like' samples). The results therefore represent a large step in understanding the origins of the differences in the conduction mechanism.

The effect of magnetic field applied parallel to the interface (instead of perpendicular) in various orientations is investigated in chapter 6. With the results of previous chapters revealing stark differences in the IVs between the two interface types, the results here prove to be no exception. Employing self-consistent calculations again, the results confirm the interface dependent results of chapters 4 and 5 and in addition provide evidence for anisotropy in the hole Fermi surface. Complicated and as yet unexplained features are observed in the 'GaAs-like' samples as the field is rotated. As the reason for the different NDR traces of the two sample types seems to be increasingly explicable through evidence for inelastic processes and even interface effects (chapters 4 to 6), these surprising results remind us that the InAs/GaSb SHET is a system worthy of continuing experimental and theoretical research.

Finally, chapter 7 provides a summary of the new discoveries contained in this thesis, a round-up of work that still has to be investigated and suggestions for continuing the research in the antimonide family of heterostructures.

1.8 References

[1] L Esaki. Physical Review 109 p603 (1958).

[2] A good historical review of NDR in semiconductor systems is given by Esaki himself in the IEEE Journal of Quantum Electronics, 22 no. 9 (1986).

[3] D M Symons *et al*, Physical Review B 49 p16614 (1994). M S Daly, *et al*, Journal of the Physics and Chemistry of Solids 56 p453 (1995).

[4] D G Austing, D.Phil. Thesis, The Pressure Dependence of Vertical Transport in Simple Semiconductor Heterostructures, Clarendon Laboratory, Oxford University (1992).

[5] U M Khan-Cheema, D.Phil. Thesis; Vertical Transport Through an InAs/GaSb Heterojunction at High Pressures and Magnetic Fields, Clarendon Laboratory, Oxford University (1996).

[6] See, for example the Drude and Sommerfield electron free electron models of chapter 6 of C Kittel, Introduction to Solid State Physics, John Wiley & Sons, Inc. (1986).

[7] A good introduction to these methods is given in chapter 2 of 'Fundamentals of Semiconductors' by P Y Yu and M Cardona, Springer-Verlag (1996).

[8] M L Cohen and T. K. Bergstresser, Physical Review 141 p789 (1966).

[9] See M J Kelly, Low Dimensional Semiconductors, Clarendon Press, Oxford (1995).

[10] R Tsu & L Esaki. Applied Physics Letters 22 p562 (1973).

[11] Sai-Halasz, Applied Physics Letters 30 p651 (1977). M Sweeny & Jingming Xu in Applied Physics Letters 54 p546 (1989).

[12] D A Collins, D H Chow, E T Yu, D Z-Y Ting, J R Söderström, Y Rajakarunanayake and T C McGill. Paper in Resonant Tunnelling in Semiconductors - Physics and Applications, edited by L L Change *et al.*, p515, Plenum Press, New York (1991).

[13] Peak to valley ratios (PVRs) of 2.6 have been recorded at 77K for the SHET. See U M Khan-Cheema, P C Klipstein, J M Smith, D G Austing, N J Mason, P J Walker & G Hill, Solid State Electronics 37 p977 (1994).

[14] K F Longenbach, L F Luo and W I Wang. Applied Physics Letters 57 p1554 (1990).

[15] J R Söderström, D H Chow and T C McGill. Applied Physics Letters 55 p1094 (1989).

[16] J F Chen and A Y Cho. Journal of Applied Physics 71 p4432 (1992).

[17] J R Söderström, D H Chow and T C McGill. Applied Physics Letters 55 p1348 (1989).

[18] L F Luo, R Beresford and W I Wang. Applied Physics Letters 55 p2023 (1989).

[19] M P Houng, Y H Wang, C L Shen, J F Chen and A Y Cho. Applied Physics Letters 60 p713 (1992).

[20] H C Liu. Applied Physics Letters 53 p485 (1988).

[21] T C L G Sollner. Physical Review Letters 59 p1622 (1987).

[22] Momentum conservation rules have interestingly been experimentally determined by Smoliner *et al.* in GaAs-GaAlAs heterostructures. J Smoliner, W Demmerle, G Berthold, E Gornik, G Weimann and W Schlapp. Physical Review Letters 63 p2116 (1989).

[23] M Altarelli. Physical Review B 28 p842 (1983).

[24] J Shen. Journal of Applied Physics 78 10 p6220 (1995).

[25] M S Daly, W Lubczynski, R J Warburton, D M Symons, M Lakrimi, K S H Dalton, M Van der Burgt, R J Nicholas, N J Mason and P J Walker. Journal of the Physics and Chemistry of Solids, 56 p453 (1995).

[26] For example, the temperature dependence of the I/V trace in a SHET with a 'GaAs-like' interface is found to be weak, with similar current peak to valley ratios (PVR) at 300 and 77K. The 'InSb-like' SHET, however has a PVR that is very close to 1 at 300K, rising above 2 at 77K [5].

[27] R Q Yang, S S Pei. Journal of Applied Physics 79 p8197 (1996). Also see R Q Yang, Superlattices and Microstructures 17 p77 (1995) and Applied Physics Letters 70 p2013 (1997).

[28] T C Hasenberg, D H Chow, A R Kost, R H Miles and L West. Electronic Letters 31 p275 (1995).

[29] M P Mikhailova and A N Titkov. Semiconductor Science and Technology 9 p1279 (1994). This review article provides further detailed information concerning luminescence and photoelectric phenomena in type II GaInAsSb/GaSb heterojunctions.

[30] See for example, J E Bower, A K Srivatsava, C A Burns, J C DeWinter, M A Pollack and J L Zyskind. Electronic Letters 22 p137 (1986).

[31] E R Brown, J R Söderström, C D Parker, L J Mahoney, K M Molvar and TC McGill. Applied Physics Letters 58 p2291 (1991).

[32] A good review of the use of InAs and GaSb based systems to design transistors, as well as other devices, is given by P S Dutta, H L Bhat, V Kumar, Applied Physics Letters 81 p5821 (1997). Readers may also find more general reading in Physics and Applications of Semiconductor Structures, by M Jaros (Oxford University Press, 1989) useful.

[33] T h Chiu and A F J Levi. Applied Physics Letters 55 p1891 (1989).

[34] A Furukawa and M Mizuta. Electronic Letters 24 p1378 (1988).

[35] K F Longenback, R Beresford and W I Wang. IEEE Transactions on Electronic Devices 37 p2265 (1990).

[36] S Tehrani, J Shen, H Goronkin, G Kramer, R Tsui, and T X Zhu. IEEE Electronic Device Letters 15 p16 (1994).

2.Experimental Techniques

2.1 Introduction 25
2.2 A Brief Overview of Sample Growth and Processing.....25
2.3 Vertical Transport IV Data Acquisition.....27
2.3.1 The High Pressure Russian Cell 29
2.3.2 Continuous and Pulsed Magnetic Fields 31
2.4 References 32

2.1 Introduction

A prerequisite of studying two dimensional semiconductor physics is the availability of *i)* high quality samples grown with near perfect interfaces, and *ii)* suitable experimental apparatus to probe the vertical transport properties of the sample. Though the work here is concerned with the physics behind resonant tunnelling in the SHET, it would be incomplete should the reader not be given an appreciation of the many years of painstaking research that have gone into optimising its growth as well as of the methods used to collect data. This chapter is intended for just this purpose.

The basis for all the experiments reported in this work were carried out on an automated rig. Once the samples were ready to be tested, such a set-up allowed measurements of IV under a combination of pressure and magnetic field (and the corresponding conductance and 2^{nd} derivative traces) to be made. In this chapter, a brief introduction to device fabrication (section 2.2) and experimental techniques (sections 2.3) will be given. For a more detailed exposition of the apparatus, readers are referred to references [1] and [2].

2.2 A Brief Overview of Sample Growth and Processing

The physics behind the work carried out here, and indeed in any modern semiconductor research be it experimental or theoretical, requires the availability of excellent quality structures on which the physicist can perform his or her experiments. Such a requirement has led to what is sometimes known as 'Quantum Engineering' – a term that appropriately describes the growing of structures uniform to the atomic level. Through a program of optimisation started in the early 1990s, the Clarendon benefits greatly from the work of Mason and Walker, the 'Quantum engineers' responsible for much of the sample growth [3]. For my specific case of the InAs/GaSb SHET success of the home grown diodes is reflected by previous reports of highest measured peak to valley ratios [4]. This section is intended to give a very brief introduction to methods used in heterostructure growth and specifically, that of

the development of the 1771 and 1772 series of samples exclusively used throughout this work. For a more detailed review, readers are referred to [3] and [4].

The most commonly method employed for sample growth is that of Metal Organic Vapour Phase Epitaxy (MOVPE) and this has been the method used in the Clarendon. This growth technique essentially passes metal-organic molecules (alkyls) of the group III elements mixed with hydrides, or organic compounds, of the group V elements over a heated substrate. The compounds react and epitaxial layers of the required III-V compound are deposited on the substrate. The source materials are carried by palladium diffused hydrogen through a mixing manifold and into a silica growth cell containing the heated substrate. (The sources used are trimethylantimony for Sb, trimethylgallium for Ga, trimethylindium for In, tertiarybutylarsene for As.) In forming heterostructures, individual layers are formed by allowing two appropriate precursors containing the required group III and group V elements respectively into the silica gel over the heated substrate. At the interface between the layers, the precursors are switched off and the appropriate new precursors are switched on. In the growth of any heterostructure of InAs and GaSb, the lack of a common anion or cation allows them to be grown with the possibility of growing an interface that is either 'InSb-like' or 'GaAs-like'. In practice, this is achieved by staggering the precursor switching in a predetermined manner.

Through a consideration of sharpness of the NDR, hysteresis and reproducibility of the IV, Khan-Cheema (see chapter 5 of [1]) identified the optimal sequence leading to the highest quality samples. In this sequence, the interface is grown by allowing only one of its constituent elements in at a time. For the 'GaAs-like' interface samples for example, the Ga precursor continues for 0.5s after the Sb has been switched off before being turned off itself. Only then is the As precursor switched on, biasing the interface towards 'GaAs-like', followed by the In precursor 0.5s later. Raman measurements and Transmission Electron Microscopy (TEM) performed by Lyapin [5] and Murgatroyd [6] have added weight to Khan Cheema's choice, revealing that this switching sequence produces the best quality of monolayer interfaces. It is this growth sequence therefore, labelling 1771 for samples with an 'InSb-like' interface and 1772 for samples grown with an 'GaAs-like' interface that is used throughout this thesis.

Figure 2.1 details the structure of the InAs/GaSb SHET. A 6000 Å nominally undoped GaSb buffer layer is grown on top of a p^+ GaSb substrate. This is followed by a 3000 Å layer of *n*-type InAs. Once in this form, further processing is required to produce contacted samples ready for testing. Because the interband resonant conduction in InAs/GaSb SHETs yields very high current densities, the size of the working devices are of the order of tens of microns to reduce the current thereby reducing Joule heating effects. This is done by G Hill and co-workers at the University of Sheffield. The details of the processing of the wafers to 10μm devices sitting in cylindrical 'H4' packages are described again in [1] and are not reproduced here.

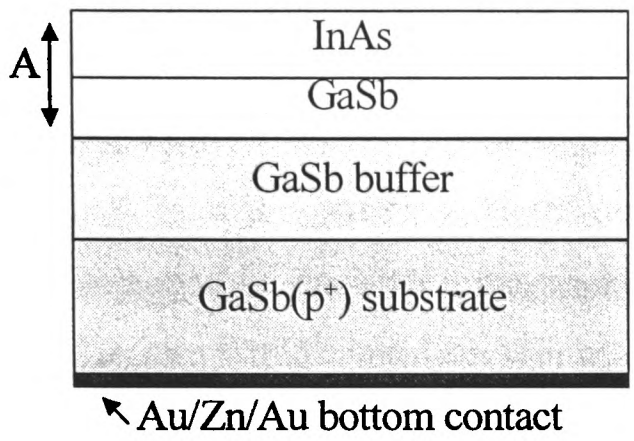


Figure 2.1. Side view of sample indicating active region, A.

2.3 Vertical Transport IV Data Acquisition

With the sample sitting conveniently in the H4 package, contacts are indium soldered to its base and rim using approximately 1 cm of gold wire. Initial measurements were made by attaching the gold wires to a basic insert consisting of copper wires which were subsequently fed to an IV measuring unit. For 4K measurements in magnetic fields, the sample was attached to specially made inserts [7, 8] carefully orientating the sample so that the magnetic field could be applied perpendicular or parallel to the interface. Once that was done, a metal jacket was placed over the insert and sealed. The air was pumped out and replaced by a low pressure of helium gas to serve as a thermal conductor during cooling of the sample in the magnet. During pressure runs or combined pressure-magnetic field experiments, the sample loaded in the cell was attached to an appropriate insert which was then cooled to 4K either in an ordinary cryostat or in the magnet cryostat. Recent improvements in insert design have allowed samples to be rotated in the magnet or to even hold spherical pressure cells allowing high pressure measurements with variable sample orientation in the magnetic field.

The principle behind the IV trace data acquisition is actually very simple and is based on the circuit diagram below (Figure 2.2). An IV unit, designed in the electronics workshop by Smith [9] provides a steady internally generated voltage, V_{in}, typically ranging from -1 to +1V. This is fed into a voltage amplifier, AMP1, which drives terminal A of the sample. Negative feedback keeps AMP2 'ideal' so V_B is equal to the voltage at its positive input, making V_B a 'virtual earth' at close to 0V. Thus, the voltage across the sample is given by V_A. The current fed back through R to the amplifier will exactly cancel the current flowing in the sample, so the sample current is given by:

$$I_S = -\frac{V_I}{R} \tag{2.1}$$

where V_I is the output from AMP 2.

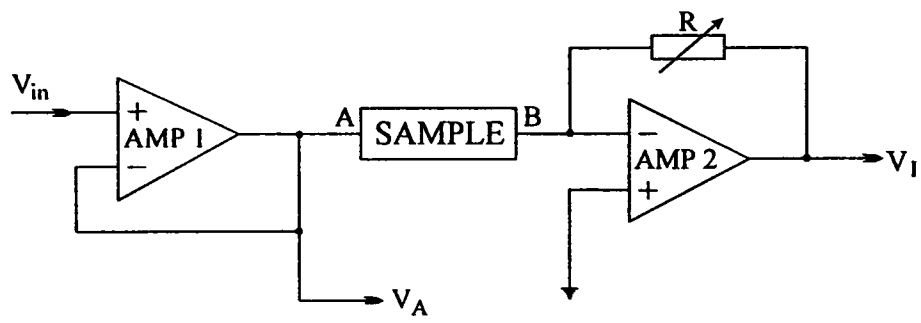


Figure 2.2. Basic circuit for IV measuring unit.

The resistor, R, can be switched between sensitivities of 10 μA/V up to 10 mA/V, allowing a corresponding voltage output range of between 0 and 10V. The current and voltage measurements are fed into two Keithley DMMs (reading V_A to an accuracy of 0.1 mV and V_I to 5 decimal places) which are triggered and read by the computer via an IEEE interface after a preset delay time of around 100ms, necessary to allow the DMMs to settle to an accurate reading. The computer then increments or decreases the DAC voltage by a preset number of bits and the process is repeated. In this way, data sets can be recorded sweeping up or down over a desired voltage range.

Weak features in the IV traces were identified by measuring the conductance (dI/dV) as a function of bias. These are carried out by modulation of the applied dc voltage with a small sinusoidal ac signal. The resulting oscillating component of the current

is measured and fed into a lock-in amplifier where it is multiplied by a reference signal of the same frequency (and phase) as the modulation. Integration of the resulting signal gives a dc voltage which is proportional to the conductance. The dc output of the lock-in amplifier is then measured with a DMM in the usual way. Weaker features still are identified by numerically calculating the derivative of the conductance traces in MicoCal Origin™. Such measurements were extensively used throughout all experiments involving pressure and magnetic field.

In practice, data acquisition is controlled by computer using "NDR for Windows" designed and written by Khan-Cheema [1]. This controls all initialisation procedures, the voltage ramps and the data acquisition.

2.3.1 The High Pressure Russian Cell

The ability to change the band structure of any semiconductor device, and hence any of its observable properties, undoubtedly will lead to a better understanding of the device operation and the physics behind it. A key tool in tunnelling research employed for just this reason is the application of hydrostatic pressure [10]. The results and conclusions of chapters 4 to 6 all have used pressure as a means to alter (reversibly) the band structure of the InAs/GaSb SHET and therefore its IV.

All the pressure measurements were taken exclusively with the 'Russian' pressure cell. This remarkable cell is ideal for combined pressure-magnetic field runs for two main reasons. Firstly, with a diameter of 27mm and length 47mm, it is the only cell available that can fit into the magnet. Secondly, an outer beryllium-copper body and an inner non-magnetic Nickel-Chromium-Aluminium (NCA) alloy allowed it to withstand enormous pressures reaching 27 kbar. In practice however, pressures rarely were raised above 20 kbar as NDR vanished by about these pressures - well within the safety margins of the cell's use. The extreme nature of its size and operating pressures results in a bore of 4 mm - just enough to house one sample, albeit intricately.

Figure 2.3 below shows a cross-section of the cell and a close up of the teflon capsule in which the sample sits. With the set up below, using petroleum spirit as the pressure

medium, the sample was simply compressed using hydraulic press. This presses on the pistons causing the teflon hat to compress. An estimate of the pressure exerted on the sample can be determined from the readings on the hydraulic press. Once this is reached, the upper screw is tightened, transferring the pressure exerted from the hydraulic press to the cell itself. An accurate measure of the pressure can simultaneously be found through a four terminal measurement of the resistance of the manganin wire, also attached to the sample stage. This takes the form,

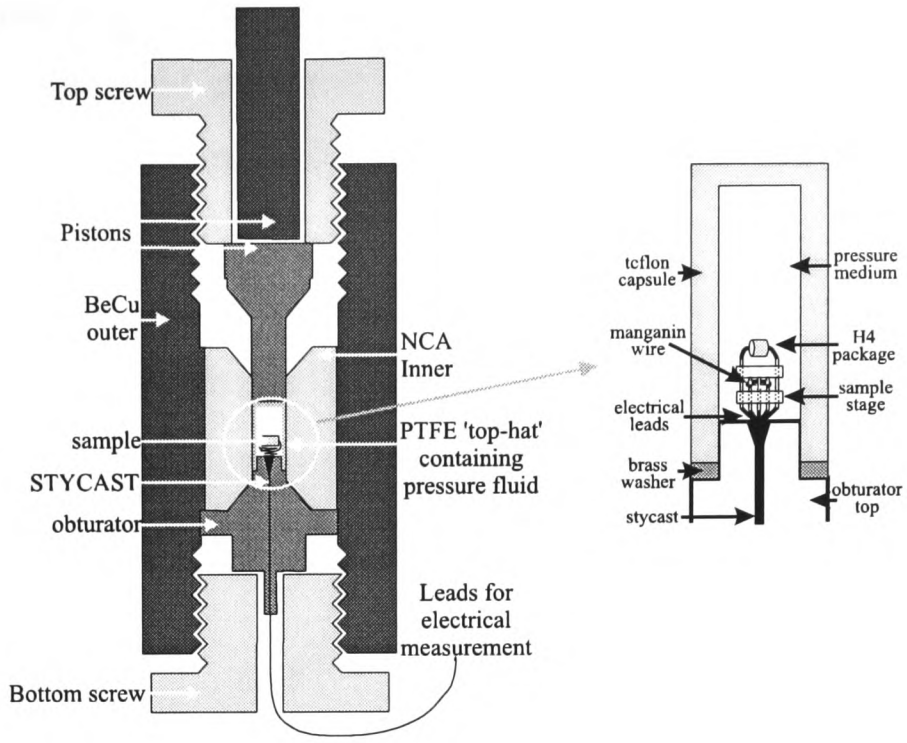


Figure 2.3. Cross-section of the Russian cell and a close up view of the teflon capsule housing the sample.

$$p = \alpha\left(\frac{\Delta R}{R_0}\right) + \beta\left(\frac{\Delta R}{R_0}\right)^2 \qquad \textbf{(2.2)}$$

where R_0 is the resistance of the wire at atmospheric pressure, R_P is the resistance at the pressure at which it is being measured and $\Delta R = R_P - R_0$. The coefficient α and β are 395.3 and 200 respectively at 300K and 391 and 200 respectively at 77K (or 4K) leading to a difference between the pressure at 77K and 300K of roughly 4 kbar [11].

The sample itself sits on a 'sample stage'. To this are connected at the very least 6 wires: two for the sample and four for the manganin manometer. These are passed to the obturator and glued into place by stycast expoxy resin. A brass washer is slotted on to the obturator, followed by a teflon hat containing the pressure medium. The brass is easily malleable so that as soon as pressure is applied by the press, a leak proof seal is made between the obturator and the teflon hat.

Future experiments will be able to exploit the latest technology in pressure cell design. Recently, spherical cells capable of fitting into the narrow superconducting

magnet cryostat have been designed [10]. With an insert designed by H Im allowing the cell to be rotated and able to withstand pressures up to 16 kbar, such apparatus will yield important information on, for example, high pressure angle resolved magnetotunnelling experiments. In the GaAs/AlGaAs double barrier system, such experiments have revealed novel Γ-X mixing effects [12]. The 1 bar equivalent experiments on the InAs/GaSb system potentially reveal information about the anisotropy of the hole Fermi surface and yet more differences in the transport properties of the two interface types (chapter 6), with the promise of further insights under pressure.

2.3.2 Continuous and Pulsed Magnetic Fields

Continuous fields were provided by an Oxford Instruments (OI) superconducting magnet. With the superconducting coils immersed in liquid helium and carrying up to 115A, fields up to 15K can be readily generated. The principle behind its use for the experiments carried out for this thesis is simple. Without any need for detailed temperature control (all measurements taken at 4.2K), liquid helium was transferred to the magnet bath via an OI GFS300 transfer tube. The sample at the end of an insert (or in a pressure cell at the end of the insert) is slowly lowered over a period of 30 minutes into the liquid helium filled magnet. The magnetic field is then swept to the required strength and the IV (or conductance) results taken by the IV measuring unit described earlier. Previous measurements have required the use of a continuous flow cryostat system to enable accurate sample temperature control [1]. This requires the use of an additional Compton pump controlling gas flow across the sample through an adjustable needle valve attached between the liquid helium bath and the cryostat where the sample resides. Extra care is then obviously required in order to maintain the sample at a steady temperature.

For higher fields, the Clarendon houses a pulsed magnet field system with a typical total pulse length of 20 ms [13]. The system consists of a 32 mF capacitor bank which is charged up to 7 kV to provide the huge discharge needed to induce fields up to 50T in the solenoid. The coil construction itself is graded such that the high stress region of the coil, typically the inner region, can be wound from the minimum necessary length of a high strength but high conductivity wire, which is usually copper-niobium

(CuNb). The outer part is Al_2O_3 being a moderate strength, higher conductivity material. The result is a coil with high strength where needed but an overall resistance as low as possible making it less vulnerable to thermal limitation [14].

The magnet is precooled in a dewar filled with liquid nitrogen and a stainless steel vacuum insulated insert is placed in the inner cavity. This in turn is filled with nitrogen or helium. The sample, attached to the end of an insert can then be placed in the inner cavity, making sure that it finally rests at the centre of the solenoid. On discharging the capacitors, the magnetic field increases, reaching a maximum before decreasing over the pulse time length. It is recorded by pick-up coils and a saw tooth voltage is applied to the sample such that the forward bias peak coincides with the maximum field. This optimises the forward bias measurements for peak field. The pick up coils attached to the insert record *dB/dt* (which is integrated by computer to yield the field *B*) and the standard IV measuring apparatus described earlier in section 2.3 is used to measure the voltage and current.

Future experiments will be able to take advantage of a new pressure cell, capable of fitting in the 18mm bore of the pulsed magnet cryostat. Again a product of Russian expertise [10], the cell is able to withstand pressures of up to 16 kbar at room temperature (12 kbar at 77K) and is highly non-magnetic. The high pressure-very high magnetic field combination that is therefore available should provide any future physicist a convenient and powerful tool to investigate the vertical transport behaviour of the InAs/GaSb SHET (or of course those of other structures).

2.4 References

[1] U M Khan-Cheema, D.Phil. Thesis; Vertical Transport Through an InAs/GaSb Heterojunction at High Pressures and Magnetic Fields, Clarendon Laboratory, Oxford University (1996).

[2] J M Smith, D.Phil. Thesis, Resonant Tunnelling in GaAs/AlAs Double Barrier Heterostructures under Elevated Hydrostatic Pressure and in High Magnetic Fields, Clarendon Laboratory, Oxford University (1996).

[3] G R Booker, P C Klipstein, M Lakrimi, S Lyapin, N J Mason, R J Nicholas, T Y Seong, D M Symons, T A Vaughan and PJ Walker. Journal of Crystal Growth 145 p778 1994 and Journal of Crystal Growth 146 p495 (1995).

[4] U M Khan-Cheema, P C Klipstein, D G Austing, J M Smith, N J Mason, P J Walker and G Hill. Solid State Electronics 37 p977 (1994).

[5] S G Lyapin, P C Klipstein, N J Mason and P J Walker. Superlattices and Microstructures 15 p499 (1994).

[6] I J Murgatroyd, N J Mason, P J Walker, G R Booker. Institute of Physics Conference Series 146 p353 (1995).

[7] Initial experiments utilised inserts borrowed from M. Lakrimi, senior research assistant of the Nicholas Semiconductor Research group, Clarendon Laboratory, Oxford University.

[8] Subsequent experiments have used a self made rotating insert capable of holding novel pressure cells.

[9] Dr David Smith is the head of the Electronics section of the Physics sub-faculty, Nuclear Physics Building, Oxford.

[10] For further details of this cell and others, the reader is referred to 'High Pressure Experimental Methods' by M I Eremets (Oxford University Press 1996).

[11] H Fujiwara, H Kadomatsu & K Tohma. Review of Scientific Instruments 51 p1347 (1980).

[12] H Im, D.Phil. Thesis; X-band Related Transport in GaAs/AlAs Heterostructures Under Pressure and in Magnetic Fields, Clarendon Laboratory, Oxford University (to be published). Also see H Im, J M Smith, P C Klipstein, R Grey, G Hill. Proceedings of the International Conference on the Physics of Semiconductors, Jerusalem, Israel, 2-7 August 1998.

[13] W J Siertsema & H Jones. IEEE Transactions on Magnetics 30 p1809 (1994).

[14] H Jones, R G Jenkins, M Van Cleemput, R J Nicholas, W J Siertsema, M van der Burgt. Physica B 201 p546 (1994).

3. k.p Theory and the Envelope Function Approximation

3.1 Introduction 35

3.2 Symmetries of the Zinc-Blende Structure.....36

3.3 **k.p** Theory for Bulk Semiconductors 38

3.3.1 Nondegenerate Perturbative Approach.....38

3.3.2 Degenerate Bands - The Kane Model.....40

3.3.3 Far Band Considerations: Löwdin Perturbation Theory 44

3.4 Heterostructures and The Envelope Function Approximation46

3.5 Computational Details and Approximations.....50

3.5.1 Calculating the Hamiltonian at finite $k_{||}$ 50

3.5.2 The Axial Approximation.....51

3.5.3 Time Reversal Symmetry and Kramers Degeneracy 51

3.6 Summary.....52

3.1 Introduction

Many properties of bulk semiconductors are dependent on the mutual interaction of the various bands in the material, and a comprehensive theoretical study cannot be complete without these interactions being taken into account. Indeed, the small band gaps of InAs and GaSb [1] imply that any realistic calculation of their band structure and those of their derivative heterostructures must include such perturbative effects. This can be done from first principles using the pseudo-potential or tight binding models, though a major drawback of these methods is the considerable computational power they require. The **k.p** method offers a way out of this apparent impasse, allowing quick and accurate determination of energy band dispersions and wavefunctions in the vicinity of an important high symmetry **k** point. Its origins lie in the work of Shockley [2] and other noted figures including Dresselhaus, Kip and Kittel [3, 4], Luttinger and Kohn [5, 6] and of course Kane [1, 15]. Its continual development now ranks it as a very fundamental theory very often used in semiconductor physics [7]. It is this model that is used in this and the following chapter. Further, this theory has been extended to include heterostructures by way of the *Envelope Function Approximation* (EFA) and the report constituted here and in the subsequent chapter is to my knowledge the first report on the application of this theory to the InAs/GaSb single heterojunction. This chapter introduces the basics of **k.p** theory and the envelope function approximation. Chapter 4 details its applications to the InAs-GaSb heterojunction.

At the time of writing of this thesis, the nearest works encountered have been those of Vaughan [8] and Altarelli [9] applied to InAs/GaSb superlattices. Vaughan exploited the periodicity of the superlattice to write the Hamiltonian and (envelope) wave functions as Fourier expansions in momentum space. However, the calculation time is proportional to the layer width of the superlattice, so in the limit of large layer thicknesses in approximating a SHET, the calculation would take a very long time. Altarelli [9] used a 3-band **k.p** model and solves by using a modified variational principle. Again he solved for superlattices. The method used here calculates solutions exactly at the Γ-point and then expands wavefunctions at other points in terms of the Γ-point basis. Those details are presented in chapter 4. With the

inclusion of magnetic field in the Hamiltonian [7, 8, 10, 11], future work should be able to take into account the effect of band mixing when a magnetic field is applied perpendicular and parallel to the interface.

The highest symmetry point in the Brillouin zone is that occurring at the zone centre (the Γ point). Furthermore the band gap extrema for most III-V and II-VI semiconductors (with the major exception of AlAs) lie at this point so that observed semiconductor phenomena are often related to carriers near this point. This chapter commences with a discussion of the symmetry properties of the conduction and valence band zone centre Bloch states (section 3.2). With the Γ-point set of basis functions, I detail **k.p** theory applied in the simple case of a single nondegenerate band (section 3.3.1) before detailing the approach used by Kane [1, 15] to treat the more realistic case of degenerate bands (section 3.3.2). Perturbative effects are considered in section 3.3.3 to finally yield the Hamiltonian used throughout this work. The EFA is described (sections 3.4) to allow the theory to be extended to heterostructures, which for this work is specifically the InAs/GaSb single heterojunction. Finally the chapter ends with a discussion on major time-saving approximations, computational shortcuts and a summary.

3.2 Symmetries of the Zinc-Blende Structure

The crystal structure shared by most III-V semiconductors is that of two inter-linked face centred cubic Bravais lattices, one each describing the loci of the group III atoms and group V atoms. The offset vector between these two Bravais lattices is $a(\mathbf{i} + \mathbf{j} + \mathbf{k})/4$, where **i**, **j** and **k** are orthogonal unit vectors and a is the lattice constant. This combination is known as the zinc-blende structure and is the same as the diamond structure but with two different constituent atoms forming each nearest neighbour pair. Consideration of the symmetry properties of such a crystal type greatly simplifies the description of the electronic states, and this is taken advantage of in the ensuing **k.p** description of band structure. This subsection is therefore intended to provide the reader with no more than an appreciation of the relevant group theoretical concepts. More detailed information can be found in [12, 23].

In the terminology of group theory, the space group of the zinc-blende structure is said to be 'symmorphic', i.e. it can be subdivided into two separate subgroups representing translational and rotational operators and thus they can be treated separately. The lattice periodicity (and hence that of the Hamiltonian describing the states, Ψ) leads to the well known Bloch theorem.

$$\Psi(\mathbf{r}) = e^{i\mathbf{k}\cdot\mathbf{r}} u_{n\mathbf{k}}(\mathbf{r}) \tag{3.1}$$

where the $u_{n\mathbf{k}}$ are rapidly varying functions (indexed by the band number n at some $\mathbf{k}$ vector belonging to the first Brillouin zone) having the same periodicity as the underlying Bravais lattice and are called Bloch functions.

Rotational symmetry further allows one to extract information about the nature of the Bloch states at very high symmetry points in the Brillouin zone. The point group of the zinc-blende structure is identical to that of the well established point group T_d of the tetrahedron [14]. The eight outermost electrons from each primitive cell in the III-V semiconductor stem from the s and p orbitals, so that the valence band edge in the crystal will have the symmetry of the bonding p orbitals which correspond to the Γ_4 irreducible representation (irrep) of T_d in the absence of spin-orbit coupling. Thus the valence band at the Γ point is threefold degenerate and the Bloch state can be labelled accordingly as $|X\rangle, |Y\rangle, |Z\rangle$ where the notation signifies that these functions have the same symmetry properties as the atomic p_x, p_y and p_z orbitals. The irrep of the conduction band is simpler still, given by the representation Γ_1 and is singly degenerate. This has s-like symmetry properties and is therefore labelled as $|S\rangle$.

The inclusion of the spin-orbit interaction requires a more complete study of the double group containing both the symmetry operations of the spin wavefunctions and those of the orbital wavefunctions. It splits the sixfold degeneracy of the valence band into a four-fold degenerate $j = 3/2$ state and a two-fold degenerate state with $j = 1/2$. From the characters of the double group [12, 14], one finds that these states belong to the Γ_8 and Γ_7 representations respectively. The conduction band representation, now Γ_6, however, remains two-fold degenerate. The Bloch states which can now uniquely be labelled according to their j and m_j numbers can be

expressed as a linear combination of the eigenfunctions of the orbital angular momentum and spin[3]. This is done specifically to diagonalise the spin interaction [15]. The states are reproduced below in Table 3.1.

3.3 k.p Theory for Bulk Semiconductors

3.3.1 Nondegenerate Perturbative Approach

Neglecting many-body effects and the spin-orbit interaction, the eigenvalue equation for an electron moving in a periodic potential V(**r**) takes the following form [13, 14, 15, 20]:

$$H_0(\mathbf{r})\Psi(\mathbf{r}) = \left\{\frac{\mathbf{p}^2}{2m_0} + V(\mathbf{r})\right\}\Psi(\mathbf{r}) = \varepsilon_0\Psi(\mathbf{r}) \qquad \textbf{(3.2)}$$

Where $V(\mathbf{r})$ is the Hartree mean field crystal lattice potential, which has the same periodicity as the underlying Bravais lattice. Substituting the Bloch form of the wavefunction (3.1) into (3.2), the Schrödinger equation can be written in terms of a modified Bloch Hamiltonian, H,

$$H(\mathbf{r})u_{n\mathbf{k}}(\mathbf{r}) \equiv \left\{H_0(\mathbf{r}) + \frac{\hbar}{m_0}\mathbf{k}\cdot\mathbf{p} + \frac{\hbar^2k^2}{2m_0}\right\}u_{n\mathbf{k}}(\mathbf{r}) = \varepsilon_{n\mathbf{k}}u_{n\mathbf{k}}(\mathbf{r}) \qquad \textbf{(3.3)}$$

For any given $\mathbf{k_0}$, the set of all $u_{n\mathbf{k}_0}(\mathbf{r})$ form a complete set of eigenfunctions with the same periodicity as the lattice. Thus the $u_{n\mathbf{k}}$ for any other $\mathbf{k}$ may be expressed in terms of an expansion of the Bloch functions at the given value of $\mathbf{k} = \mathbf{k_0}$. Following on from the discussion at the end of the introduction (3.1), the Bloch states at $\mathbf{k}$ are expanded in terms of the zone centre Bloch functions,

$$u_{n\mathbf{k}}(\mathbf{r}) = \sum_m c_{nm}(\mathbf{k})u_m^{\Gamma}(\mathbf{r}) \qquad \textbf{(3.4)}$$

[3] This is made possible because the eigenfunctions of the spin-orbit interaction are eigenstates of the total angular momentum $\boldsymbol{j} = \boldsymbol{l} + \boldsymbol{s}$ and its z component. This follows through noting that since $\boldsymbol{l}$ depends on spatial coordinates and $\boldsymbol{s}$ does not, they will commute: $[\boldsymbol{l}, \mathbf{s}] = 0$. It is therefore evident that the components of the total angular momentum will satisfy the angular momentum commutation relations.

where the Γ-point Bloch functions, $u_m^\Gamma(\mathbf{r})$, form a complete set of eigenfunctions of the crystal Hamiltonian at $\mathbf{k_0} = 0$ $\left(H_0(\mathbf{r})u_m^\Gamma(\mathbf{r}) = \varepsilon_m^\Gamma u_m^\Gamma(\mathbf{r})\right)$. Substituting (3.4) into (3.3) leads to the eigenvalue equation,

$$\sum_m [H_{nm} - \varepsilon_{n\mathbf{k}}\delta_{nm}]c_{nm}(\mathrm{k}) = 0 \tag{3.5}$$

where the matrix elements $H_{nm} = \left\langle u_n^\Gamma \middle| H \middle| u_m^\Gamma \right\rangle$ are given by,

$$H_{nm} = \left[\left(\varepsilon_n^\Gamma + \frac{\hbar^2 k^2}{2m_0}\right)\delta_{nm} + \frac{\hbar}{m_0}\mathbf{k.p}_{nm}\right] \tag{3.6}$$

The diagonal terms are essentially the eigenvalue solutions to the crystal Hamiltonian H_0 at the Γ-point. The off-diagonal terms describe the **k**-dependent interactions between the n different (non-degenerate) electronic bands.

The Schrödinger equation may be written in the form

$$H(\mathbf{r})u_{n\mathbf{k}}(\mathbf{r}) = \left[H_0(\mathbf{r}) + W(\mathbf{k})\right]u_{n\mathbf{k}}(\mathbf{r}) = \lambda_{n\mathbf{k}}u_{n\mathbf{k}}(\mathbf{r}) \tag{3.7}$$

where,

$$W(\mathbf{k}) = \frac{\hbar}{m_0}\mathbf{k}\cdot\mathbf{p} \text{ and } \lambda_{n\mathbf{k}} = \left(\varepsilon_{n\mathbf{k}} - \frac{\hbar^2 k^2}{2m_0}\right) \tag{3.8}$$

For small values of **k** in the vicinity of the Γ-point, the **k.p** term can be treated as a perturbation, yielding eigenvalues ε_{nk} to second order:

$$\varepsilon_{n\mathbf{k}}(\mathbf{k}) = \varepsilon_n^\Gamma + \frac{\hbar^2 k^2}{2m_0} + \frac{\hbar^2}{m_0^2}\sum_{n\neq m}\frac{\left|\mathbf{k.p_{nm}}\right|^2}{\left(\varepsilon_n^\Gamma - \varepsilon_m^\Gamma\right)} + \ldots \tag{3.9}$$

This describes an essentially parabolic dispersion for the different electronic bands in the vicinity of the Γ-point, modified by a non-parabolicity introduced by **k**-dependent interband ($n \neq m$) interactions. Using the effective mass relation,

$$\frac{1}{m_n} = \frac{1}{\hbar^2}\frac{\partial^2 \varepsilon_{nk}}{\partial k^2} \tag{3.10}$$

equation (3.9) leads to an expression for the effective mass tensor m_n in the vicinity $\mathbf{k}\sim 0$, given to second order for the n^{th} band as:

$$\frac{1}{m_n} = \frac{1}{m_0} + \frac{2}{m_0}\sum_{n\neq m}\frac{\left|\mathbf{i}\cdot\mathbf{p}_{nm}\right|^2}{\left(\varepsilon_n^{\Gamma} - \varepsilon_m^{\Gamma}\right)} \tag{3.11}$$

where the **i** are the unit vectors of the principal crystal axes. The free electron mass m_0 is perturbed by dispersive interband terms, originating from the **k.p** interaction. The effect of the neighbouring bands on the effective mass depends on two factors:

- In a lattice with inversion symmetry, such as diamond, the first order matrix elements of the **k.p** perturbation in equation (3.11) are zero. Although the zinc-blende structure lacks inversion symmetry, the first order elements are small and can be neglected [1, 16][4].
- The energy separation $\varepsilon_n^{\Gamma} - \varepsilon_m^{\Gamma}$ between the two bands determines the relative importance of the contribution of m to the effective mass of band n. The contribution to the mass m_n can be negative as well as positive, causing m_n to become negative in some cases.

3.3.2 Degenerate Bands - The Kane Model

Kane noticed that for the principal III-V and II-VI semiconductor systems at the Γ-point, the lowest Γ_6 ($J = \frac{1}{2}$) conduction band and the highest Γ_8 ($J = \frac{3}{2}$) and Γ_7 ($J = \frac{1}{2}$) valence band edges (the so called 'near' states) are well separated from the other crystal bands (the 'far' states), which to a first approximation can be neglected, but included later through a second-order perturbative treatment (3.3.3). For a detailed account of the derivation of the Hamiltonian, the reader is referred to his review papers and the work of Bir and Pikus [7] who obtain the same result through the use of complex group theoretical arguments. Here, only the first step in Kane's analysis will be considered. This was essentially finding a $\boldsymbol{k} = 0$ basis in which the (non-zero) spin-orbit coupling in III-V semiconductors became diagonal.

[4] A Taylor expansion about the assumed extremum at the Γ point would lead to the same conclusion.

The spin-orbit interaction has up to this point been ignored (in equation (3.2)) but of course plays an important role in many semiconducting materials. It takes the form [15],

$$H_{so} = \frac{\hbar}{4m_0^2c^2}\left(\nabla V(\mathbf{r}) \times \mathbf{p}\right)\cdot\sigma \tag{3.12}$$

Where σ are the Pauli operators on the electron-spin variable. H_{so} leads to two terms in equation (3.6), namely H_{so} itself and,

$$H_{kso} = \frac{\hbar^2}{4m_0^2c^2}\left(\nabla V(\mathbf{r}) \times \mathbf{k}\right)\cdot\sigma \tag{3.13}$$

H_{kso} is usually very small compared to H_{so} [5] and hence is frequently neglected [15].

Instead of using the set of eight zone centre Bloch wavefunctions functions $|S\rangle, |X\rangle, |Y\rangle$ and $|Z\rangle$ (each band having two degenerate spin states and which transform according to the symmetry properties of the atomic *s*, p_x, p_y, and p_z wavefunctions) linear combinations of the basis functions can be formed such that the total angular momentum, **J**, and its linear projection, m_j, are diagonal in the new basis. The explicit form of the eight Γ-point Bloch functions u_{n0} are given in Table 3.1 below. In Kane's framework therefore, these are the 'near' states, as opposed to all the other 'far' bands, which are included by perturbation theory. The Hamiltonian itself is reproduced in Appendix C.

[5] The reason is that the main contribution to the spin-orbit interaction comes from the core region of the atom where ∇V and **p** are very large. ***k*** is at most ½ a reciprocal lattice vector and hence small compared to **p**.

u_n^Γ *and* $\left\|j,m_j\right\rangle$	E_Γ
$u_1(\mathrm{r}) = u_{c\uparrow}(\mathrm{r}) = i\left\|S\uparrow\right\rangle$	0
$u_2(\mathrm{r}) = u_{c\downarrow}(\mathrm{r}) = i\left\|S\downarrow\right\rangle$	0
$u_3(\mathrm{r}) = \left\|3/2,+3/2\right\rangle = u_{hh\uparrow}(\mathrm{r}) = \sqrt{1/2}\left\|(X+iY)\uparrow\right\rangle$	$-E_G$
$u_4(\mathrm{r}) = \left\|3/2,-3/2\right\rangle = u_{hh\downarrow}(\mathrm{r}) = \sqrt{1/2}\left\|(X-iY)\downarrow\right\rangle$	$-E_G$
$u_5(\mathrm{r}) = \left\|3/2,+1/2\right\rangle = u_{lh\uparrow}(\mathrm{r}) = \sqrt{1/6}\left\|(X+iY)\downarrow\right\rangle - \sqrt{2/3}\left\|Z\uparrow\right\rangle$	$-E_G$
$u_6(\mathrm{r}) = \left\|3/2,-1/2\right\rangle = u_{lh\downarrow}(\mathrm{r}) = -\sqrt{1/6}\left\|(X-iY)\uparrow\right\rangle - \sqrt{2/3}\left\|Z\downarrow\right\rangle$	$-E_G$
$u_7(\mathrm{r}) = \left\|1/2,+1/2\right\rangle = u_{so\uparrow}(\mathrm{r}) = \sqrt{1/3}\left\|(X+iY)\downarrow\right\rangle + \sqrt{1/3}\left\|Z\uparrow\right\rangle$	$-E_G-\Delta_{so}$
$u_8(\mathrm{r}) = \left\|1/2,-1/2\right\rangle = u_{so\downarrow}(\mathrm{r}) = -\sqrt{1/3}\left\|(X-iY)\uparrow\right\rangle + \sqrt{1/3}\left\|Z\downarrow\right\rangle$	$-E_G-\Delta_{so}$

Table 3.1. The eight band Γ-point Bloch functions for a zinc blende or diamond crystal structure, given in terms of the periodic atomic basis functions (see Appendix C where the Kane Hamiltonian is reproduced for which these are used as a basis). The linear combinations are such that the spin-orbit interaction is diagonal.

In this representation, the spin-orbit interaction H_{so} (3.12) (though not necessarily $H_{\mathbf{k}so}$) is diagonal and does not contribute to the off-diagonal interband matrix elements, which simply reduce to $\frac{\hbar}{m_0}\left\langle n^\Gamma\left|\mathbf{p}\right|m^\Gamma\right\rangle$. Equation C1 can then be diagonalised to give the eigenvalue equation,

$$\varepsilon_{n\mathbf{k}} = \lambda_{n\mathbf{k}} + \frac{\hbar^2 k^2}{2m_0} \tag{3.14}$$

where n runs over the four doubly degenerate bands. In the [001] direction, $k_\pm = k_x \pm ik_y = 0$, $k = k_z$ and the Kane Hamiltonian becomes block diagonal. It is then easy to show that the eigenvalues are solutions of,

$$\lambda_{n\mathbf{k}} = -E_g \tag{3.15}$$

and,

$$\lambda_{n\mathbf{k}}\left[\lambda_{n\mathbf{k}}+E_g\right]\left[\lambda_{n\mathbf{k}}+E_g+\Delta_{so}\right]=\hbar^2k^2P^2\left[\lambda_{n\mathbf{k}}+E_g+\tfrac{2}{3}\Delta_{so}\right] \qquad \textbf{(3.16)}$$

where E_g is the fundamental band gap at the Γ-point $\left(E_{\Gamma_6}-E_{\Gamma_8}\right)$ and Δ_{so} is the spin orbit splitting $\left(E_{\Gamma_8}-E_{\Gamma_7}\right)$. The Kane interband matrix element P,

$$im_0P=\langle S|p_x|X\rangle=\langle S|p_y|Y\rangle=\langle S|p_z|Z\rangle \qquad \textbf{(3.17)}$$

describing the interactions between the conduction and valence band states has a value that depends on functions that vary on the atomic scale. As the lattice constants for many III-V materials are approximately the same, one would expect and indeed finds that this value is fairly constant [20]. Also note the solutions for equations (3.15) and (3.16) correspond for any k_z to a given value of m_j: $m_j = \pm 3/2$ for equation (3.15) and $m_j = \pm 1/2$ for equation (3.16).

Expanding equations (3.15) and (3.16) to second order in k (the higher order terms give rise to non-parabolicity), the [001] direction dispersions and effective masses of the conduction and valence bands near the Γ-point are obtained (Table 3.2). Notice that the $m_j = \pm 3/2$ state (equation (3.15)) lacks any coupling leading to an effective mass which coincides with the bare electron mass. This is due to restricting the **k.p** interaction to the Γ_6, Γ_7 and Γ_8 basis. A more thorough calculation would need to consider remote band effects outside this basis. This is the subject of the next section.

Band	$\left\|J,m_j\right\rangle$	Energy dispersion $\varepsilon_{n\mathbf{k}}$	Effective mass $(1/m_n)$
Electron	$\left\|\frac{1}{2},\pm\frac{1}{2}\right\rangle_{\Gamma_6}$	$E_g+\frac{\hbar^2k^2}{2m_0}+\frac{P^2k^2}{3}\left(\frac{2}{E_g}+\frac{1}{\left(E_g+\Delta_{so}\right)}\right)$	$\frac{1}{m_0}+\frac{4P^2}{3E_g}+\frac{2P^2}{3\left(E_g+\Delta_{so}\right)}$
Heavy hole	$\left\|\frac{3}{2},\pm\frac{3}{2}\right\rangle_{\Gamma_8}$	$-\frac{\hbar^2k^2}{2m_0}$	$\frac{1}{m_0}$
Light hole	$\left\|\frac{3}{2},\pm\frac{1}{2}\right\rangle_{\Gamma_8}$	$-\frac{\hbar^2k^2}{2m_0}-\frac{2P^2k^2}{3E_g}$	$\frac{1}{m_0}-\frac{4P^2}{3E_g}$
Spin-orbit	$\left\|\frac{1}{2},\pm\frac{1}{2}\right\rangle_{\Gamma_7}$	$-\Delta_{so}-\frac{\hbar^2k^2}{2m_0}-\frac{P^2k^2}{3\left(E_g+\Delta_{so}\right)}$	$\frac{1}{m_0}-\frac{2P^2}{3\left(E_g+\Delta_{so}\right)}$

Table 3.2. The eigenvalue solutions and effective masses for the principal spin-degenerate conduction and valence bands in the vicinity of the Γ-point from an 8 band Kane analysis in the [001] direction. Any attempt to diagonlise the Kane Hamiltonian (in any other direction besides [100], [001] etc., leads to non zero $k_{\pm}$ ($k_x \pm ik_y$) terms due to admixing between various m_j states - the algebra is therefore more complicated). Note the obviously incorrect prediction of a heavy hole mass equal to that of a free electron mass.

3.3.3 Far Band Considerations: Löwdin Perturbation Theory

The Kane model, though allowing interactions between bands, does so in the limit of a restricted subspace. The consequence is that in many cases it still does not reproduce correct band structure. For example, it still predicts heavy holes with an effective mass equal to the free electron mass. To resolve this inconsistency, the so-called 'far' states need to be considered. This is done by a second order perturbative method, known as Löwdin perturbation theory. In this method, the Bloch functions for arbitrary **k** ($u_{n\mathbf{k}}$) are expanded in terms of the band edge (Γ-point) Bloch functions u_m^{Γ} which can be divided into two classes corresponding to 'near' and 'far' states. The aim is to describe the behaviour of the near band states, in the context of **k**-dependent interactions between the different near band states and also with the far band states.

Löwdin showed that the Hamiltonian can be renormalised to operate entirely within the set of near bands, with the interactions with the far bands introduced as a perturbation [17, 18]. The effect introduces four independent parameters in the Hamiltonian (Table C2, Appendix C): F, γ_1, γ_2 and γ_3. These modified Luttinger parameters are similar in principle to the Kane interband matrix element P, describing the far band interactions in terms of experimentally determinable parameters. Diagonalising the matrix for k_z (which is along the [001]) axis in the vicinity of the Γ-point then leads to a better description of the corresponding band edge effective masses,

$$\frac{1}{m_e} = \frac{2\left(F+\frac{1}{2}\right)}{m_0} + \frac{4P^2}{3E_g} + \frac{2P^2}{3\left(E_g+\Delta_{so}\right)} \tag{3.18}$$

$$\frac{1}{m_{hh}} = \frac{\gamma_1 - 2\gamma_2}{m_0} \tag{3.19}$$

$$\frac{1}{m_{lh}} = \frac{\gamma_1 + 2\gamma_2}{m_0} + \frac{4P^2}{3E_g} \tag{3.20}$$

$$\frac{1}{m_{so}} = \frac{\gamma_1}{m_0} + \frac{2P^2}{3\left(E_g+\Delta_{so}\right)} \tag{3.21}$$

Notice how the perturbative inclusion of the 'far' band terms now leads to a heavy hole mass that is not equal to the free electron mass, unlike in the earlier case (see Table 3.2). The bulk dispersion curves for InAs and GaSb can be solved for a range of k near the Γ point by diagonalizing the Hamiltonian (C2), and are presented below in Figure 3.1.

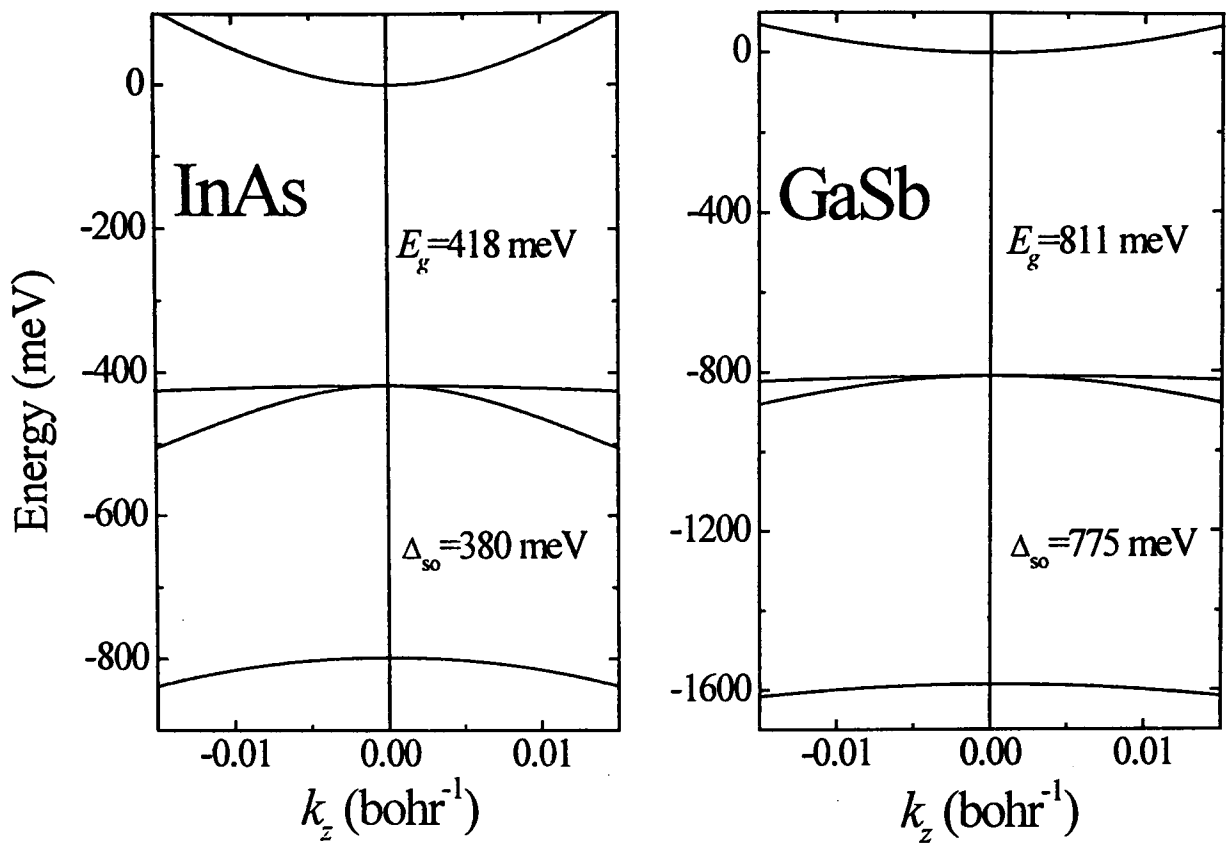


Figure 3.1. Energy dispersions of InAs and GaSb near the Γ point, calculated by diagonalization of the bulk **k.p** matrix for each material (Table C2). In contrast to the free electron model or even the more complex Kane model, the eigenvalue solutions are no longer isotropic. The far band interactions distort the energy surfaces about the Γ-point extrema, introducing band warping which is found to be particularly strong for the Γ_8 valence bands [4].

3.4 Heterostructures and The Envelope Function Approximation

Advanced growth techniques allowing the formation of heterostructures with interfaces that are flat up to one atomic layer means that the problem of calculating bulk III-V eigenstates needs to be extended to take into account the abrupt change of bulk material at the interface. Consider, for example the simplest case of a single heterojunction formed between two perfectly lattice matched A and B semiconductors. For $z > 0$, the electron experiences a one-electron potential which is identical to that of one of the perfect bulk materials, say A. For $z<0$ then, it experiences a one electron potential which is the same as is found in a perfect bulk B layer. Such a case will of course encompass the InAs/GaSb SHET samples grown in the Clarendon that are used throughout this work. HRTEM images of the SL sample actually show the ordering of the rows of the heavy constituent III-V atoms as well as the abrupt one monolayer interface [19].

Though global descriptions such as the tight binding and pseudopotential methods have been extended to describe heterostructure band structure with some success, they continue to be mathematically and computationally complex in comparison to the relatively limited descriptions required by experiment. A much more widely used approach is the so-called Envelope Function Approximation (EFA), based on the **k.p** model, describing the band structure in the vicinity of a critical point (usually the Γ point). This is described here, starting with the two key steps in its derivation,

• As $V(\mathbf{r})$ will now consist of the microscopic periodically rapidly varying part due to the host materials and a macroscopic slowly varying part due to the differing band gap energies of the respective materials, the Bloch states will be mixed. Inside each layer the heterostructure eigenstates will consist of a rapidly varying component (the periodic parts of the Bloch functions) and a slowly varying component, the *envelope function f*. Thus, if the heterostructure is composed of two materials *A* and *B*, then in *A*:

$$\psi(\mathbf{r}) = \sum_l f_l^A(\mathbf{r}) u_l^{A,\Gamma}(\mathbf{r}) \qquad \textbf{(3.22)}$$

and in *B*

$$\psi(\mathbf{r}) = \sum_l f_l^B(\mathbf{r}) u_l^{B,\Gamma}(\mathbf{r}) \qquad \textbf{(3.23)}$$

where the point in the Brillouin zone around which the heterostructure states are built is the Γ-point ($\mathbf{k} = 0$, denoted by the superscript 'Γ' on the Bloch functions above). The summation over *l* runs over as many edges as are included in the analysis. Note the EFA by-passes any ambiguity concerning the description of the electronic states that exist at the interface. This is a well justified assumption as the electron and hole states will have very small probability amplitudes of being found in this region.

• Secondly, the periodic parts of the Bloch functions are assumed to be the same in each kind of layer which constitutes the heterostructure. This essentially implies that the Kane matrix element *P* is assumed to be similar in the two (or more) materials, and is in fact confirmed by the similarity of the Kane matrix element over a wide range of III-V semiconductors [20]. It does however mean that the calculation sees no

difference between the two materials other than their differing band offsets and band gaps, and consequently information about the interfaces and other atomic phenomena are lost. Thus,

$$u_l^{A,\Gamma}(\mathbf{r}) = u_l^{B,\Gamma}(\mathbf{r}) \tag{3.24}$$

So that the heterostructure wavefunction can then be written for material A or B as:

$$\psi(\mathbf{r}) = \sum_l f_l^{A,B}(\mathbf{r}) u_l^{\Gamma}(\mathbf{r}) \tag{3.25}$$

and the objective is then to determine f.

The fact that the summations in equations (3.22) and (3.23) extend to the first l bands limits the range of k measured from the k point in the Brillouin zone around which the heterostructure states are built. This range of bands, from which the $\psi(\mathbf{r})$'s are constructed, must be large enough to allow the calculated dispersion relation for the heterostructure to approximate the real dispersion relations.

If the plane $z = z_0$ is the interface separating the A and B layers (and assuming that the growth axis is the z axis), then applying the continuity of ψ across the interface and remembering that the u's are linearly independent, we must have:

$$f_l^A(\mathbf{r}_\parallel, z_0) = f_l^B(\mathbf{r}_\parallel, z_0) \tag{3.26}$$

where the $\parallel$ sign signifies the (x, y) plane. Since the lattice constants of the host layers are assumed to the same, the heterostructure becomes translationally invariant in the layer plane. Thus the f's can be factorized into:

$$f_l^{A,B} = \frac{1}{\sqrt{\Omega}} \exp(i\mathbf{k}_\parallel \cdot \mathbf{r}_\parallel) \chi_l^{A,B}(z) \tag{3.27}$$

Writing the heterostructure Hamiltonian in the form:

$$H = \frac{\mathbf{p}^2}{2m} + \left[V_A(\mathrm{r}) + \frac{\hbar}{4m_0^2c^2}(\sigma \times \nabla V_A) \cdot \mathbf{p} \right] Y_A + \left[V_B(\mathrm{r}) + \frac{\hbar}{4m_0^2c^2}(\sigma \times \nabla V_B) \cdot \mathbf{p} \right] Y_B \tag{3.28}$$

where Y_A (Y_B) are step functions which are unity if **r** corresponds to an A layer (to a B layer). We have:

$$Hu_l^{\Gamma}(\mathbf{r}) = \left(\varepsilon_l^{A,\Gamma} Y_A + \varepsilon_l^{B,\Gamma} Y_B\right) u_l^{\Gamma}(\mathbf{r}) \tag{3.29}$$

where $\varepsilon_l^{A,\Gamma}, \varepsilon_l^{B,\Gamma}$ are the energies of the lth band edge at the zone centre of the A and B materials respectively.

Substituting the envelope function form of $\psi(\mathbf{r})$, the periodic Schrödinger equation leads to the following eigenfunction equation,

$$\sum_m \left[H_{nm} - \varepsilon_m \delta_{nm}\right] \chi_m^{A,B}(\mathbf{r}) = 0 \tag{3.30}$$

Thus, the Hamiltonian is described by an $m \times m$ matrix H_{nm}, operating on an m-dimensional column matrix $\chi_m{}^{A,B}(\mathbf{z})$ where,

$$H_{nm} = \left[\left(\varepsilon_n^{A,\Gamma} Y_A + \varepsilon_n^{B,\Gamma} Y_B + \frac{\hbar^2 k_{\|}^2}{2m} - \frac{\hbar^2}{2m}\frac{\partial^2}{\partial z^2}\right)\delta_{nm} + \frac{\hbar}{m}\mathbf{k}.\mathbf{p}_{\|,nm} - \frac{i\hbar}{m} p_{z,nm} \frac{\partial}{\partial z}\right] \tag{3.31}$$

where $\mathbf{p}_{\|,nm} = \left\langle u_n^{\Gamma} \middle| \mathbf{p}_{\|} \middle| u_m^{\Gamma} \right\rangle$, $p_{z,nm} = \left\langle u_n^{\Gamma} \middle| p_z \middle| u_m^{\Gamma} \right\rangle$ and the subscripts denote the direction of the momentum operator and the spin-orbit interaction is neglected. If the set of Bloch wavefunctions $u_m{}^{\Gamma}$ are restricted to the eight $|J, m_j\rangle$ functions used in the Kane approach [1, 15], the momentum operator matrix elements $\mathbf{p}_{nm}$ can be replaced by the Kane matrix elements im_0P, describing the interactions between the conduction and valence band states. Far band interactions can then be included as a second order perturbation using Löwdin perturbation theory.

The bulk Hamiltonian matrix elements H_{nm} (see Appendix C) can thus be rewritten to operate on the heterostructure z-component envelope function $\chi_m{}^{A,B}(z)$. Comparing (3.31) with (3.6) shows that this matrix is just the bulk **k.p** matrix except that

1. k_z is replaced by $-i\partial/\partial z$[6].

[6] Note that there are multiple definitions of z. Throughout the derivation of the **k.p** theory equations, the z direction has been taken to be a well-defined direction in the crystal lattice, determined by the

2. the band edges are now position-dependent and vary in a steplike manner.

With the bulk Hamiltonian known and the appropriate transformations 1 and 2 above required to generate the correct heterostructure Hamiltonian, the problem of calculating the eigenfunctions and eigenvalues of any semiconductor system has essentially been reduced to the solution of a set of second order coupled differential equations which govern the spatial behaviour of the slowly varying envelope functions. The microscopic details of the heterostructures, i.e. all the parameters which depend on the rapidly varying phenomena at the scale of the hosts' unit cells have disappeared. However, this is compensated by gaining knowledge of the envelope functions from which can be extracted more useful observable macroscopic data.

3.5 Computational Details and Approximations

It would be instructive at this point to introduce various approximations used in the algorithm, computational details and shortcuts improving the speed of the calculations.

3.5.1 Calculating the Hamiltonian at finite $k_{||}$

Using the zone centre wavefunctions as a basis, the states at finite $k_{||}$ can now be calculated, using the Hamiltonian shown in Appendix C. This needs to be done for many $k_{||}$ points, and was typically done for 250 points extending to 0.025 bohr^{-1}. In practice, simply recalculating the Hamiltonian for each $k_{||}$ would be very time consuming and would be unlikely to yield the complete solution in the available span of time. To overcome this obstacle, Rau [23] has made use of the fact that the Hamiltonian is a function of $k_{||}$, $k_{||}^2$ and various overlaps between electron and hole wavefunctions only. Once these (Γ point) wavefunctions are calculated however, the

---

orientation of the tetragonal chemical bonds between atoms (and given in Figure 1.1 and Figure 1.3 of the first chapter). However, the growth direction has also been defined as the z direction. The two definitions of z will coincide only for structures grown in the [001] direction. Fortunately, this being popular growth direction is the direction in which the samples used throughout all this work were grown. Thus all the Hamiltonians presented in this chapter, and given in the appendices, are acceptable as they stand.

overlaps can be calculated and therefore the Hamiltonian be written as a superposition of three matrices.

$$H = H_0 + k_{\|} H_\alpha + k_{\|}^2 H_\beta \tag{3.32}$$

where H_0 is the Hamiltonian calculated at $k_{||} = 0$. By calculating the Hamiltonian for two other $k_{||}$ points allows $H\alpha$ and $H\beta$ to be calculated. Any subsequent calculation of the Hamiltonian at any $k_{||}$ point can utilise equation (3.32) above providing a very time saving shortcut to the calculation of the band structure where solutions are required for many $k_{||}$ points.

3.5.2 The Axial Approximation

The cubic symmetry of III-V semiconductors leads to a directional dependence of the dispersion in $k_{||}$ space (strictly speaking, due to lack of inversion symmetry, III-V semiconductors belong to the two fold symmetry tetrahedral group and not the four fold cubic group though this has a negligible effect on band structure calculations). Thus, a rigorous calculation would take this into account, and the algorithm would proceed to calculate states all over the two-dimensional (k_x, k_y) plane. It is very fortunate then, that following from the work of Altarelli *et al* [9, 21][7], this directional dependence can be averaged and the calculation can proceed assuming a radial dependence in $k_{||}$. This *Axial Approximation* thus assumes eigenvalues of the Hamiltonian are independent of the direction in the $k_{||}$ plane. This is done by setting the Luttinger parameters γ_2 and γ_3 in the Hamiltonian to their average $\frac{1}{2}(\gamma_2+\gamma_3)$. This causes the dispersion of the energy levels in the layers planes to be isotropic and therefore gives the system more symmetry than actually exists but is a good approximation allowing the calculations to be feasible.

3.5.3 Time Reversal Symmetry and Kramers Degeneracy

Time reversal symmetry, under the operator taking **x** into **x** and **p** into **-p,** leaves the Hamiltonian unchanged and therefore applies to almost all quantum systems. It is the

---

[7] Reference [21] introduces and shows the validity of the axial approximation, while [9] is an example of its use in the study of InAs/GaSb superlattices.

origin of what is known as Kramers' degeneracy. This requires a spin state at a general **k** point to have the same energy as the opposite-spin state at –**k**. If the crystal has inversion symmetry, all states at a given **k** are therefore doubly degenerate. The situation is more subtle for the zinc-blende structure as it lacks a centre of inversion. Then generally, all states become non-degenerate, the splitting being, of course, the result of the spin-orbit interaction. These are fortunately small enough to be neglected and it is therefore assumed that Kramers' degeneracy still holds in such structures. From the point of view of the calculations, this additional piece of information means that only one of the degenerate states need be calculated, thus further reducing computational time. For a more detailed discussion on this, the reader is referred to [3],[22], [23] and [24].

3.6 Summary

This chapter has provided an introductory review of the **k.p** method of determining the band structure of bulk semiconductors near a given point in k space. The discussion has reviewed the Kane model for degenerate bands within a restricted subspace, with the inclusion of Löwdin theory to perturbatively treat the effect of 'far' bands, thus leading to the Hamiltonians given in Appendix C. Through the use of the EFA, the theory can be extended to cover semiconductor heterostructures. Finally, in section 3.5 a number of approximations are given making it easier to implement the ideas computationally. With the machinery now in place, one can proceed to apply the theory to the InAs/GaSb single heterojunction. This is the subject of the next chapter.

3.7 References

[1] E O Kane. Journal of Physics and Chemistry of Solids 1 p249 (1957).

[2] W Shockley. Physical Review 78 p173 (1950).

[3] G Dresselhaus. Physical Review 100 p580 (1955).

[4] G Dresselhaus, A F Kip and C Kittel. Physical Review 98 p368 (1955).

[5] J M Luttinger. Physical Review 102 p1030 (1956).

[6] W Kohn and J M Luttinger. Physical Review 96 p529 (1954).

[7] For a very detailed and extensive **k.p** review brave readers are referred to Symmetry and Strain Induced Effects in Semiconductors by G L Bir and G E Pikus, John Wiley & Sons Inc., (1974). The full derivation of the Kane Hamiltonian (and also including the effect of strain) is given through symmetry arguments. Readers might also find Semiconductors and Semimetals by M H Weiler useful (edited by R K Willardson and A C Beer (Academic, New York, 1981) 16 p119).

[8] T A Vaughan, D.Phil. Thesis; The Magneto-optics of InAs/GaSb Heterostructures, Clarendon Laboratory, Oxford University (1996).

[9] M Altarelli. Physical Review B 28, p842 (1983). Also see U Ekenberg and M Altarelli, Physical Review B 32 p3712 (1985).

[10] G M Sundaram, R J Warburton, R J Nicholas, G M Summers, N J Mason and P J Walker. Semiconductor Science and Technology 7 p985 (1992).

[11] Hamiltonians taking into account the effect of in-plane field have been used by Zawadzki *et al.* (W Zawadzki, S Klahn and U Merkt. Physical Review B 33 p6916 (1986)) and Xia *et al.* (Jian-Bai Xia and Wei-Jun Fan. Physical Review B 40 p8508 (1989)).

[12] V Heine, Group Theory in Quantum Mechanics, Dover Publications Inc., New York (1993).

[13] C Kittel, Quantum Theory of Solids, John Wiley & Sons, Inc. (1986)

[14] P Y Yu and M Cardona. Fundamentals of Semiconductors, Springer Verlag, Berlin Heidelberg (1996).

[15] E O Kane, Energy Band Theory, in Handbook in Semiconductors, edited by W Paul (North-Holand Publishing Company 1982) 1 p193.

[16] The lifting of the spin degeneracy due to lack of inversion symmetry in GaSb/InAs/GaSb quantum wells has been investigated by J Luo, H Munekata, F F Fang and P J Stiles. Physical Review B 38 p10142 (1988) & Physical Review B 41 p7685 (1990).

[17] P Löwdin. The Journal of Chemical Physics 19 p1396 (1951).

[18] R Warburton, D. Phil. Thesis, Clarendon Laboratory, Oxford University (1991).

[19] U M Khan-Cheema, D.Phil. Thesis; Vertical Transport Through an InAs/GaSb Heterojunction at High Pressures and Magnetic Fields, Clarendon Laboratory, Oxford University (1996).

[20] G Bastard, Wave Mechanics Applied to Semiconductor Heterostructures, Halsted Press, Les Editions de Physique.

[21] M Altarelli, U Ekenberg, A Fasolino. Physical Review B 32 p5138 (1985).

[22] See, for example, chapter 9 of C Kittel, Introduction to Solid State Physics, John Wiley & Sons, Inc. (1986).

[23] G Rau, D.Phil. Thesis; Theory of the Electronic and Optical Properties of GaAs/AlGaAs Quantum Wells under Uniaxial Stress, Clarendon Laboratory, Oxford University (1998).

[24] M. Cardona, N E Christensen and G Fasol. Physical Review B 38 p1806 (1988).

4. Measurements at Hydrostatic Pressure and Analysis Using a Self-Consistent k.p Algorithm

4.1 Introduction 56

4.2 Self-Consistent Calculations 57

4.2.1 Method of Calculation 57

4.3 Interface Type and the Band Overlap 69

4.4 Presenting Experimental and Theoretical Results 71

4.4.1 Dependence of NDR on Hydrostatic Pressure 71

4.5 Phonon Processes in InAs/GaSb Structures.....81

4.5.1 A Detour into Raman Spectroscopy 81

4.5.2 Observed Phonon Cascades.....83

4.6 Band Gaps, Wavefunctions and In-Plane Dispersion Curves86

4.7 Summary.....91

4.8 References 91

4.1 Introduction

The close proximity of the conduction band of InAs and valence band of GaSb immediately makes the InAs/GaSb system an interesting choice for **k.p** modelling. With the vast improvements in growth during the last ten years, the InAs/GaSb system has been the subject of many experimental groups world-wide the results of whom can only be interpreted through the subtle effects of band mixing [1, 2, 9, 10]. Previous work initially has utilised decoupled models, where the electrons and heavy holes are assumed to be independent and non-parabolicity is ignored, as are light holes. Though approximate, the results have nevertheless been fruitful. Work by Symons *et al* [3] and Daly *et al* [4] neglecting band mixing and non-parabolicity has provided information about Δ and its variation with pressure. More recently, Khan-Cheema *et al* [5, 22] has also used a decoupled model to prove that conduction mechanisms existing in the SHET are sensitive to the interface type. Such models are employed in the later chapters of this work in treating the effect of magnetic field on the SHET. However, as informative as they are, they are nevertheless approximations providing limited information about the heterostructure band structure. More realistic calculations would of course have to take band mixing into account especially when the conduction band of one material lies very close to its valence band, as is the case of InAs in the InAs/GaSb SHET.

Initial multi-band models taking into account mixing were used by Yu *et al* [6, 7]. They focused on InAs/GaSb/InAs tunnelling devices. Working assuming flat band conditions in their calculations, they were able to show that transport occurred through electrons tunnelling into light hole states in the GaSb wells, but noted that additional resonances would occur due to heavy hole mixing [8]. The first multi-band self-consistent **k.p** treatment of the InAs/GaSb system dates back to the work of Altarelli [9]. He showed that in an intrinsic superlattice, no truly semimetallic band structure results, but rather a zero-gap or very small gap (E_g < 10 meV) semiconductor (even when the layer widths are very large). He thus concluded that doping and temperature effects must play a key role in the observed semimetallic behaviour. The only other work to my knowledge is that of Vaughan [10] who extended Altarelli's work by also including the effect of the spin-orbit split-off band

in his calculations. Here we employ a 6-band model to present the results of the first multi-band and self-consistent calculation of the InAs/GaSb SHET.

4.2 Self-Consistent Calculations

Charge transfer at the interface leads to coulombic band-bending and any realistic calculation must include such effects. This is done by simultaneously solving the Schrödinger and Poisson equations. The fundamental algorithm used in the calculations consists of *i)* making an initial guess at the band edge potential $V(z)$, *ii)* calculating the band structure (energies $E(k_{||})$ and envelope functions $f(k_{||})$) from the potential $V(z)$, *iii)* determining the Fermi level from the band structure, *iv)* recalculating $V(z)$ by solving Poisson's equation and finally returning to *ii)* until convergence. These points are elaborated in more detail below.

4.2.1 Method of Calculation

4.2.1.1 Initial Potential Approximation

The approximate initial potential is provided by a Fang-Howard variational calculation [11] which gives for the conduction band in InAs ($z<0$) and valence band in GaSb ($z>0$),

$$V(z)=\begin{cases}\dfrac{e^2 n}{\varepsilon_r^{InAs}\varepsilon_0}\left(\dfrac{3}{b}-\left\{-2z+\dfrac{3}{b}+\dfrac{bz^2}{2}\right\}e^{bz}\right) & z\le 0\\ \Delta-\dfrac{e^2 p}{\varepsilon_r^{GaSb}\varepsilon_0}\left(\dfrac{3}{b}-\left\{2z+\dfrac{3}{b}+\dfrac{bz^2}{2}\right\}e^{-bz}\right) & z>0\end{cases} \qquad \textbf{(4.1)}$$

where $n(p)$ is the two dimensional (2D) electron (hole) concentration, ε_r^x is the relative permittivity of substance x, Δ is the band overlap and z is the direction of growth with the interface of the SHET situated at z=0. The variational parameter b is shown to be,

$$b = \begin{cases} \left(\dfrac{33 m_z^{e^*} e^2 n}{8 \varepsilon_r^{InAs} \varepsilon_0 \hbar^2} \right)^{1/3} & z \le 0 \\ \left(\dfrac{33 m_z^{h^*} e^2 p}{8 \varepsilon_r^{GaSb} \varepsilon_0 \hbar^2} \right)^{1/3} & z > 0 \end{cases} \qquad \textbf{(4.2)}$$

4.2.1.2 Calculating Band Structure

The zone centre electron and hole states are commonly used as a basis as then analytical expressions can usually be derived for them [12, 13]. This is not possible for the InAs/GaSb SHET, due to the complicated shape of the band profile edges. These therefore have to be calculated numerically before they are used as a basis set (in fact this is the only set of basis states numerically calculable and therefore available anyway, thus necessarily making them the only choice as a basis set). The choice of a suitable number of zone centre states with which the states at finite $k_{||}$ can be expanded is discussed below in section 4.2.1.2.1.

At zero $k_{||}$, valence band coupling is non-existent and the only band mixing effect between the conduction and valence bands is through the k_z operator operating between the electron and light hole states. But as the overlap of the electron and light hole wavefunctions near the interface will be small even these terms too can be neglected. Thus the Γ point Hamiltonian is (very nearly) diagonal and the eigenfunctions of the zone centre electron, heavy hole and light hole states ψ^{Γ}_{n} and their eigenvalues ε^{Γ}_{n} can be calculated by solving the appropriate one dimensional Schrödinger equation under an effective mass (m_z^*) approximation, which for the electrons is,

$$\left[-\frac{\hbar^2}{2m_z^*} \frac{\partial^2}{\partial z^2} + V(z) \right] \psi^{\Gamma}_{n} = \varepsilon^{\Gamma}_{n} \psi^{\Gamma}_{n} \qquad \textbf{(4.3)}$$

Where V is the conduction band profile in the SHET.

Once these are calculated, the matrix elements of the **k.p** Hamiltonian (Appendix C) can be used to construct a 60×60 matrix detailing the interactions between each and every other electron and hole state. Diagonalising this final matrix leads to the correct (mixed) eigenfunctions and eigenstates, including the true states at the zone centre.

Equation (4.3) is solved using a transfer matrix formalism. This method simply splits z up into a mesh of intervals where V can be treated as constant in each interval. With ψ_{nL}^{Γ} and ψ_{nR}^{Γ} the values of the nth subband at the left and right hands sides of an interval and assuming continuity of the wavefunction and its gradient, it is easy to show that,

$$\begin{bmatrix} \psi_{nR}^{\Gamma} \\ \dfrac{1}{m_z^*}\dfrac{d\psi_{nR}^{\Gamma}}{dz} \end{bmatrix} = \tilde{\mathbf{T}} \begin{bmatrix} \psi_{nL}^{\Gamma} \\ \dfrac{1}{m_z^*}\dfrac{d\psi_{nL}^{\Gamma}}{dz} \end{bmatrix} \tag{4.4}$$

The transfer matrix $\tilde{\mathbf{T}}$ is:

$$\tilde{T} = \begin{bmatrix} \cos k\delta z & \dfrac{m_z^*}{k}\sin k\delta z \\ -\dfrac{k}{m_z^*}\sin k\delta z & \cos k\delta z \end{bmatrix} \quad \text{where} \quad k = \sqrt{\frac{2m_z^*(\varepsilon_n^{\Gamma} - V)}{\hbar^2}} \tag{4.5}$$

and δz is the interval size for $V(z)$,

The SHET is assumed to sit in a larger quantum well thus forcing the necessarily essential boundary conditions that the confined states (i.e. those confined by the approximate triangular conduction and valence bands at the interface) and continuum states are zero at both ends of the box. Further boundary conditions for the confined states can be derived by noting that far from the interface in the both the InAs and GaSb where the band profile is flat, the solution to (4.3) requires, for example, the electron wavefunction to exponentially decay to zero. Similarly, a zone centre hole state confined by the SHET must exponentially decay to zero at both ends of the large QW as such states exist above the GaSb and InAs valence bands. Such exponential decays on one side of the interface exist only for the confined states. The continuum states though decay exponentially in only one side of the interface. The zone centre electron continuum states, again as an example, existing above the conduction band edge in the InAs and below the conduction band in GaSb, will be plane-wave like in the InAs, but will of course decay rapidly to zero in the GaSb.

The total transfer matrix relating the wavefunction and its gradient on either side of the larger QW is then given by,

$$T = \prod_{All\ z} \tilde{T}_z \tag{4.6}$$

Using the appropriate boundary conditions, the requirement for confined states can be derived (and shown in Appendix B), which for the zone centre electrons for example occurs when the following example is satisfied,

$$\left(T_{1,2} + T_{2,2} \frac{k_i}{m^*_{z,InAs}} \right) \frac{m^*_{z,GaSb}}{k_f} + T_{1,1} + T_{1,2} \frac{k_i}{m^*_{z,InAs}} = 0 \tag{4.7}$$

where $T_{x,y}$ is the (x, y) entry in T, k_i is the initial k value at $z = 0$, k_f is the k value at the opposite side of the structure in the GaSb and m_z^* is the effective electron mass (0.023 in InAs and 0.04 in GaSb). The expression derived for an electron continuum state incorporating the modified boundary conditions is also shown in Appendix B and is unsurprisingly different,

$$T_{2,2} + T_{1,2} \frac{k_f}{m^*_{z,InAs}} = 0 \tag{4.8}$$

Thus, by scanning in energy until one of the above two expressions holds true, the zone centre electron eigenvalues can be calculated. Equation (4.3) is then used to calculate the zone centre envelope wavefunctions. In a similar way, all the heavy hole and light hole confined and continuum states can be calculated.

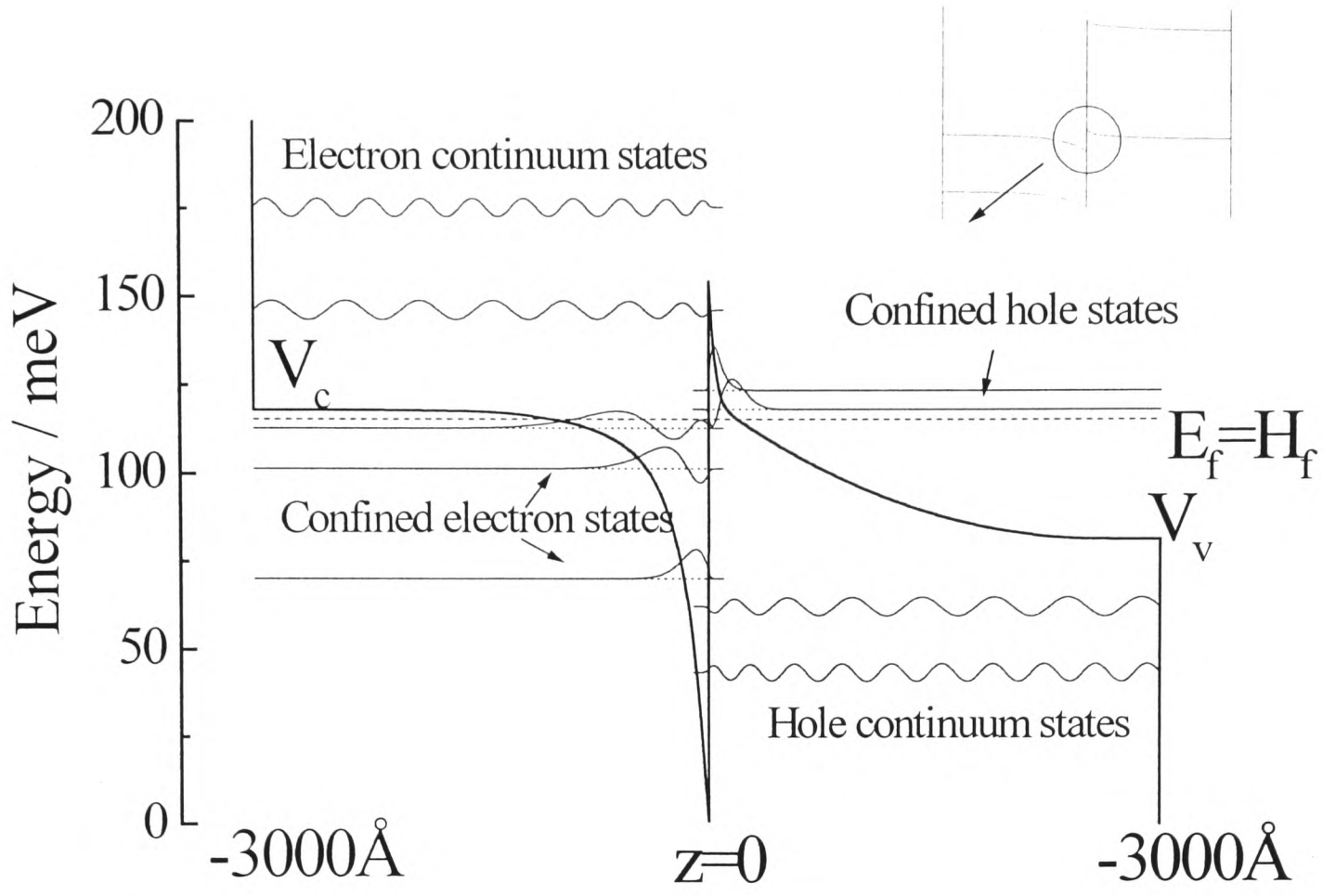


Figure 4.1. The SHET in a larger quantum well, illustrating the confined and continuum states (discussed in [14]).

4.2.1.2.1Choosing an Appropriate Number of Zone Centre Basis States

States at finite $k_{||}$ are expanded in terms of the finite number of the calculated zone centre basis states. A suitable limit to this number was found by fully performing the calculations using a fixed number l of electron, heavy hole and light hole zone centre envelope functions each as a basis and then comparing the results with calculations repeated for a higher value of l. Sample results for $l = 5$, 10 and 11 are given in Table 4.1 below showing that the results (given for fixed electron concentrations n) for $l =$ 10 and 11 are very close. This confidently allows the calculations to proceed using 10 electron, heavy hole and light hole wavefunctions each as a basis set, in the knowledge that including higher zone centre states in the basis will negligibly affect the final output.

	$n_5 = 5\times10^{15}$ cm^{-3}	$n_{10} = 5\times10^{15}$ cm^{-3}	$n_{11} = 5\times10^{15}$ cm^{-3}
E_0^{Γ}	65.78	61.56	61.05
E_1^{Γ}	93.88	88.60	87.93
E_2^{Γ}	103.46	98.15	97.94
E_F	104.65	99.45	98.93
HH_0^{Γ}	127.32	126.94	126.93
HH_1^{Γ}	118.81	117.98	117.91
LH_0^{Γ}	117.90	117.02	116.89
H_F	115.25	113.56	113.16
Bias	-17.67	-26.50	-27.00
	$n_5 = 7.5\times10^{15}$ cm^{-3}	$n_{10} = 7.5\times10^{15}$ cm^{-3}	$n_{11} = 7.5\times10^{15}$ cm^{-3}
E_0^{Γ}	73.71	69.04	68.74
E_1^{Γ}	109.71	103.14	102.75
E_2^{Γ}	123.94	116.86	116.15
E_F	127.54	121.24	120.95
HH_0^{Γ}	120.73	120.04	120.46
HH_1^{Γ}	110.46	108.41	108.76
LH_0^{Γ}	109.46	107.20	107.85
H_F	112.23	116.14	116.56
Bias	15.31	5.09	4.78

Table 4.1. Sample results of **k.p** self-consistent calculations performed using either 5, 10 or 11 electron, heavy hole and light hole wavefunctions each as a basis (denoted by the subscript on the electron concentration *n*). The values indicated are those of the 1st, 2nd, etc confined electron and hole states at the gamma point, and also the electron and hole Fermi energies and the resulting bias.

The combination of calculating a suitable number of zone centre (confined and continuum) states and subsequently using them to generate solutions at finite $k_{||}$ easily

makes this part of the algorithm the most time consuming. The thirty zone centre states yielded matrices of size 60×60 to be diagonlized. This itself was done 250 times per iteration of calculation for each equally spaced k point between 0 and 0.025 $bohr^{-1}$.

4.2.1.3 Calculating the Fermi Level

This is an iterative procedure in and of itself. For an electron concentration n, a trial quasi electron Fermi energy is selected. For this quasi Fermi energy, the electron population of the heterostructure subbands can be calculated using the method described below. If it found to be greater than n, the quasi electron Fermi energy is reduced and the population is recalculated. If it is less, the quasi electron Fermi energy is increased and the population recalculated. This interpolation continues until a suitable convergence is obtained. A similar procedure is used for calculating the hole quasi Fermi energy.

The 2D electron and hole systems require calculating the 2D density of states (DOS). Given a 2D plane of height and breadth L, the number of allowed $k_{\|}$ points within a circle of radius $k_{\|}$ is:

$$N = \left(\frac{L}{2\pi}\right)^2 \pi k_{\|}^2 \tag{4.9}$$

The 2D DOS is then the number of allowed $k_{\|}$ points per unit area:

$$\rho(E) = \frac{1}{L^2}\frac{dN}{dE} = \frac{1}{L^2}\frac{dN}{dk_{\|}}\frac{dk_{\|}}{dE} = \frac{1}{(2\pi)^2} 2\pi k_{\|}\frac{dk_{\|}}{dE} \tag{4.10}$$

The next step requires calculating the electron and hole 'character' of each state. This is done by diagonalizing the Hamiltonian, leading to a wavefunction that can be written as a linear combination of all the calculated gamma-point wavefunctions:

$$\Psi = \sum_i a_i \psi_{ie}^{\Gamma} u + \sum_j b_j \psi_{jh}^{\Gamma} v_j \tag{4.11}$$

with

$$\sum_i |a_i|^2 + \sum_j |b_j|^2 = 1 \tag{4.12}$$

where u and v_j are the Bloch crystal periodic functions for the bulk electron state and bulk hole states respectively, and ψ^{Γ}_{ie} and ψ^{Γ}_{jh} are the calculated electron and hole envelope functions. Note the summation for the electron component involves only one Bloch function u while the hole component will involve two Bloch functions v_j, corresponding to the heavy hole and light hole states.

For a state with a wavefunction given by (4.11), the total number of electron populated states per unit area is, utilising (4.10),

$$n_l = \left(\sum_i |a_i|^2\right)\int_{\Phi} \rho(E)dE = \left(\sum_i |a_i|^2\right)\frac{1}{(2\pi)^2}\int_{\Phi} 2\pi k_{\|}\, dk_{\|} \qquad \textbf{(4.13)}$$

where the integral is over the set Φ of all populated states (i.e. existing below the electron quasi Fermi energy). The total electron concentration for a given quasi Fermi energy can then be written as a summation over all subbands l:

$$n_{tot} = \sum_l n_l \qquad \textbf{(4.14)}$$

A similar treatment is used to calculate the hole quasi Fermi energy. Note that the usual factor of 2 for spin degeneracy is not explicitly included in equation (4.13) because the 6×6 Hamiltonian (Appendix C) treats each spin state individually.

4.2.1.4 Calculating the 'New' Potential - The Poisson Equation

With the Fermi energy now established, the charge distribution of a single state at a particular in-plane vector (described by equation (4.11)) can be calculated,

$$q_{k_{\|}}(z) = e\left\{\sum_j |b_j|^2 \left|\psi^{\Gamma}_{jh}\right|^2 \beta - \sum_i |a_i|^2 \left|\psi^{\Gamma}_{ie}\right|^2 \alpha\right\} \qquad \textbf{(4.15)}$$

where $\alpha = F_{InAs}$, $\beta = F_{GaSb}$ and F_{InAs} and F_{GaSb} are like Fermi-Dirac factors defined with respect to the quasi-Fermi levels in the respective materials (at 0K, $F_{InAs/GaSb} = 1$ or 0 only).

The total charge density is finally calculated by summing over all bands and all $k_{||}$ points:

$$q(z) = \sum \int \frac{1}{(2\pi)^2} q_{k_\parallel}(z) 2\pi k_\parallel dk_\parallel \tag{4.16}$$

With the charge density calculated the new potential is constructed by solving Poisson's equation. Neglecting many body interactions, this can be written as:

$$\frac{d^2\phi(z)}{dz^2} = -\frac{q(z)}{\varepsilon_r \varepsilon_0} \tag{4.17}$$

with,

$$V(z) = \begin{cases} -e\phi(z) & z < 0 \\ \Delta - e\phi(z) & z \geq 0 \end{cases} \tag{4.18}$$

Under the boundary conditions,

$$\left.\frac{d\phi}{dz}\right|_{z=0} = \begin{cases} \dfrac{en}{\varepsilon_r \varepsilon_0} \\ \dfrac{ep}{\varepsilon_r \varepsilon_0} \end{cases} \quad \text{and} \quad \phi(0) = \begin{cases} 0 & z < 0 \\ \Delta & z \geq 0 \end{cases} \tag{4.19}$$

equation (4.17) can be doubly integrated to give *V(z)*.

The presence of impurities in the background charge, however, modifies the above equations slightly. This is considered below.

4.2.1.5 Background Doping

Nominally undoped GaSb and InAs grown in-house by MOVPE have a background doping of magnitude ~10^{16}cm^{-3} which is capable of altering band profiles away from the interface. In bulk GaSb the Fermi level is known to be pinned to the acceptor level, the implications of which are discussed in below. For InAs, such studies have not been carried out. The following section also details the assumptions made in the absence of such information.

GaSb

Nominally undoped GaSb grown in-house by MOVPE is *p*-type with p^{bulk}~10^{16}cm^{-3}. Far from the SHET interface, GaSb acts like the bulk material pinning the Fermi level 34 meV above the valence band edge [15].

Although residually *p*-type, the material is compensated by a smaller concentration of donors. It is the ionization of these donors that can contribute to the band bending. Far away from the interface, the Fermi level is pinned to the acceptor level. The donors have ionized, losing their electrons to the acceptors leaving each positively charged donor balanced by a negatively charged acceptor. As the valence band edge (and therefore the acceptor level) bends upwards, the ionized acceptor, now above the Fermi level, is unable to retain its extra electron. The acceptors are neutral and the ionized donors thereby contribute a 2D charge density $N_D^{GaSb} z_A$ to the band bending where N_D^{GaSb} is the compensated donor concentration and z_A is the (acceptor) depletion length.

InAs

The hydrogenic ionization energy (IE) is 13.6eV. For semiconductors, an electron in the presence of a donor impurity can be represented as a particle of charge *e* and mass m^* moving in free space in the presence of a positive charge e/ε_r. This is a modified hydrogen problem with the IE multiplied by m^*/ε_r^2 yielding an IE for InAs donors of 2 meV.

Compensation means that in this material acceptors will be present. All the acceptors and donors must be ionized far away from the interface in the Fermi level is assumed to be pinned to the donor level. In the depletion region, acceptors remain ionized but donors become neutral contributing a net negative 2D charge density $N_A^{InAs} z_D$ to the band bending where N_A^{InAs} is the compensated acceptor concentration and z_D is the (donor) depletion length.

With background doping, Poisson's equation becomes,

$$\frac{d^2\phi(z)}{dz^2} = \begin{cases} -\dfrac{q(z)}{\varepsilon_r\varepsilon_0} + \dfrac{eN_A^{InAs}}{\varepsilon_r\varepsilon_0} & z < 0 \\ -\dfrac{q(z)}{\varepsilon_r\varepsilon_0} - \dfrac{eN_D^{GaSb}}{\varepsilon_r\varepsilon_0} & z \geq 0 \end{cases} \tag{4.20}$$

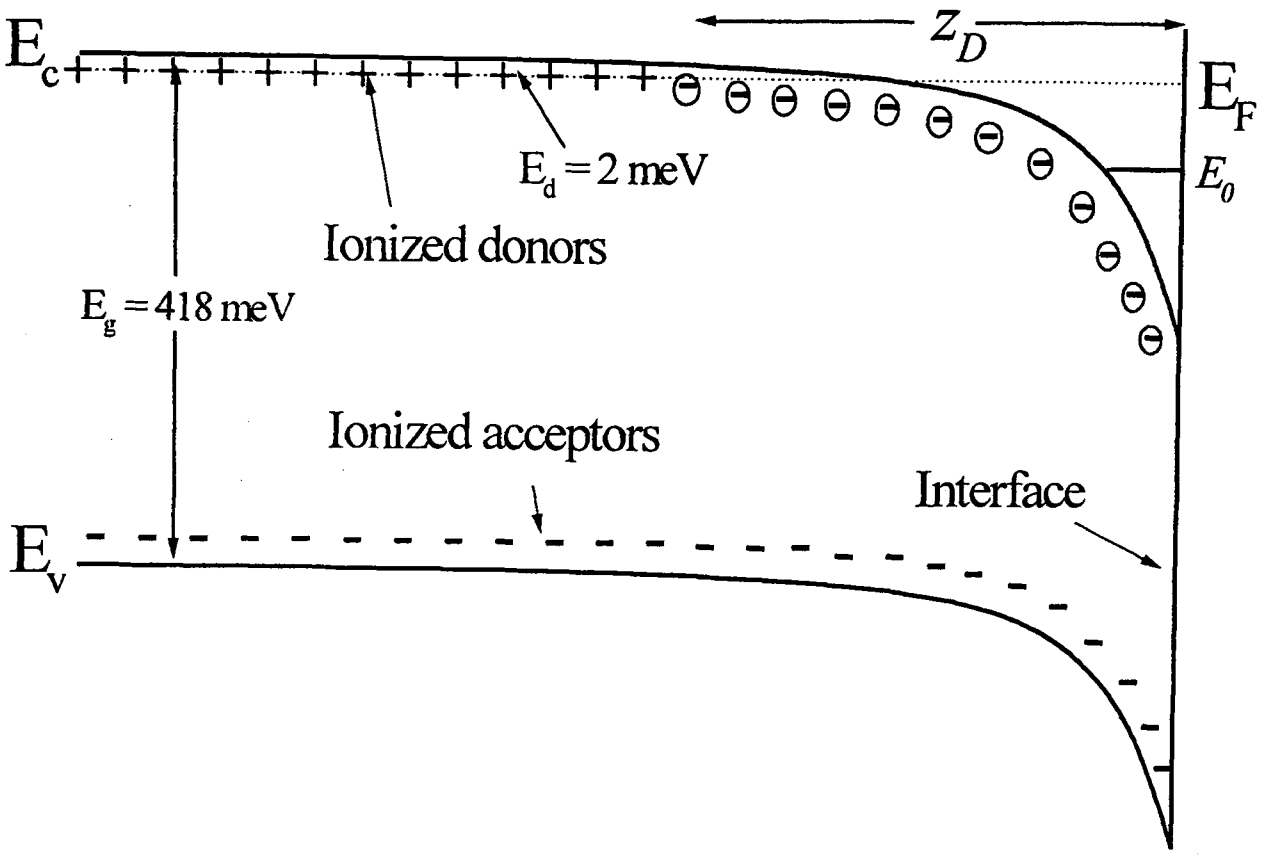


Figure 4.2. Schematic showing the formation of negative background charge for the InAs side of the SHET. The Fermi level away from the interface is pinned by the donor level. The concentration of acceptors, N_A^{InAs}, multiplied by the distance of band bending, z_D, yields a 2D charge density that contributes to the band bending.

where N_A^{InAs} is the compensated acceptor concentration (in InAs) and N_D^{GaSb} is the compensated donor concentration (in GaSb). The effect of changing N_A^{InAs} and N_D^{GaSb} on the band profile was studied by Khan-Cheema [5] who found that by varying their values between 10^{15} and 4×10^{15} cm^{-3}, the output confinement energies changed only by less than 2%. In the calculations presented in this chapter therefore, N_A^{InAs} and N_D^{GaSb} are both assumed to be 10^{15} cm^{-3}.

4.2.1.6 Convergence

After calculating the newly calculated band-edge potential, a weighted average of the new and old potential is taken (30% new and 70% old) and the algorithm is repeated to whatever degree of accuracy is required of the confinement energies or biases. After 8-10 iterations, I found the difference between successive E_0's to be less than 0.001meV, typically taking 24 hours on a 180 MHz Pentium processor.

4.2.1.7 Pressure Dependence

The changes that hydrostatic pressure makes can be summarised below:

- Bulk InAs and GaSb have Γ-point band gaps that increase with pressure at the rate of 10 and 14 meV/kbar respectively [16, 17, 18].
- Hydrostatic pressure decreases the band overlap, Δ, at a rate of -9.5 meV/kbar. The band overlaps at 1 bar are taken as 155 meV for the 'InSb-like' interface samples and 125 meV for the 'GaAs-like' interface samples [4].
- The InAs conduction band m_0^* edge zone centre effective mass as a function of pressure is given by the following expression [19],

$$m_P^* = \left(m_e^* + 6.67 \times 10^{-4} P\right) \tag{4.21}$$

where P is the pressure in kbar and m_e^* is the electron effective mass in the absence of any applied pressure. There is no available literature on the variation in electron mass of the GaSb conduction band edge. This doesn't affect the calculations greatly as the penetration of the electron wavefunctions into the GaSb layer is small. However, it can be estimated from the results of the eight band **k.p** model presented earlier. From Table 3.2,

$$\frac{1}{m_e^*} = \frac{1}{m_0} + \frac{4P_k^2}{3E_g} + \frac{2P_k^2}{3\left(E_g + \Delta_{so}\right)} \tag{4.22}$$

and thus,

$$\frac{dm_e^*}{dP} = \frac{m_e^2}{m_0}\left\{\frac{4P_k^2}{3m_0E_g^2} + \frac{2P_k^2}{3m_0\left(E_g + \Delta_{so}\right)}\right\}\frac{dE_g^\Gamma}{dP} \tag{4.23}$$

where I write P_k as the Kane interband matrix element to distinguish it from the pressure P. For GaSb, substituting the values Δ_{so} = 0.75 eV, E_g = 0.811 eV, $E_P = 2P_k^2/m_0$ = 22.88 eV and dE_g^Γ/dP = 0.014 eV/kbar [20] into equation (4.23), I estimate the variation of the electron mass in GaSb to be $dm_e^*/dP = 5.896\times10^{-4}m_0$ kbar^{-1}.

It was assumed that the Luttinger parameters remained constant throughout the range of pressures under which experiments were carried out.

Strain effects due to the slight lattice mismatch between InAs and GaSb were also neglected. No additional strain is induced by the pressure since the compressibilities of the two materials are nearly equal [21].

4.3 Interface Type and the Band Overlap

The lack of any common element in the bulk materials of the InAs/GaSb heterojunction allows structures to be grown that are nominally identical except for the monolayer at the interface. Two possibilities exist; either an 'InSb-like' or 'GaAs-like' interface may be grown (Figure 1.11) each with a different band overlap. As Khan-Cheema [5] and the work here shows, the vertical transport properties of the SHET are clearly very sensitive to the interface type of the SHET. This is immediately apparent in the simple IV trace taken in the absence of any magnetic field or externally applied pressure (Figure 4.3 and Figure 4.8). NDR occurs at about 0.15V for the samples with an 'InSb-like' interface but at 0.3V for samples with 'GaAs-like' interfaces (and at a higher peak current too). Applying pressure (section 4.4, [5, 22]), or magnetic field (chapter 5 and 6), confirms the difference in the response of the two sample types. These differences reveal one of the main reasons for studying the InAs/GaSb SHET. The question arises: 'Is the difference in the response of each sample type explicable by the band overlap?' The answer is a resounding no [5, 22] - the 'InSb-like' interface behaves predictably, revealing a conduction mechanism consistent with that described earlier 1.5.1, while samples with a 'GaAs-like' interface must harbour a different conduction mechanism.

This chapter represents the starting point of the investigation into this inconsistency by showing the pressure behaviour of the SHETs and attempts to understand the data through a 6 band **k.p** model. For that and for future magnetic field related work, the value of the Δ needs to be ascertained. The remainder of this subsection is reserved for just this purpose.

Early experiments by Sai-Halasz *et al* [23] and Beerens *et al* [24] led to values of Δ of 150±50 meV and between 150 and 163 meV respectively. These are surprisingly close to the values generally agreed upon now [3] but reveal the huge disparity between other groups who determined it with a much greater error. This class of groups includes, for example, Gualtieri *et al* [25] who reported Δ a value of 90±100 meV. On the theoretical front, Van de Walle *et al* [26], using model solid theory, calculated a band overlap of 160 meV - also a value close to the values used in this work. With interface type considered, the work of Foulon and Priester [27] predicted a 31 meV larger band overlap for an 'InSb-like' interface than for a 'GaAs-like' interface, while Dandrea *et al* [28] calculated the difference to be 44 meV.

The values used here are those obtained from relatively recent magnetotransport measurements on superlattice samples grown in the same reactor and under the same conditions (temperature, switching sequence etc.) as the SHETs studied. The experiments, carried out under hydrostatic pressure by Daly *et al* [4] suggest the change in the bulk band gaps alters the band overlap Δ at a rate of -9.5±0.5 meV/kbar. Also, by fitting their results to a self consistent effective mass calculation, they obtain 1 bar values of Δ that differ depending upon the composition of the monolayer interface, with a Δ for the 'InSb-like' interface of 155±5 meV and one for the 'GaAs-like' interface of 125±5 meV.

These values are consistent with reverse bias measurements of the InAs/GaSb SHET IV by Khan-Cheema [5]. At a fixed high reverse bias, the current due to full bulk GaSb valence band states overlapping empty states in the InAs conduction band is expected to fall with pressure as the band overlap Δ falls fairly linearly. At some critical pressure P_c however, the band overlap is reduced to zero and conduction is then only possible through tunnelling. On increasing P through P_c the current is therefore expected to decrease exponentially, reflecting the change in conduction mechanism. A plot of current versus pressure at such a fixed reverse bias is therefore expected to exhibit an inflexion at P_c. Khan-Cheema has shown through such a study that *i)* P_c is approximately 3 kbar larger for the 'InSb-like' interface than the 'GaAs-like' interface, and *ii)* $d\Delta/dP$ is similar for both interfaces.

4.4 Presenting Experimental and Theoretical Results

With the single heterojunction **k.p** machinery described, the remainder of this chapter will be devoted to presenting, analysing and comparing its results with that of experimentally obtained data. Additionally, a comparison between the full 6-band model used here and the decoupled model used earlier [5] will show if **k.p** theory supports the earlier conclusions on the nature of resonant conduction in the SHET obtained from the decoupled model. The aims of this section can be summarised as follows:

- To determine whether the predicted model of resonant conduction (1.5.1) is actually the method by which NDR arises in SHET structures.
- To check the validity of the **k.p** approach (and therefore that of the more simple decoupled model).

4.4.1 Dependence of NDR on Hydrostatic Pressure

Pressure is a way of varying Δ for both sample types in a controlled way whilst retaining the ability to monitor the forward bias resonant conduction characteristics. Increasing pressure reduces Δ, causing the intrinsic charge to be transferred back across the interface from the GaSb into the InAs and thus reducing n and p. A direct consequence of falling n and p is to reduce the current at a given bias. Additionally, as E_0 and HH_0 are closer, V_c (the voltage at which E_0 lines up with HH_0) will occur at a lower bias, thereby decreasing the peak and valley voltages (V_p, V_v). For an ideal SHET therefore, I_P and V_P should decrease with increasing pressure until at a critical pressure P_c when $\Delta = 0$, the 2DEG and 2DHG concentrations are zero and NDR has disappeared at zero bias and zero current. Thus hydrostatic pressure is an ideal tool for probing the origin of NDR in SHETs.

4.4.1.1 Results for the 'InSb-like' Interface

Figure 4.3 and Figure 4.4 show the IV characteristics of an 'InSb-like' interface at increasing pressures. The experiments were performed at 77K using the Russian cell described in chapter 2. The peak and valley voltages fall as expected as the pressure is increased which is consistent with E_0 moving closer to HH_0 at zero bias. The peak and valley currents also fall which, again, agrees with the model where charge recombination as the pressure is increased leaves a lower 2D charge concentration at the interface. Figure 4.4 shows the results at higher pressure. The NDR region can be seen at 8.7 kbar, although it is considerably diminished in magnitude, and a feature is visible at 12.7 kbar. At this pressure, there is no NDR but clearly the conductance rises and falls before the current merges with the background current at roughly 0.1V which points to the existence of a resonant conduction process drowned out by an additional conduction mechanism (involving, for example, interface impurity states, or a thermionic component). By 18 and 19.8 kbar, the IV traces are nearly coincident and show no features. This indicates the conduction path is the same for both pressures and therefore independent of band overlap. The NDR feature thus vanishes at very small biases which is consistent with E_0 and HH_0 at zero bias being very close together. Though an exact value of P_c, the pressure at which all trace of resonant conduction is not possible, an approximate value of 16 kbar does, however, fit the data well and the results seem to show that for the 'InSb-like' interface the resonant conduction path giving rise to NDR is suppressed by ~16 kbar.

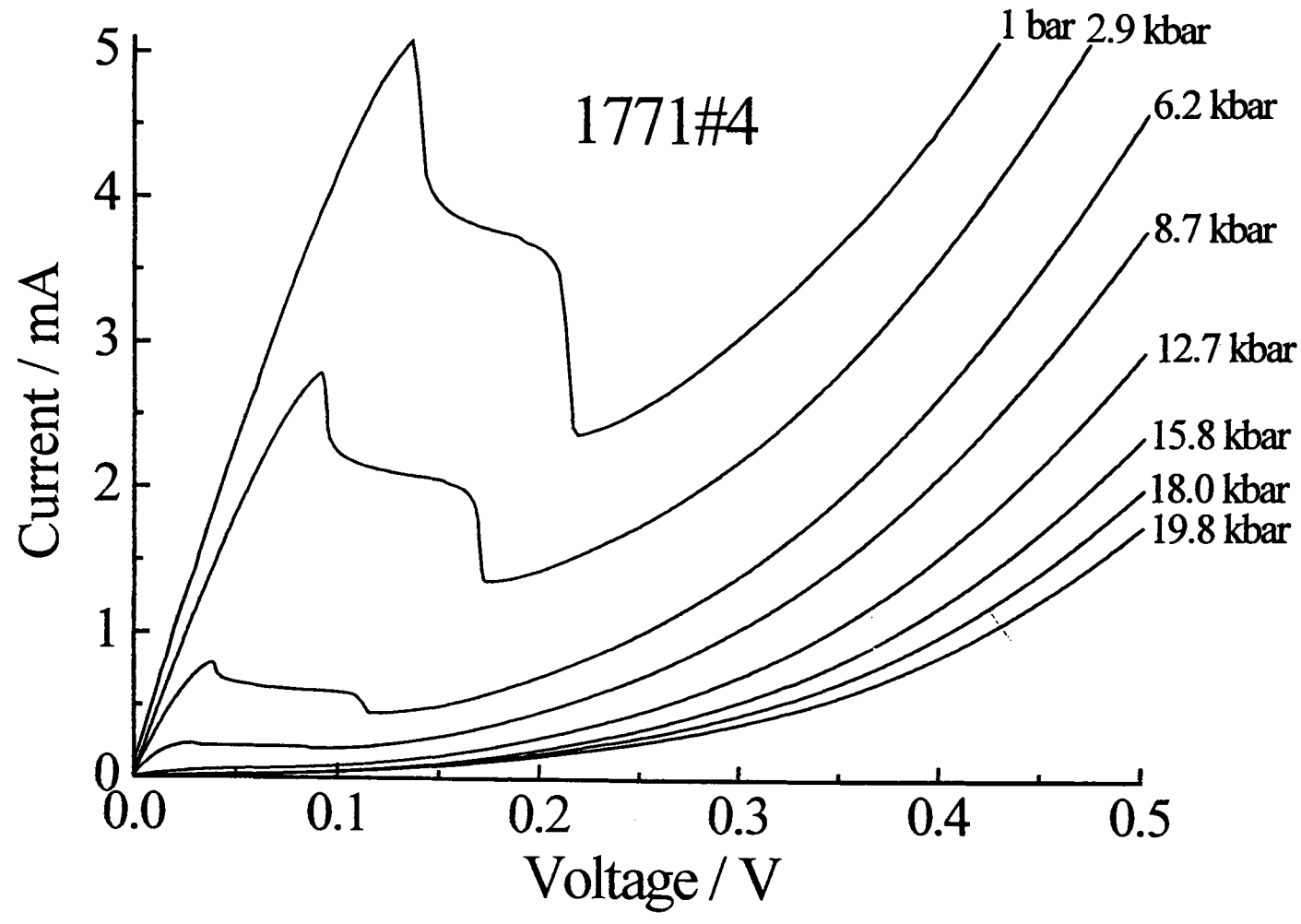


Figure 4.3. Forward bias IV data for 1771#4 measured at 77K for pressures up to 19.8 kbar measured earlier [5].

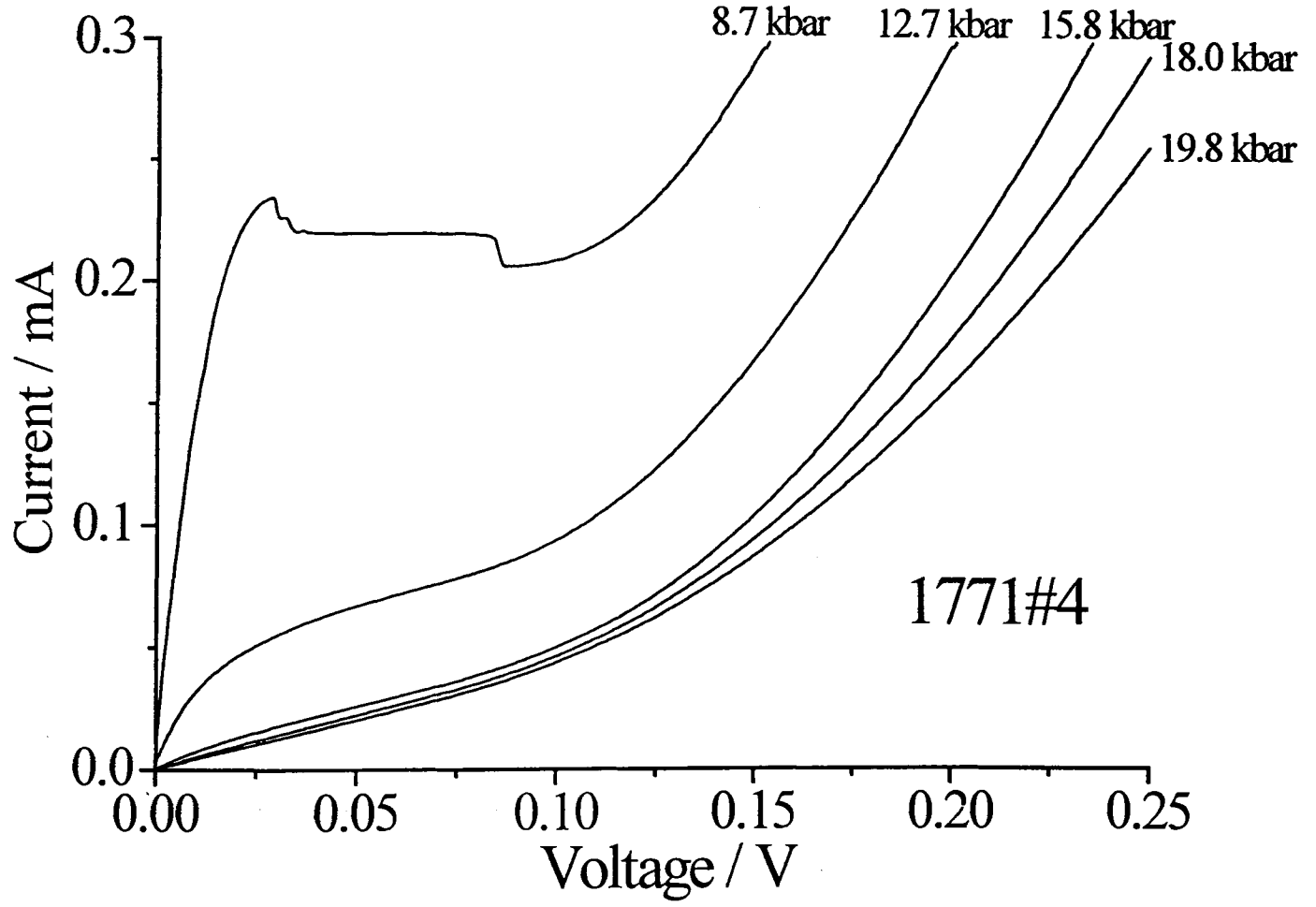


Figure 4.4. High pressure IV plots for 1771#4 taken at 77K from [5]. The resonant feature has almost vanished by 15.8 kbar, indicating the NDR is dependent upon the existence of a positive band overlap, Δ, which falls to zero by P_c=16±0.5 kbar.

The positions of the 2D electron and hole subbands with applied forward bias for this type of SHET at 1 bar calculated using the full 6 band model is given below in Figure 4.5b. For comparison Figure 4.5a shows the results obtained using the decoupled model. The zone centre electron and heavy hole confinement energies, E_0 and HH_0, are seen to cross at 87 mV. This should be compared with the observed peak and valley voltages at 77K of 147 mV and 213 mV respectively. However, before any comparisons can be made, the following two considerations should be made. Firstly resonant conduction can be, and probably is, phonon assisted (see section 4.5). Thus a better indication of the theoretically expected position of the peak is at the bias where E_0 is a typical phonon energy (30 meV) beyond HH_0. This value, V_{30}, is 142 mV. Secondly, a proportion of the applied voltage is dropped across any parasitic resistance R in the circuitry used to measure the IV trace. This was deduced earlier to be about 20Ω [29]. Taking this into account, the 'true' peak voltage is $(V_p - I_pR) = 44$ mV and the 'true' valley voltage is 165 mV. Comparing the values now shows that V_{30} is approximately equal to the corrected valley voltage.

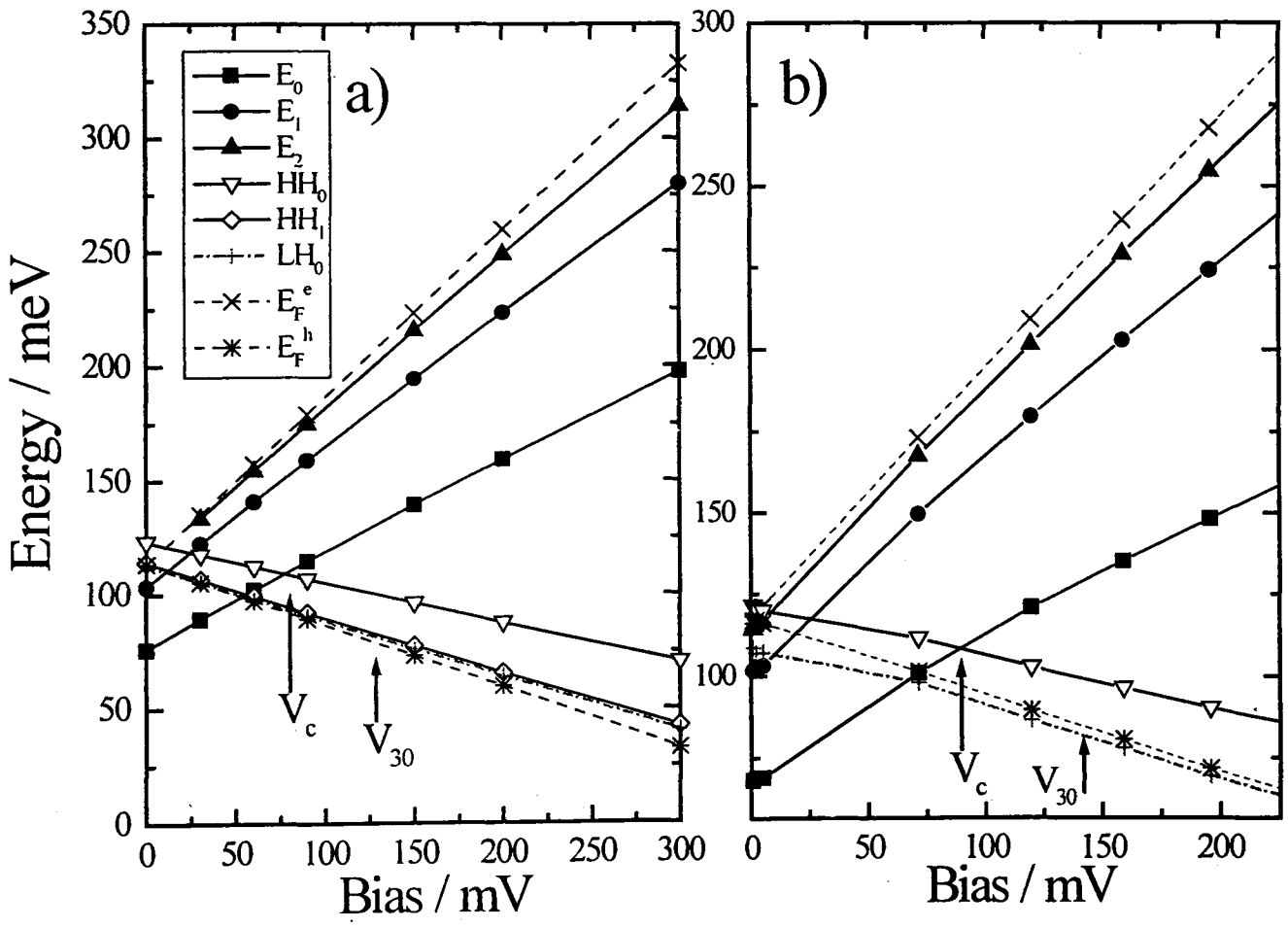


Figure 4.5. Movement of the Γ point energies at 1 bar calculated in *a*) by a decoupled model [5], and *b*) **k.p** method using 10 subband Γ electron, heavy hole and light hole wavefunctions each as a basis. In *a*), $V_c = 77$ meV and $V_{30} = 127.6$ meV. In *b*), $V_c = 89.5$ meV and $V_{30} = 142.5$ meV.

Figure 4.6 shows the movement of the zone centre electron and hole subbands at the higher pressures of 5 and 10 kbar calculated using **k.p** theory. Indicated are V_c and V_{30}, the biases at which $E_0 = HH_0$ and $E_0 - HH_0 = 30$ meV. Plotting these values as a function of pressure allows a comparison to be made with the results of the decoupled model of Khan-Cheema. This is done in Figure 4.7, demonstrating excellent agreement between the two approaches and hence validating his earlier conclusions based on his experimentally collected data. This confirmation that the decoupled model agrees well with the **k.p** method means that the decoupled model can be used to predict values for V_c and V_{30} accurately and quickly, but obviously will not be able to provide detailed information about band mixing and non-parabolicity which only the **k.p** model can provide.

Notice that each model provides conclusive proof that the light hole states do not make a significant contribution to the resonant current as they are found to lie below the hole quasi Fermi energy. The resonant current is therefore due primarily to mixed electron and heavy-hole states at finite in-plane vector.

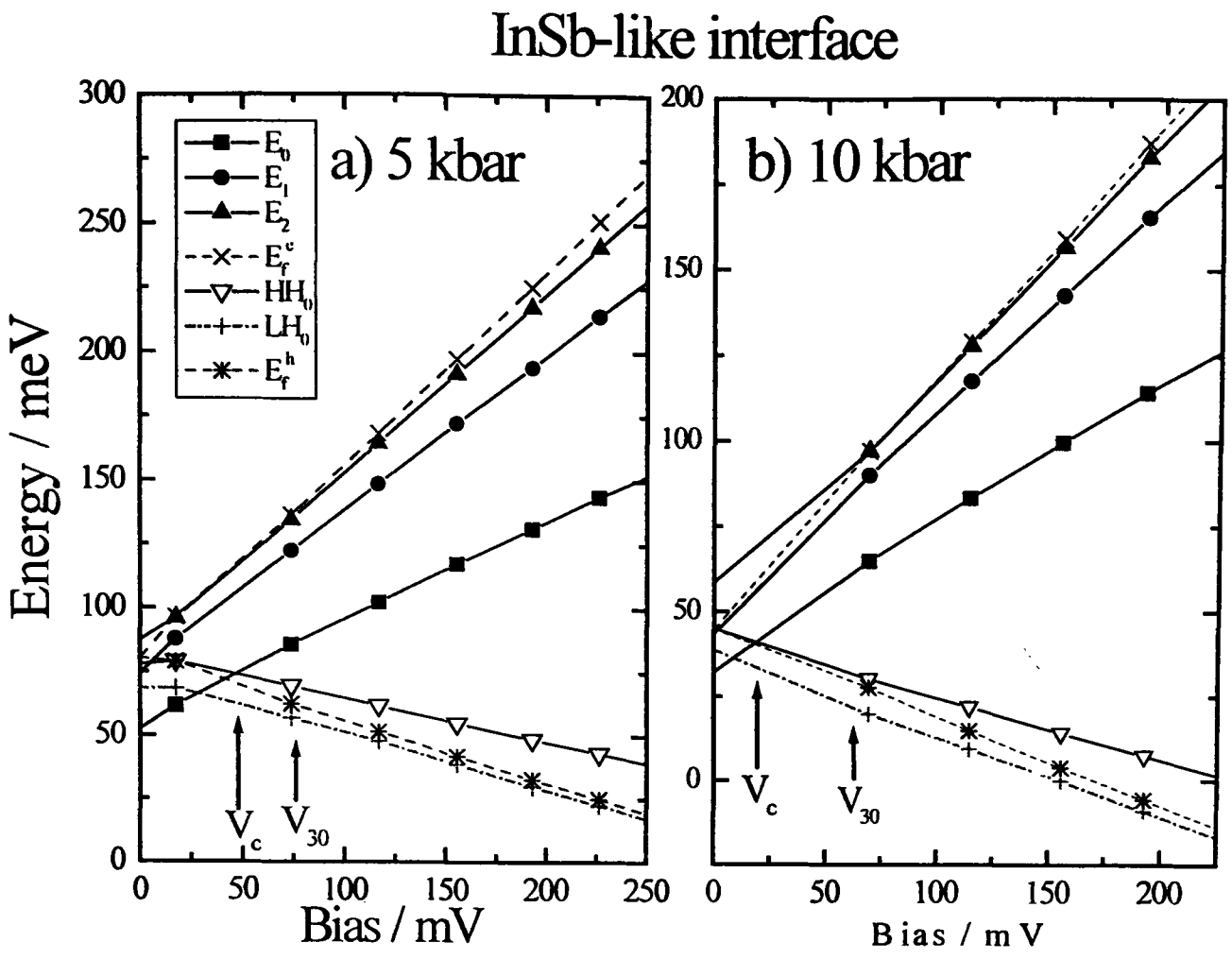


Figure 4.6. Movement of the Γ point energies at 5 and 10 kbar calculated using **k.p** using 10 subband Γ electron, heavy hole and light hole wavefunctions each as a basis. In a), V_c = 45.51 mV and V_{30} = 98.07 mV. In b), V_c = 19.59 mV and V_{30} = 64.96 mV.

Figure 4.7 further plots the calculated position of the peak and valley voltages for two 'InSb-like' samples. The data for 1771b#3 are earlier measurements taken by Khan-Cheema at 77K, while the data for 1771b#8 are careful measurements taken during the course of this work at 4.2K. From the former plot, Khan-Cheema concluded V_{30} followed V_v well (with a series resistance of 20Ω) taken into account, and hence that the valley is likely to be due to phonon emission. Though my theoretical results bear striking similarity to his, my experimental results do not, owing of course to the different temperatures at which the pressure runs were conducted. From the 4K data, I find that it is in fact V_p (corrected for 10Ω) that follows V_{30} well. The exact point at which NDR occurs, clearly appears to vary slightly with temperature, though the overall picture of resonant conduction in the 'InSb-like' SHET is consistent with the bias dependent electron-hole overlap described earlier 1.5.1 with complicated phonon coupling that allows conduction well after the electron and hole bands have uncrossed. This point is corroborated by the high pressure 4K results that strongly indicate that up to three phonons are indeed involved in conduction (section 4.5).

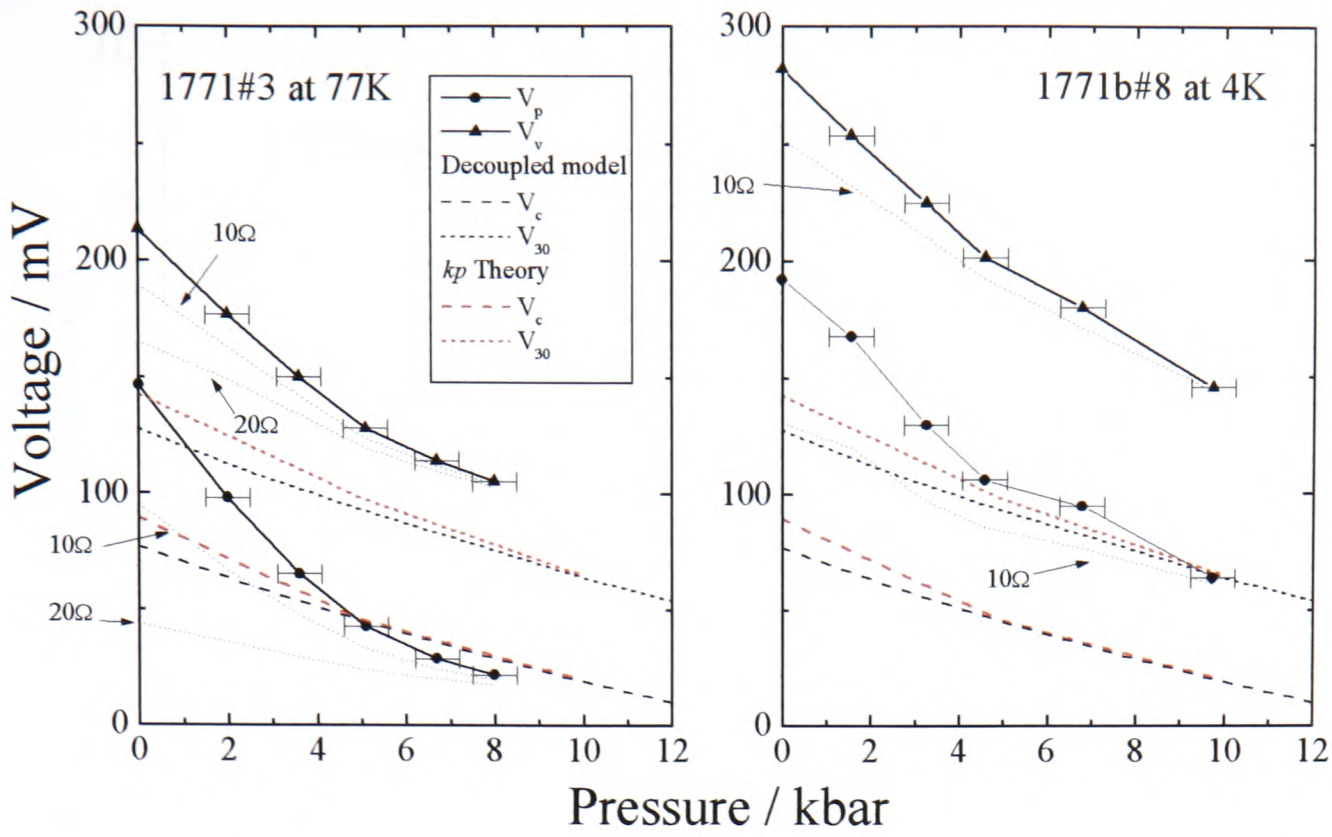


Figure 4.7. Peak and valley voltages V_p and V_v plotted against pressure for 1771#3 (from [5]). The error bars indicate the ±0.5 kbar uncertainty in the manometer readings. The dashed lines indicates the calculated peak voltage. The dotted lines shows how the inclusion of series resistances of 10 and 20 Ω affect the experimental data. Shown are V_c and V_{30} calculated using a decoupled model employed by Khan-Cheema and **k.p** theory. Notice the good agreement between the two approaches, thus validating the earlier work.

4.4.1.2 Results for the 'GaAs-like' Interface

The experimental results of samples with a 'GaAs-like' interface are presented below. Again, consistent with a decreasing band overlap Δ, the peak and valley voltages and currents fall with pressure. Initially, Δ is 125 meV and $d\Delta/dP$ is –9.5 meV/kbar [3], implying the pressure at which Δ is reduced to zero, P_c, should be about 13 kbar. Moreover, in order for this interface to support the same conduction mechanism as the 'InSb-like' interface the resonance certainly should disappear at a pressure no greater than 16 kbar with $V_p \rightarrow 0$ and $I_p \rightarrow 0$. However, as previously reported [5], the results show resonant conduction persists beyond P_c and even at higher pressures still (see Figure 4.9). With a resonant feature observed at pressures of up to 18 kbar where Δ is close to –50 meV, the conduction mechanism in these samples is clearly very different to that observed in 'InSb-like' samples.

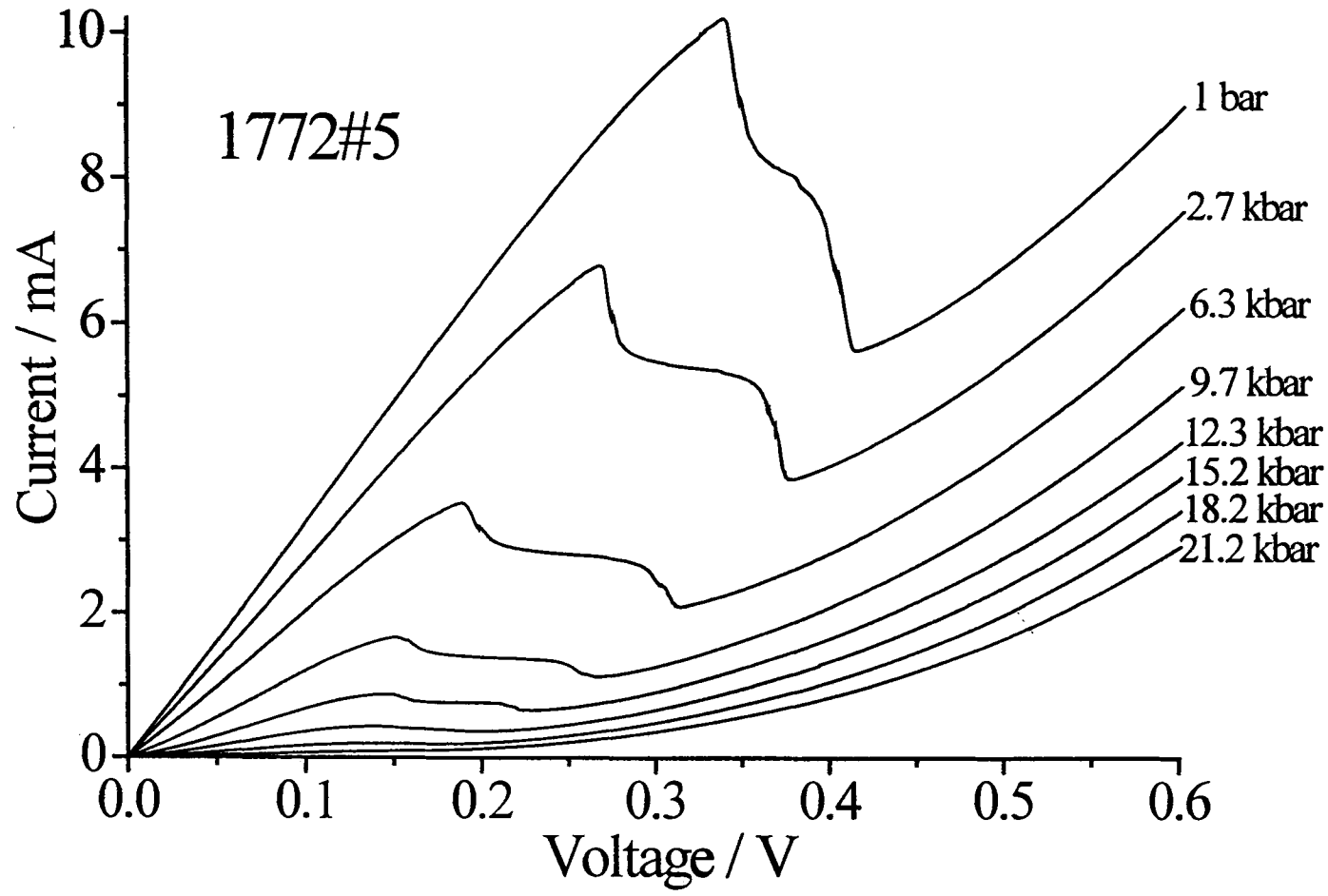


Figure 4.8. Forward bias IV curve for 1772#5 measured in an earlier work [5] at 77K for various pressures between 1 bar and 21.2 kbar.

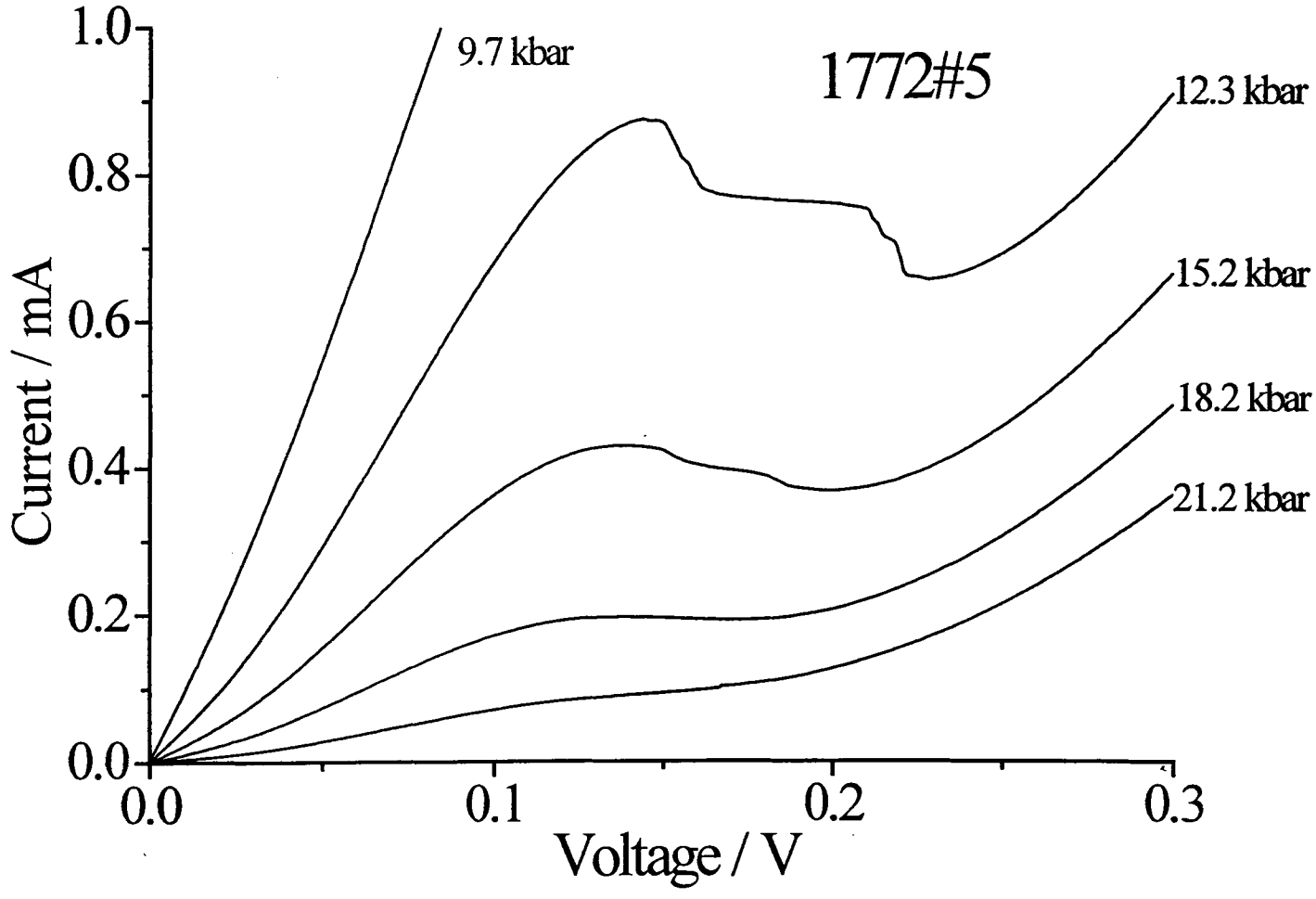


Figure 4.9. High pressure IV plots for 1772#5 taken at 77K. The resonant feature can still be seen at 21.2 kbar as a small hump I the IV curve, way beyond the zero band overlap condition at P_c=13±0.5 kbar. From [5].

Figure 4.10 shows the movement of the zone centre electron and heavy hole confinement energies, E_0 and HH_0 with bias for 'GaAs-like' samples at 1 bar. The plot corresponding to a pressure of 10 kbar, when Δ has fallen to 30 meV, is shown in the same figure. In both cases, and indeed in all the calculations carried out for 'GaAs-like' samples, V_c occurs at a significantly lower bias than either V_p or V_v. This difference is better highlighted in Figure 4.11 where V_p and V_c are plotted as a function of pressure, along with calculated V_c, V_{30} and V_{120} (the bias position at which E_0 and HH_0 are separated by approximately three phonon energies). The plot also shows V_p and V_c corrected for a series parasitic resistance. The results show a central point to this thesis: there is no agreement on the position of the NDR in 'GaAs-like' samples between experimentally obtained values and theoretically obtained values unless conduction is assumed to be strongly mediated by at least three phonons.

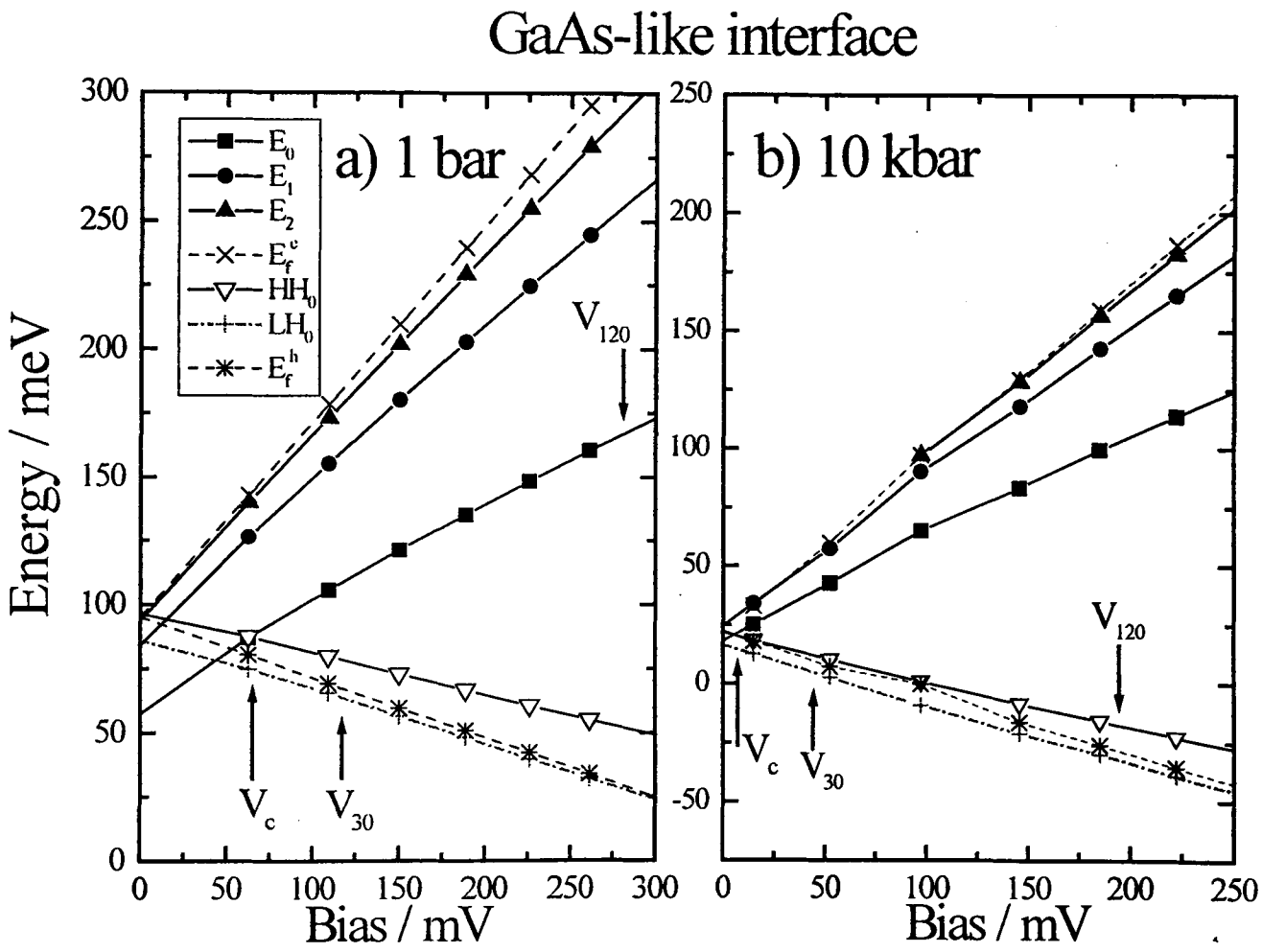


Figure 4.10. Movement of the Γ point energies at 5 and 10 kbar calculated using **k.p** using 10 subband Γ electron, heavy hole and light hole wavefunctions each as a basis. In a), V_c = 63.48 mV, V_{30} = 116.32 mV, V_{120} = 286.32mV. In b), V_c = 5.05mV and V_{30} = 48.77mV, V_{120} = 193.97mV.

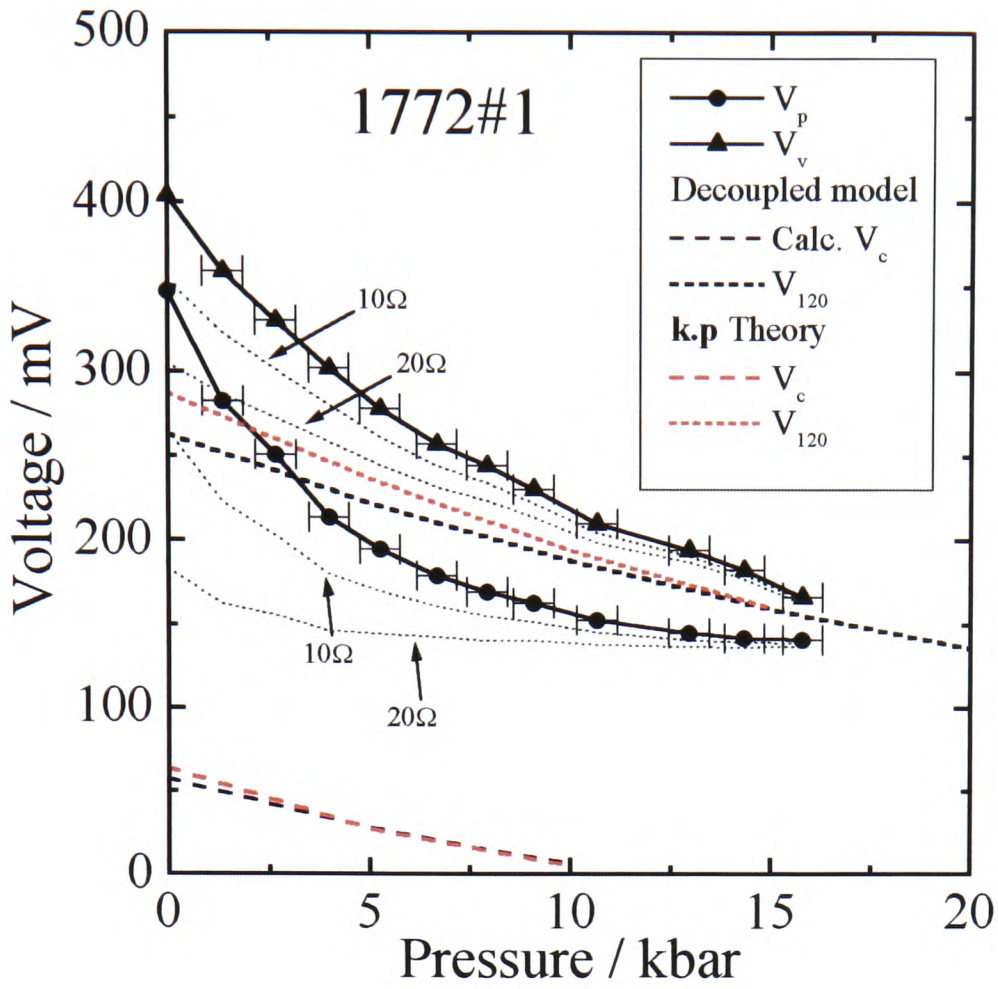


Figure 4.11. Peak and valley voltages V_p and V_v plotted against pressure for 1772#1 (from [5]). The error bars indicate the ±0.5 kbar uncertainty in the manometer readings. The dashed lines indicates the calculated peak voltage. The dotted lines shows how the inclusion of series resistances of 10 and 20 Ω affect the experimental data. Shown are V_c and V_{120} calculated using a decoupled model employed by Khan-Cheema and **k.p** theory. Notice the good agreement between the two approaches.

To summarise, the **k.p** method has yielded solutions which are close to those obtained earlier assuming a decoupled model [5]. Thus, it supports those earlier conclusions that the behaviour of the samples with an 'InSb-like' interface can be understood in general terms by the resonant conduction process described in 1.5.1 and summarised here. At zero bias, there are no overlapping electron and hole states with equal energy and $k_{||}$. Increasing the bias causes an overlap to occur that is proportional to the applied voltage. The current therefore is initially expected to rise with bias as the number of overlapping electron and hole states increases. Comparison between **k.p** calculations and measured data suggest the maximum tunnelling current (the peak) is not reached however until the highest hole level has passed the lowest occupied electron level by 30 meV (a typical phonon energy) implying that phonons are involved in the conduction process. Beyond this point, the current is expected to decrease leading to NDR. No such process can be attributed to the 'GaAs-like' samples unless multiple phonon processes occur between electron states and hole states once they have passed one another in energy. With multiple phonon processes

unlikely, and no other explanation forthcoming, resonant conduction in 'GaAs-like' interface samples has continued to be puzzling. However, very careful low temperature and high pressure IV and first derivative measurements reveal a startling result - *multiple phonon processes do occur*. These results, discussed in section 4.5.2, may be the key to reconciling experiment and theory in 'GaAs-like' samples and thereby will help to provide a more comprehensive understanding of resonant conduction in the SHET.

4.5 Phonon Processes in InAs/GaSb Structures

This initial foray into the pressure response of the IV characteristics of InAs/GaSb SHETs clearly demonstrates a strong interface dependence. For 'InSb-like' interface samples, the NDR peak occurs close to V_{30} when electron and hole bands no longer overlap, with the NDR valley occurring soon after. The results for the 'GaAs-like' interface samples show that the resonance is not directly related to the band overlap but takes place through some inelastic mechanism when a bandgap of roughly 120 meV exists between the electron and hole systems. The more expected behaviour of 'InSb-like' samples and the rather surprising behaviour of 'GaAs-like' samples is a feature which I return to in later chapters dealing with magnetic fields applied to the SHET.

It is the aim of this subsection to present experimental verification of phonon assisted tunnelling in the SHETs.

4.5.1 A Detour into Raman Spectroscopy

The calculated phonon dispersion of an InAs/GaSb superlattice (with alternating 'GaAs-like' and 'InSb-like' interfaces) reveals so-called 'interface modes' (IFMs) that fall within the acoustic-optic gap (between 166 and 212 cm^{-1}) and above the superlattice optic branch (above 240 cm^{-1}) [30]. Monolayers with a 'GaAs-like' interface display two interface modes, whose eigenvectors are given in [30, 31] and reproduced below in Figure 4.12. The higher frequency mode at ~250 cm^{-1} is identified as an optic interface mode because all the atoms (i.e. on both sides of the interface) move in antiphase, while the lower mode at 185 cm^{-1} is longitudinal

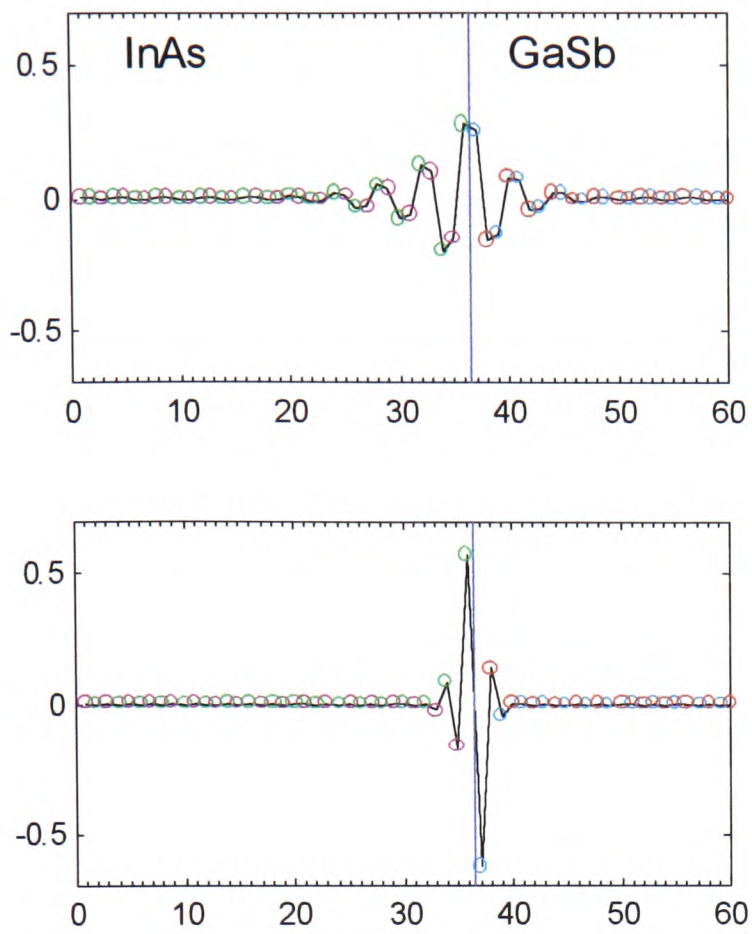


Figure 4.12. Calculated displacement (y-axis) patterns of the ~185 cm^{-1} Acoustic GaAs IFM (top) and the ~250 cm^{-1} Optical GaAs IFM (bottom) modes in InAs/GaSb superlattices. The optical IFM was found to be present regardless of the superlattice period. Courtesy of Lyapin [31, 33].

acoustic (LA) in character because the atoms in a given unit cell on each side of the interface move in phase. The 'InSb-like' interface only shows one interface mode at 190 cm^{-1} which is also acoustic in character. Calculating the Raman strength of the longitudinal interface modes for scattering by the deformation potential [32] suggests that the 'GaAs-like' interface type optic mode should have a Raman strength comparable to that of the superlattice LO modes and the strengths of the 'InSb-like' optic and 'GaAs-like' interface acoustic modes should be much weaker. This was attributed to the strong localisation at the interface of the 'GaAs-like' optic mode compared to the 'GaAs-like' acoustic and 'InSb-like' interface modes.

By checking for the existence of the relevant optical and interface modes, an accurate assessment of the interface quality is possible. This is done by Raman spectroscopy. Lyapin [34] has performed such experiments the results of which do show peaks in the spectra corresponding to the energy of the LO phonon and weaker IFM signals for SLs of each interface type. A good review of the results in the context of interface characterisation is given in [5].

The aim of this subsection is to convey to the reader evidence for strongly localised interface modes, and in particular that of the 'GaAs-like' interface optical mode at ~240 cm^{-1} (29.76 meV). This is likely to affect the affect the transport characteristics in samples with such an interface type but several phonons would need to be involved to be consistent with the ~120 meV separation of electron and hole Fermi gases close to resonance found experimentally (section 4.4.1.2). The section ahead details

experiments that have been performed at high pressure providing just this evidence. Multiple phonons each of energy ~240 cm^{-1} are found to be involved in conduction in the 'GaAs-like' samples. These are likely to be the strongly localised 'GaAs-like' optical interface mode described here. In addition, the similar features observed in 'InSb-like' samples (section 4.5.2) suggests that phonons of nearly equal energy are also involved in conduction in such sample types. In the absence of a ~240 cm^{-1} interface mode, these may be bulk LO phonons. In short, established research on phonons may well explain the type of phonons (interface or bulk) that the following section shows to play a key part in conduction.

4.5.2 Observed Phonon Cascades

The pressure results presented earlier were all taken at 77K and no first derivative or second derivative measurements were taken at that stage as the primary goal was to measure NDR as a function of pressure. The experiments were repeated here, but at a lower temperature of 4K and with the use of a lock-in amplifier to measure the first and second derivatives of the IV trace. The results are surprising, revealing features that are strong candidates for phonon cascades occurring in both sample types. Figure 4.13 shows very high pressure, reverse bias second derivative measurements of a sample with a 'GaAs-like' interface. These features, absolutely invisible in the IV and barely visible in the conductance are very clear in the 2nd derivative and are found only in reverse bias. The number of features observed increases with pressure and furthermore, each peak on the plot is separated by about 30 mV, a value equal to a phonon energy.

A smaller number (2~4) of reverse bias features were observed in the second derivative for samples with an 'InSb-like' interface. Additionally, the high pressure, low temperature forward bias results show very slight features, *even* in the IV. These occur at and near the NDR bias, and are highlighted below also in Figure 4.14. Each feature is again separated by about 30 mV, suggesting that multiple phonon processes occur in these samples too, in forward as well as reverse bias.

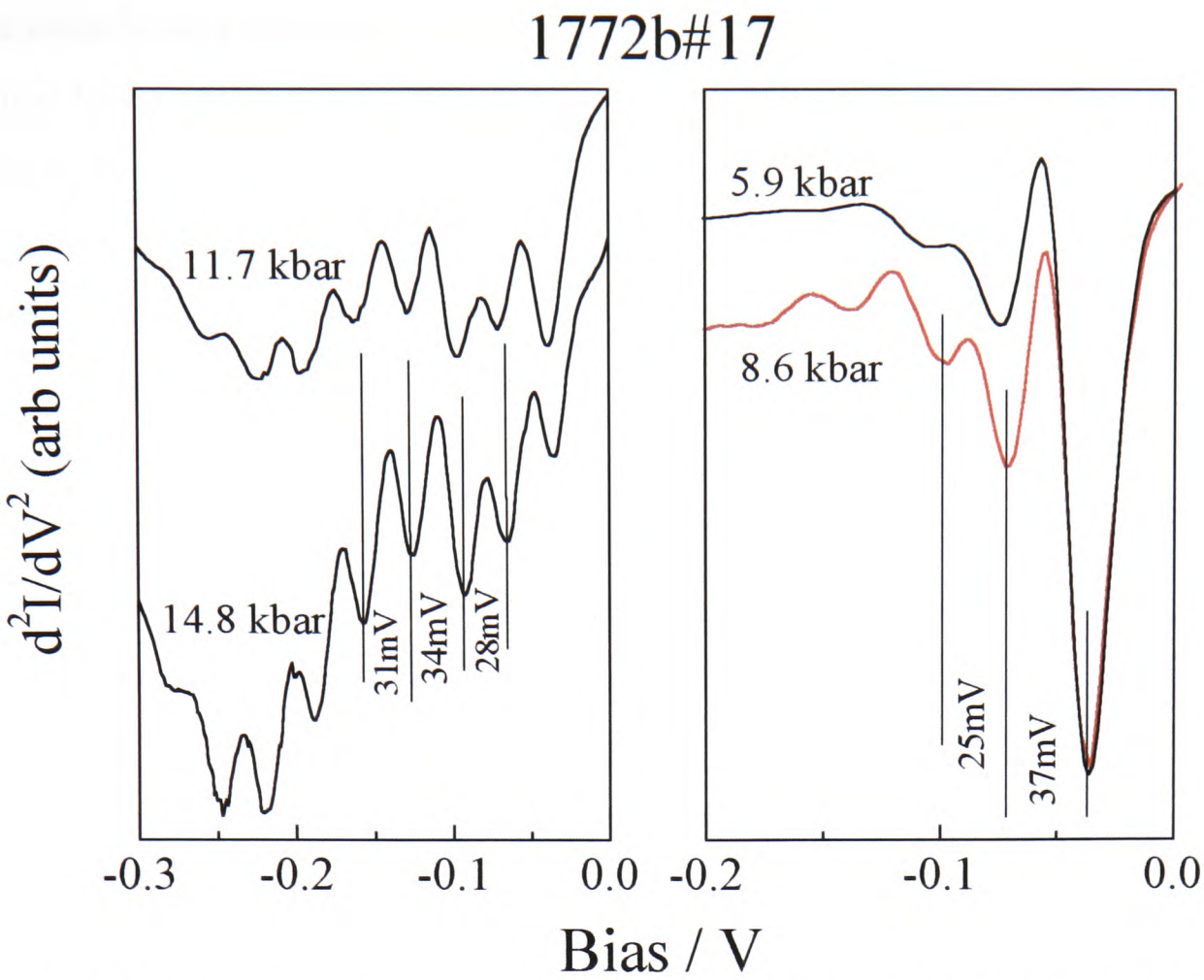


Figure 4.13. High pressure measurements performed on samples with a 'GaAs-like' interface showing reverse bias phonon cascades at various pressures.

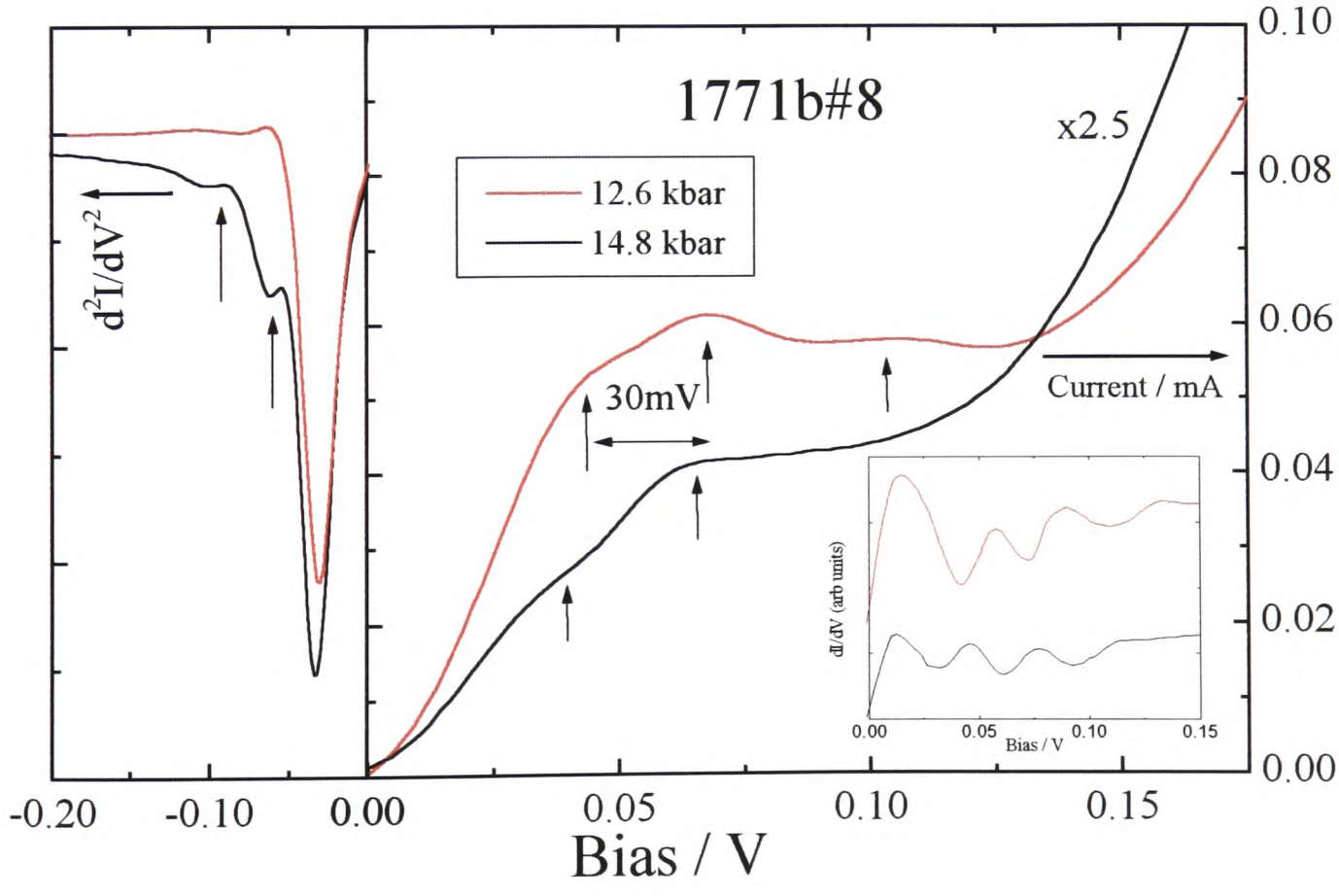


Figure 4.14. High pressure measurements repeated in this work but now at a much lower temperatures reveal weak forward and reverse bias features in the IV in 'InSb-like' interface samples near the NDR region. The inset is a plot of the first derivative of the IV traces showing the forward features more clearly.

The underlying reason why pressure allows such features to be observed more readily than at lower pressures is that it reduces the electron and hole concentrations on either side of the interface. At lower pressures, there is the possibility that phonon assisted interactions will take place between multiple regions in the electron and hole Fermi gases. The criterion for conduction would of course be that the electron and hole region interacting are separated by a phonon in energy, but there could be many pairs of regions which satisfy such a condition. This would make such phonon assisted conduction features difficult to observe. At higher pressures, with smaller concentrations and therefore smaller values of $|E_0 - E_F|$ and $|HH_0 - H_F|$ there would not be a large Fermi gas of electrons or holes. Far fewer points in the electron gas would be a phonon in energy away from the hole gas than at low pressure. Phonon assisted conduction would then not 'wash' itself out as at low pressure, making the associated features easier to observe in the IV or first derivative.

The results here therefore provide evidence for multiple phonon processes in the InAs/GaSb SHET. Resonant conduction may after all be possible in the 'GaAs-like' interface samples when the 2DEG and 2DHG are many phonon energies apart through multiple phonon cascades, which have now been clearly observed. This would also immediately reconcile the experimental and theoretical results presented in Figure 4.11 by explaining why V_{120} follows V_v well. Hence the implication is that resonant conduction in the two sample types is not too dissimilar after all - the only difference really lies in the number of phonons assisting in tunnelling. In 'InSb-like' samples, this is less than three longitudinal optical phonons. In 'GaAs-like' interface samples the evidence here suggests that multiple phonons can indeed aid in tunnelling. These may be LO phonons, or the optical IFMs. The results here cannot differentiate between the two types, as both are of energy ≈ 30 meV. This evidence for inelastic processes is augmented later when the experimental and theoretical results of the SHET in a magnetic field are presented (chapters 5 and 6).

4.6 Band Gaps, Wavefunctions and In-Plane Dispersion Curves

The results of the calculations for a heterostructure with an 'InSb-like' interface at 1 bar and zero bias are shown below. Figure 4.15 is a composite picture showing the final self-consistent band profile and the subband in-plane dispersions. The inclusion of coupling into the band structure calculation tends to make the electron and hole bands repel one another. As there are many electron and hole subbands in close proximity to one another, this ultimately leads to extremely non-parabolic bands and a very complex band structure results.

As mentioned earlier, Altarelli was the first to include a realistic calculation for $k_{||}$ into the **k.p** formalism to self-consistently calculate the band structure of an InAs/GaSb SL [35]. He used a three band model, the results of which did indeed show mixing of the conduction-band-like and valence-band-like subbands for $k_{||}$, resulting in an anticrossing with an energy gap of <5 meV. Vaughan [10] has recently improved upon Altarelli's original work by using an 8×8 **k.p** formalism, again predicting minigaps (at the point where the electron and hole dispersions cross) at finite $k_{||}$ of the same order. His work has been experimentally verified through recent magneto-optical experiments by Poulter *et al* [36, 37] who attributed strong absorption to direct transitions across the minigap.

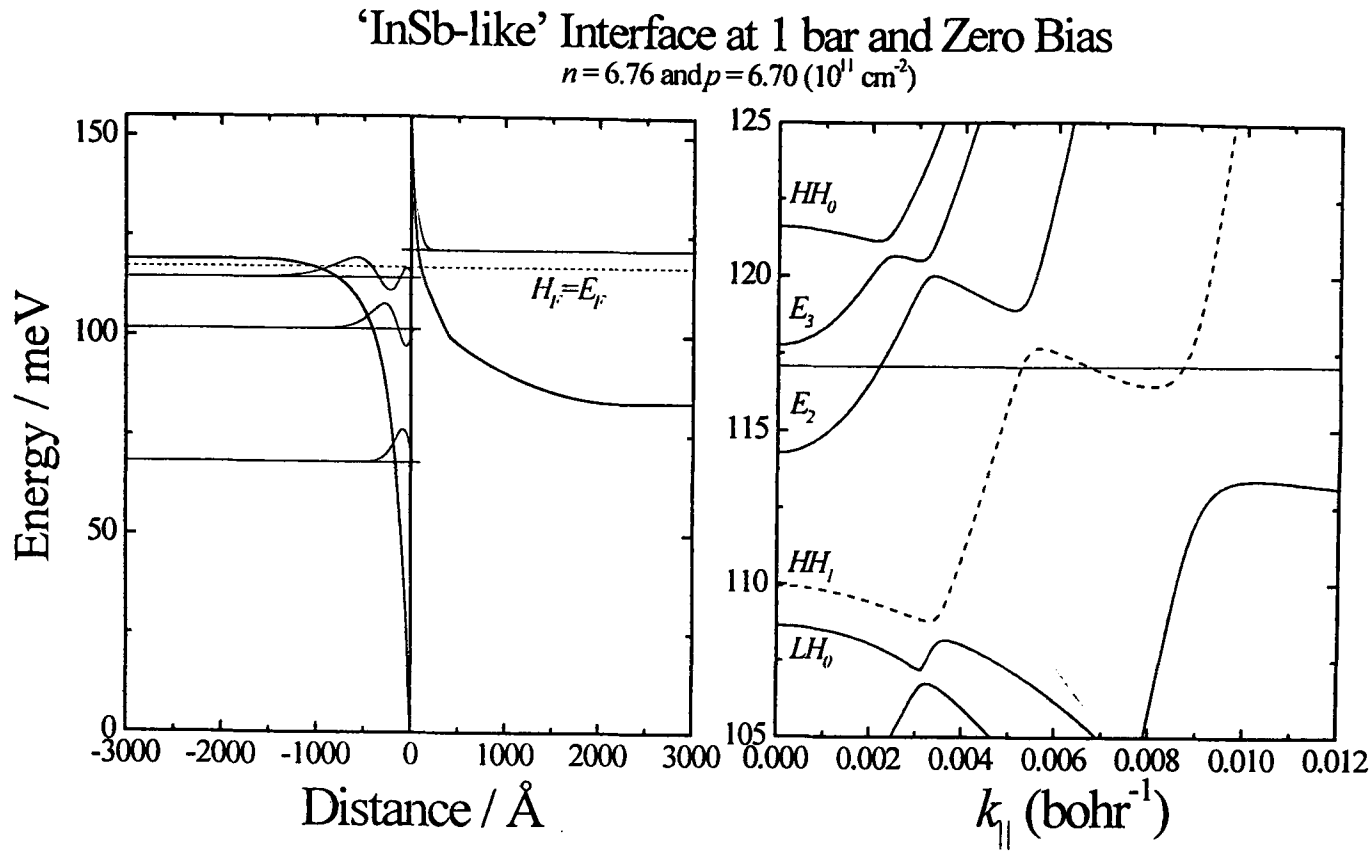


Figure 4.15. Results of the self-consistent **k.p** calculations carried out for an 'InSb-like' sample at 1 bar and zero bias.

The zero bias, zero pressure results here show that the largest minigap is just less than 5 meV (at approximately 0.01 bohr^{-1}), in good agreement with both Altarelli and Vaughan. Many other smaller minigaps are found at other values of $k_{||}$.

The states at the Γ-point are totally unmixed and are thus completely electron-like or completely hole-like (and calculated by the method described in 4.2.1.2). The dispersion curves in Figure 4.15 are labelled according to these unmixed Γ states. This is done only for convenience to aid in the reading of the ensuing discussion. As one moves away from $k_{||} = 0$, the states are no longer purely electron-like or purely heavy/light-hole like but rather a linear combination of the chosen set of basis states, with the proportion of each contributing determined of course through the **k.p** Hamiltonian. Consider for example the dashed curve labelled by the second confined (Γ) heavy hole state HH_1. For very small $k_{||}$, the dispersion falls almost parabolically indicative of it being nearly pure heavy hole-like. However, for larger $k_{||}$, the coupling with nearby states increases so much so that by about 0.004 bohr^{-1}, the state can neither be categorised as being made up of predominantly Γ hole-like or predominantly Γ electron-like states. At such anticrossing points, the mixing between the various electron and hole states (which in the above example is mostly between

the Γ point HH_1 and E_1 states) is greatest. Beyond this point, the curve begins to slope upwards thus describing a predominantly electron-like state.

The proportion of the basis states at each $k_{||}$ point along this curve is actually shown in Figure 4.16 while Figure 4.17 plots the calculated square modulus of the wavefunction $|\Psi|$ at selected values of the in-plane wavevector. The first plot (4.16*a*), shows the uncoupled Γ-point confined 2nd heavy hole confined state (calculated by the method described earlier in 4.2.1.2). Due to the large separation between the valence bands of GaSb and InAs, it decays extremely quickly for $z < 0$ and the probability of finding the particle in the InAs side of the interface is for all intents and purposes zero. With increasing $k_{||}$, electron-heavy hole coupling increases and the contribution of the HH_1 basis to the state falls. Simultaneously, the LH_0 and E_1 character of the state increase (Figure 4.16). By ~0.0045 bohr^{-1} the state has lost its HH_1 character and is predominantly E_1-like. At a $k_{||}$ of 0.0033 bohr^{-1}, which is roughly the point at which the zeroth electron subband would intersect the first heavy hole subband in an uncoupled parabolic model, and which corresponds to the first anticrossing point in Figure 4.15, the LH_0 mixing component is at a maximum. However, the state is also strongly of E_1 character and accordingly its calculated value of $|\Psi|$ has a large probability on either side of the interface (Figure 4.17*d* and *e*). At higher $k_{||}$ values still, the dispersion moves upwards and the corresponding state now mostly exists in the InAs side of the interface. Figure 4.16 shows that the state now is predominantly of E_1 character (>95%). Thus on crossing an anticrossing in $k_{||}$ space, the state has shifted from being

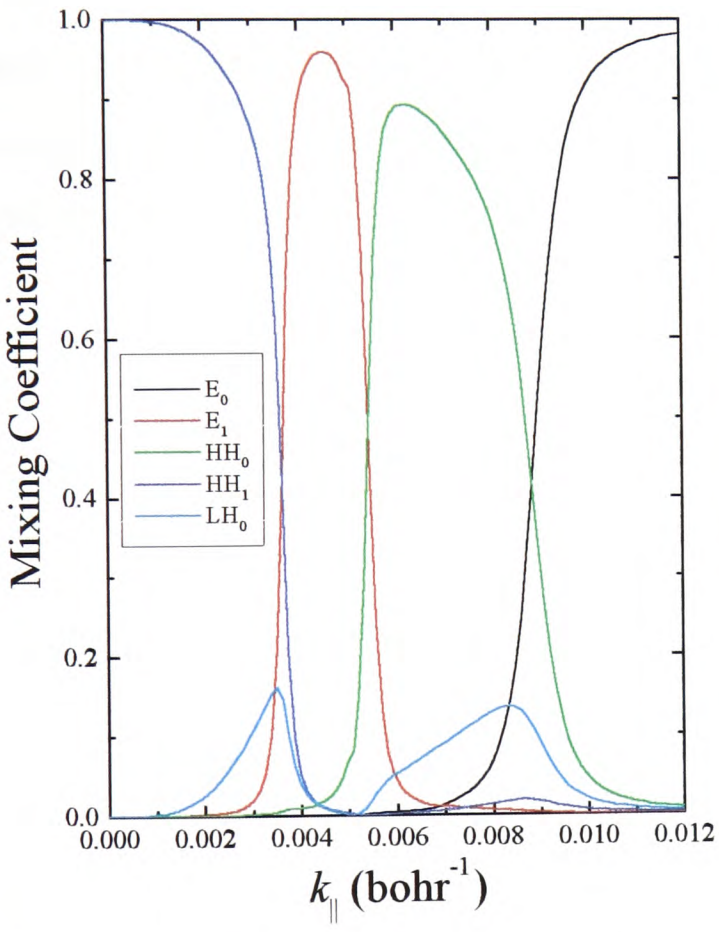


Figure 4.16 The major electron, heavy hole and light hole proportions of the state described by the dashed dispersion in Figure 4.15.

predominantly composed of Γ hole-like (i.e. existing mostly in the GaSb side of the interface) to predominantly composed of Γ electron-like (and has a large probability of existing in the InAs side of the interface). The next anticrossing point occurs at just under 0.006 bohr^{-1}. Figure 4.16 shows that on increasing through this point, the state returns to being more hole-like (HH_0) at the expense of its E_1 electron character. Examples of $|\Psi|$ at these points are shown in Figure 4.17*g*, and *h*. Finally, on crossing $k_{||}$ of about 0.008 bohr^{-1}, the state again reverts from being more hole-like to being electron-like (Figure 4.17*i*, *j*). The HH_0 character of the state falls as its LH_0 and E_0 character rises (Figure 4.16), but eventually by about 0.01 bohr^{-1} and above, the state is by far E_0 type (98%). Now of course, the $|\Psi|$ resembles the 1st confined electron Γ-point wavefunction (Figure 4.17*j*). Previously (at ~0.004 – 0.006 bohr^{-1}) the greatest electron mixing component was from the 2nd confined subband electron and the state near the first anticrossing point accordingly resembled the probability density due to the 2nd Γ-point electron wavefunction (Figure 4.17*e*).

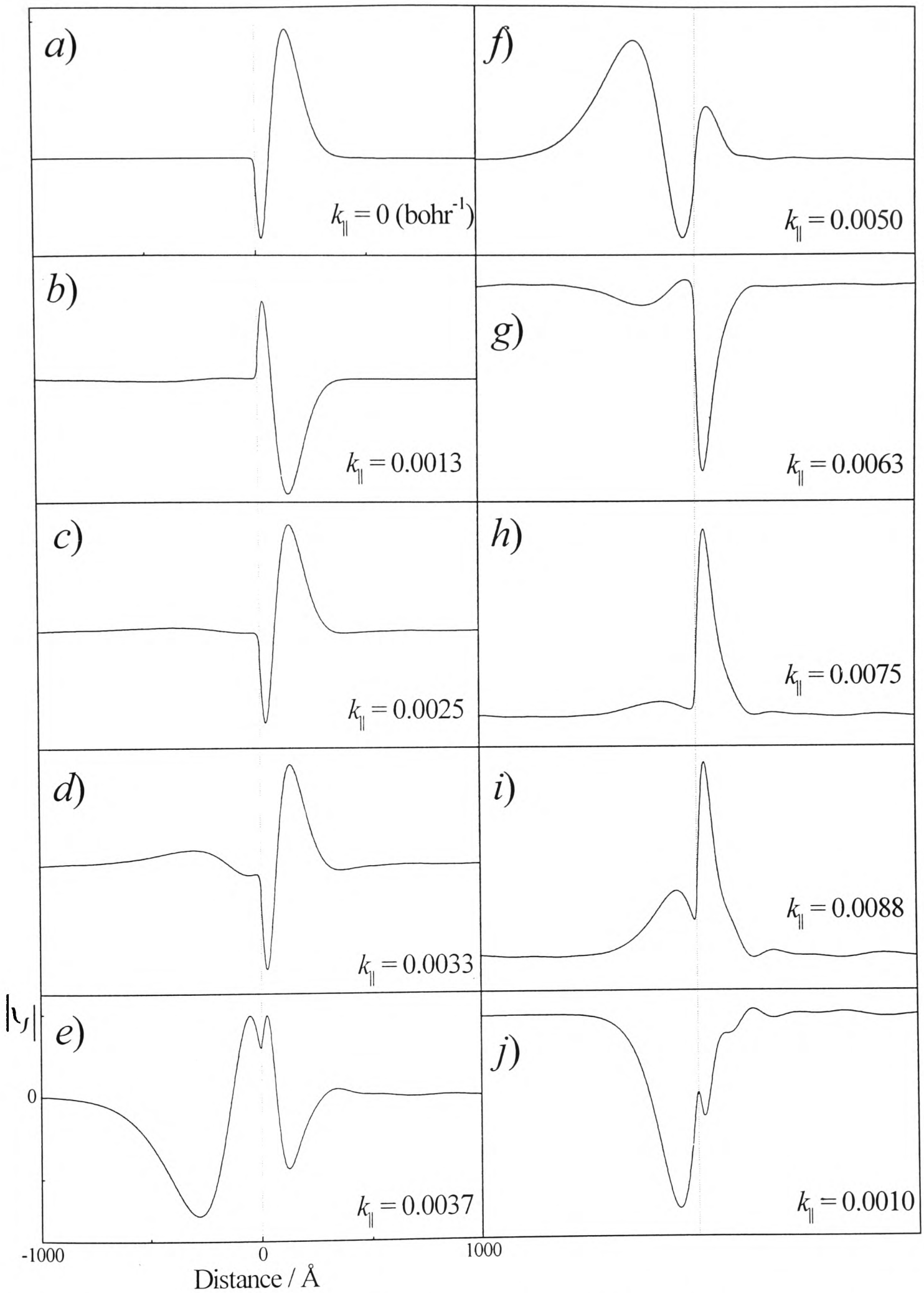


Figure 4.17. Displaying the modulus of the wavefunctions at various $k_{\|}$ points along the highlighted dispersion curve of Figure 4.15. It is initially purely heavy hole like (2nd confined state) at the Γ-point at zero bias and 1 bar. The interface is at $z = 0$ for each plot (InAs exists on the RHS and GaSb on the LHS) and is indicated by the dashed lines.

4.7 Summary

This chapter has provided the first detailed **k.p** algorithm to calculate the SHET band profile, confined (and continuum) wavefunctions and band structure. It is found that an earlier decoupled model is in fact a good approximation to the more realistic **k.p** case, thereby supporting its earlier conclusions.

The results confirm that the 'InSb-like' interface behaves far more predictably than 'GaAs-like' samples with a resonant conduction mechanism consistent with varying electron-hole overlap (described in section 1.5.1). By comparing the results of the **k.p** calculations and the measured position of the peak and valley at 4K, instead of earlier 77K measurements, it is found that at 4K the peak voltage for 'InSb' interfaces occurs when E_0 and HH_0 are about a phonon in energy apart. Furthermore, features in forward bias separated by a constant 30 meV at the NDR region at high pressure have been observed lending strong experimental support to up to three phonons being involved in the resonant tunnelling process.

The 'GaAs-like' interface does not behave so predictably under forward bias. Instead, a clear resonance is visible well after Δ has fallen to zero and the NDR occurs at a much higher bias than expected. The pressure dependence of the peak and valley voltages is consistent with the resonance occurring when $E_0 - HH_0$ is between 120 and 140 meV. Again, large phonon cascades have been observed (also at high pressure) in 2nd derivative measurements in such sample types thereby offering a means to at least partially reconcile experiment and theory.

The observation of phonons in both samples is a fact that will be drawn upon the analysis of the SHET behaviour in subsequent chapters.

4.8 References

[1] M Lakrimi, S Khym, R J Nicholas, D M Symons, F M Peeters, N J Mason, P J Walker in the Physical Review Letters 79 p3034 (1997) and M Lakrimi, S Khym, D M Symons, R J Nicholas, F M Peeters, N J Mason, P J Walker; Physica E 2 p363 (1998).

[2] M J Yang, C H Yang, B R Bennett, and B V Shanabrook. Physical Review Letters 78 p4613 (1997).

[3] D M Symons, M Lakrimi, R J Wa ɔurton, R J Nicholas, N J Mason, P J Walker, M I Eremets and G Hill, Physical Review B 49 p16614 (1994).

[4] M S Daly, W Lubczynski, R J Warburton, D M Symons, M Lakrimi, K S H Dalton, M Van der Burgt, R J Nicholas, N J Mason and P J Walker, Journal of the Physics and Chemistry of Solids 56 p453 (1995).

[5] U M Khan-Cheema, D.Phil. Thesis; Vertical Transport Through an InAs/GaSb Heterojunction at High Pressures and Magnetic Fields, Clarendon Laboratory, Oxford University (1996).

[6] E T Yu, D A Collins, D Z-Y Ting, D H Chow, T C Mcgill. Applied Physics Letters 57 p2675 (1990).

[7] D Z-Y Ting, E T Yu and T C McGill. Applied Physics Letters 58 p292 (1991).

[8] Similar results have been obtained by Y X Liu *et al* who used a **k.p** theory including the effect of in-plane field to show that the primary interband transport mechanism in InAs/GaSb/AlSb systems arises from the coupling between InAs conduction band states and GaSb light hole states. Their theoretical analysis did show that the hole mixing would lead to coupling between InAs conduction band states and GaSb heavy hole states, resulting in noticeable shoulder peaks in current-voltage characteristics. Y.X Liu, R R Marquardt, D Z-Y Ting and T C McGill. Physical Review B 55 p7073 (1997).

[9] M Altarelli. Physical Review B 28 p842 (1983).

[10] T A Vaughan, D.Phil. Thesis; The Magneto-optics of InAs/GaSb Heterostructures, Clarendon Laboratory, Oxford University (1996).

[11] T Ando, A B Fowler & F Stern. Review of Modern Physics 54 p437 (1982).

[12] D A Broido and L J Sham. Physical Review B 31 p2056 (1985); Physical Review B 34 p3917 (1986).

[13] G Rau, D.Phil. Thesis, Theory of the Electronic and Optical Properties of GaAs/AlGaAs Quantum Wells Under Uniaxial Stress, Clarendon Laboratory, Oxford University (1998).

[14] U Ekenberg and M Altarelli. Physical Review B 32 p3712 (1985).

[15] E T R Chidley, S K Haywood, A B Henriques, N J Mason, R J Nicholas and P J Walker. Semiconductor Science and Technology 6 p45 (1991).

[16] R A Noack & W B Holzapfel. Solid State Communications 28 p177 (1978).

[17] R Zallen & W Paul. Physical Review 155 p703 (1967).

[18] J F Tsay, S S Mitra and B Bendow. Physical Review B 10 p1476 (1974).

[19] M L Shubnikov, D V Masovets and R V Parfenev. Soviet Physics Semiconductors 9 p989 (1976).

[20] A review of the material properties of GaSb is given by P S Dutta, H L Bhat in the Journal of Applied Physics 81 p5821 (1997).

[21] G Martinez, in Optical Properties of Solids, edited by M. Balkanski, Handbook on Semiconductors (North-Holland, Amsterdam) 2 p194 (1980).

[22] U M Khan-Cheema, N J Mason, P J Walker, P C Klipstein, G Hill. Journal of Physics and Chemistry of Solids 56 p463 (1995).

[23] G A Sai-Halasz, L L Chang, J M Welter, C A Change and L Esaki. Solid State Communications 27 p935 (1978).

[24] J Beerens, G Grégoris, J C Portal, E E Mendez, L L Chang and L Esaki. Physical Review B 36 p4742 (1987).

[25] G J Gualtieri, G P Shcwartz, R G Nuzzo, R J Malik and J F Walker. Journal of Applied Physics 61 p5337 (1987).

[26] C G Van de Walle and R M Martin. Journal of Vacuum Science and Technology B 4 p1055 (1986).

[27] Y Foulon and C Priester. Physical Review B 45 p6259 (1992).

[28] R G Dandrea, C B Duke and A Zunger. Journal of Vacuum Science and Technology B 10 p1744 (1992).

[29] Khan-Cheema deduced in [5] a value of about 20Ω for the series parasitic resistance by fitting the calculated value of V_{30} with the observed valley voltage V_v.

[30] R J Springett, D. Phil. Thesis, *Raman Scattering Studies of III-V Semiconductor Superlattices*, Clarendon Laboratory, Oxford University (1992).

[31] S G Lyapin, P C Klipstein, N J Mason and P J Walker. Physical Review Letters 74 p3285 (1995).

[32] A Fasolino, E Molinari and J C Maan. Superlattices and Microstructures 3 117 (1987). The method employed models the vibrations of the superlattice in terms of planar force constants, which are

themselves determined *ab initio* for one constituent (e.g. GaAs bulk) and extended to the other constituent (e.g. AlAs) by introduction of the 'mass and charge approximation'. As the method takes into account long-range forces between individual planes, it is a significant improvement on the linear chain model.

[33] S Lyapin – Private communication.

[34] S G Lyapin, P C Klipstein, N J Mason and P J Walker. Superlattices and Microstructures 15 p499 (1994).

[35] M Altarelli. Physical Review B 28, p842 (1983).

[36] A J L Poulter, M Lakrimi, D Dur, R J Nicholas, N J Mason, P J Walker. Physica E 2 p345 (1998).

[37] A J L Poulter, D.Phil. Thesis; The Magneto-optics of InAs/GaSb Heterostructures, Clarendon Laboratory, Oxford University (1998).

5. Magnetic Field Perpendicular to the SHET Interface

5.1 Introduction 96

5.2 'InSb - like' Interface Experimental Results 97

5.2.1 1 bar Results.....97

5.2.2 Results at Higher Pressures 99

5.3 Semiclassical Dynamics of Electrons in Magnetic Fields 103

5.4 Quantum Mechanical Approach to Electrons in a Magnetic Field 105

5.5 The SHET under a Perpendicular Field 106

5.5.1 Method of Calculation 108

5.6 Calculated Results and Discussion 116

5.7 General Behaviour..... 116

5.7.1 Analysis at High Pressure..... 118

5.7.2 Analysis at 1 bar 124

5.8'GaAs - like' Interface..... 129

5.9 Summary..... 133

5.10 References 135

5.1 Introduction

Attention has so far been devoted to the effect of pressure on the InAs/GaSb SHET. Using high pressure cell techniques, the interface dependent resonant conduction mechanism has been investigated showing that 'InSb-like' samples behave far more predictably than 'GaAs-like' samples. With evidence for multiple phonon processes (see 4.5.2 and section 5.8) to explain this discrepancy mounting, the SHET IV characteristics need to be further explored before any conclusions can be reached. This is done using magnetic fields and the aim of the rest of this thesis is to present results of experiments and calculations for just this purpose.

The use of magnetic fields is not new in semiconductor physics. Though difficult to produce, they provide a richer insight into the underlying physics than is possible by studying electrons in electric fields alone. Well established techniques based on magneto-optics and magnetotransport provide us with much of what we know about the symmetry of the electronic states in the Brillouin zone, carrier masses at band edges; effects like the quantum Hall effect provide details on the many-body interactions in low dimensional systems, etc. With the added advantages of being able to orientate the field at an arbitrary angle relative to the sample and of setting the field to any value, magnetic fields offer a very wide range of flexibility.

Here, I focus on one special orientation of the magnetic field, i.e. perpendicular to the interface of the SHET. Under this configuration, the carriers' in-plane energy will become quantised into Landau energies. This has been found to lead to additional features in vertical transport IV characteristics of antimonide heterostructures, as well as in other material systems [1]. Mendez *et al* for example observed multiple NDR features induced by magnetic fields applied perpendicular to the interface of GaSb/AlSb/InAs/AlSb/GaSb heterostructures [2, 3]. They explained their results in terms of resonant interband tunnelling of GaSb holes through Landau levels in the conduction band of the InAs quantum well. Here in this work, I too find new features in the IV as a result of applying magnetic fields, though I do not attribute the observed features as being due to tunnelling between occupied Landau levels.

The chapter commences with section 5.2 detailing the experimental results obtained with magnetic field perpendicular to the interface of the 'InSb-like' samples at 1 bar, followed by the results obtained at higher pressure (5.2.2). Prior to the quantitative analysis of the measured data, section 5.3 and 5.4 briefly introduce the reader to the behaviour of electrons in a magnetic field, the conclusions of which are utilised in deriving the self-consistent algorithm for the SHET in a magnetic field (section 5.5). The results of these calculations are initially used to analyse the higher pressure results 5.7.1 before being applied to the 1 bar results 5.7.2. With the 'InSb-like' samples treated, section 5.8 considers similar experiments and calculations for 'GaAs-like' samples. The chapter concludes with a collection of the most important results obtained in this particular study.

5.2 'InSb - like' Interface Experimental Results

Section 5.2 summarises the observed data from the 1771 'InSb-like' interface series of samples under magnetic field applied perpendicular to the interface at 1 bar. Experiments were carried out at 4K using the DC superconducting magnet and the pulsed field set-up described in chapter 2. Its vertical transport characteristics are indeed found to alter with field, with sharp features occurring beyond the main NDR. Section 5.2.2 presents experimental results, again with field perpendicular to the interface, but this time under very high pressure. Then, no sharp features are found, with the obvious exception of the main NDR. However, intriguing field induced weak features are shown through 2nd derivative measurements.

5.2.1 1 bar Results

Figure 5.1 shows how the IV trace for an 'InSb-like' SHET evolves with $B_{\perp}$ up to 15T. From 5T onwards, a second region of (mini) NDR appears after the main resonance, moving up in bias as the field is increased. This NDR has been observed before [4], but now detailed measurements of the 1st and 2nd derivatives of the IV trace reveal it not to be a single feature but in fact to consist of two distinct features (these are labelled A and B in Figure 5.1). Figure 5.2, showing the measured first derivative of the IV trace, clearly shows their movement with increasing magnetic field. At low fields (<5T), they are very close to the valley and very close together and hence

difficult to observe. However, at higher fields, as they move up in bias while the valley moves down, they become increasingly clear. By 15T, the main NDR peak and valley voltage are approximately 0.15V and 0.2V respectively while A and B are at about 0.5V and 0.6V.

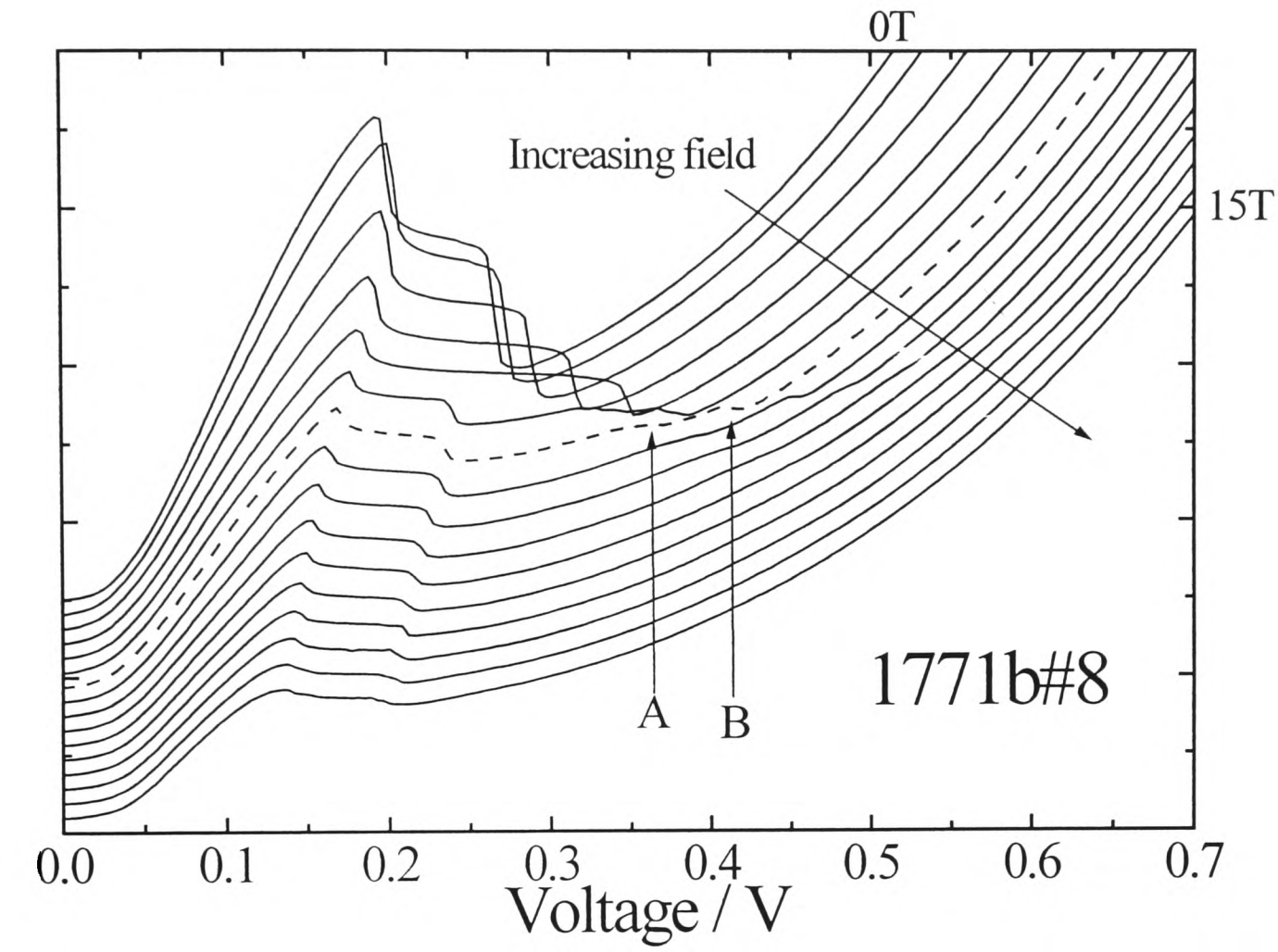


Figure 5.1. IV characteristics for a sample with an 'InSb-like' interface under magnetic field perpendicular to the interface. The IV trace at 6T has been highlighted here to illustrate two new features. Feature B was observed by Khan-Cheema [4], but a weaker resonance, feature A, wasn't. As it is weaker than B, it is very difficult to see its evolution with increasing B until ones looks at the conductance results below. The traces are offset along the *y*-axis for clarity.

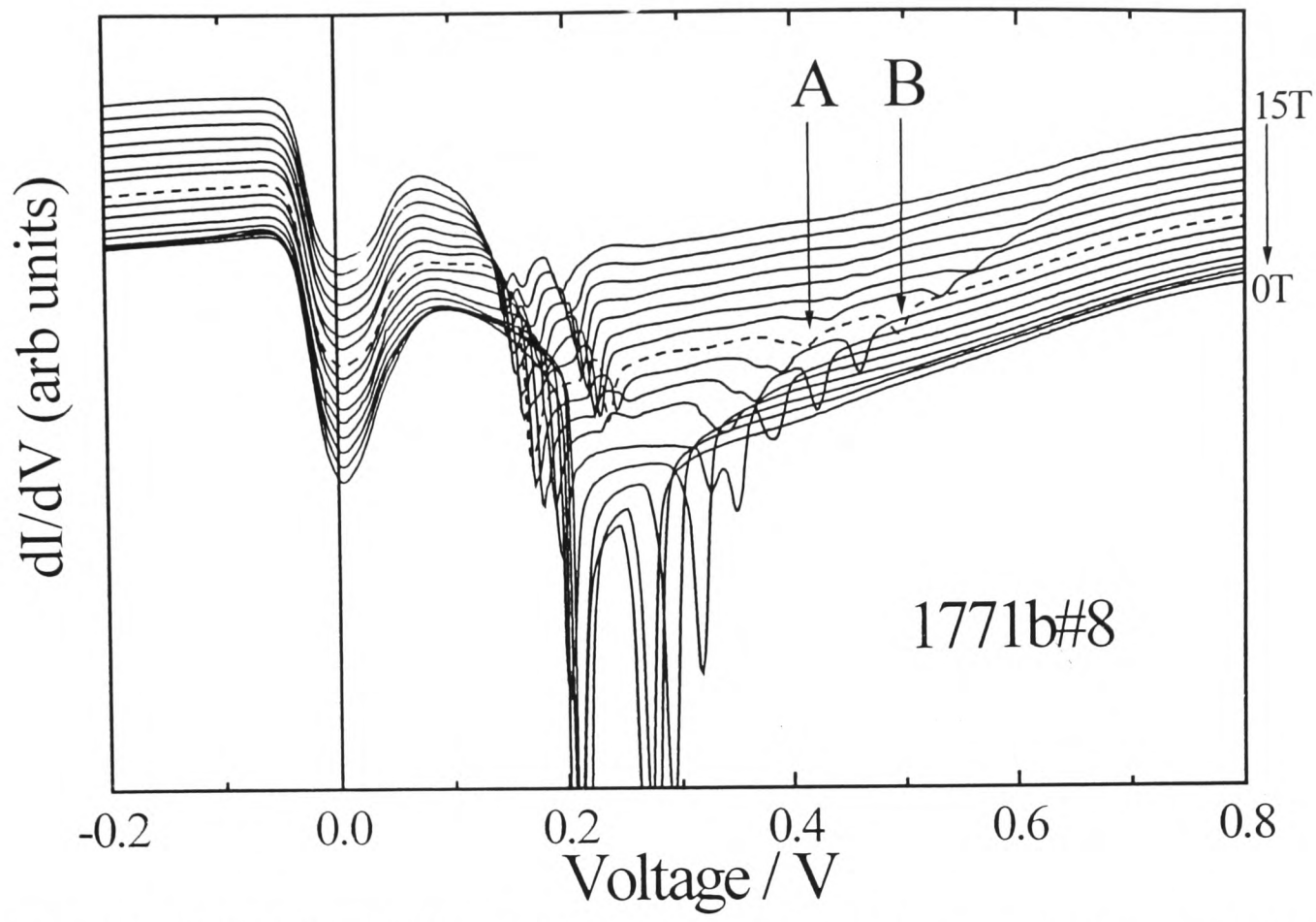


Figure 5.2. The conductance trace highlighted here corresponds to an applied field of 8T. Feature B is seen to move up in bias and the movement of feature A can now be seen throughout the entire field range.

5.2.2 Results at Higher Pressures

A series of combined pressure-(perpendicular) magnetic field experiments were subsequently carried out. For pressures below about 4 kbar, the results were very similar to those obtained at 1 bar. NDR was found to fall with field and at fields above 5T, a second feature beyond the main resonance appeared, moving up in bias. At pressures beyond this point, however, the secondary features disappeared and the IV trace was found to consist only of a complicated NDR region. Figure 5.3 below for example, shows the results at 4.59 kbar and shows the clear lack of weak 'secondary NDR' features in the IV. However, careful conductance measurements show beyond the main NDR, the emergence of very weak magnetic field dependent oscillatory features (Figure 5.4). At higher pressure, these features are still observable. The results at 9.73 and 14.8 kbar show these features more clearly in 2nd derivative measurements (labelled A to E in Figure 5.6). The high degree of magnetic field sensitivity of all these features indicate that they are specifically induced by the perpendicular magnetic field.

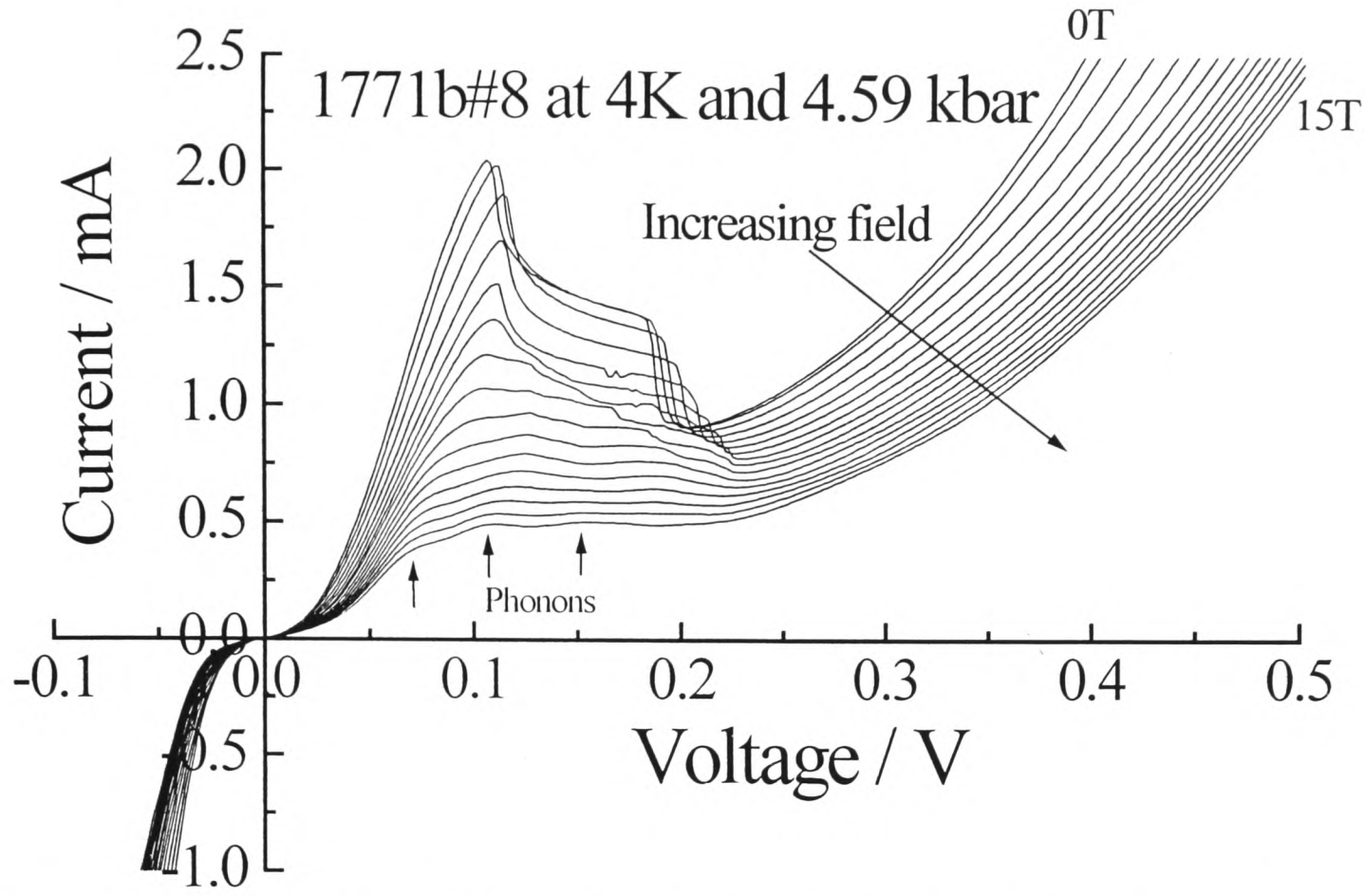


Figure 5.3. IV response for an 'InSb-like' interface sample under 4.59 kbar at 4K with a magnetic field between 0 and 15T applied in 1T steps perpendicularly to its interface. The NDR itself has an increasingly complicated structure at this intermediate pressure as the magnetic field is applied. Circuit oscillations make this region of the trace difficult to analyse though the peak voltage and peak current are clearly seen to fall with field. Phonon features are seen clearly at the highest fields.

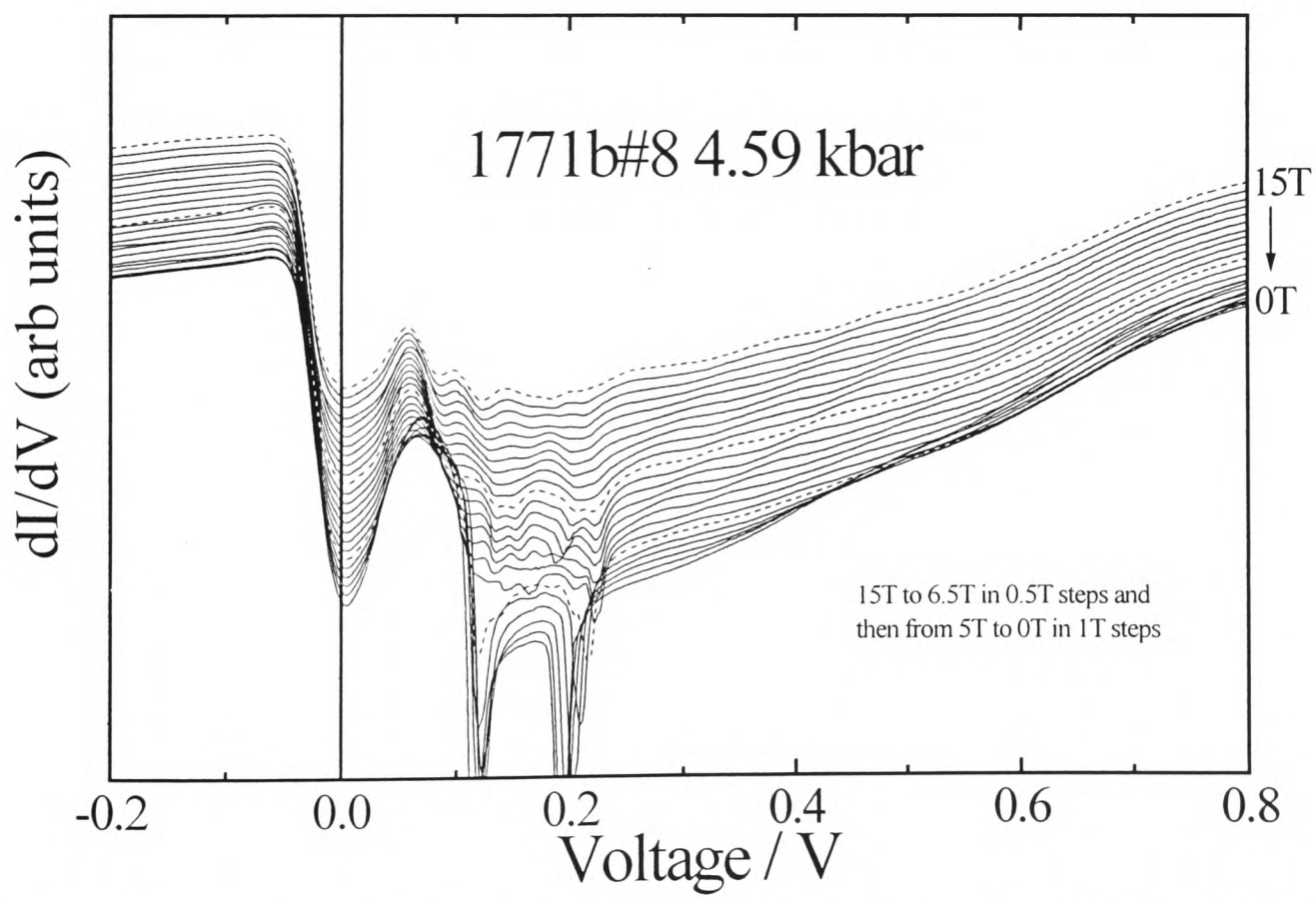


Figure 5.4. Conductance results for an 'InSb-like' interface sample under 4.59 kbar at 4K with a magnetic field between 0 and 15T applied in perpendicular to its interface. Dashed lines represent data collected at 15T, 10T and 5T.

Turning attention away from the high bias region (i.e. beyond the NDR peak), I now focus on the IV data at lower bias. At higher pressures, features near the NDR region that were earlier proposed (4.5.2) to be phonons are observed[8]. These can be seen best in Figure 5.5 and Figure 5.6 and clearly show that applying field does not alter their bias position (they are even visible in the IV traces at 4.59 kbar, Figure 5.3, between 8-15T). The magnetic field insensitivity of the these peaks is therefore further evidence that they are indeed due to phonons. These experimental results therefore further support the proposal that multiple phonon processes are present in both sample types.

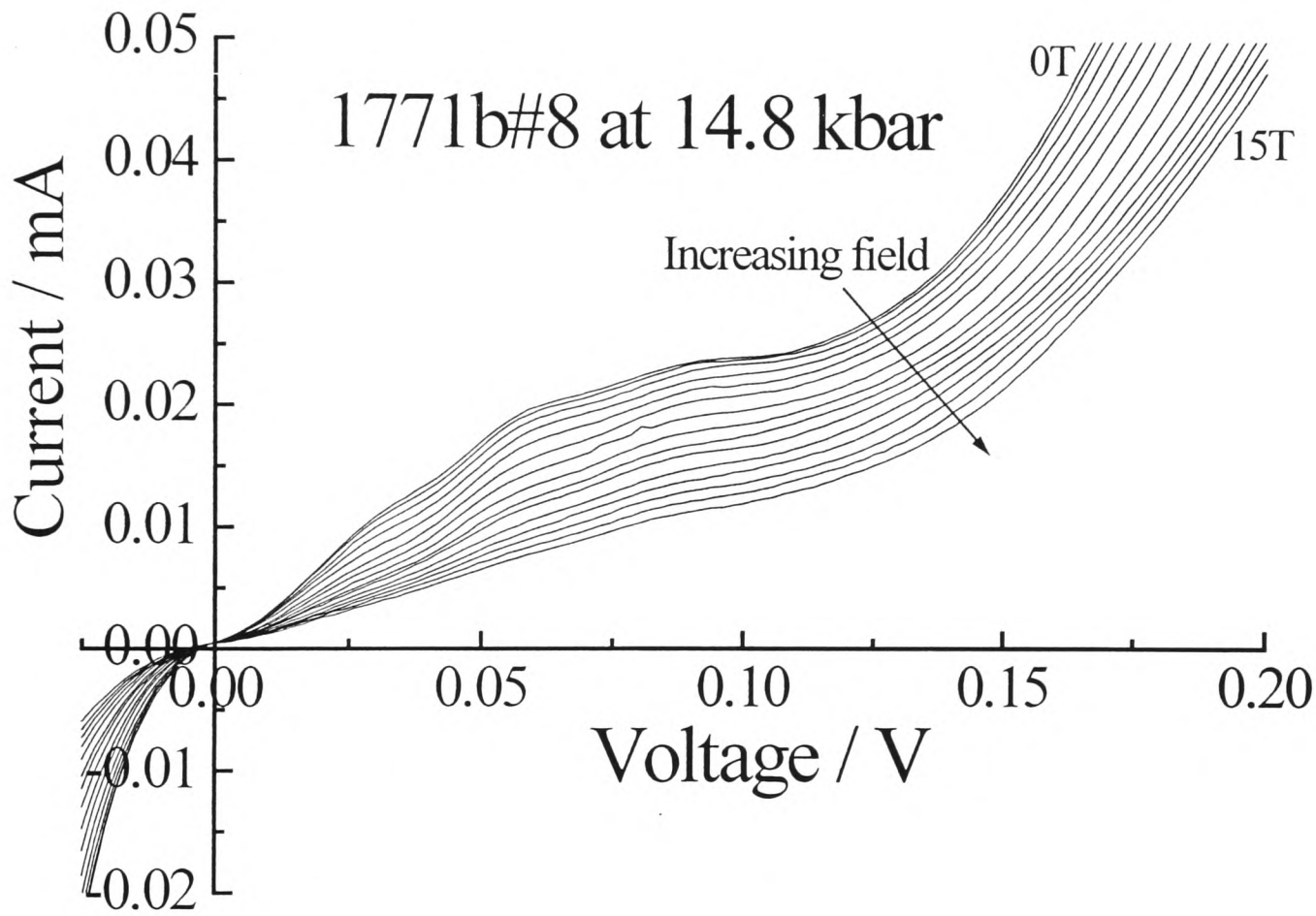


Figure 5.5. 1771b#8 at a pressure of 14.8 kbar and with a magnetic field between 0 and 15T applied in 1T steps perpendicular to the interface.

[8] The application of pressure reduces the band overlap and therefore the concentration of the electrons and holes in the system falls. It therefore has the effect of suppressing the IV characteristic. Weaker intrinsic phonon features are then more easily visible because the Fermi sea of electrons and holes is smaller and there is less background current. Here, magnetic field further reduces n and p (at zero bias,

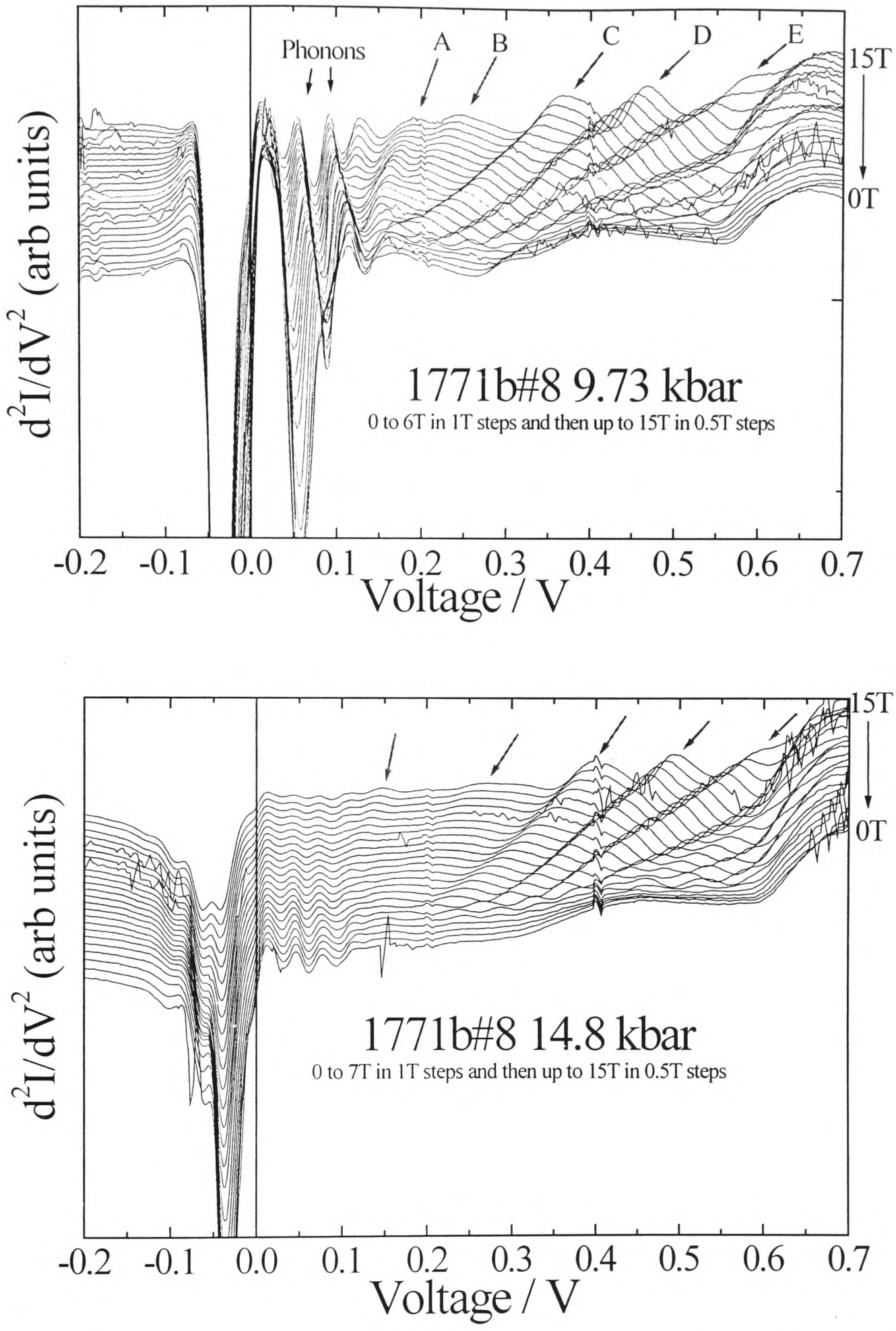


Figure 5.6. 2nd derivative measurements performed at high pressure and with field applied. The high bias features appear very clearly. The arrows indicate the positions of the first two weak and strong features - the gradient of the arrows roughly indicating the direction in which the peaks move. The trace highlighted in red in the 9.73 kbar plot indicates peaks exist beyond the five first features (indicated by the arrows). These are thought, however, to be of the same origin (section 5.7.1).

---

see section 5.7) and may be the reason why the phonon features become even more visible in the IV with field (see Figure 5.3).

With the vast amount of experimental data collected, there now remains the task of explaining the results under a self-consistent framework. This is a formidable problem as the effect of magnetic field perpendicular to the interface leads to secondary NDR features with fine structure observed in the first derivative (section 5.2.1) as well as features at high pressure in the 2nd derivative (section 5.2.2). Any model would have to offer convincing arguments to explain the origin of these multiple features. In this respect, modelling the effect of field perpendicular to the interface is far more challenging than modelling the SHET IV behaviour without field (chapter 4) or even magnetic field parallel to the interface (chapter 6) as then the aim has been (and will be) to model the movement of the NDR region alone. What is clear however, is that the $B_\perp$ induced features must be very closely related to the additional in-plane (Landau) quantisation of the electrons.

This first detailed attempt at modelling the InAs/GaSb heterostructure with magnetic field perpendicular to the interface assumes a decoupled system treating electrons and heavy holes exactly at the Γ-point [5]. The assumption of neglecting the effect of light holes and the effect of band mixing relies on the results of chapter 4 which show that the decoupled model is a good approximation to a **k.p** model. A more comprehensive treatment in the future should of course treat the effect of magnetic field perpendicular to the interface through an appropriate **k.p** Hamiltonian [6, 11]; this has been avoided as it would be obviously premature to use such a sophisticated approach before trying the simpler decoupled model.

5.3 Semiclassical Dynamics of Electrons in Magnetic Fields

The equation of motion for electrons in a magnetic field is neatly described by the following equation [7]:

$$\frac{d\boldsymbol{k}}{dt} = -\frac{e}{\hbar}\boldsymbol{v} \times \boldsymbol{B} \tag{5.1}$$

The velocity itself is normal to the constant energy surface,

$$\boldsymbol{v}_k = \frac{1}{\hbar}\nabla_k E(\boldsymbol{k}) \tag{5.2}$$

Equation (5.1) shows that the change in the $\boldsymbol{k}$-vector is normal to $\boldsymbol{B}$ and also normal to the velocity. The second equation shows that the magnetic field alters $\boldsymbol{k}$ along the intersection of the constant energy surface and the plane perpendicular to the magnetic field. This is exemplified using an arbitrary constant energy surface in Figure 5.7. In reality, these can be quite simple as for the spherical Fermi surface of the conduction band of direct semiconductors or complex as for the distorted cube constant energy surfaces of valence bands. Writing equation (5.1) in terms of the electron position $\boldsymbol{r}$, we have:

$$\frac{d\boldsymbol{k}}{dt} = -\frac{e}{\hbar}\dot{\boldsymbol{r}} \times \boldsymbol{B} \tag{5.3}$$

where $\boldsymbol{v} = \dot{\boldsymbol{r}}$ and has a component $\dot{\boldsymbol{r}}_\perp$ perpendicular to $\boldsymbol{B}$ and a component $\boldsymbol{r}_\parallel$ parallel to $\boldsymbol{B}$. Equation (5.3) shows that $\dot{\boldsymbol{k}}$ has a component $\dot{\boldsymbol{k}}_\perp$ perpendicular to $\boldsymbol{B}$ while $\dot{\boldsymbol{k}}_\parallel$ is zero and can be solved for $\boldsymbol{r}_\perp$ giving:

$$\boldsymbol{r}_\perp(t) = \frac{\hbar}{eB}\boldsymbol{k}_\perp(t) + \pi/2 \text{ rotation} \tag{5.4}$$

Thus the electrons will move on the constant energy surface in a plane perpendicular to the field. If the energy surface is spherical, the electron will execute a circular (cyclotron) orbit and if its velocity parallel to the field is non-zero the electron will move in a helical trajectory. (The rotation is included since the cross product of a unit vector with a perpendicular vector simply gives the second vector rotated by 90°). This rather simple semiclassical argument therefore shows that when a magnetic field is applied to electrons (or holes), their motion will be unaffected along the field direction, and they will execute orbits in the direction perpendicular to the field. This is compared with the quantum mechanical approach below.

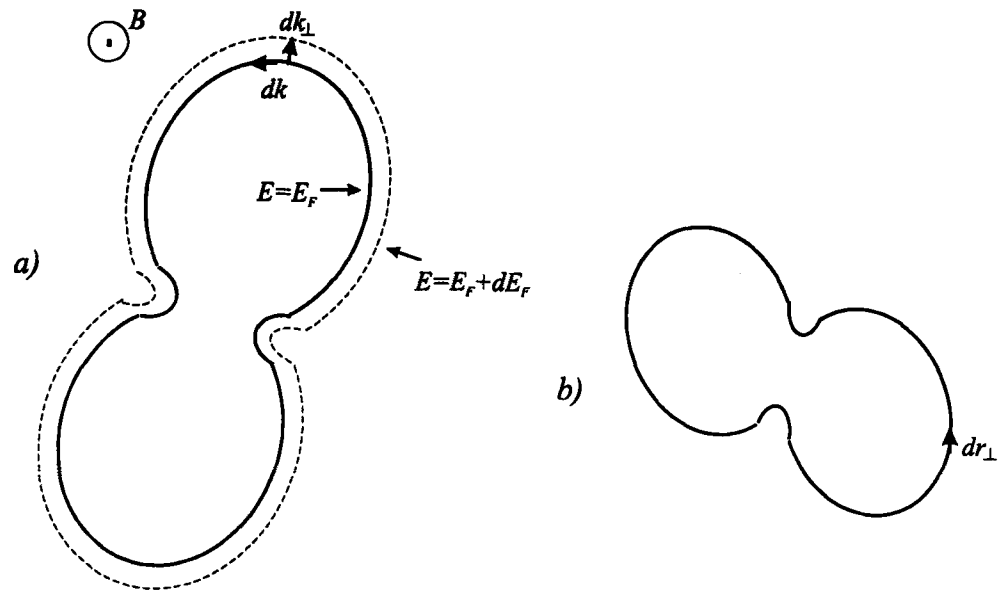


Figure 5.7. a) A cyclotron orbit in *k*-space is around the Fermi surface in a plane perpendicular to *B*. *b*), The projection into the plane perpendicular to the field of the real space orbit corresponding to the k-space orbit of *a*) has the same shape and rotation sense but is rotated by 90° about the field direction.

5.4 Quantum Mechanical Approach to Electrons in a Magnetic Field

Assuming an isotropic, parabolic energy band, the single particle time independent Schrödinger equation in the presence of a magnetic field can be written with the Hamiltonian momentum operator replaced by $\mathbf{p} \rightarrow \mathbf{p} - e\boldsymbol{A}$, where $\boldsymbol{A}$ is the vector potential associated with the magnetic field such that $\boldsymbol{B} = \nabla \times \boldsymbol{A}$ [7]. Thus,

$$\frac{1}{2m^*}\left(\frac{\hbar}{i}\nabla - e\boldsymbol{A}\right)^2 \Psi = E\Psi \tag{5.5}$$

Writing this in the gauge $\boldsymbol{A}$ = (0, Bx, 0) so the magnetic field $\boldsymbol{B}$ is applied along z results in a Hamiltonian that does not involve y or z explicitly. After separating the variables, the wavefunction can be written as:

$$\Psi(x,y,z) = \exp\{i(k_y y + k_z z)\}u(x) \tag{5.6}$$

This leads to motion in the x-y plane described by:

$$-\frac{\hbar^2}{2m^*}\frac{\partial^2 u(x)}{\partial x^2} + \frac{1}{2}m^*\left(\frac{eB}{m^*}x - \frac{\hbar k_y}{m^*}\right)^2 u(x) = E'u(x) \tag{5.7}$$

This is recognised as the Schrödinger equation for the Simple Harmonic Oscillator with centre at $-r_c^2 k_y$ where $r_c = \sqrt{\hbar / eB}$ is the classical cyclotron radius of the lowest oscillator (compare this result with the corresponding semiclassical results given by equation (5.4)). Equation (5.7) has eigenvalues $E' = \left(k + \frac{1}{2}\right)\hbar\omega_c$ and eigenfunctions,

$$u_k = \exp\left(-\frac{m\omega_c x^2}{2\hbar}\right) H_k\left(\frac{m\omega_c}{\hbar} x\right) \tag{5.8}$$

where the H_k are the Hermite polynomials given by,

$$H_k(\xi) = (-1)^k \exp(\xi^2) \frac{d^k}{d\xi^k} \exp(-\xi^2) \tag{5.9}$$

where

$$\omega_c = \frac{eB}{m^*} \text{ and } k \text{ is an integer}$$

The first few of the Hermite polynomials are: $H_0 = 1$, $H_1 = 2\xi$, $H_2 = 4\xi^2 - 2$, … and follow the recursive relation $H_{k+1}(\xi) - 2\xi H_k(\xi) + 2kH_{k-1}(\xi) = 0$.

Equation (5.7) reveals the z dependent wavefunction to be unchanged from that of the free electron, with $E_z = \hbar^2 k_z^2 / 2m^*$. Hence the field quantizes the motion of the electron gas in the plane normal to B leading to Landau levels and leaves it unchanged along B's axis. This is in agreement with the semiclassical approach, with the energy of the electrons in the plane normal to B having a transformation of energy under the action of the field; the orbit corresponding to the kth Landau level given by $\frac{\hbar^2}{2m}\left(k_x^2 + k_y^2\right) \rightarrow \left(k + \frac{1}{2}\right)\hbar\omega_c$.

5.5 The SHET under a Perpendicular Field

From the preceding discussions, the effect of a magnetic field perpendicular to the interface will quantize the electron (hole) energy in the x-y plane into Landau levels in accordance with equation (5.7) and will leave it unchanged along the growth (z) axis.

Ignoring spin and writing E_z as the confinement energy of the electrons due to a conduction band profile *V(z)*, the electron total energy is[9],

$$E = E_z + \left(k + \tfrac{1}{2}\right)\hbar\omega_c \qquad \textbf{(5.10)}$$

where the E_z's are the solution to the Schrödinger equation,

$$\left[-\frac{\hbar^2}{2m_z^*}\frac{\partial^2}{\partial z^2} + V(z)\right]\psi = E_z\psi \qquad \textbf{(5.11)}$$

Further, the magnetic field will effectively change the density of states from a continuous distribution to one of a discrete set of δ functions, each with a density of states equal to *2eB/h* assuming spin degeneracy (see 5.5.1.2 and ref. [8]). In reality, however, phonons, interface roughness and ionised impurities will scatter the electrons (holes) and add uncertainties to their energies.

In modelling the effect of field perpendicular to the SHET interface, a number of approximations are made. Spin splitting is ignored, but this is justifiable as the Landau level energy separation, $\hbar\omega_c$, is an order of magnitude greater than the spin splitting $g^*\mu_B m_{e,h}$. It is worth noting, however, that the very fine structure that would be indicative of closely spaced spin-split levels has been observed in tunnelling experiments by Mendez *et al* in the GaSb/AlSb/InAs/AlSb/GaSb system [9, 10]. Temperature effects and the Landau level broadening mentioned above (due to the presence of defects and impurities) are also ignored. Fortunately both are much less than $\hbar\omega_c$. For example, at a low field of about 10T, $\hbar\omega_c$ = 50 meV for the InAs electrons. This is much greater than their thermal energy, *kT*, which at 4K is only about 0.3meV. Also, the InAs bulk scattering time (at 300K) is $\tau = 4\times10^{-13}$s, yielding an associated uncertainty in energy of the electrons of $\Delta E \sim \hbar/\tau$ = 4.5 meV, again much less than $\hbar\omega_c$ (at 4K, τ is much greater and correspondingly, ΔE is smaller still). Similar conclusions can be reached for GaSb. Thus, with experiments carried out at such low temperatures, these approximations seem very reasonable.

---

[9] I later write the hole confinement energies as HH_z and in order to distinguish between the electron and hole cyclotron frequencies, I add the superscripts *e* and *h* respectively on the symbol ω Note that the InAs electron mass is isotropic in space, but the GaSb heavy hole mass is not, taking values of $0.3m_0$ along the growth direction and $0.1m_0$ in the plane.

The self-consistent algorithm with B perpendicular to the interface is described in the following section. It solves for electrons in InAs and heavy holes in GaSb exactly at the Γ-point in a self-consistent way and is therefore an example of a decoupled model as band mixing is completely neglected in contrast to the zero field calculations of chapter 4. In reality of course, the Landau levels will have a permanently mixed character [11] and in order to accurately predict the movement of the valence band Landau levels with field, it would be necessary to include the relevant mixing potentials in a band structure calculation. Such calculations would be very lengthy and in the light of good agreement between the zero field decoupled model used by Khan-Cheema [4] and the **k.p** model presented earlier, the use of the decoupled model is justifiable. Section 5.7.1 and 5.7.2 detail its results and compares them with experimental results to shed light on the origin of the second NDR feature observed under field (Figure 5.1) as well as evidence for phonon aided conduction in both sample types.

5.5.1 Method of Calculation

The calculation is again a simultaneous solution of the Schrödinger and Poisson equations for both sides of the interface. The steps in the algorithm consist of *i*) solving equation (5.11) to determine the electron confined states and wavefunctions, *ii*) the determination of the Landau level energies and the occupancy of each, *iii*) the construction of the electron density which determines the total potential in the Poisson equation, *iv*) determination of the InAs background doping depletion length and finally, *v*) calculation of the 'new' weighted conduction band and iteration to convergence. Once this is done for the InAs side, the process if repeated for the GaSb side of the interface until the band profile gradients match at the interface. These steps are elaborated in greater detail below (for the InAs side).

5.5.1.1 Calculating the Confined States

The electron confinement energies E_z (equation (5.11)) are calculated using the transfer matrix method assuming a Fang-Howard initial potential approximation and initial conditions on $\psi(z)$ always,

$$\psi(0) = 0 \qquad \left.\frac{d\psi}{dz}\right|_{z=0} = -1 \tag{5.12}$$

The first condition corresponds to zero barrier penetration of ψ. This is a fair assumption because of the barrier height between symmetry-matched band edges. The second condition is an arbitrary assignment as the real value of the initial gradient of the wavefunction is determined by normalisation. A confined electron state of energy E_z exists when ψ is found to decay exponentially at large z far from the interface where the potential profile is flat. For a transfer matrix T across the InAs side of the interface, this condition is met when equation B5 of Appendix B is satisfied. This is reproduced here,

$$T_{2,2} - \frac{ik_f}{m^*_{z,InAs}} T_{1,2} = 0 \tag{5.13}$$

where $T_{x,y}$ is the (x,y) entry in T and k_f is the k value far from the interface edge. The values of E_z at which the above equation is true define the 1st, 2nd, 3rd, etc. confined subbands (E_0, E_1, E_2, ...) with z component wavefunctions ψ_0, ψ_1, ψ_2 ...etc.

5.5.1.2 Calculating the Landau Level Energies and Occupancies

With the confined subbands E_0, E_1, E_2, a ladder of 'Landau' energies can constructed:

$$E_0 + \tfrac{1}{2}\hbar\omega_c,\ E_0 + \tfrac{3}{2}\hbar\omega_c, \ldots\ E_1 + \tfrac{1}{2}\hbar\omega_c,\ E_1 + \tfrac{3}{2}\hbar\omega_c, \ldots\ E_2 + \tfrac{1}{2}\hbar\omega_c, \ldots$$

or in shorthand, E_{00}, E_{01}, ...,E_{10}, E_{11}, ...E_{30}, ...and placed in ascending order. Each electron in a particular Landau level will have a z component of wavefunction equal to the wavefunction corresponding to the subband number. The number of states associated with each Landau level is finite but, because the width of the level is zero, the density of states is infinite. As in the 3D case, the number of states associated with each Landau level can be determined by requiring that the average density of states is the same with and without the field. Ignoring spin, there are two Landau levels in an energy range $\hbar\omega_c$; if each level contains N states then the averaged density of states in the presence of a field is $N/\hbar\omega_c$. Equating this to the constant 2D density

of states in the absence of a field (equation (1.4)) gives the maximum population of states that can be accommodated by each Landau level,

$$N_L = \frac{2eB}{h} \tag{5.14}$$

Once the population of a Landau level exceeds this value, additional charge will then be accommodated by the next (previously) unoccupied Landau level and the Fermi level will accordingly jump and pin itself to that level. One would therefore expect a discontinuous variation in calculated bias at points when the number of occupied Landau levels increases. This is avoided in practice by setting the position of the Fermi level to lie in between the two Landau levels, while keeping the electron concentration constant so that the higher Landau level (which I shall call the $(k+1)$th level) remains unoccupied. For example, consider the simplest case where there is only one confined subband and only one Landau level, k, fully occupied (and therefore $n = N_L$ always) and at an energy E. The electron Fermi level can be set at a value of $E+\alpha$ where $0<\alpha<\hbar\omega_c$. Calculating the corresponding profile of the GaSb side of the interface for various α yields a set of biases that are in between the values that would be calculated if $\alpha = 0$ (i.e. the Fermi level is pinned to the fully occupied kth Landau level, and the $(k+1)$th Landau level is empty) and $\alpha = \hbar\omega_c$, (i.e. the Fermi level is pinned to the just occupied $(k+1)$th Landau level). For further increases in n now the Fermi level will remain pinned to this $(k+1)$th Landau level, until of course this Landau level itself becomes full. Then this description of the unpinning of the Fermi level applies once more, and so on. In this way it is possible to obtain solutions for the SHET under a perpendicular magnetic field for a continuous range of bias.

5.5.1.3 Solving the Poisson Equation

The charge distribution of the electrons (holes) is proportional to the modulus of the wavefunction squared $|\psi_{e,l}|^2$ ($|\psi_{h,l}|^2$). Poisson's equation for this problem is:

$$\frac{d^2\phi(z)}{dz^2} = \begin{cases} \sum_l \frac{en_l}{\varepsilon_r\varepsilon_0}\left|\psi_{e,l}\right|^2 & z \le 0 \\ -\sum_l \frac{ep_l}{\varepsilon_r\varepsilon_0}\left|\psi_{h,l}\right|^2 & z \ge 0 \end{cases} \tag{5.15}$$

with:

$$V(z)=\begin{cases}-e\phi(z) & z\le 0\\ \Delta-e\phi(z) & z\ge 0\end{cases} \tag{5.16}$$

where the summation is over all occupied Landau levels l and n_l is the number of electrons in each Landau level.

Double integration of the above leads to the following equation for $V(z)$:

$$V(z)=\begin{cases}-\dfrac{e^2}{\varepsilon_r^{InAs}\varepsilon_0}\sum_l n_l\left[z+\int_0^z(z-z')\left|\psi_{e,l}(z')\right|^2dz'\right] & z\le 0\\ \Delta-\dfrac{e^2}{\varepsilon_r^{GaSb}\varepsilon_0}\sum_l p_l\left[z-\int_0^z(z-z')\left|\psi_{h,l}(z')\right|^2dz'\right] & z\le 0\end{cases} \tag{5.17}$$

using the boundary conditions,

$$\left.\frac{d\phi}{dz}\right|_{z=0}=\begin{cases}\dfrac{en}{\varepsilon_r\varepsilon_0}\\ \dfrac{ep}{\varepsilon_r\varepsilon_0}\end{cases}\quad\text{and}\quad\phi(0)=\begin{cases}0 & z\le 0\\ \Delta & z\le 0\end{cases} \tag{5.18}$$

where $n = p$ to ensure the continuity of the electric field at the interface. Taking background doping into account, the equations above need to be slightly modified. This is treated below.

5.5.1.4 Background Doping and the Fermi Level

The effect of background doping on the band profile in the absence of field was discussed in detail earlier in chapter 4. For the GaSb, the impurity donors contribute to the band profile in a depletion region of length z_A. This ensures that without magnetic field the hole quasi Fermi level is pinned to the acceptor level E_a 34 meV above the bulk valence band edge. With a magnetic field applied perpendicular to the interface, the pinning condition must be altered to take into account the Landau quantisation of the 2DHG and of bulk carriers. The hole Fermi level HH_F of the 2DHG must be equal to the lowest occupied hole Landau level which in turn must be pinned to the acceptor energy. The acceptor energy (tied to the bulk Landau level)

must equal HH_F. Symbolically, if V_{far} is the flat GaSb valence band profile value far from the interface, then $V_{far} - E_a + \frac{1}{2}\hbar\omega_c^h = HH_F$. The background doping is incorporated into the calculation as an additional term in the Poisson equation,

$$\frac{d^2\phi}{dz^2} = -\frac{ep}{\varepsilon_r\varepsilon_0}\sum_l p_l\left|\psi_{k,l}\right|^2 - \frac{eN_D^{GaSb}}{\varepsilon_r\varepsilon_0} \qquad \textbf{(5.19)}$$

The relatively large 34 meV acceptor level comfortably allows the calculation to converge for this side of the interface, typically within 15 iterations.

The situation is slightly more complex for the InAs side of the SHET owing to the small donor ionization energy E_d of 2 meV. Without magnetic field applied perpendicular to the interface (i.e. zero magnetic field or field applied in the plane (chapter 6)), the calculations proceed treating the background charge as described in 4.2.1.5. In the depletion region, the acceptors remain ionized but the impurity donors are neutral, contributing a net negative 2D charge density, $N_A^{InAs}z_D$, to the band bending where N_A^{InAs} is the compensated acceptor concentration and z_D is the (donor) depletion length (Figure 5.8). The Poisson equation is then,

$$\frac{d^2\phi}{dz^2} = \frac{en}{\varepsilon_r\varepsilon_0}\sum_l n_l\left|\psi_{e,l}\right|^2 + \frac{eN_A^{InAs}}{\varepsilon_r\varepsilon_0} \qquad \textbf{(5.20)}$$

To maintain the continuity of the quasi electron Fermi energy throughout the InAs with magnetic field perpendicular to the interface, the donor energy (tied to the lowest bulk Landau level) must be equal to the 2DEG Fermi energy. Self-consistent solutions for this side of the interface were obtained under perpendicular field with the above background consideration using equation (5.20) when an electron Landau level became only just occupied. The vast majority of the solutions, however, required an alternative consideration of acceptors and donors to give a combination of net negative and net positive depletion regions. This is described as follows. Again far from the interface all the acceptors must be ionised and the Fermi level is assumed to be pinned to the donor level. Near the interface, the acceptors remain ionised but the donors become neutral when the conduction band profile is below a value of (E_F – $\frac{1}{2}\hbar\omega_c$ – E_d) less than the donor energy so that there is a net negative charge density contributing to the band bending. If the compensated acceptor concentration is N_A^{InAs}

and z_{Dneg} is the depletion length over which this occurs, then the negative contribution will be $N_A^{InAs} z_{Dneg}$. Beyond z_{Dneg} and less than a distance z_{Dpos}, however, there is a hump in the profile above the Fermi level. All the donors now being far above the quasi Fermi level in that region ionise, thereby contributing a net positive background charge density to the band bending. With a donor concentration N_D^{InAs} the positive contribution in the length of this bump will be $(N_D^{InAs} - N_A^{InAs}) z_{Dpos} \approx N_D^{InAs} z_{Dpos}$. Then Poisson's equation becomes,

$$\frac{d^2\phi}{dz^2} = \frac{en}{\varepsilon_r \varepsilon_0} \sum_l n_l \left|\psi_{e,l}\right|^2 - \frac{eN_A^{InAs}}{\varepsilon_r \varepsilon_0} \tag{5.21}$$

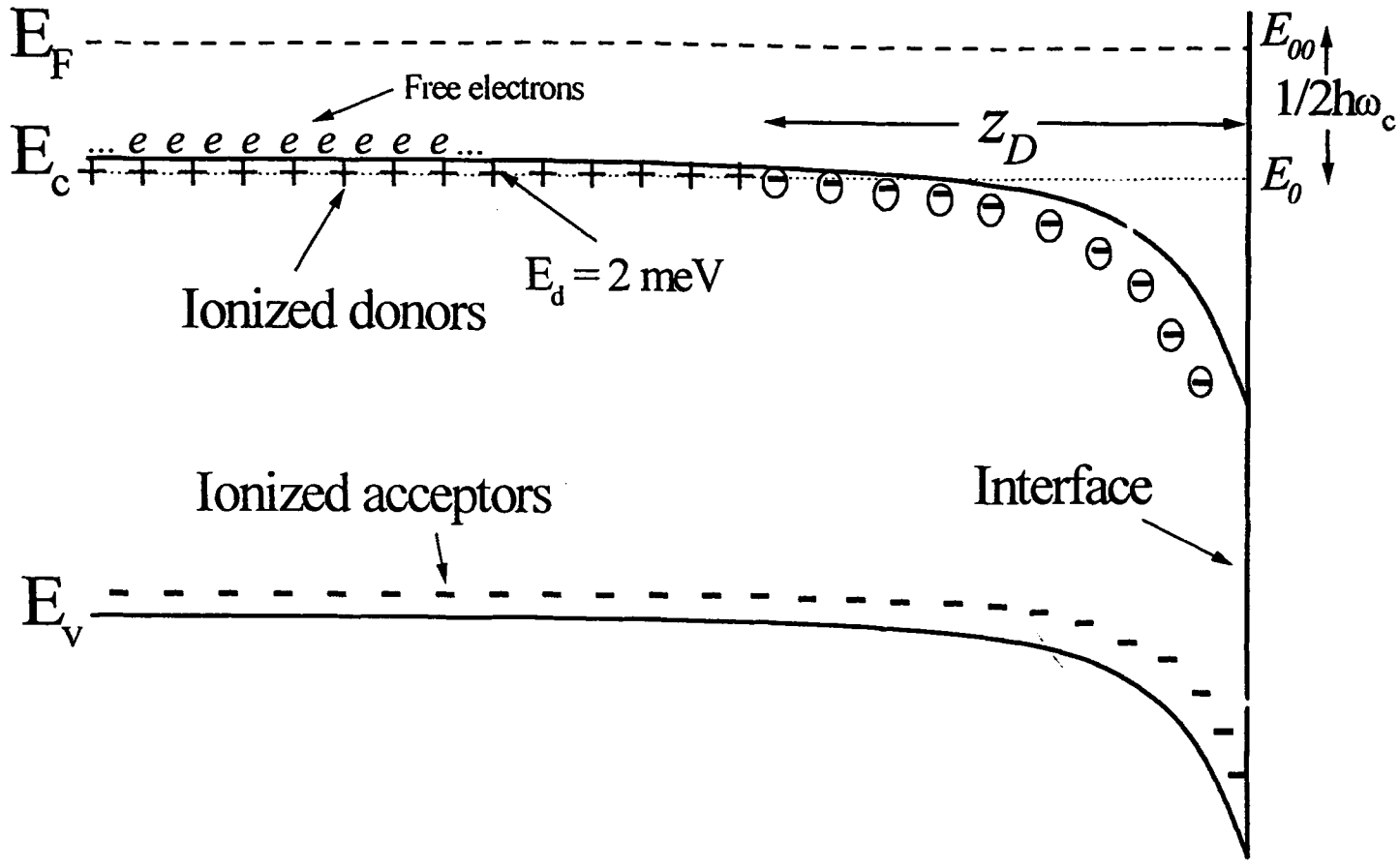


Figure 5.8. Example of a band profile under a perpendicular field for the InAs side of the interface where the electron concentration is less than N_L, i.e. the 2D electrons can all occupy one Landau level. The Fermi level has to be pinned to the bulk magnetic donor level, i.e. if V_{far} is the value of the conduction band profile far from the interface, then $V_{far} - E_d + \frac{1}{2}\hbar\omega_c = E_F$. As the first subband Landau level is $E_{00} = E_0 + \frac{1}{2}\hbar\omega_c$ then the E_0 itself has to be pinned 2meV below the bulk flat band.

Figure 5.9. Schematic showing band profiles under a perpendicular field for the InAs side of the interface. Notice that all donors (10^{16} cm^{-3}) with energy > E_F (located at $z_{Dneg} + z_{Dpos} > z > z_{Dneg}$) are ionised leading to a net positive reservoir of background charge (and a smaller negative background charge contribution closer to the interface at $z < z_{Dneg}$).

5.5.1.5 Approximations

As $z_{Dneg} << z_{Dpos}$ the contribution from the negative background charge is less than 1% of the positive background charge. The negative background is therefore neglected and the calculations are carried out as if the positive background charge extends from the interface to the point where the bands flatten. This assumption also reduces the complexity of the Poisson equation which otherwise would require two parameters to be determined (z_{Dpos} and z_{Dneg}). The calculations are consequently faster to perform.

With the value of N_D^{InAs} given (10^{16} cm^{-3}), the self-consistent calculations using equation (5.21) typically took in excess of 50 iterations to converge. As a consequence, a series of calculations were carried out varying the value of N_D^{InAs}. With a value of 10^{15} cm^{-3}, self-consistent calculations were found to take less than 12 iterations with a final energy output error of less than 2 meV (sample results are shown in Table 5.1). Thus, as the difference was small with a large saving in computational time, the calculations were carried out taking $N_D^{InAs} = 10^{15}$ cm^{-3}.

B (T)	N_D^{InAs} (cm^{-3})	n (cm^{-2})	E_0 (meV)	E_1 (meV)
40	10^{15}	15x10^{11}	155.50	
40	10^{16}	15x10^{11}	157.10	
40	10^{15}	19x10^{11}	181.50	
40	10^{16}	19x10^{11}	183.06	
40	10^{15}	23x10^{11}	208.24	274.37
40	10^{16}	23x10^{11}	209.35	276.76
10	10^{15}	3x10^{11}	52.98	
10	10^{16}	3x10^{11}	54.96	
10	10^{15}	6.5x10^{11}	91.71	124.75
10	10^{16}	6.5x10^{11}	93.45	128.16
10	10^{15}	13x10^{11}	144.93	198.19
10	10^{16}	13x10^{11}	146.32	200.89

Table 5.1. Some results for the InAs side of the interface at fixed electron concentrations and with a humped profile with a net positive background. The results show that the error in the first confinement energies of the subband assuming that $N_D^{InAs} = 10^{15}$cm^{-3} is negligible in comparison to the more realistic case where $N_D^{InAs} = 10^{16}$cm^{-3}.

5.6 Calculated Results and Discussion

Following the procedure outlined above, solutions for the SHET at any field can be obtained for any n up to approximately $5N_L$ corresponding to up to 6 occupied Landau levels. Beyond this point, convergence is very difficult to obtain as between iterations, the Fermi level may be pinned to multiple degenerate Landau levels with differing subband indices. An example of a final output is given in Figure 5.10, showing the SHET at zero bias and 20T in a simple case of one occupied electron and hole Landau level each. By plotting the movement of the Landau levels with bias, it becomes possible to relate observed experimental behaviour to specific predicted phenomena. For reasons that will become apparent, I choose to tackle the results at high pressure (section 5.7.1) before applying my analysis to the 1 bar experimental results (section 5.7.2).

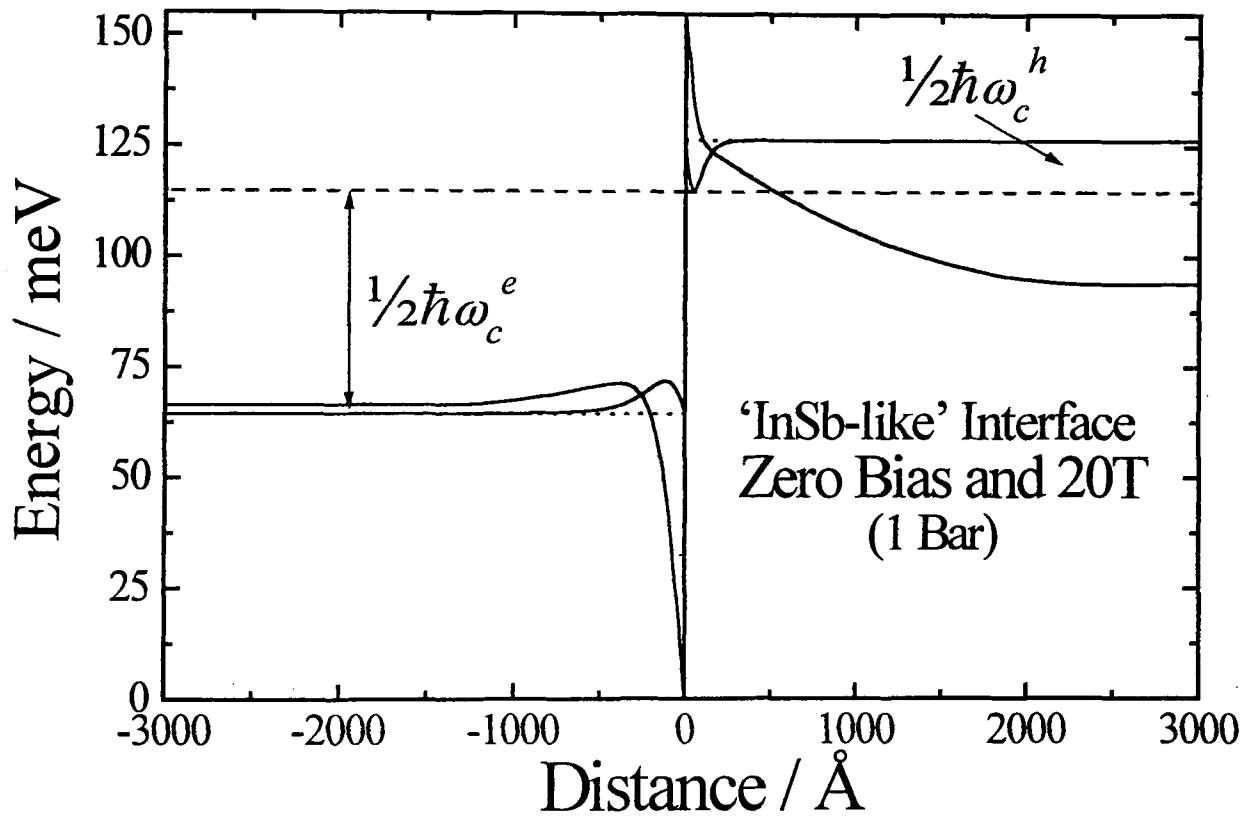


Figure 5.10. Result of a self-consistent calculation for an 'InSb-like' sample at zero bias under a magnetic field of 20T applied perpendicular to its interface.

5.7 General Behaviour

It is clear from Figure 5.1 and Figure 5.16 below that magnetic field suppresses the peak current. This can be understood by considering the effect of the field on the lowest spin split electron and hole Landau levels at zero bias. The spin splitting has

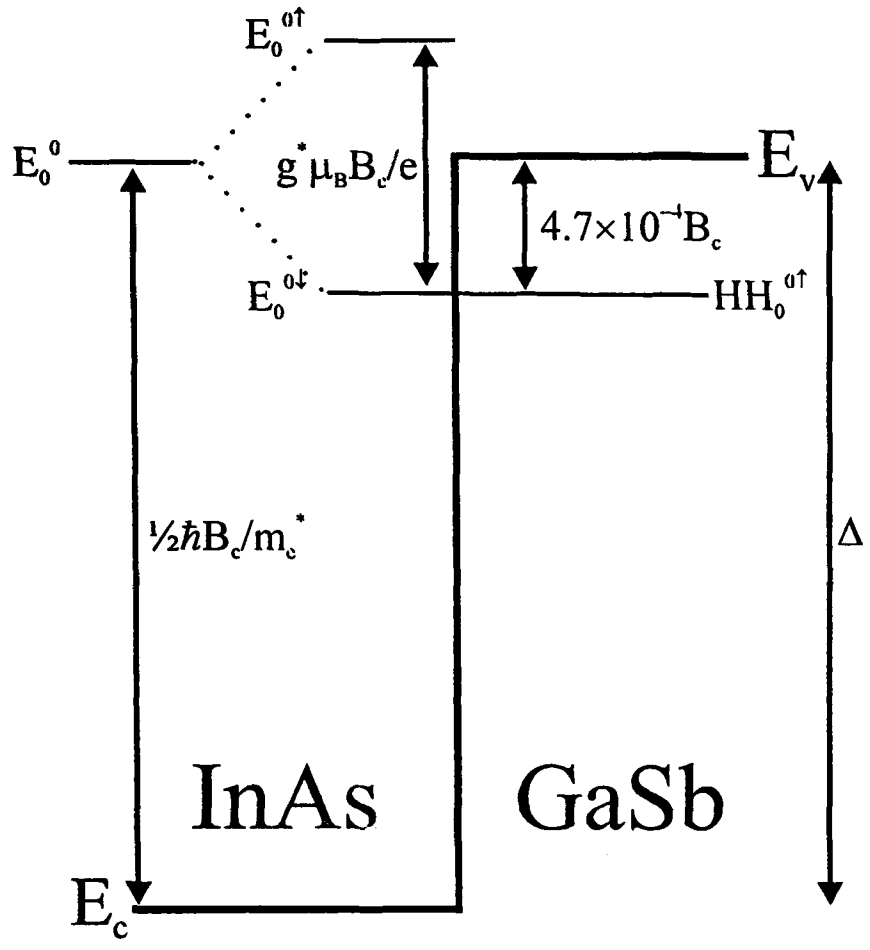


Figure 5.44. Schematic representation of the SHET band profile at the magnetic field induced semimetal to semiconductor transition B_c. All values are in electron- volts. From [4].

hitherto been neglected but splits the electron Landau levels by $\pm\frac{1}{2}g^*\mu_B B$ where g^* is the effective gyromagnetic ratio and μ_B is the Bohr magneton. The movement of the spin-split valence Landau levels is, however, made more complex by band mixing[10]. This fortunately has been calculated using **k.p** theory by Vaughan [11] who showed that the lowest spin split hole Landau level $HH_0^{0\uparrow}$ moves approximately linearly with field at a rate of -0.47 meV/T. In the limit where only these levels, $E_0^{0\downarrow}$ and $HH_0^{0\uparrow}$, are occupied, the two spin-split levels should pin together at the Fermi energy. Any increase in field will tend to push $E_0^{0\downarrow}$ above $HH_0^{0\uparrow}$. Hence in order to preserve the continuity of the Fermi level across the interface, electrons must recombine with hole states, thus decreasing n and p. Consequently E_0 and HH_0 become smaller, allowing $E_0^{0\downarrow}$ and $HH_0^{0\uparrow}$ to pin together once more. This continues until n and p fall to zero at a magnetic field induced semimetal to semiconductor transition B_c. This should be compared with the effect of pressure which also suppresses NDR by reducing n and p but does so by reducing the band overlap Δ. Under perpendicular field Δ remains constant. Following Khan-Cheema [4], an expression to estimate B_c can be easily derived,

$$B_c = \frac{2\Delta m_{e,\|}^* e}{\hbar e - \left|g^*\right|\mu_B m_{e,\|}^* + 9.4\times10^{-4} m_{e,\|}^* e} \qquad \textbf{(5.22)}$$

[10] For InAs, $g^* \sim 15$. However, there is evidence to suggest that g^* is not a constant, but actually varies with field [10].

this yields a value of B_c of 61T for an 'InSb-like' SHET and 49T for a 'GaAs-like' SHET - in rough agreement with the results presented in Figure 5.16 and Figure 5.53 (and with those of Barnes *et al* [12]).

5.7.1 Analysis at High Pressure

Figure 5.47 shows the calculated movement of the Landau levels against bias at a pressure of 10 kbar and magnetic fields of 5, 10 and 15T. The plots clearly show that at very low voltages, there is only one occupied hole and electron Landau level each, crossing of course at zero bias. Consider the effect of increasing the bias on the electrons alone. This is simply equivalent to an increasing electron concentration n, and the electron Landau levels move up in energy as the confinement energy E_0 of the self-consistent profile increases. A point will be reached when the first occupied Landau level becomes fully occupied (occurring when $n = N_L$). Additional electrons will then begin to occupy the next (previously unoccupied) Landau level. The **k.p** results of chapter 4 and the results of Khan-Cheema [4] have shown that the peak under zero field occurs at a bias close to when E_0 and HH_0 pass one another. NDR at this magnetic field and pressure would therefore be expected in the region when E_{00} and HH_{00} have similarly crossed and have separated by about a phonon in energy. Figure 5.47 clearly shows that this is expected to be below 70 mV for each field calculated though little quantitative comparison can be confidently made owing to the suppression of the NDR by the magnetic field and the presence of multiple phonons that mask the NDR region (Figure 5.5 and Figure 5.6).

Beyond the NDR resonance region, there are five clear features highlighted by arrows in Figure 5.6 (and labelled A to E) that move up in bias with field. At 15T and 9.73 kbar, the voltage positions of the first four (A, B, C, D) are 193, 245, 370, and 468 mV respectively (the position of E cannot be conclusively determined but is approximately located at 590 mV). By 10T, the positions of B, C, D and E are 164, 269, 350, and 431 mV respectively. Contrast these with the calculated values of the bias when the number of electrons exactly fills an integer number of Landau levels. Figure 5.47 shows these to be at 107, 263, 364 and 474 mV at 15T which agree well with the observed positions of A, B, C and D at 9.73 kbar and at the same field At 10T, Figure 5.47 predicts this to occur at 63, 175, 258 and 328 mV, which again are

close to the observed positions of the features B, C, D and E at the same field (see Figure 5.6). Excellent correspondence between the position of the observed features and calculated bias positions at which n fills an integer number of Landau levels is obtained. The first two features are both weak and broad making it difficult to follow their movement with field. However, the peak positions of the stronger waves can be clearly mapped as a function of field and further quantitatively compared with theory. This is done in Figure 5.45 highlighting graphically the excellent agreement between the bias at which $n=3N_L$ and $n=4N_L$ and the positions of the peaks C and D for a range of field values (at pressures of 9.73 and 14.8 kbar). The algorithm reached its computational limit at $n \sim 5N_L$ making any comparison with higher bias peaks impossible[11]. This not only includes the third strongest peak, which at 15T is at approximately 596 mV, but also peaks beyond it which are more clearly visible at lower fields. The trace highlighted in red in Figure 5.6 for example, shows peaks beyond the first five features indicated by the arrows in the same diagram. It is probable that these are due to similar Landau level unpinning effects described earlier, though now of course, the process will involve higher Landau levels still (belonging to perhaps fourth or fifth confined subbands). This fact is lent support by the roughly equidistant position of each peak which would be consistent with an increase in the amount of electrons in the InAs side of the interface by a constant number N_L.

[11] In fact, the bias positions at which $n = 5N_L$ could be calculated, but only for the highest fields.

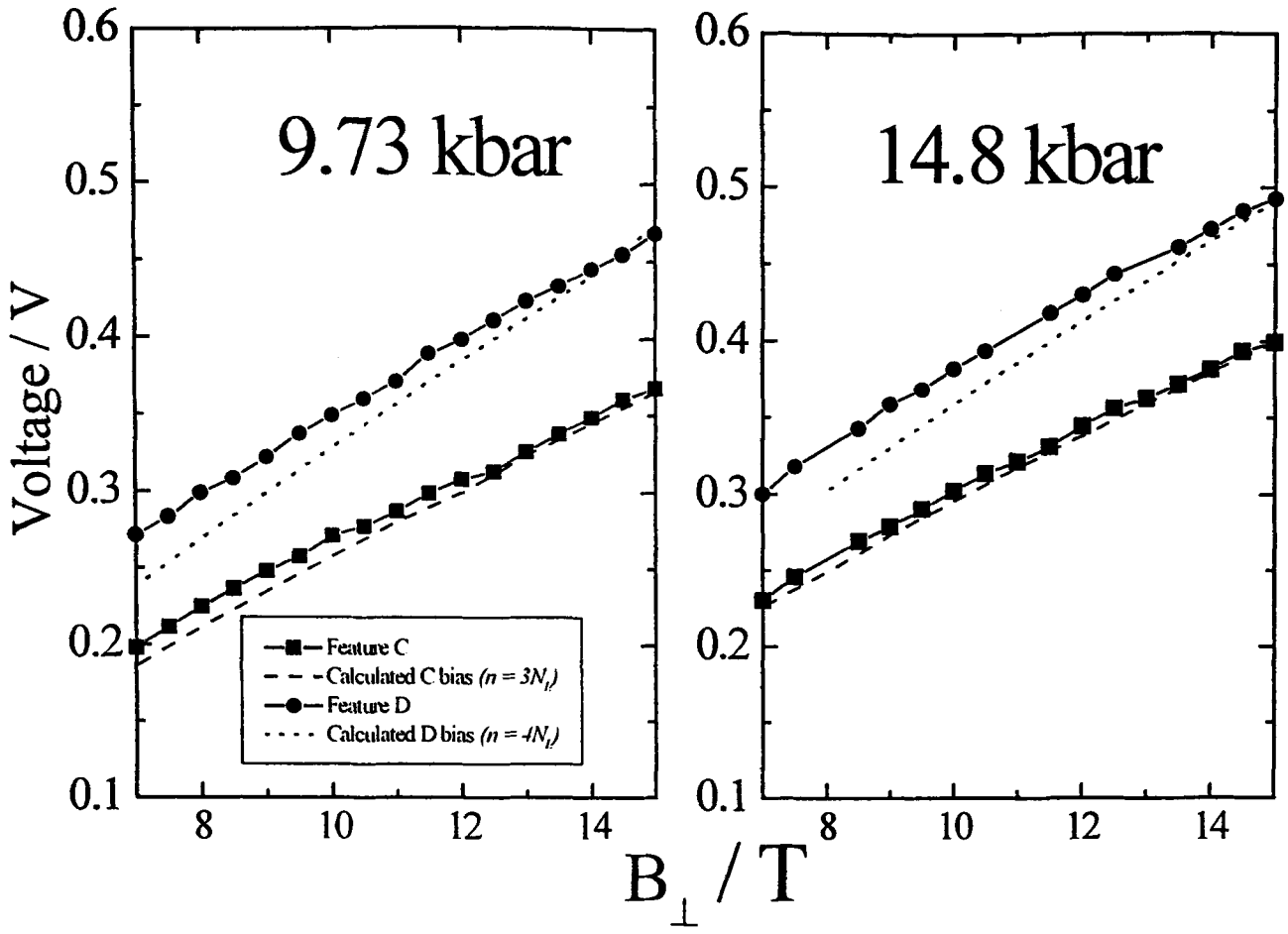


Figure 5.45. Results showing the position of features C and D in Figure 5.6 at 9.73 kbar, and the same feature at 14.8 kbar, as a function of magnetic field (solid line connected with squares) compared with the bias results of the self-consistent calculations performed with $n = 3N_L$ and $n = 4N_L$ at pressures of 9.73 kbar and 14.8 kbar (dashed line) respectively.

These results provide compelling evidence that the obviously perpendicular magnetic field induced features at high pressure are due to the filling of a previously unoccupied Landau level. It would be instructive to review in detail the electronic band structure through such a point. Consider again, for example, the low bias regime of Figure 5.47 at 15T. E_{00} is the only occupied Landau level, and the electron quasi Fermi level is accordingly pinned to it. As the bias increases (n increasing), E_{00} ($=E_F$) moves up in energy and the positive reservoir of background charge (forming a hump in the InAs side of the interface) in the band profile increases in size until $n = N_L$. The bias can subsequently increase infinitesimally only by unpinning the electron Fermi level so that it actually lies above E_{00} (n now of course remains constant at N_L). The hump in the band profile then begins to fall until it disappears when the background charge becomes wholly negative. At higher bias still, E_F will pin itself to the now occupied E_{10} Landau level ($n > N_L$) and the hump will gradually reappear. In general, on increasing the bias so that the number of Landau levels increases, such Fermi level unpinning and re-pinning to a Landau level will always take place leading

to a variation in the shape of the band profile. This is schematically illustrated in Figure 5.46.

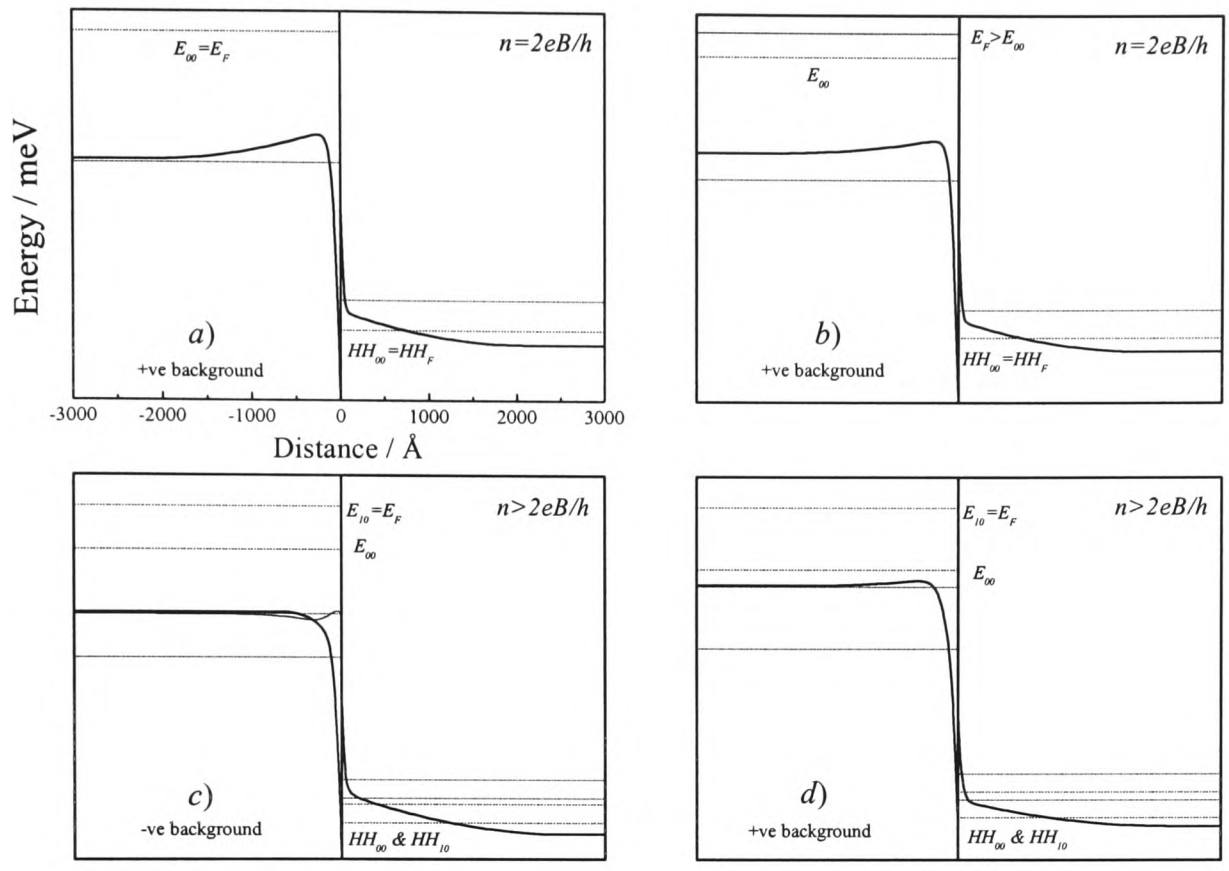


Figure 5.46. Schematic of Fermi level unpinning from a Landau level as n remains constant. When it does re-pin itself to a Landau level, the profile would have undergone substantially altered as the net background doping type varies.

Note that the 'secondary' features observed are not likely to be due to the holes in the GaSb side of the interface as the cyclotron energy for the holes is much less than that for the electron (i.e. the electron Landau levels are much more spaced apart than the hole Landau levels). Furthermore, less band profile variation occurs in the GaSb side of the interface. The relatively large 34 meV acceptor level energy comfortably allows convergence to be obtained assuming the usual impurity positive background concentration (5.5.1.4). I therefore conclude that it is the filling of previously unoccupied electron Landau levels in the InAs side of the interface leading to a change in the shape of the band profile there that is responsible for the features observed in Figure 5.6.

At high pressure, features observed are likely to be intrinsic to the sample alone owing to very low device currents. The experiments therefore agree with theory very well. At 1 bar, unfortunately, the uncertainty caused by high parasitic resistance and high sample currents contribute greatly to the lack of any definitive quantitative

comparison between experiment and theory. The physics of conduction in the SHET at 1 bar can therefore only be inferred through observing and comparing predicted trends. I now do this in the subsequent section, aiming to determine whether or not the 1 bar 'secondary NDR' features have the same origin to that proposed for the high pressure features.

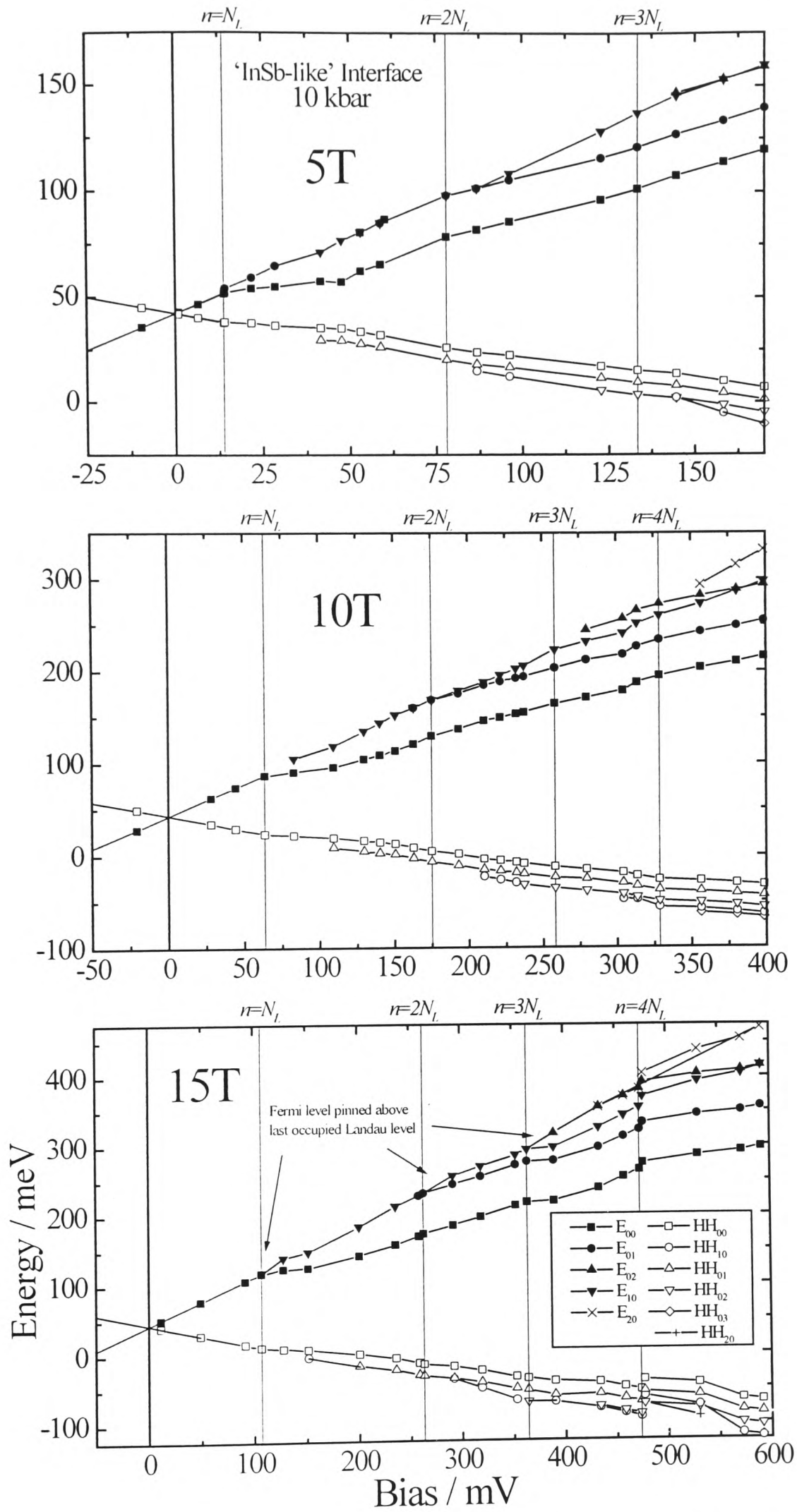


Figure 5.47. Calculated Landau level energy versus bias results for an 'InSb-like' sample at 10 kbar under a fields of 5, 10 and 15T applied perpendicularly to the interface.

5.7.2 Analysis at 1 bar

5.7.2.1 Low Fields (<20T)

The number of states in a Landau level at low field is much less than at high field. Figure 5.1 shows that at very low fields (less than 5T) where many occupied Landau levels are closely spaced, the form of the resonance is similar to that obtained without field. This is consistent with broadening which would produce a quasi-continuous $k_{||}$ dispersion. But as described in section 5.2.1, from 5T onwards, secondary features are observed after the main resonance, moving up with bias as the field is increased.

The complete results of the calculations at 1 bar are shown for a range of fields in Figure 5.48. Notice at high fields, E_{00} and HH_{00}, cross only once at zero bias rather like the calculated results for low fields and high pressure. But at 1 bar and lower fields (<15T), the calculations predict a second electron-hole Landau level crossing. E_{10} crosses HH_{00} at zero bias, while E_{00} and HH_{00} cross at a higher bias. It is conceivable that in this pressure-field regime, one would expect two NDR regions at the two biases when an electron Landau level is approximately 30 meV above a hole Landau level. By 15T, the number of Landau level crossings is again the usual one. The single Landau level crossing at high field and double crossing at low fields immediately offers a plausible explanation of the observed number of NDR features at 1 bar. This option can be excluded for three important reasons. Firstly the two calculated positions of V_{30} for the 5T and 10T results yields a practically constant splitting between the two NDR regions (46.6 mV at 5T and 48.7 mV at 10T) when it is in fact observed to increase very rapidly with field. Secondly, the so-called 'secondary NDR' is actually composed of two different features - both of which move up with field but at different rates. These are observable in the first derivative and are shown in Figure 5.1 and Figure 5.2 (labelled A and B). Finally such a proposal would not adequately account for the lack of features that would be expected by electron quasi Fermi level unpinning that has been shown to be the likely cause of weak high pressure-field features.

I therefore draw upon the conclusions of previous and forthcoming discussions on the resonant conduction mechanism operating in the SHET. Firstly, no distinct features are observed in the IV under zero field when individual electron-hole subbands cross.

Again, as will be demonstrated in chapter 6, no features in the IV (beyond the main NDR) are observed under in-plane field as the electron and hole dispersions cross. This behaviour is likely to be due to inelastic processes such as the multiple phonon processes, reported in chapter 4, which would mask the effect of such crossings. Armed with this knowledge, I postulate that multiple electron-hole Landau level crossings under a perpendicular magnetic field would also be masked by phonons. This implies we should in fact expect only the one main NDR feature associated with even multiple electron-hole Landau levels crossing.

With the possibility of the secondary NDR being due to electron and hole Landau levels crossing ruled out, alternatives must be explored. By analogy with the conclusions of the analysis at high pressure (5.7.1), the most likely candidate for secondary NDR features is the same electron quasi Fermi level unpinning that occurs when an integer number of Landau levels are completely filled. At 5T, this occurs when $n = iN_L$ ($i \geq 3$ to ensure that it is beyond any NDR region), the first of which corresponds to a bias of 107 mV. At 10T, this criterion is met when $i \geq 2$, the first two of which correspond to biases of 107 and 185 mV, and so on for higher fields. Note that as i increases, any signature of Fermi level unpinning and band profile variation would decrease rapidly due to the increasing background current. For low i (consistent of course with a bias beyond NDR V_{30}), the signature could again be drowned out - but this time by it being in close proximity to the main NDR. Taking these points into consideration, the most likely point when secondary NDR is expected to be exhibited at 5T occurs when $n = 5N_L$. At 10T, it is $n = 3N_L$; at 15T, it is when $n = N_L$. For higher fields still, when $n = N_L$, the bias is far beyond V_{30} making it the most likely candidate for any secondary NDR features observed then. These choices follow the observed trends of the upward movement in bias of the 'secondary NDR' feature and its increasing separation with the main NDR.

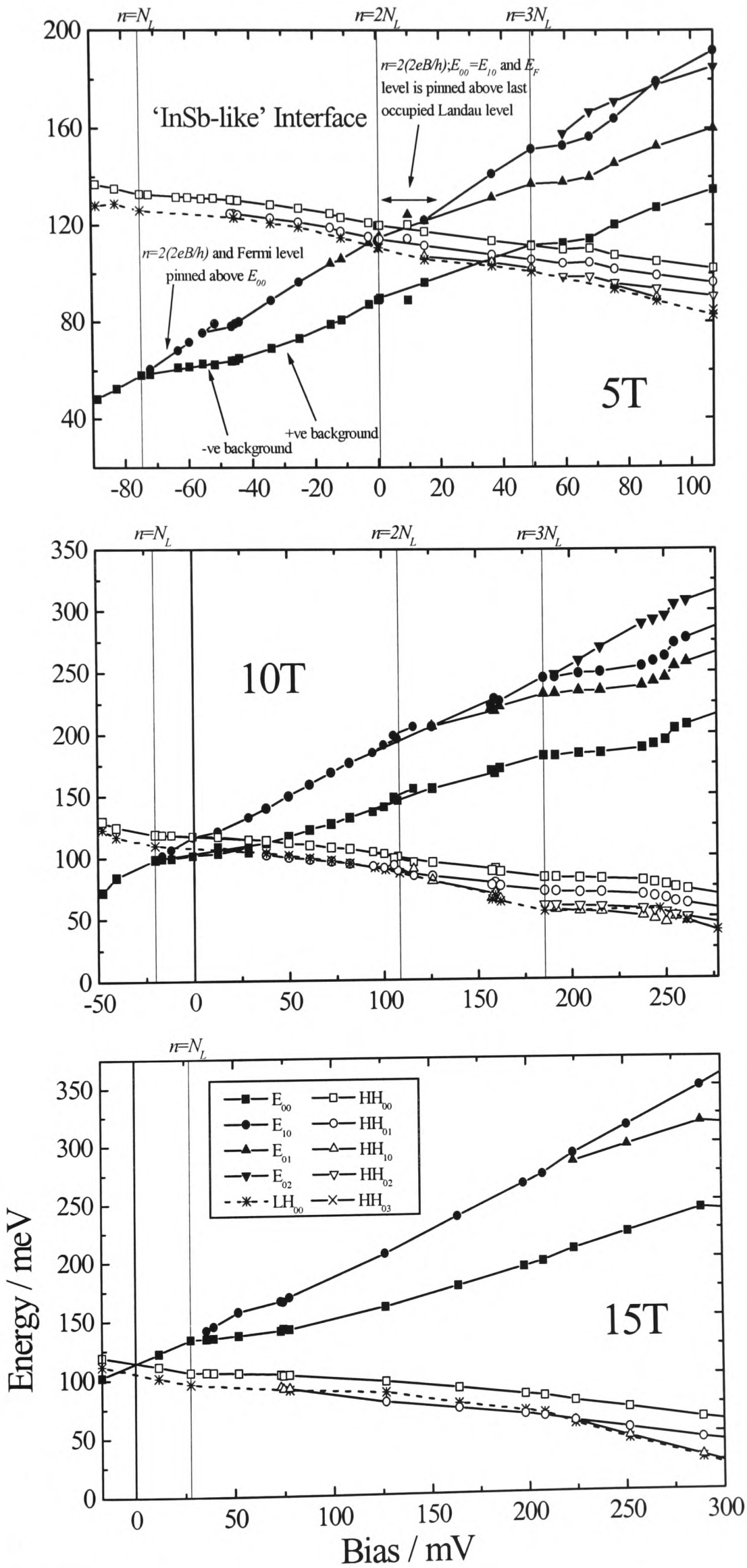


Figure 5.48. Calculated Landau level energy versus bias results for an 'InSb-like' sample at 1 bar under a fields of 5, 10 and 15T applied perpendicularly to the interface.

5.7.2.2 High Fields (>20T)

Figure 5.16 shows the response of an 'InSb-like' sample under high (pulsed) fields taken with the set up described earlier in chapter 2. The secondary NDR is expectedly visible at low fields, though at very high fields (above say 25T), it has disappeared. But as the results show, at very high fields, additional IV structure at approximately 200 mV appears. At 40T, this is in striking agreement with Fermi level unpinning calculated to take place at $n = N_L$ at a bias of ~230 mV (which I call $V_{2eB/h}$). This suggests that Fermi level pinning/unpinning is in fact the origin of this feature.

A possible reason why such a feature is more difficult to observe at lower fields (15 - 20T) could be because then $V_{2eB/h}$ and V_{30} are very close. The proximity of NDR would make any signature of Fermi level unpinning at $V_{2eB/h}$ difficult to observe. With higher field, and with $V_{2eB/h}$ moving increasingly further away from V_{30} (Figure 5.50), Fermi level unpinning effects would become less clouded by the NDR region and appear stronger. At the very highest fields, this could make them visible in the IV. Note also that the low current at high field also reduces the effect of contact resistance and leads to quite good quantitative agreement of bias position.

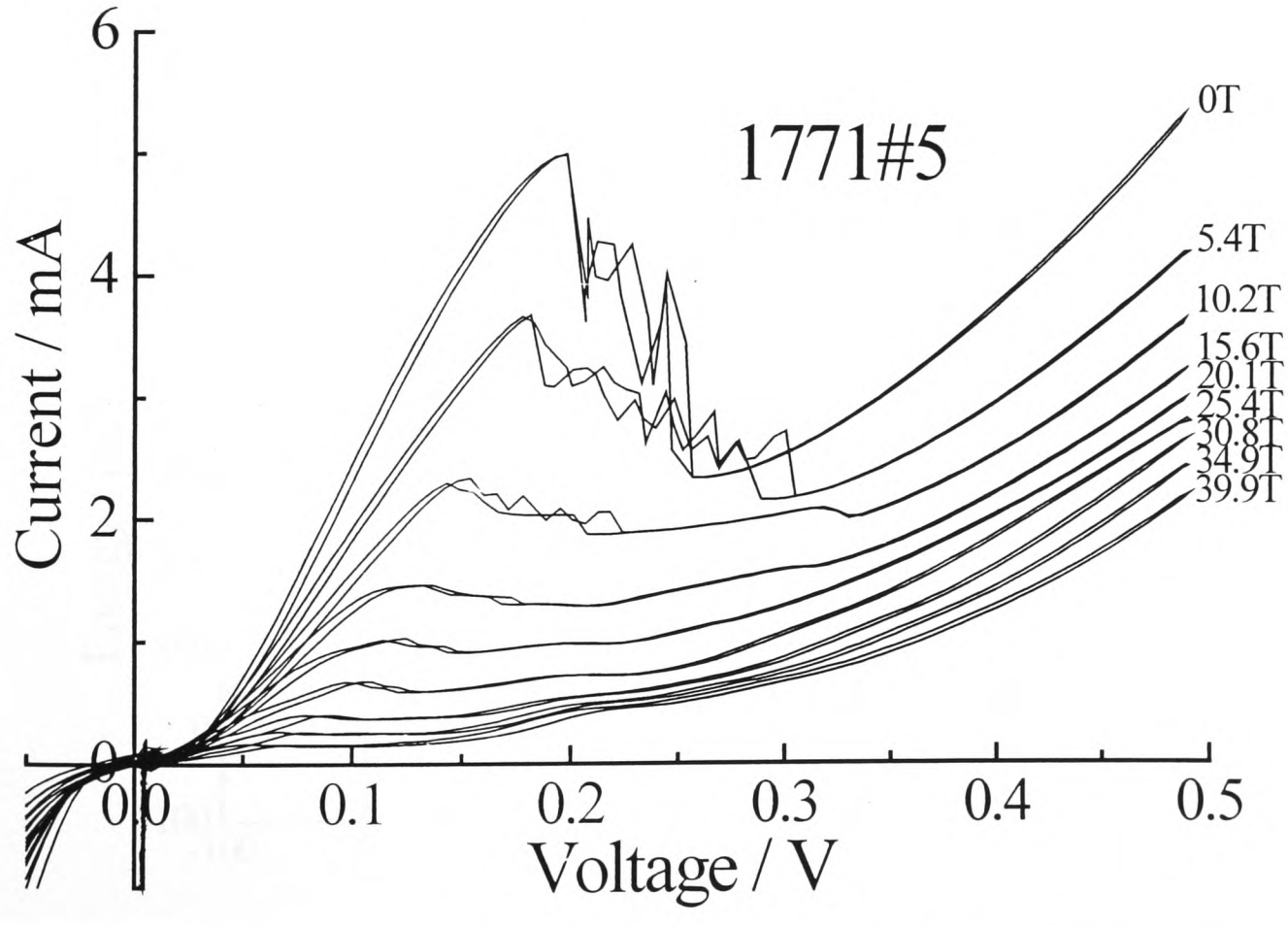


Figure 5.16. IV traces for 1771b#5 taken at pulsed field up to 40T applied perpendicular to the SHET interface at 4K. The slight difference in the plots for measurements taken with increasing and decreasing voltage is due to an induced component in the measuring circuit.

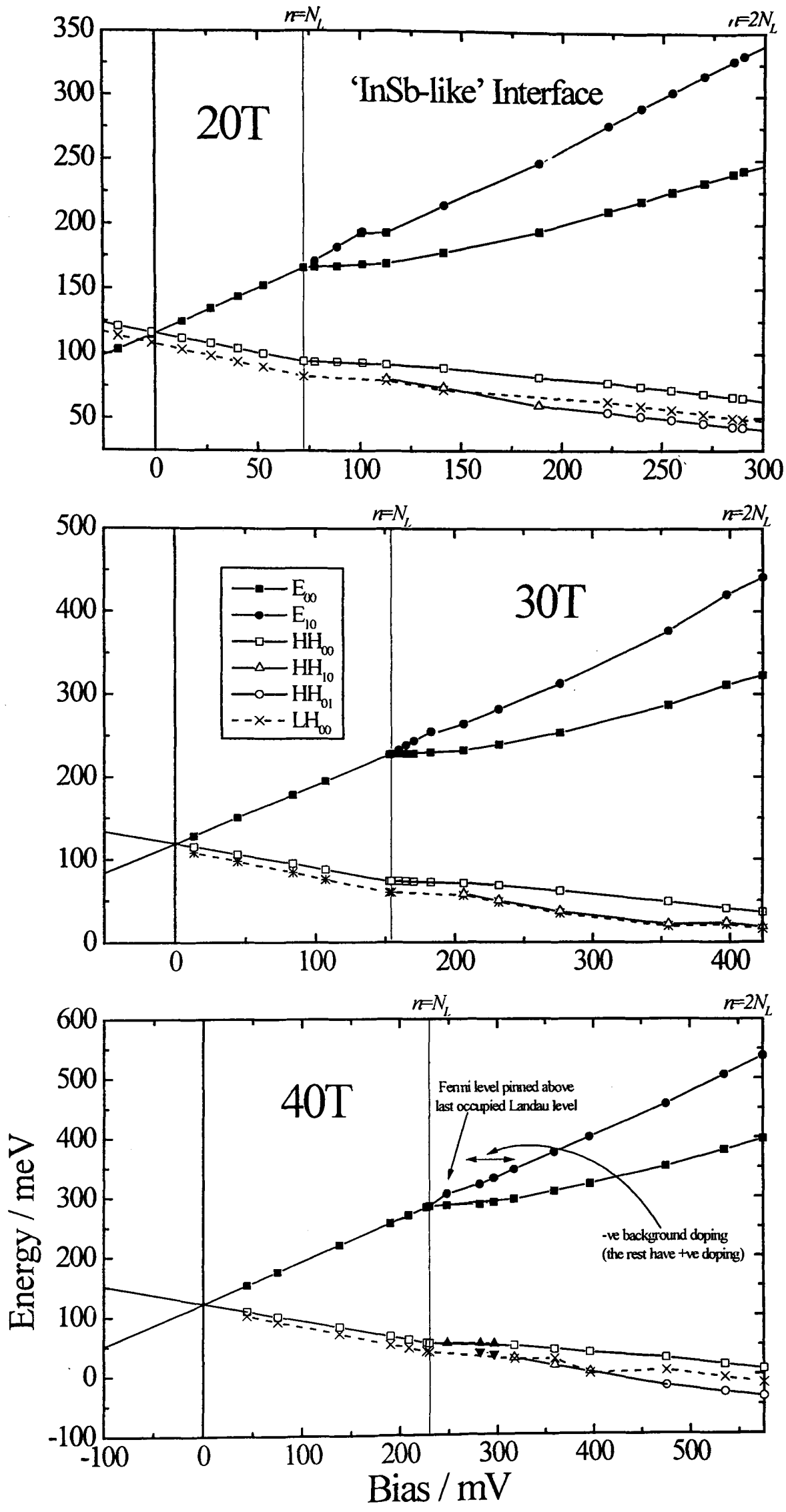


Figure 5.50. Calculated Landau level energy versus bias results for an 'InSb-like' sample at 1 bar under magnetic fields of 20, 30 and 40T applied perpendicularly to the interface. V_{30} = 30 mV by definition.

5.8 'GaAs - like' Interface

Figure 5.51 and Figure 5.53 show the IV response of 1772b#17 to $B_\perp$, illustrating the large difference between the field dependence of vertical transport for the two interface types. The peak current and voltages again decrease as the field is increased but at a much slower rate than for the 1771 series. No magnetic field induced features before the main resonance are observed. Notice though that $B_\perp$ does cause additional features beyond the main resonance as it did in 'InSb-like' samples (see Figure 5.1). These were not observed in earlier work [4] and thus the second resonance was thought to occur only in 'InSb-like' samples. The data here suggests otherwise; a second perpendicular magnetic field induced resonance beyond the main resonance is common to both sample types. Though difficult to observe in the IV, they are clearly visible in the conductance measurements (Figure 5.52). Such measurements were not made earlier and evidence for the secondary resonance relied solely on the IV results. This would explain why these features were missed in 'GaAs-like' samples and attributed only to samples with an 'InSb-like' interface.

Measurements using high pulsed magnetic fields were also made and are shown in Figure 5.53. As was found with pressure, NDR is found to be harder to suppress in 'GaAs-like' SHETs than in 'InSb-like' SHETs. It clearly disappears at a much higher field for this interface, whereas the smaller band overlap would imply that it should vanish sooner (according to equation (5.22)).

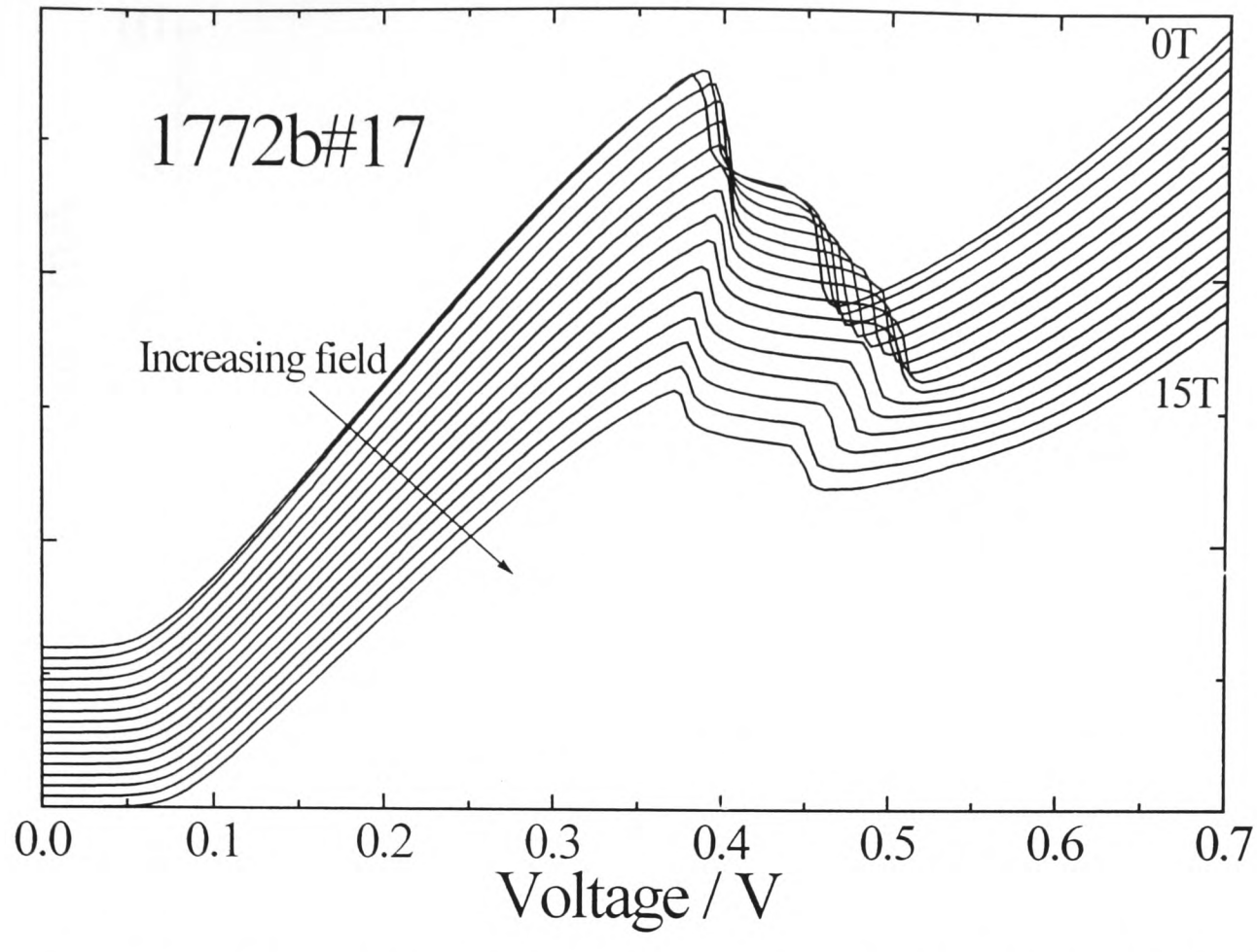


Figure 5.51. IV response of a 'GaAs-like' SHET at 1 bar and 4K under field perpendicular to its interface.

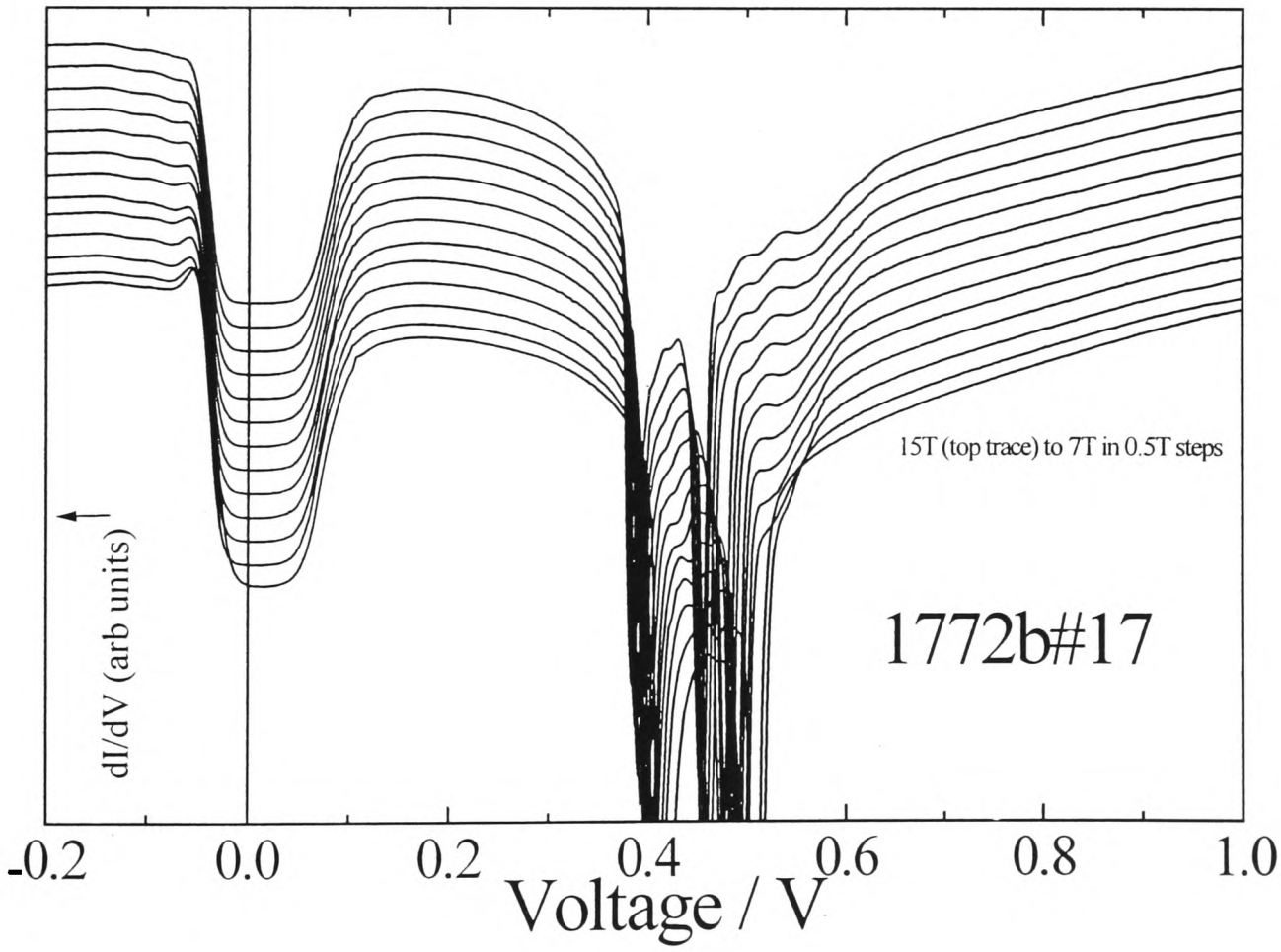


Figure 5.52. Conductance response of a 'GaAs-like' SHET at 1 bar and 4K under field perpendicular to its interface.

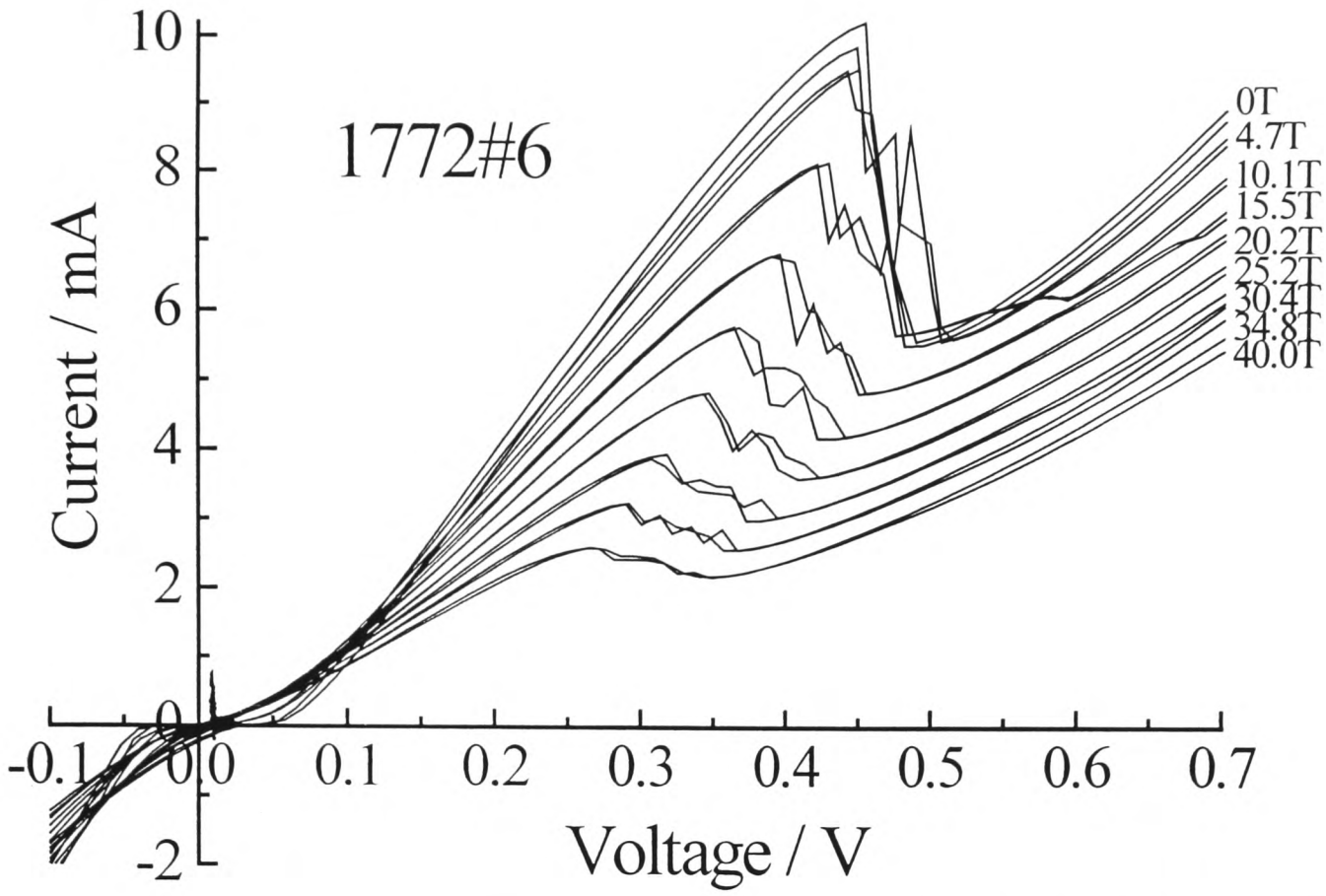


Figure 5.53. Response of a 'GaAs-like' SHET to a perpendicular field from 0 to 40T (pulsed).

A series of pressure runs combined with (perpendicular) magnetic field were also carried out on these sample types. As with the 1 bar results, NDR was found to always be difficult to suppress. Figure 5.54 presents the IV results at high pressure and shows that the peak current falls slightly in the magnetic field range 0-15T at an approximately constant peak voltage. By analogy with the results on the 1771 series any magnetic field induced effects in the conductance or IV would be expected to be enhanced with pressure. However, the opposite is found to be the case. Any trace of (secondary) magnetic field induced features beyond the main NDR actually disappears with increasing pressure. As NDR in 'GaAs-like' samples occurs at a higher bias than in 'InSb-like' samples at the same pressure, the background current would be correspondingly larger and that could severely drain any trace of the second resonance at high pressure. Alternatively, as the 1 bar results of Figure 5.52 show, the weak secondary features occur very near the main resonance - certainly much nearer to the main resonance than the secondary features in 'InSb-like' samples. It is possible that any high pressure weak secondary features occur between the peak and valley of the NDR region. Figure 5.54 does show a high pressure zero magnetic field NDR region altering significantly altering under increasing field. Though both these suggestions plausibly explain why the secondary NDR features become invisible at

higher pressures in 'GaAs-like' samples, a clear definitive reason as yet cannot be given.

The high pressure results did yield evidence for phonon ladders in reverse bias that were introduced in section 4.5.2. These 2nd derivative phonon features are shown below, and their positions were found to be unaffected by the magnetic field (Figure 5.55). This key result lends strong support for phonon assisted tunnelling in the SHETs.

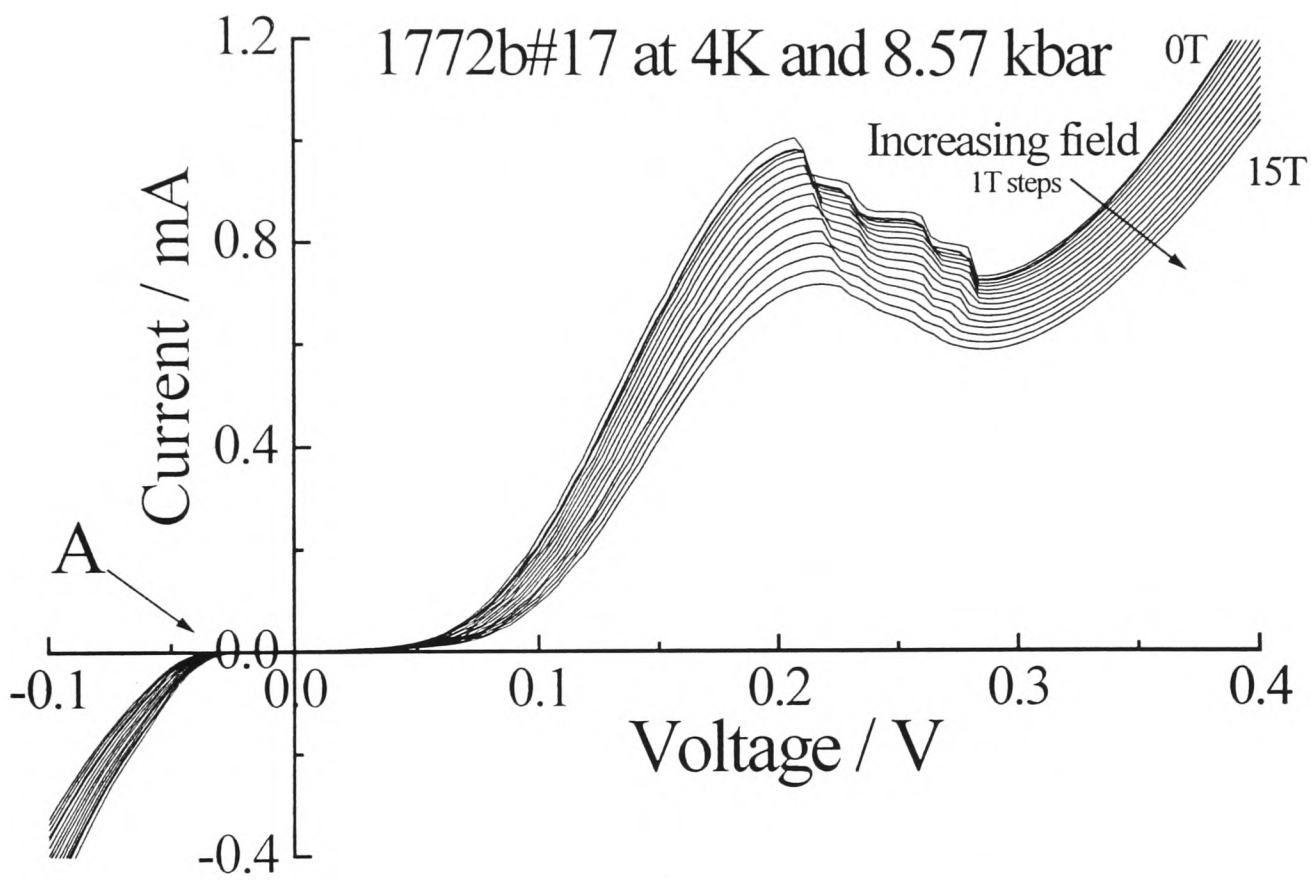


Figure 5.54. IV characteristic at high pressure under field for a 'GaAs-like' interface.

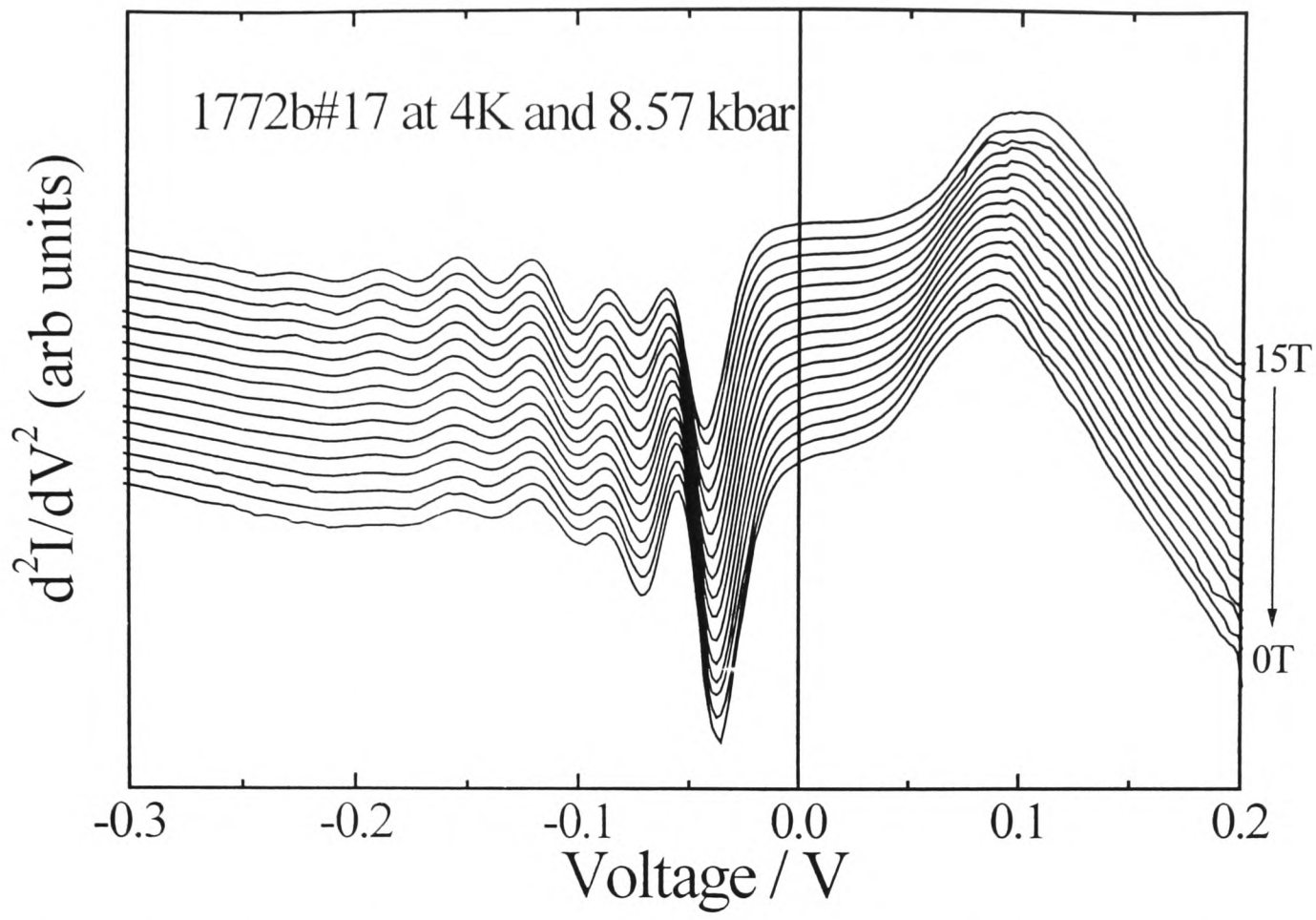


Figure 5.55. 2nd derivative results for 1772b#17 under pressure with field perpendicular to the interface. Notice the reverse bias features, each peak separated by 30 meV and unaffected by the field. Each peak is separated by 30 meV - the equivalent of a phonon energy.

The actual theoretical calculations produced for the 'InSb-like' interface samples yielded qualitative predictions for the number of NDR features expected and possible explanations for weak high bias features. As the model fails to predict any quantitative outcome at 1 bar then this also applies to the 'GaAs-like' samples.

5.9 Summary

This chapter has provided a very thorough investigation of the combined effects of pressure and magnetic field perpendicular to the SHET interface. A number of interesting features are observed in the 'InSb-like' samples,

- At 1 bar, the emergence of weak 'secondary NDRs' beyond the main resonance are observed at fields greater than 5T and found to move up in bias as the field is increased. By 15T, they become too weak to observe, probably due to the increased background thermal current at high bias.
- At high pressures, very weak 2nd derivative features are observed, and

- multiple forward bias phonons are observed.

Subsequent modelling has shown that the first two of these points are likely to be due to the Fermi level unpinning that takes place when a complete number of Landau levels are filled and not due to electron-hole Landau levels crossing. At this point the band profile loses its reservoir of net positive background charge, being replaced by a net negative background and therefore undergoes a dramatic change in shape. This provides a comprehensive understanding for the origins of the sharp secondary NDR at 1 bar, the high pressure features and the features observed at 1 bar and high (pulsed) fields.

Similar features at 1 bar were originally thought to be absent in 'GaAs-like' samples but have been found here through careful 1st derivative measurements. It is thought these features are due to the same underlying physics as in the 'InSb-like' samples. The IV trace itself is found to be far more difficult to suppress than its 'InSb-like' counterpart at all pressures. At 1 bar for example, the latter has an NDR signal that weakens with field and seems to be altogether disappearing at very high experimentally available fields (Figure 5.16). This is consistent with the calculated value of the magnetic field induced semimetal-semiconductor transition B_c of 61T at which NDR is expected to cease (see equation (5.22)). The 'GaAs-like' samples, on the other hand, exhibit strong NDR at even high fields (Figure 5.53), whereas the smaller band overlap value associated with such sample types suggests it should have completely disappeared by 49T (equation (5.22) again). The question of why NDR is exhibited in 'GaAs-like' samples beyond the point expected (with or without field) is a central area of investigation, but the clear observation of multiple phonons suggest strongly phonon aided tunnelling as a viable and at least a partial solution. The details of phonon coupling are currently unknown, leaving this question open to further investigation.

5.10 References

[1] Smoliner *et al* have directly observed the tunnelling between Landau levels in barrier separated two dimensional electron-gas systems. J Smoliner, E Gornik and G Weimann, Physical Review B 39 p12937 (1989).

[2] E E Mendez, H Ohno and L Esaki. Physical Review B 43 p5196 (1991).

[3] E E Mendez L Esaki and W I Wang. Physical Review B 33 p2893 (1986).

[4] U M Khan-Cheema, D.Phil. Thesis; Vertical Transport Through an InAs/GaSb Heterojunction at High Pressures and Magnetic Fields, Clarendon Laboratory, Oxford University (1996).

[5] Self-consistent calculations of a simple inversion layer in the two-subband state and under a perpendicular magnetic field have, however, been performed by Trott *et al*. They too describe the effect of the field on a 2D electron gas and present a similar algorithm for obtaining solutions. S Trott, G Paasch, G Gobsch and M Trott. Physical Review B 39 p10232 (1989).

[6] J Los, A Fasolino and A Catellani. Physical Review B 53 p4630 (1996).

[7] See for example chapter 17 of J Singh, Physics of Semiconductors and their Heterostructures, International Edition, McGraw-Hill, Singapore (1993).

[8] See C Kittel, Quantum Theory of Solids, John Wiley & Sons, Inc. (1986).

[9] E E Mendez, J Nocera, W I Wang, Solid State Electronics 37 p779 (1994).

[10] E E Mendez, J Nocera, W I Wang. Physical Review B 47 p13937 (1993).

[11] T A Vaughan, D.Phil. Thesis; The Magneto-optics of InAs/GaSb Heterostructures, Clarendon Laboratory, Oxford University (1996).

[12] D J Barnes, R J Nicholas, R J Warburton, N J Mason, P J Walker and N Miura. Solid State Electronics 37 p1027 (1994).

6. Magnetic Field Parallel to the SHET Interface

6.1 Introduction 137

6.2 Experimental Results 138

6.2.1 'InSb-like' Interface 138

6.2.2 'GaAs-like' Interface 141

6.3 The SHET in an in-Plane Magnetic Field 142

6.3.1 Perturbative Method 143

6.3.2 Fully Self-Consistent Calculations 144

6.3.3 Results 148

6.4 Comparison with Experiment 153

6.5 Angle-Resolved Magnetotunnelling 158

6.6 Summary 163

6.7 References 165

6.1 Introduction

The previous chapter dealt with the application of a magnetic field perpendicular to the interface of the SHET. Under such a configuration, the electrons execute cyclotron orbits which are quantised into Landau levels and lead to new features in the IV beyond the main resonance. This chapter will deal with a different geometrical arrangement of the magnetic field and the SHET, i.e. the situation in which the magnetic field lies in the plane of the electron-hole gases. In this case, there is a significant modification of the electronic states due to the combined effects of the Lorentz force and the confining potential (sect 6.3). The most pronounced effect of the parallel magnetic field is a shift of the subband energy dispersion curves, as predicted by Stern and Howard [1]. According to their lowest order perturbation theory treatment, the wavevector position of a subband minimum shifts linearly with magnetic field B, while the energy of the minimum experiences a quadratic diamagnetic shift. In both cases, the magnitude of the shift increases with subband number due to the increasing spatial extent of the higher subband wavefunctions and as a result, it is possible to alter the individual subband populations to the point where higher lying subbands are completely depopulated [2, 3].

In the case of the InAs/GaSb SHET, the analysis is not so easy because of the non-trivial coupling of the various subbands and their subsequent mixing, and the seemingly explicit dependence of the resonant conduction mechanism on $\boldsymbol{k}_{||}$. The lowest order perturbative method would not provide a particularly realistic description of the heterojunction electronic structure and the subject of this chapter presents the first ever in-depth self-consistent calculation. It must be stressed however as was the case with $B_{\perp}$ calculations, that the model employed here does not include the expected electron-hole mixing. That would be the subject of a separate **k.p** theory, including the effect of in-plane field in the Hamiltonian matrix. Thus, the model assumes the in-plane dispersions are parabolic in the absence of field. Under such circumstances, it will be shown that applying the field then will cause the motion of the electrons (holes) perpendicular to the interface to couple with electron (hole) motion in one of the in-plane directions.

The layout of this chapter is as follows. First, in section 6.2, the experimental results of applying an in-plane field (both DC and pulsed) parallel to the interface, will be presented for both the 'InSb' and 'GaAs' interface type samples. Drastic differences between the responses of the two interfaces will be shown. Further, previously unobserved 2nd derivative measurements of the IV traces for the 'GaAs-like' interface type samples will be presented at the end of section 6.2.2 and in section 6.5 The movement of the IV traces with field will then be compared with a model detailed in section 6.3.2. Its conclusions are presented in 6.4, and will again yield conclusive evidence for a difference in conduction mechanism between the two interface type samples not explicable solely due to the difference in band overlap. Section 6.5 presents detailed measurements of the movement of the peak of the NDR at fixed field as the in-plane orientation is varied. These results can possibly lead to information about the anisotropy of the hole Fermi surface. Finally, section 6.6 provides a summary of the major conclusions obtained from this work.

6.2 Experimental Results

The following two sections contain data from samples under an in-plane field. Section 6.2.1 considers 'InSb-like' SHETs and section 6.2.2 considers 'GaAs-like' SHETs. All the experiments were carried out at 4K using the superconducting magnet described in chapter 2.

6.2.1 'InSb-like' Interface

Figure 6.1 shows the IV trace for 1771b#8 under an in-plane field $B_{||}$ up to 15T. The sample itself was randomly orientated, but detailed measurements with field at all orientations show differences in the IV for various orientations to be small (section 6.5). The peak voltage, V_p, increases, and no additional features emerge. This should be compared with the results obtained under $B_{\perp}$, where a secondary NDR feature was observed. This provides clear proof that this second resonance, and indeed other weaker features, are genuine features induced *only* by the application of field perpendicular to the interface, $B_{\perp}$.

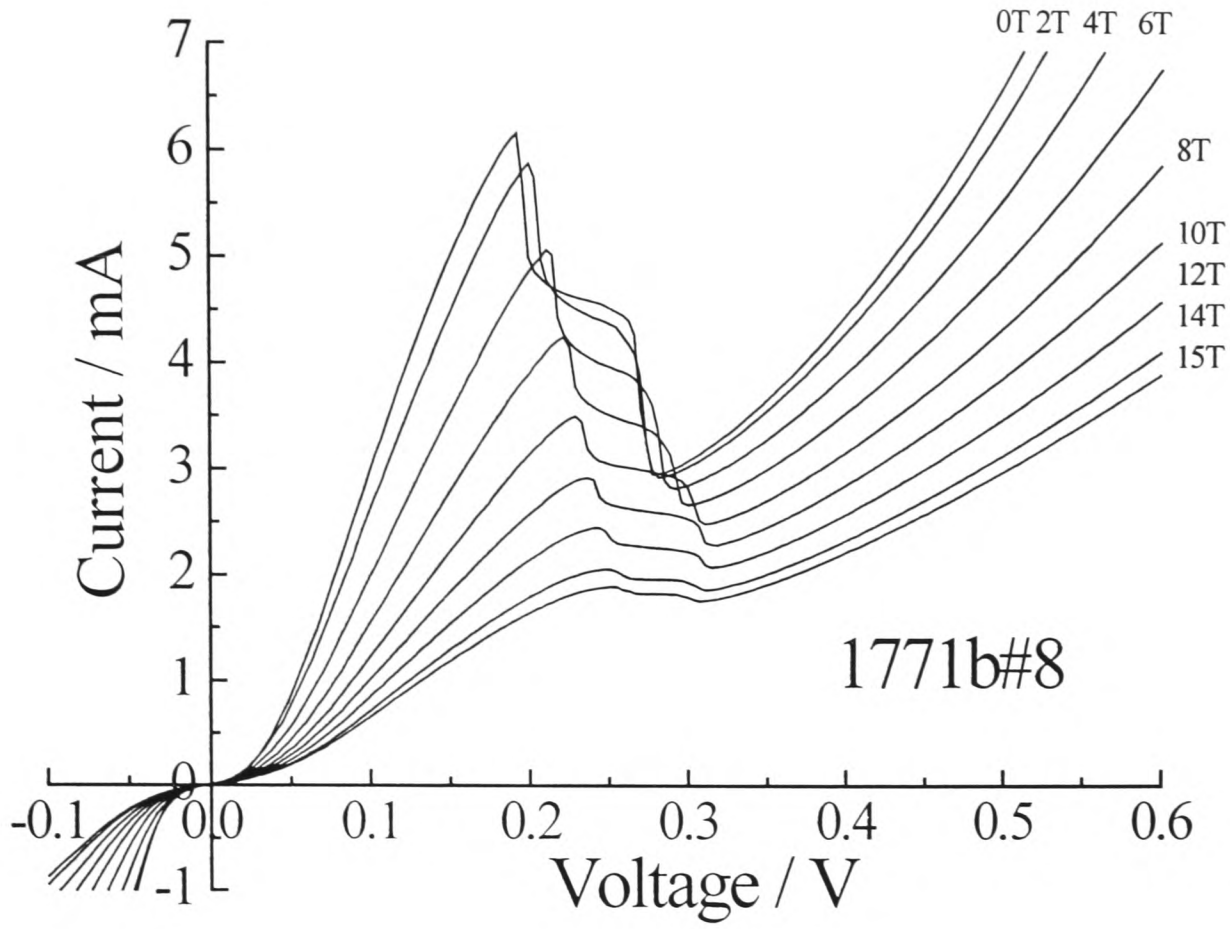


Figure 6.1. Response of the SHET with an 'InSb-like' interface (1771b#8) at 4K and 1 bar under a DC field applied parallel to the interface.

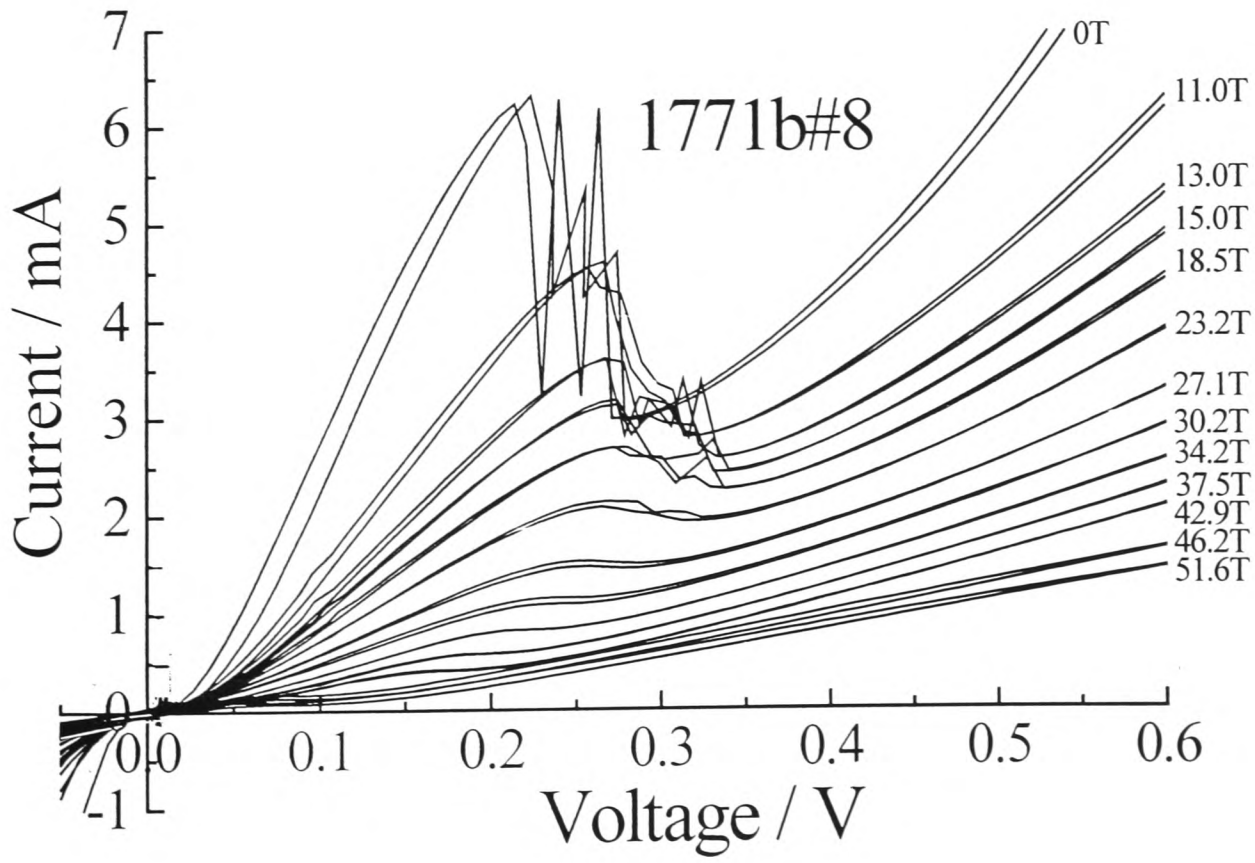


Figure 6.2. IV traces for 1771b#8 taken at pulsed magnetic fields greater than 50T applied parallel to the SHET interface at 4K. The two lines per trace correspond to the voltage being swept up and down.

Figure 6.2 shows results from the same mesa, but at higher fields, produced by using the pulsed field set-up. Again, V_p can be seen to move up with field initially, though at higher fields (~25T), it begins to fall. By 46T, NDR has vanished.

The results observed are qualitatively similar to those observed by Takamasu *et al.* [4] from an InAs/GaSb/InAs DHET structure with pulsed $B_{||}$ up to 40T. Again, they observed a peak voltage increase followed by a decrease. They attempted an explanation of the behaviour by using a two band model of a SHET. However, the results were disappointing reflecting their use of a very simple model. In this chapter, the first realistic calculations on an InAs/GaSb SHET will be presented, taking into account coupling between the motion of the electrons along the growth direction and along a direction perpendicular to it.

A series of pressure runs were carried out in this orientation of B field. Shown in Figure 6.3 are the results carried out on 1771b#2 at 3.67 kbar. Again, the peak voltage of the NDR, V_p, increases with field with no other additional features observed as a result of the field. At higher pressures still, no additional $B_{||}$ induced features were observed before or beyond the NDR in the IV, conductance or 2nd derivative measurements.

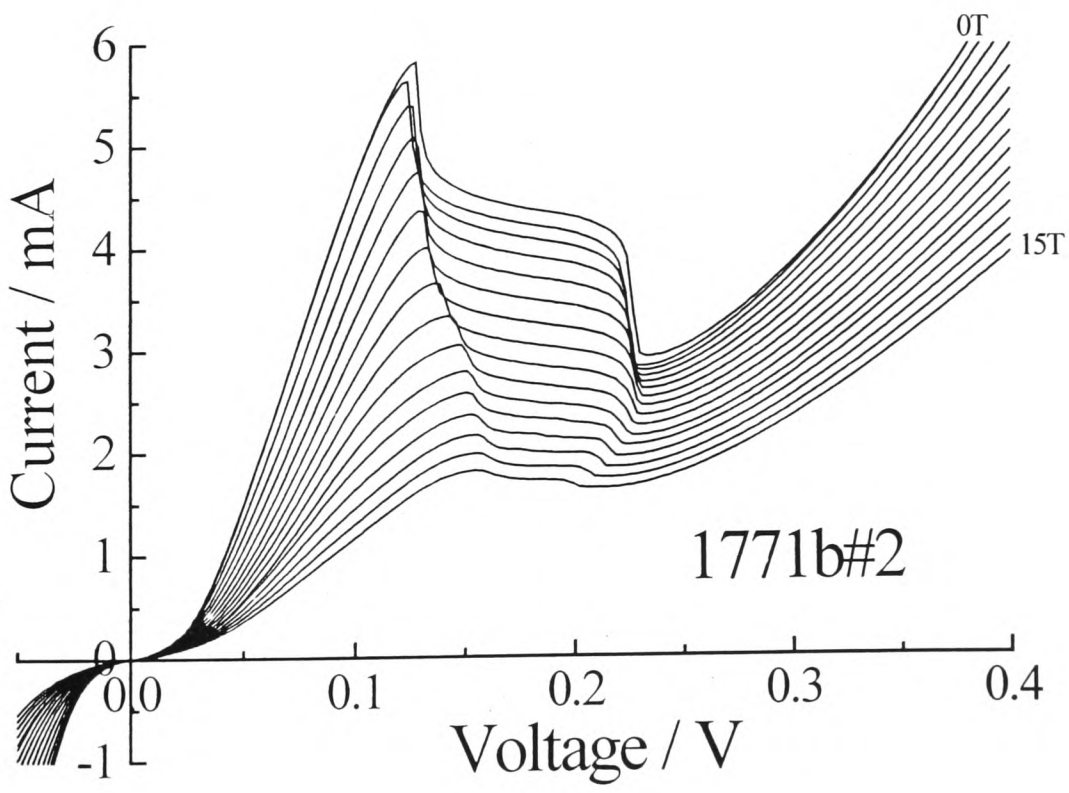


Figure 6.3. Response of the SHET IV for 1771b#2 at 4K and 3.67 kbar under a DC field applied parallel to the interface ranging from 0 to 15T in 1T steps.

6.2.2 'GaAs-like' Interface

Figure 6.5 shows the IV plots for 1772b#17 under $B_{||}$ up to 15T. Again, the trends exhibited by this 'GaAs-like' SHET are very different from those observed in the 'InSb-like' interface sample 1771b#8 above. V_p is seen to increase rapidly with $B_{||}$. The same results are found with the field pulsed - the resonant voltage seems to increase throughout the entire $B_{||}$ range from 0 to 40T. This is in stark contrast to the results obtained in the 'InSb-like' SHET which show V_p increasing initially and then decreasing rapidly at higher fields (greater than ~25T).

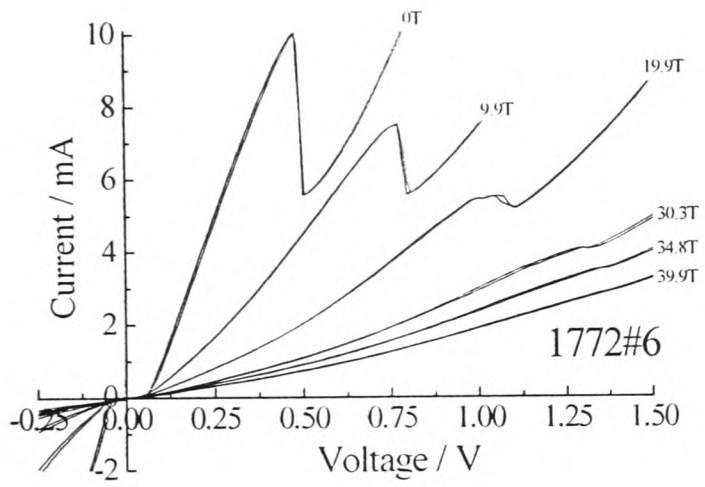


Figure 6.4. IV traces for 1772#6 taken at pulsed fields up to 40T applied parallel to the SHET interface at 4K.

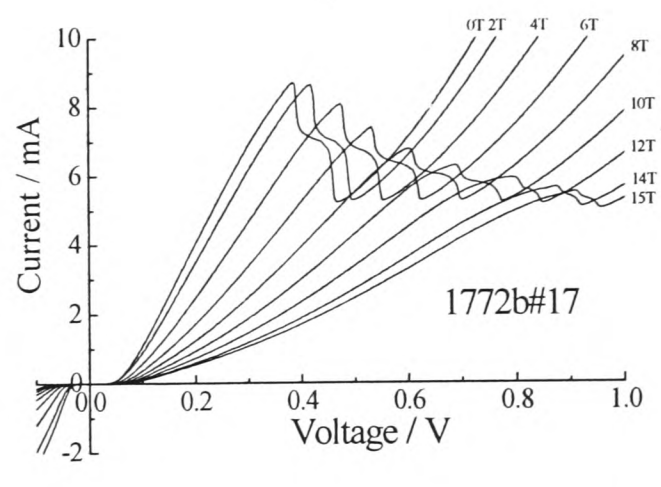


Figure 6.5. Response of a 'GaAs-like' sample SHET to a DC magnetic field applied parallel to the interface at 4K.

A magnetic field perpendicular to the interface of both 'InSb-like' and 'GaAs-like' SHETs leads to new features in the IV. Applying field parallel to the interface for 'InSb-like' SHETs changed the shape of the IV trace; the peak and valley voltages and currents were altered but no new sharp additional features were observed (in the IV, conductance or 2^{nd} derivative measurements) unlike the situation with B perpendicular to the interface. Similar results in the IV were obtained when applying field parallel to the interfaces for 'GaAs-like' samples. However, careful 2^{nd} derivative measurements (Figure 6.6) did reveal additional weak forward bias features caused by the in-plane field. It is interesting to note the positions at which these features appear. One set occurs just before the onset of NDR. Another set appear at very low biases of approximately 0.04V. This is exactly the bias at which tunnelling is allowed by energy and in-plane momentum conservation [5]. At lower voltages, the current is therefore suppressed, leading to the formation of an 'S' shape kink at the origin. It is very puzzling that such features occur only at the point where tunnelling

is just allowed and at the point where NDR occurs. Again these features are unique to the 'GaAs-like' interface samples. Further, the results of section 6.5 show that the shape of the NDR is greatly affected by the orientation of the field in the plane. At some orientations, NDR is very sharp while at others, a distinct feature can be seen before NDR. The 2nd derivative result here is probably due to having the sample placed on the insert so that the field is applied at a random in-plane angle. Clearly more experiments and detailed calculations perhaps taking into account light holes and the warped nature of the bands are needed to understand these phenomena.

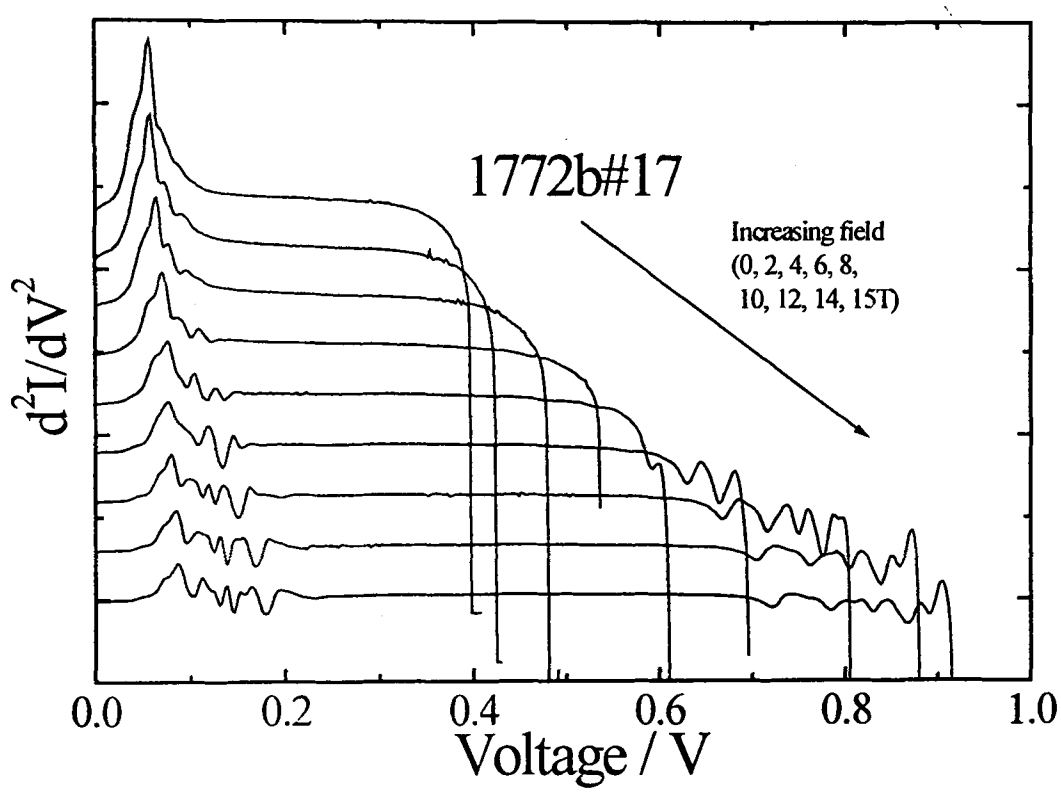


Figure 6.6. 2nd derivative measurements of 1772b#17 ('GaAs-like' sample) at 4K and 1 bar under an in-plane field revealing very weak features near zero bias and just before the onset of NDR.

6.3 The SHET in an in-Plane Magnetic Field

Again denoting the growth direction to be z, and the direction of the applied field to be in the x direction (this would be the direction out of the paper in Figure 1.8), then by following the treatment in [6], the Schrödinger equation for the electrons can again be written as:

$$\frac{1}{2m^*}\left(\frac{\hbar}{i}\nabla - eA\right)^2 \Psi = E\Psi \qquad \textbf{(6.1)}$$

However, we now use the gauge $\boldsymbol{A} = (0, -Bz, 0)$ so the magnetic field B is applied along the right axis. Again, after separating the variables and writing the wavefunction as

$$\Psi(x,y,z) = \exp\{-i(k_x x + k_y y)\}u(z) \tag{6.2}$$

One finds that the motion in the growth direction is coupled with the y-direction according to the following equation:

$$-\frac{\hbar^2}{2m^*}\frac{\partial^2 u(z)}{\partial z^2} + \frac{1}{2}m^*\left(\frac{eB}{m^*}z - \frac{\hbar k_y}{m^*}\right)^2 u(z) + V(z)u(z) = E_{zy}u(z) \tag{6.3}$$

with the motion in the x-direction being that of a free particle.

The motion of the electrons along the growth direction (z) is therefore coupled to its motion along a direction perpendicular to z according to equation (6.3). The problem to calculate the self-consistent profile $V(z)$ hence requires calculation of all occupied states in k_y space and will therefore be correspondingly more lengthy than the calculations with the field perpendicular to the interface.

6.3.1 Perturbative Method

The use of perturbation theory to describe the effect of a parallel magnetic field was first considered by Stern and Howard [1]. The perturbation is taken to be those terms in equation (6.3) which depend explicitly on the magnetic field, i.e.:

$$H' = -\hbar k_y \omega_c z + \frac{1}{2}m^*\omega_c^2 z^2 \tag{6.4}$$

where,

$$\omega_c = \frac{eB}{m^*} \tag{6.5}$$

The energy shift of the state $|k_y\rangle$ to first order is given by:

$$\Delta E_{k_y} = -\hbar k_y \omega_c \langle z\rangle + \frac{1}{2}m^*\omega_c^2\langle z^2\rangle \tag{6.6}$$

where the expectation values are computed with the envelope function at zero magnetic field. In this approximation, the energy curves remain parabolic but the energy band minimum is shifted in k_y by the amount

$$\Delta k_y^{\min} = \frac{m^* \omega_c \langle z \rangle}{\hbar} = \frac{eB}{\hbar} \langle z \rangle \tag{6.7}$$

and in energy by

$$\Delta E_{k_y}^{\min} = \frac{1}{2} m^* \omega_c^2 \left[\langle z^2 \rangle - \langle z \rangle^2 \right] = \frac{1}{2} m^* \omega_c^2 \langle \Delta z^2 \rangle \tag{6.8}$$

Owing to the greater extent of the upper subband wavefunctions, the diamagnetic energy shift increases with subband number and the energy separation between subbands always increases with the application of a parallel magnetic field. Thus, upper subbands which may be populated when $B = 0$ are progressively depopulated with increasing field strength.

Equation (6.7) has been used by Hayden *et al* [7] to probe the in-plane dispersion curves of confined holes in the valence band of a GaAs/AlGaAs/GaAs/AlGaAs/GaAs double barrier structure by studying the shift in voltage position of the resonant peaks with $B_{||}$ allowing them to reveal experimentally the light hole/heavy hole admixing.

6.3.2 Fully Self-Consistent Calculations

Solving for the electronic structure self-consistently in semiconductor systems under in-plane field has been used by Heisz *et al* [8]. His study, focusing on GaAs/Al_xGa_{1-x}As single heterojunctions highlighted the unreliability of using the perturbative method by comparing the prediction of carrier densities from both models with experimentally observed results. The same method has also been used by B Mitrovic *et al* [9] and by Zawadzki [10]. Here, the aim is to present the theory, and results of the first ever fully self-consistent electronic structure calculations for the InAs/GaSb SHET.

Any accurate quantitative method, in a nutshell, would require equation (6.3) in section 6.3 to be solved fully and simultaneously with Poisson's equation. The main

steps in the calculation consist of *i*) the numerical solution of (6.3) for a range of k_y values, *ii*) the determination of E_F, *iii*) the construction of the electron density which determines the total potential in (6.3) and finally, *iv*) iteration to convergence. The process is repeated for the GaSb side until the gradients at the interface match. These steps are discussed in more detail below.

6.3.2.1 Calculating the wavefunction

The transfer matrix method is again employed to calculate the energies and wavefunctions at k_y [11]. Again the initial conditions on the wavefunction and its gradient are that they are 0 and -1 respectively. However, the potential to be entered in the algorithm is now a summation of the self-consistent band profile potential $V_{Band\ Profile}$ and the parabolic potential $V_{Magnetic\ Field}$ due to the in-plane magnetic field:

$$V_{Total} = V_{Band\ Profile} + V_{Magnetic\ Field} = V(z) + \frac{1}{2}m^*\left(\frac{eB}{m^*}z - \frac{\hbar k_y}{m^*}\right)^2 = V(z) + \frac{1}{2}m^*\omega_c^2(z - z_0)^2 \quad \textbf{(6.9)}$$

where $\omega_c = eB/m^*$, $z_0 = \hbar k_y / eB$ and at $z = 0$, the electron and holes are assumed to see an infinite barrier. The eigenvalue solutions for the first subband are labelled E_{0zy}, for the 2nd subband E_{1zy}.

6.3.2.2 Calculating the Fermi energy

After calculating the solution to (6.3) for a range of closely spaced k_y values, and assuming that in the x-direction the dispersion is parabolic, the Fermi energy is calculated. For a 2D system, the population of a given subband is proportional to the area of populated states in $k_{||}$ space. As the $k_{||}$ dispersions are now known, the problem reduces to calculating an energy such that the area in $k_{||}$ space, A_{total}, at that energy gives the correct electron concentration which assuming spin degeneracy is given by:

$$n = \frac{A_{Total}}{2\pi^2} \quad \textbf{(6.10)}$$

The values of k_y used ranged from -0.095Å^{-1} to 0.15Å^{-1} (-0.05 to 0.08 bohr^{-1}) with a mesh spacing of 0.001Å^{-1}. After calculating all the confinement energies for this

range of k_y space a trial Fermi energy is selected. The confinement energies are compared with the Fermi energy and if they are below, are retained. For these resulting energies, the free particle wavevector k_x is calculated and the incremental ΔA_k area at these k_x and k_y points occupied by the electrons is calculated:

$$\Delta A_k = k_x \Delta k_y \tag{6.11}$$

where

$$k_x^2 = \frac{2m^*\left(E_F - E_{zv}\left(k_y\right)\right)}{\hbar^2} \tag{6.12}$$

The summation of these areas $A_{Total} = \sum_{k_x} \Delta A_k$.

If the electron concentration calculated from equation (6.10) is less than the electron concentration in the heterostructure (an input constant), the Fermi energy is increased and the process is repeated. Similarly, if the calculated concentration is greater, the Fermi energy is decreased. This process is repeated until the calculated electron concentration equals the number of electrons in the heterostructure.

6.3.2.3 Solving the Poisson Equation

The method to solve the Poisson Equation is identical to that shown in section 5.5.1.3 except now the number of electrons at various k points is modulated by the number of electrons at that k point itself.

For each (k_x, k_y) point, with the number of electrons at that point is:

$$\Delta n_{k_y} = \frac{\Delta A_k}{2\pi^2} = \frac{k_x \Delta k_y}{2\pi^2} \tag{6.13}$$

The Poisson equation is:

$$\frac{d^2\Phi}{dz^2} = \begin{cases} \dfrac{e}{\varepsilon_r^{InAs}\varepsilon_0} \displaystyle\sum_{k_y}^{E<E_F} \Delta n_{k_y} \left|u_{k_y}^e\right|^2 & z < 0 \\ -\dfrac{e}{\varepsilon_r^{GaSb}\varepsilon_0} \displaystyle\sum_{k_y}^{E>H_F} \Delta p_{k_y} \left|u_{k_y}^p\right|^2 & z \geq 0 \end{cases} \tag{6.14}$$

Such that,

$$V(z)=\begin{cases}-e\Phi(z) & z<0\\ \Delta-e\Phi(z) & z\geq 0\end{cases} \tag{6.15}$$

and the solution under the boundary conditions,

$$\left.\frac{d\Phi}{dz}\right|_{z=0}=\begin{cases}\dfrac{en}{\varepsilon_r\varepsilon_0}\\ \dfrac{ep}{\varepsilon_r\varepsilon_0}\end{cases}\quad\text{and}\quad\Phi(0)=\begin{cases}0 & z<0\\ \\ \Delta & z\geq 0\end{cases} \tag{6.16}$$

is,

$$V(z)=\begin{cases}-\dfrac{e^2}{\varepsilon_r^{InAs}\varepsilon_0}\displaystyle\sum_{\Delta n_{k_y}}\left[z+\int_0^z(z-z')\left|u^e_{k_y}(z')\right|^2dz'\right]\Delta n_{k_y} & z<0\\ \Delta-\dfrac{e^2}{\varepsilon_r^{GaSb}\varepsilon_0}\displaystyle\sum_{\Delta p_{k_y}}\left[z-\int_0^z(z-z')\left|u^p_{k_y}(z')\right|^2dz'\right]\Delta p_{k_y} & z\geq 0\end{cases} \tag{6.17}$$

6.3.2.4 Background Doping

Background doping has been discussed in 5.5.1.4. As with the case without field, the background charge in GaSb is positive for a distance z_A as in this region, the donors are ionised and acceptors neutral. Similarly, the background charge in InAs is negative for in the depletion region (length z_D), acceptors remain ionised, but donors are neutral. Poisson's equation is therefore accordingly modified,

$$\frac{d^2\Phi}{dz^2}=\begin{cases}\dfrac{e}{\varepsilon_r^{InAs}\varepsilon_0}\displaystyle\sum_{k_y}^{E<E_F}\Delta n_{k_y}\left|u^e_{k_y}\right|^2+\dfrac{eN_A^{InAs}}{\varepsilon_r\varepsilon_0} & z<0\\ -\dfrac{e}{\varepsilon_r^{GaSb}\varepsilon_0}\displaystyle\sum_{k_y}^{E>H_F}\Delta p_{k_y}\left|u^p_{k_y}\right|^2-\dfrac{eN_A^{InAs}}{\varepsilon_r\varepsilon_0} & z\geq 0\end{cases} \tag{6.18}$$

where N_A^{InAs} is the compensated acceptor concentration, and N_D^{GaSb} is the compensated donor concentration. It is known the MOVPE-grown InAs is *n*-type with $n^{bulk}\sim 4\times10^{16}$ cm^{-3}, and GaSb is *p*-type with $p^{bulk}\sim 10^{16}$ cm^{-3}. Their compensated minority charge, however, is not known and for the purposes of the calculation, N_A^{InAs} and N_D^{GaSb} were both were taken to be equal to 10^{15} cm^{-3}. A detailed analysis at $B = 0$ of the effect of changing these values was undertaken in [12] with N_A^{InAs} and N_D^{GaSb}

varying between 10^{15} and 4×10^{15} at various pressures. The conclusions proved that the resulting change in calculated confinement energies was small, and could be quoted with a maximum error of ±2 meV.

Again, the presence of an in-plane magnetic field will cause Landau levels in the bulk material to form. Taking into account the pinning of the electron Fermi energy to the donor ionisation energy and that of the hole Fermi energy to the acceptor ionisation energy again,

i) The quasi electron Fermi energy will be pinned (2meV – $\frac{1}{2}\hbar\omega_c^{Electrons}$) below the $B = 0$ conduction band edge far away from the interface in InAs.

ii) The quasi hole Fermi energy will be pinned (34meV – $\frac{1}{2}\hbar\omega_c^{Holes}$) above the $B = 0$ valence band edge far away from the interface in GaSb.

where $\omega_c^{Holes} = \frac{eB}{m_{Holes}}$ and $\omega_c^{Electrons} = \frac{eB}{m_{Electrons}}$.

6.3.3 Results

6.3.3.1 Potential Profiles and Wavefunctions

Figure 6.7a below shows the first confined wavefunctions at the InAs side of the interface at zero bias and 40T. At this high magnetic field, $V_{Magnetic\ Field} >> V_{Band\ Profile}$ so that the electrons are confined to a very near parabolic potential with minimum varying along the z-axis for $z < 0$ and a barrier at $z = 0$. From equation (6.9), the minimum of the potential is farther from the interface for increasing k_y so that a confined electron will have a greater probability of being found close to the interface at low k_y values than at higher k_y values. Figure 6.7b also shows the solution for the GaSb side at this bias. Unsurprisingly, the results are qualitatively not too dissimilar to the results for the InAs side of the interface. Again, the wavefunction is calculated to be have a maximum near the interface, but is found to broaden with increasing $|k_y|$ as the minimum of the confining potential shifts farther out along the z-axis away from the interface. Figure 6.8 shows the final resulting self-consistent band profile potential.

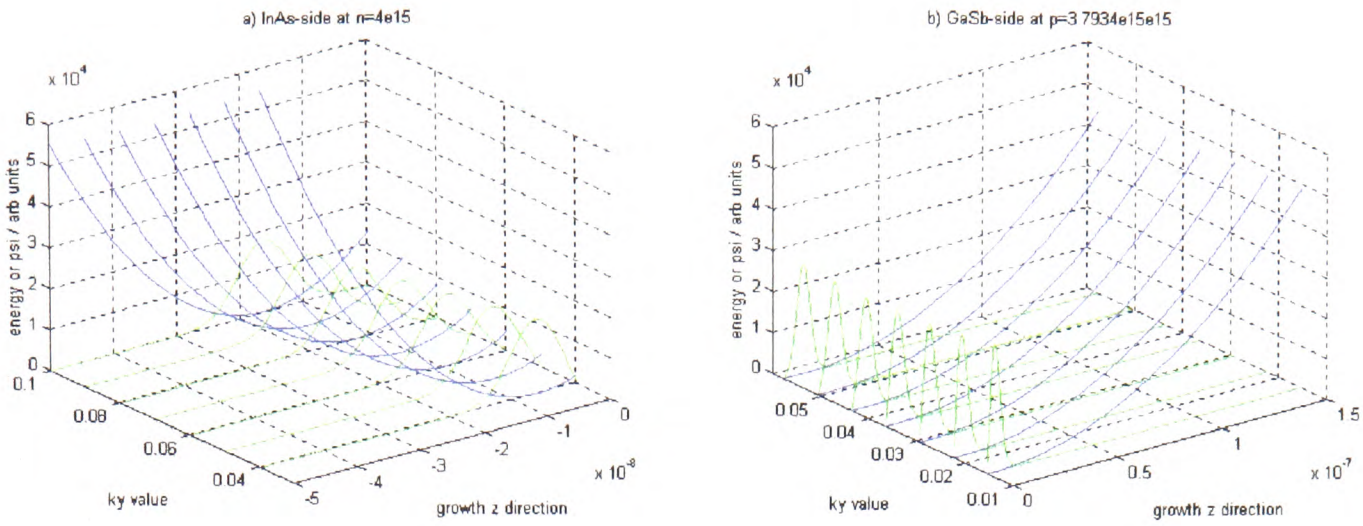


Figure 6.7. Results showing the wavefunctions (solutions to (6.3)), coloured green and total potential profiles (self-consistent band-profile plus the magnetic term, equation (6.9)) coloured blue on either side of the interface as a function of k_y for an 'InSb-like' interface sample under an in-plane field of 40T at a bias of 34.4mV. Note the different range of k_y values used on the axis for side of the interface type reflecting the different values of the Fermi wavevectors for the electrons and holes.

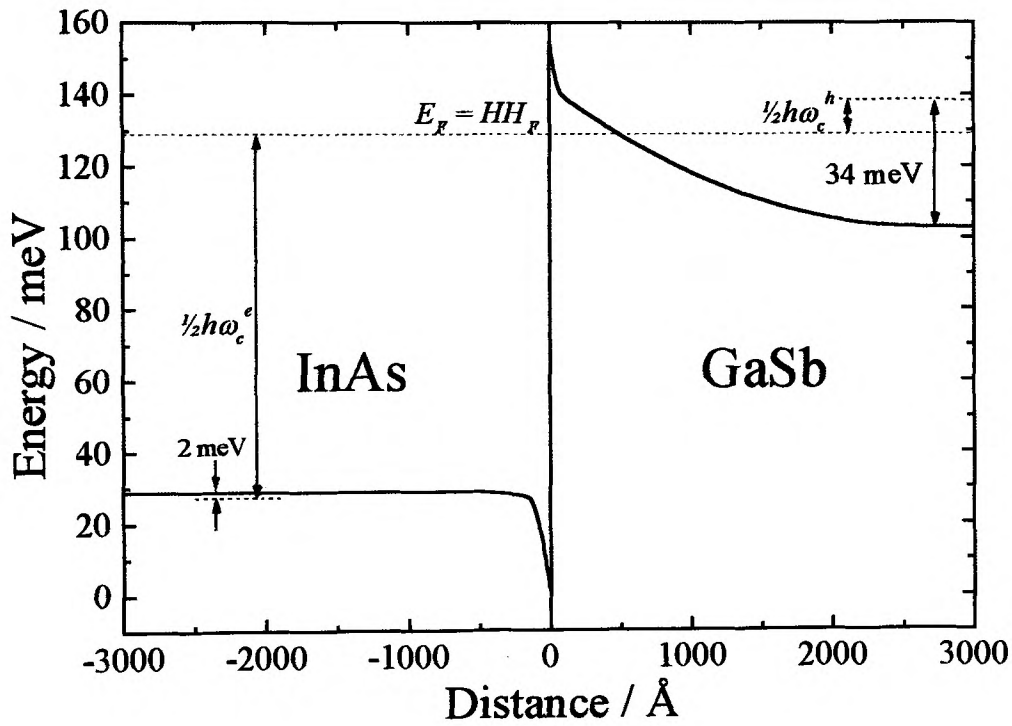


Figure 6.8. Self-consistent solution for the band profile at zero bias under an in-plane field of 40T for an 'InSb-like' interface. $n = 2.1$ and $p = 1.9$ ($\times 10^{11}$ cm^{-2}).

Figure 6.9 and Figure 6.10 show the wavefunctions along with the total potential as a function of k_y (equation (6.9)) and the final self-consistent band profile at 5T and zero bias respectively. At these lower magnetic fields, the magnetic field contribution to the total potential V_{Total} experienced by the carriers in equation (6.9) is a lot less than in the case with $B = 40$T presented earlier. V_{Total} is then highly non-parabolic, but the wavefunctions are still of course broadened with increasing $|k_y|$.

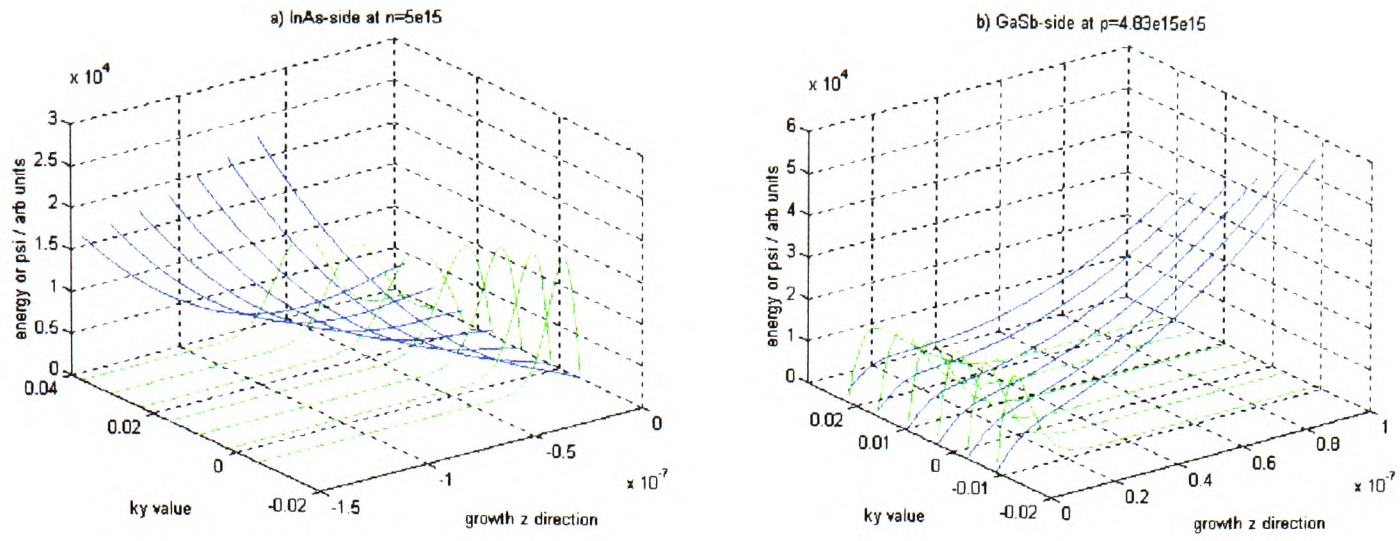


Figure 6.9. Schematic showing the wavefunctions (solutions to (6.3)) and total potential profiles (self-consistent band-profile plus the magnetic term, equation (6.9)) on either side of the interface as a function of k_y for an 'InSb-like' interface under an in-plane field of 5T at zero bias. Notice that as the field is now small, the distortion of the potential from near parabola by the self-consistent band profile is easily visible.

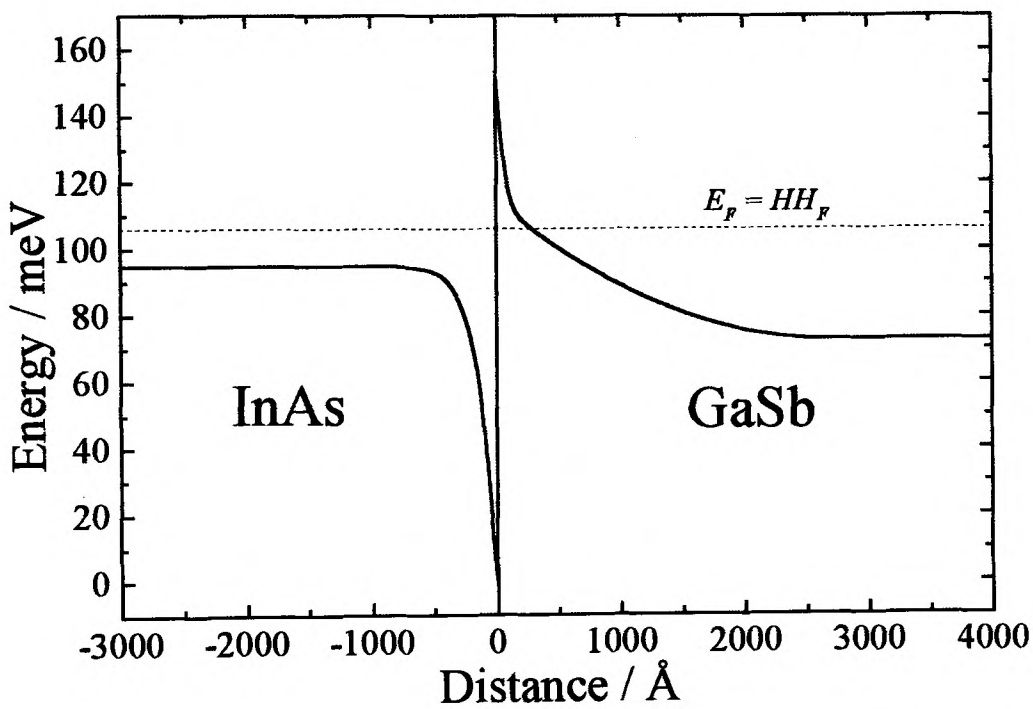


Figure 6.10. Self-consistent solution for the band profile at zero bias at 5T for an 'InSb-like' interface. $n = 4.2$ and $p = 4.0$ ($\times 10^{11}$cm^{-2}).

6.3.3.2 Dispersion Curves

Consider the InAs E_{0zy} electron dispersion curve shown in Figure 6.11 at, for example, 40T. For high k_y the total potential will be a sum of the InAs band profile edge and a parabolic potential with minimum far away from the interface and coinciding with the very flat part of the InAs band profile. At $z = 0$, the parabolic potential will be much greater than the InAs self-consistent band profile near the interface. So to a good approximation, the electron will be subject to a parabolic-type potential. Increasing k_y at this point and thereby moving the parabolic potential further from the interface

will therefore hardly affect the energy of the confined state for the electron will be subject to the same potential but just shifted in space. (However, the position of maximum electron probability will change as the minimum of the potential varies along z). Thus at high fields and large $|k_y|$ values, the wavefunctions become localised in the remote magnetic well rather than the potential well at the interface. As a result, the subband energies in this region will tend to the constant values given by the oscillator energy $(n+\frac{1}{2})\hbar\omega_c$ (Figure 6.11). At lower k_y values however, the parabolic potential would have a minimum at $z < 0$. Lowering k_y will shift this pseudo-minimum increasingly to negative z thereby increasing the value of the potential at $z = 0$. Thus one would expect the confined energy E_{0zy} to increase as k_y is lowered. A similar argument applies to the qualitative understanding of the dispersion curves for the holes except the sign of z and k_y are the opposite. At lower fields, the parabolic potential contribution to the total potential at a particular k_y point is much less than at 5T. The consequence of this is that one needs to go very far in k_y space in order to see the flattening of the dispersion curves.

Note also that increasing in-plane field shifts the dispersion curves relative to each other in k space, reducing their overlap. At high fields, they are completely separated leading one to expect the SHET to exhibit semimetallic character with an indirect band overlap. Conduction is still however observed at these fields, suggesting the operation of inelastic processes.

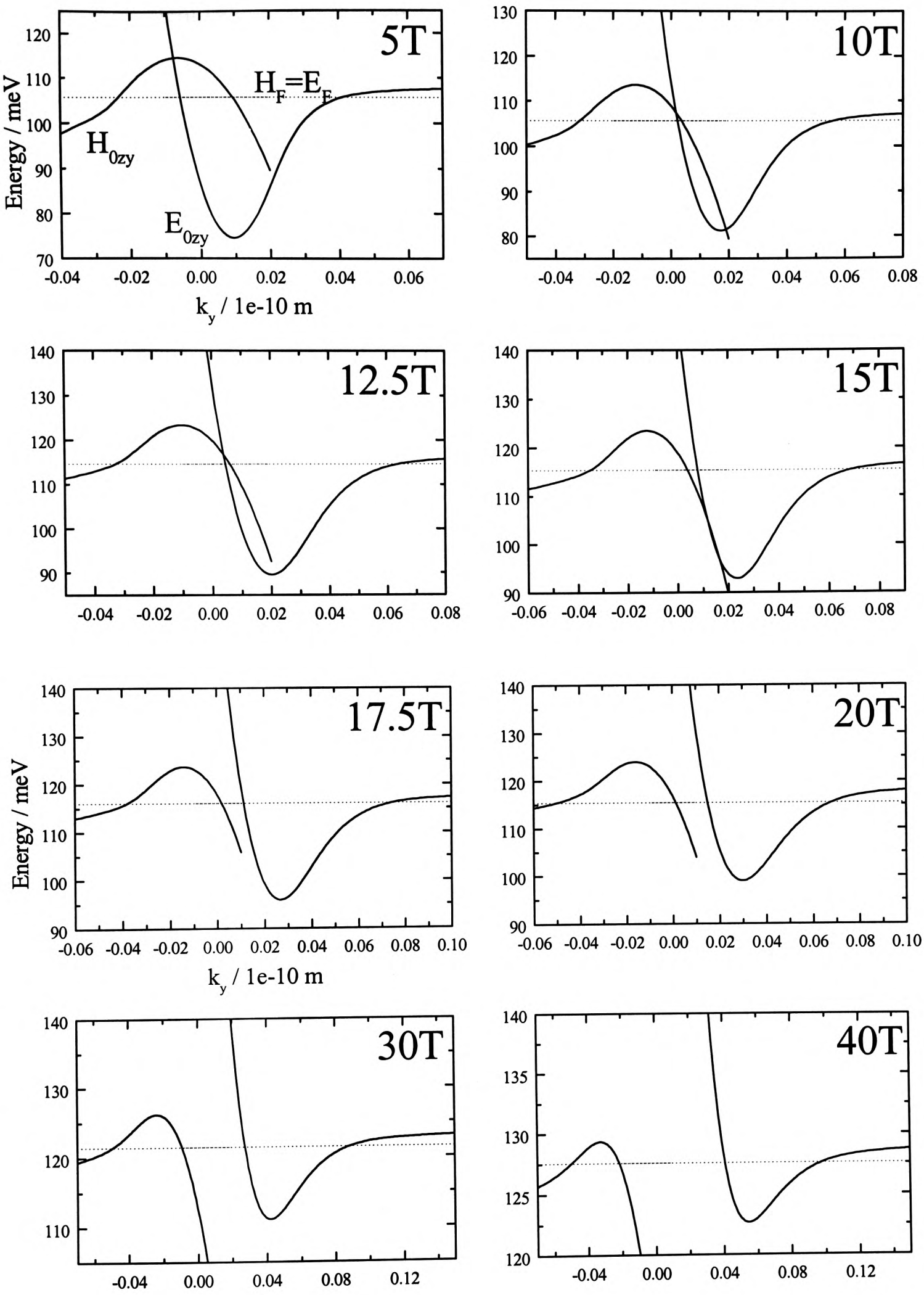


Figure 6.11. Calculated results showing the dispersion curves at zero bias for each field and the increasing separation between electron and hole dispersion curves with increasing in-plane field. At large k_y the dispersion diverges away from the parabolic shape one would expect from an application of a simple Stern Howard perturbative method.

The self-consistent calculation is carried out for a particular concentration of electrons in the InAs. It is repeated for a hole concentration (in GaSb) until the gradients of the band profiles on either side of the interface are equal. Continuing this way, one can produce a plot of the Fermi energies and of the minimum of the electron dispersion curves and the maximum of the hole dispersion curves against bias. Figure 6.12 shows the results for a sample with an InSb-type interface at 5 and 40T:

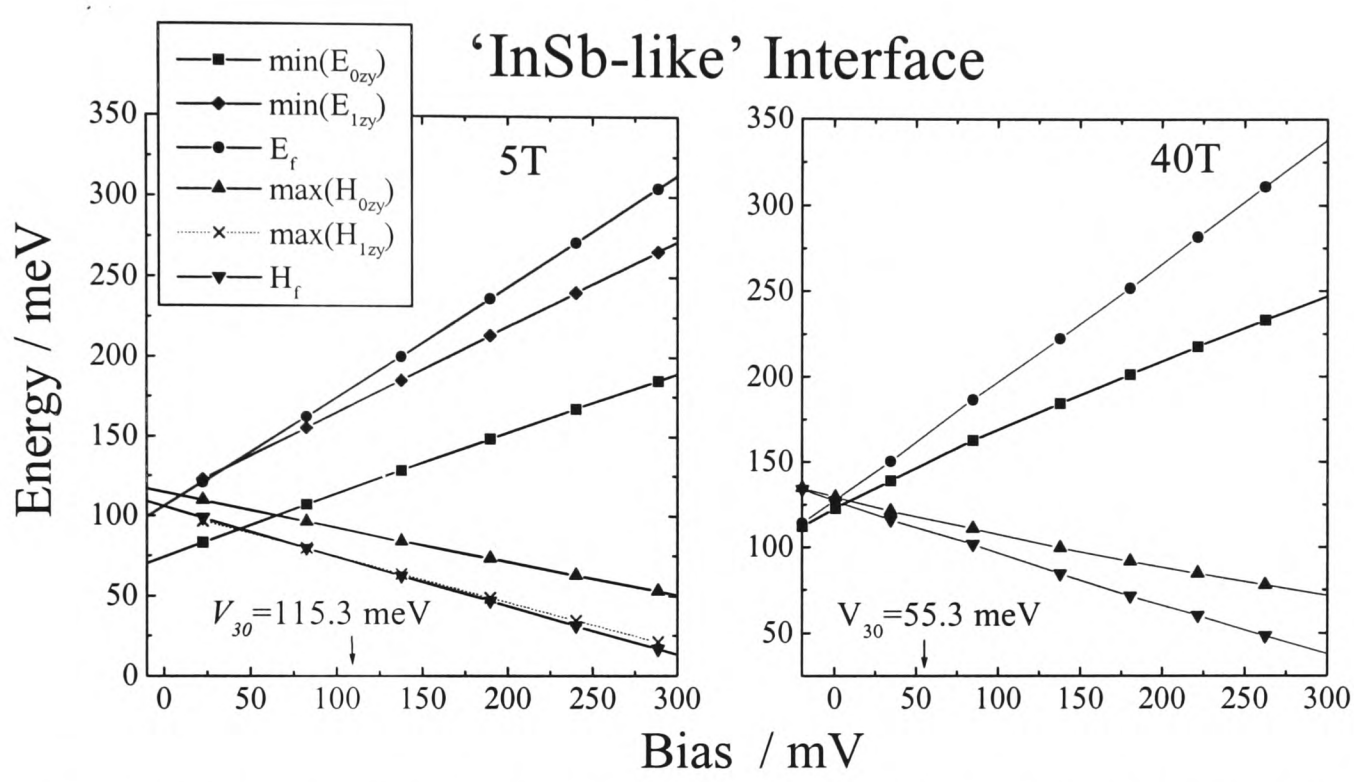


Figure 6.12. Results showing the calculated positions of the minimum of the electron and maximum of the hole dispersions against bias at 5 and 40T. Indicated is the voltage V_{30} at which min(E_{0zy}) and max(H_{0zy}) are separated by 30 meV.

Notice the calculations show that only one subband of each type was found to be occupied at zero bias. As pointed out earlier, this result is because the diamagnetic energy shift (equation (6.6)) increases with subband number as a 2nd confined wavefunction has greater spatial extent than a 1st confined state. Consequently, the energy separation between subbands always will increase with increasing in-plane field causing higher states, which were populated at $B = 0$, to become progressively depopulated.

6.4 Comparison with Experiment

It is interesting to note that no additional features are observed in the IV under in-plane field (see Figure 6.1 through to Figure 6.5) as the electron and hole dispersions

completely separate at just over 12.5T. A similar observation was initially made by Khan-Cheema [12]. There the analysis of the SHET under zero field showed, surprisingly, no features in the IV as individual electron subbands crossed the hole subbands. The lack of features associated with electron subbands crossing hole subbands in energy and k_y space is strong evidence for the presence of inelastic processes occurring in the system. At this point, I would like to digress and discuss the results of the perpendicular field calculations and measurements. The evidence for inelastic processes would also support the claim that features in the IV trace would not result when an electron Landau level crosses a hole Landau level with the field applied perpendicular to the interface. Thus, despite there being complicated Landau level versus bias relations (Figure 5.47 and Figure 5.48), particularly at low fields, one would not expect each point at which the Landau levels cross to result in a mini-NDR. Instead, only one NDR, the main NDR, would be expected as the inelastic processes smear the effects of individual Landau level crossings. Consequently, as borne out by experiment, the NDR with perpendicular field would not be too dissimilar to the NDR without field. This further lends evidence to the postulate that the 2nd resonance observed under magnetic field applied perpendicular to the interface (5.2 onwards) is not in fact due to the electron and hole Landau levels crossing, but rather due to the drastic variation in band profile at high biases.

The presence of at least two particle types in the GaSb (heavy and light holes) causes a transverse magnetoresistance [13], however, and this needs to be taken into account when comparing experimentally obtained peak and valley voltages for $B_{||}$ with any theoretical results. A good indication of this can be found from high reverse bias measurements of the SHET. At such a large bias, many electron and hole states will overlap in energy, and the interface will hardly contribute to the magnetoresistance. Figure 6.13 below shows the results of an 'InSb-like' interface sample, showing the variation of the reverse bias resistance with in-plane field.

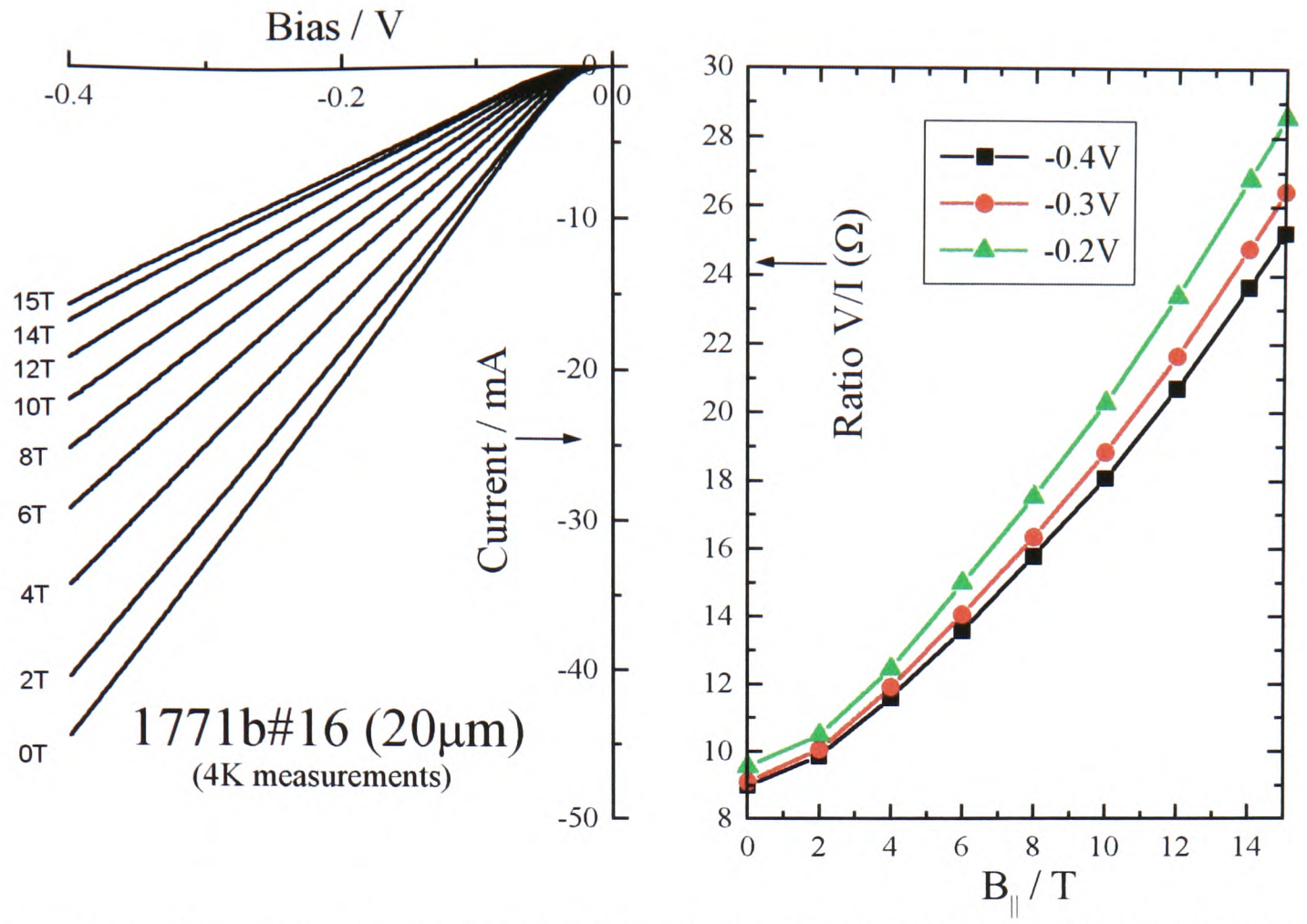


Figure 6.13. Reverse bias IV traces as a function of field. At a fixed bias, the ratio *V/I* gives a good indication of the field dependent magnetoresistance in the sample.

Figure 6.14 displays the bias V_p at which the minimum of the electron dispersion curve ($\min(E_{0zy})$) crosses the maximum of the hole dispersion curve ($\max(H_{0zy})$) as a function of in-plane field. Also shown on this plot is V_{30}, the bias position at which $\min(E_{0zy})$ and $\max(H_{0zy})$ are separated by 30 meV (the approximate equivalent of an InAs longitudinal optical phonon energy). These can be compared with the position of the observed peak and valley voltages. However, following the treatment given earlier in 4.4.1, the true position of the peak and valley voltages is obtained by subtracting the voltage drop across the series parasitic (magneto)resistance $R(B_{||})$ from the total voltage across the device. This resistance is given in Figure 6.13 above. If V_p is the observed peak voltage, the true position of the peak voltage across the interface V_t is then given by

$$V_t = V_p - I_p R(B_{||}) \tag{6.19}$$

and similarly for the valley. These values are also plotted Figure 6.14 for a more accurate comparison between V_{30} and the true position of the NDR across an 'ideal' device.

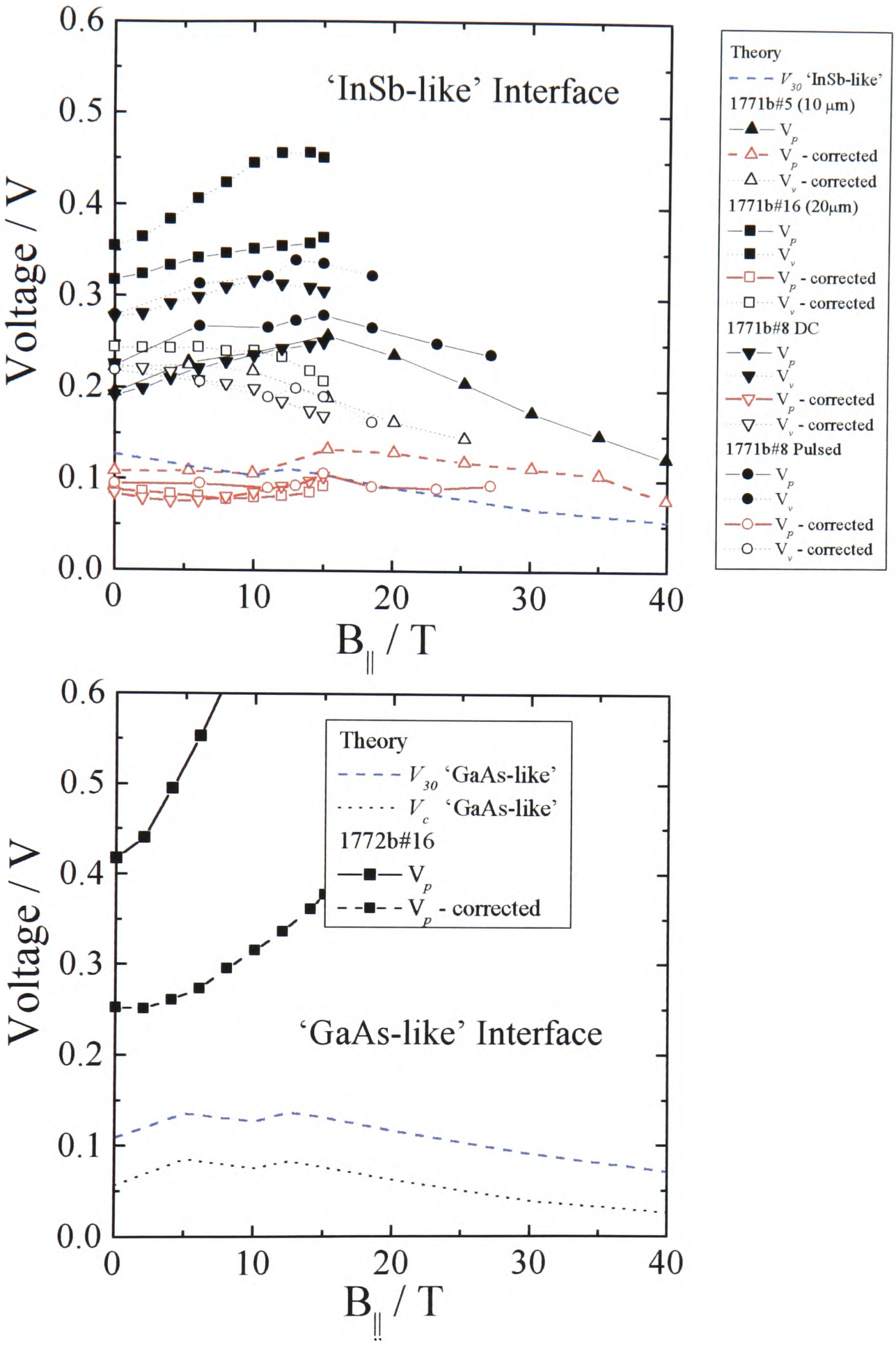


Figure 6.14. Comparison of the measured peak voltages at 4K (uncorrected and corrected for increasing transverse magnetoresistance) and V_{30} (also V_c for 'GaAs-like' interface samples) , the self-consistently calculated position of the NDR bias. Notice good agreement between theory and experiment for samples with an 'InSb-like' interface, while for the 'GaAs-like' samples, there is striking disparity. Note that for the pulsed data, by the time the high fixed reverse bias is reached, the peak of the field would have been passed. There is therefore a slight error in the calculated magnetoresistance at high pulsed fields.

The results show the peak voltage of 'InSb-like' interface samples, corrected for increased magnetoresistance, follows V_{30} very well. Notice also that not only does V_{30} predict the general trend of a falling V_p with increasing $B_{||}$, but that its sudden jump at 10T is also as observed. This provides confirmation of the results of chapter 4 where it was shown through **k.p** self-consistent calculations that the peak of the NDR, V_p, at 4K as a function of pressure is equal to V_{30} (the bias position when E_0 has passed HH_0 by a phonon energy). Khan-Cheema [12], using the results of his decoupled model and data collected at 77K instead of the 4K data that I use here, concluded that it is in fact V_v that follows V_{30}, i.e. that the valley may be due to phonon emission (he also showed that V_c lies between V_p and V_v). As the results of his decoupled model agree very well with my **k.p** results, the origin of our different conclusions is simply as a result of our measurements being taken at different temperatures. With evidence of phonons in both sample types presented in 4.5.2 and in this chapter, Khan-Cheema's conclusion that the 'InSb-like' response is consistent with the NDR mechanism described in chapter 1 but with NDR occurring a number of phonon energies after V_c still holds. Our combined results provide strong experimental and theoretical evidence of a phonon component in the conduction process in such sample types.

The 'GaAs-interface' samples' peak voltage, again corrected for increased magnetoresistance, bears no resemblance to the expected trend. The peak and valley voltages increase with field, whereas V_{30} falls with field. It is again evident that the 'InSb-like' sample has NDR that can be explained by an overlap in energy and momentum space of the back to back electron and hole gases confined on either side of the interface, with possibly the aid of a phonon. No such explanation of the NDR can be attributed to the 'GaAs-like' interface samples unless multiple phonons are involved. In short therefore, in-plane magnetic field experiments and self-consistent calculations have again shown that the 'GaAs-like' interface sample supports a different conduction mechanism to that exhibited by the more predictable 'InSb-like' one, at least in the number of phonons involved in the conduction process.

6.5 Angle-Resolved Magnetotunnelling

In section 6.3.1 it was shown that when a magnetic field is applied parallel to the interface, the carriers acquire an additional contribution to the momentum allowing tunnelling to occur through to final states with in-plane momenta larger than k_F. The dispersions will separate in k space gaining an in-plane wavevector perpendicular to the field, which by perturbation theory is:

$$\Delta k_y^{\min} = \frac{eB}{\hbar}\langle z \rangle \qquad \textbf{(6.20)}$$

This law of conservation of canonical momentum allows the possibility of using resonant magnetotunnelling as a probe in the in-plane dispersion relation of the valence band and specifically that of the heavy hole band. This has been used by Hayden *et al* [7] to reveal the highly non-parabolic nature of the valence band in GaAs/AlAs double barrier resonant tunnelling structures, but the added dimension of orientation of the field in the plane allows the possibility of the *band warping* itself to be measured (see also [14]). The electron Fermi surface is known to be (very nearly) spherical but the valence constant energy surfaces have the approximate anisotropic form [15, 16],

$$E(k) = Ak^2 \pm \left[B^2k^4 + C(k_x^2k_y^2 + k_y^2k_z^2 + k_z^2k_x^2)\right]^{1/2} \qquad \textbf{(6.21)}$$

and are distorted cubes, as indicated in Figure 6.15. By rotating the field in the plane of the interfaces, it is possible to investigate any anisotropy between different crystal directions in this plane. This angle-resolved magnetotunnelling, the first ever to be applied to the InAs/GaSb SHET, does not average over all k space, but directly probes states with specific k values.

The direction of the shift in k space will be dependent on the orientation of the in-plane magnetic field. As the electron Fermi surface is spherical and the hole Fermi surface roughly square, one should be able to observe differences in the NDR depending on the direction these Fermi surfaces separate with increasing field. Figure 6.16 and Figure 6.17 show the results of such an experiment taken by rotating the sample in the cryostat at a fixed magnetic field. These results show that the bias

position of the resonance for the 'InSb-like' device is not only a function of the size of the magnetic field but also of its angle in the plane parallel to the interface, because the peak bias is larger when the field is parallel to [110] than when it is parallel to [100]. They thus represent to my knowledge the first conclusive proof for the variation of the 'InSb-like' SHET NDR peak with field orientation.

Such a method was also used by Gennser *et al* [17] to investigate the band anisotropy of the valence band of $Si/Si_{1-x}Ge_x$ quantum wells. Their conductance measurements allowed the anisotropy of the heavy hole and light hole bands to be measured and revealed the expected 45^0 phase difference in warping of the two bands. Here, as the primary conduction mechanism causing NDR is between electron and heavy holes, the observed results reflect the anisotropy in the heavy hole band only.

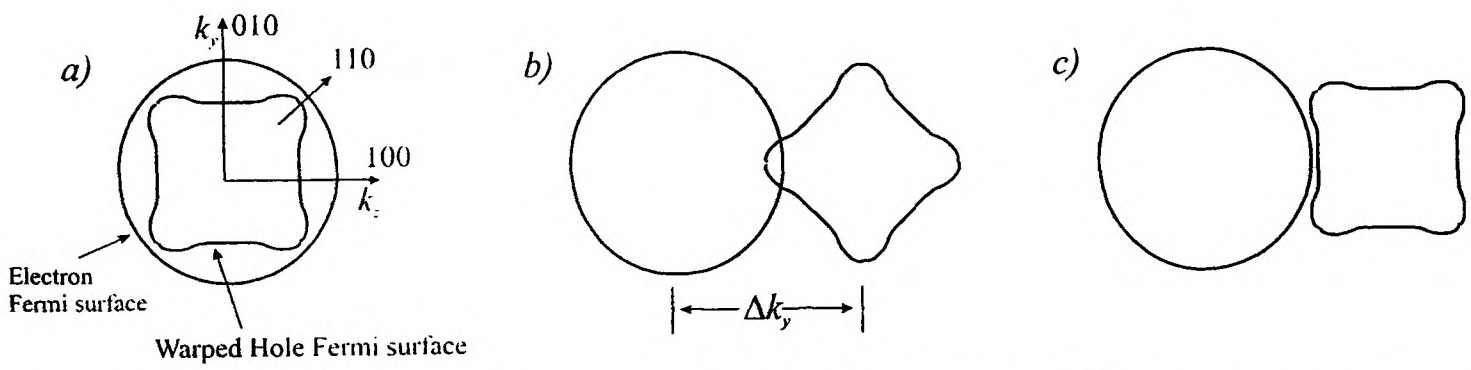


Figure 6.15. Figure (*a*) showing the directions in which the electron and hole Fermi energies move under the application of an in-plane field in a particular orientation. Note however, the size and directionality of the warping effect in the valence band depends on the band mixing and hence on any strain in the structure. Thus. it is difficult to predict the actual translational direction of the constant energy surfaces with field and hence difficult to predict the relative position of the peaks and valleys in the IV traces. Figures *b* and *c* show the positions of the Fermi surfaces under an in-plane field applied in two orientations, 100 and 110 respectively.

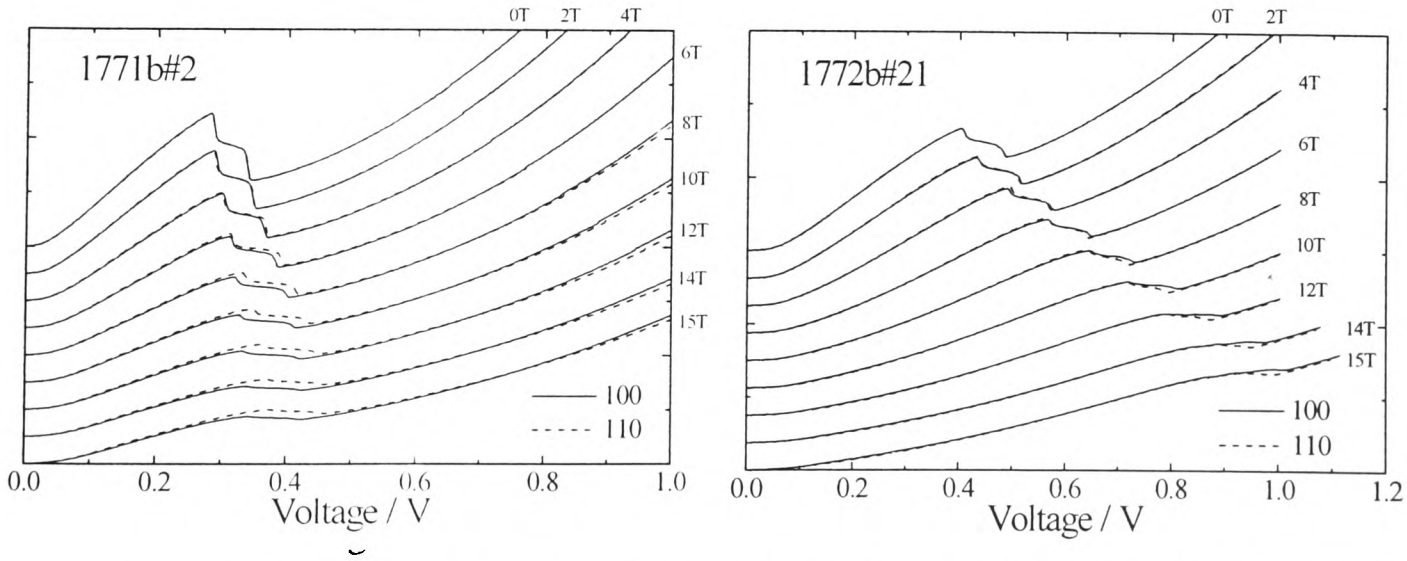


Figure 6.16. An 'InSb-like' (1771b#2) interface at various in-plane fields show the IV traces taken with a rotating insert. Notice the difference between the IV when the field is directed along the 100 and 110 axis increases with field. Similar results are shown in the figure on the left for a 'GaAs-like' sample (1772b#21).

Figure 6.17 shows the shift of the peak bias position as a function of the in-plane field angle where 0° corresponds to the [110] direction. The shift appears as a clover leaf (4 fold symmetry) except that it is elongated in one of the [110] directions. Figure 6.15 shows that we would expect such a four fold symmetry with field angle for tunnelling between electrons and heavy holes reflecting, of course, the underlying four fold symmetry of the hole Fermi surface itself. Even if phonons are involved in the tunnelling, the square shape of the hole Fermi surface will ensure that different phonon wavevectors are involved when the hole Fermi surface is displaced by the field along [110] than when it is displaced along [100]. A similar argument can be made for tunnelling between electrons- and light-holes because again the light hole Fermi surface has a square symmetry.

The most unusual aspect of Figure 6.17 is the elongation along one of the [110] directions. The reason is not clear but may perhaps be due to interface induced mixing between heavy and light holes [18]. In this case, the underlying mechanism is mixing between the p_x and p_y orbitals of the Bloch states which splits their degeneracy, even at the BZ zone centre, and creates new states with Bloch orbital symmetry along the two [110] directions. Such mixing is a consequence of the reduced symmetry due to the presence of a heterointerface between two zinc-blende type materials and can be shown to operate in the Γ_8 subspace (heavy and light holes) only. It may be considerably enhanced in the InAs/GaSb system compared with the GaAs/AlAs system considered in ref. [18] due to the special nature of the InSb-like or GaAs-like interfaces, though as it is dependent on the envelope function overlap at the interface, it is expected to be small. However, it has recently been shown to be responsible for an *optical* anisotropy in heterostructures with no common anion or cation. That may be analogous to the electrical anisotropy observed here [19].

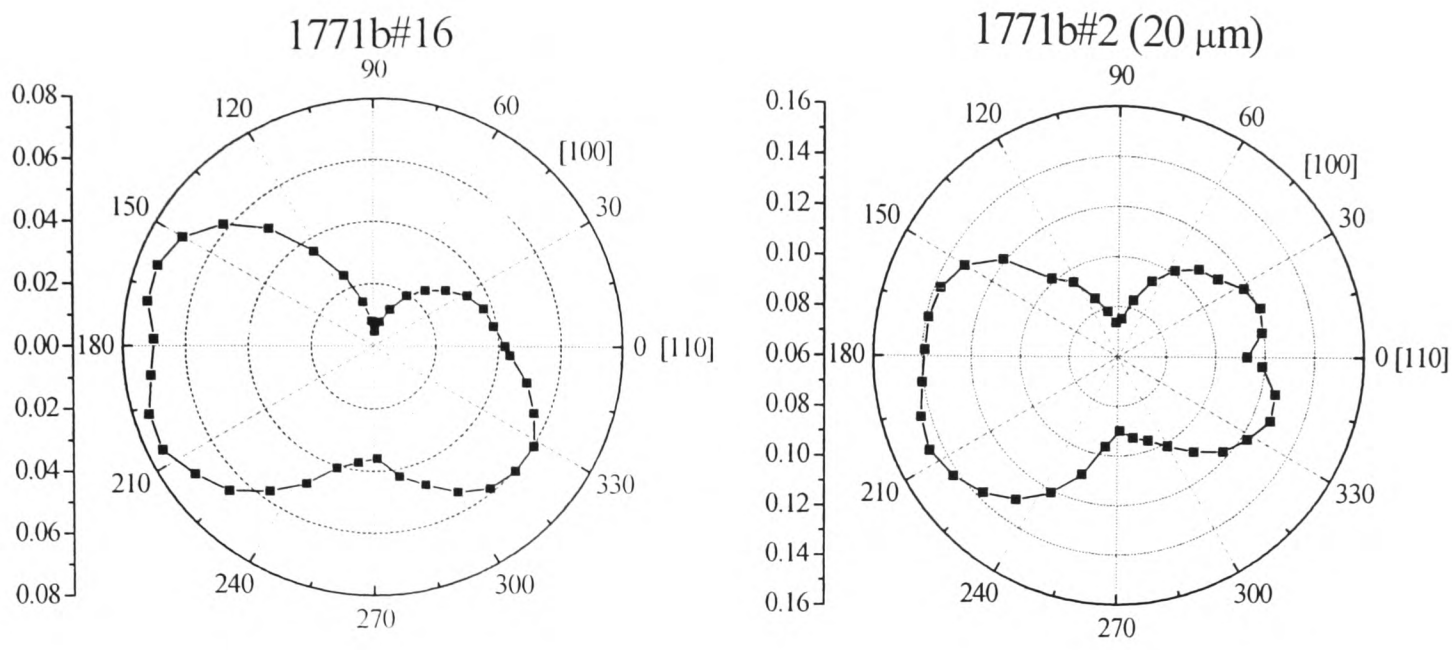


Figure 6.17. Results of the difference between the peak voltage under an in-plane field of 15T and the peak voltage at 0T versus orientation of an 'InSb-like' sample in the magnetic field. The radial coordinate is the difference between the peak voltages at 0 and 15T. The second figure shows the results for a second 'InSb-like' sample at 10T.

Similar experiments were carried out on the 1772 'GaAs-like' interface type samples revealing yet more remarkable differences between the responses of the two interface types. Figure 6.18 and Figure 6.19 show these results. The first thing to be noticed is the remarkable result that NDR actually disappears at some orientations. The sharp shape of NDR is only present at some orientations while at others three mini-NDR features are present (e.g. see the trace highlighted in blue corresponding to 290.625^0 in Figure 6.19). This is again in stark contrast to the results of the 'InSb-like' interface where only the position of NDR varied with orientation, and no variation in its sharp shape was observed. Note that Khan-Cheema [12] observed what he described as a secondary feature in the NDR of 'GaAs-like' interface samples under in-plane field just before the onset of NDR. The work here suggests that this secondary feature was simply the result of having the sample at a random orientation in the cryostat. It is also equally possible that the 2^{nd} derivative results presented in section at the end of section 6.2.2 may have the same origin as the angular dependent NDR features observed here. Again, the sample was at a random orientation in the pressure cell submerged in the cryostat. This further leads to the speculation that the features observed there near zero bias may be closely related to the features observed just before the onset of NDR. However, the angular variation of those 2^{nd} derivative measurements can only be measured by similar rotation experiments involving small experimental cells capable of fitting inside a magnet cryostat. The technology for

such a formidable experimental challenge has only just been realised. Im [20] has recently undertaken a high pressure study on GaAs/AlAs double barrier heterostructures capable of being rotated in an in-plane magnetic field through the use of a novel type of small spherical pressure cell [21]. Though this research is in its infancy, the simultaneous use of high pressure and rotating in-plane field promises to lead to an understanding of fundamental quantum phenomena. Similar experiments need to be carried on the InAs/GaSb SHET to determine whether the 2nd derivative results of section 6.2.2, and the features shown here induced by varying the in-plane field orientation are of the same origin. This in turn may also determine the underlying reasons why they only occur in 'GaAs-like' interface sample types.

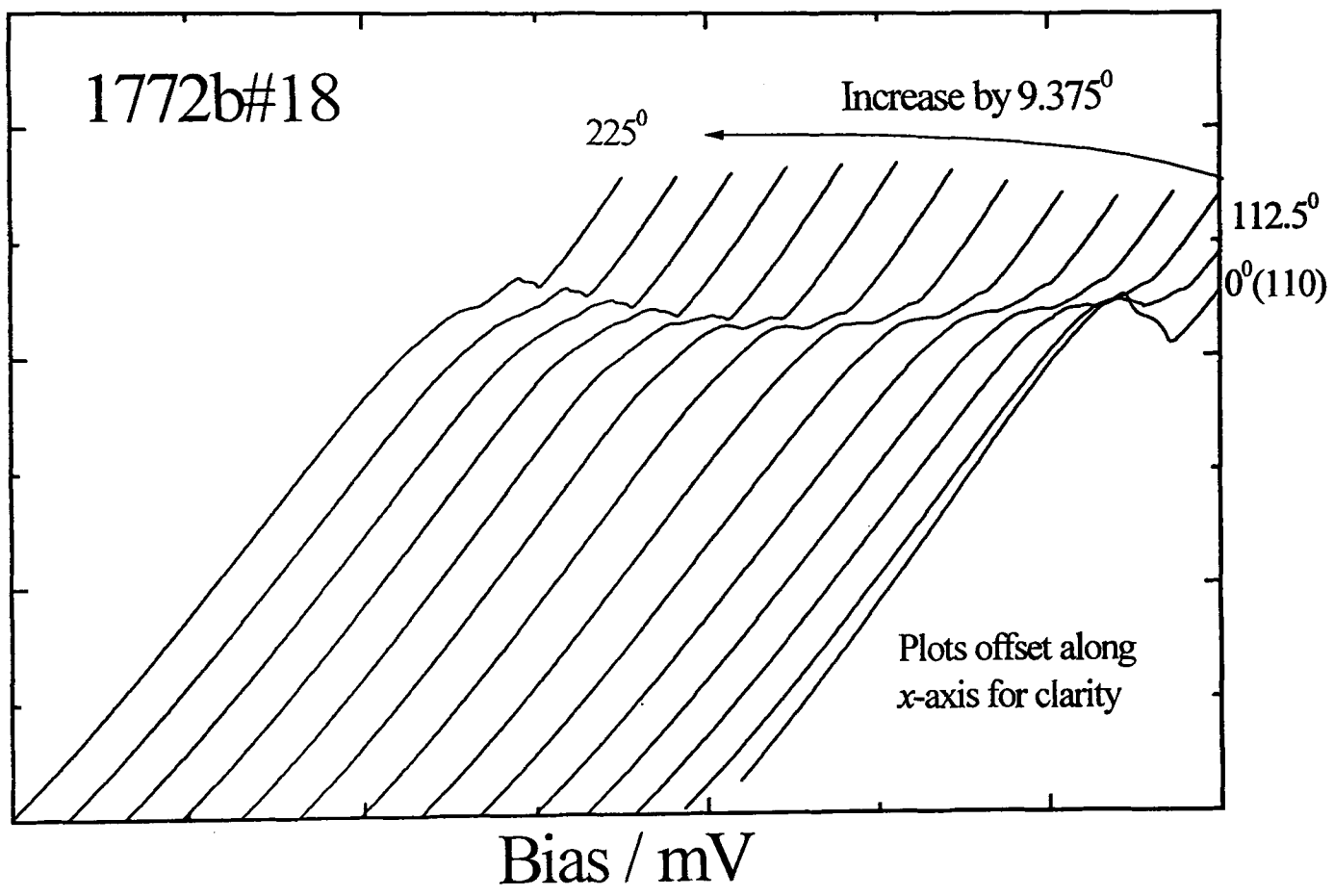


Figure 6.18. Angular variation of the IV trace for a sample with a 'GaAs-like' interface 1772b#18 under a constant in-plane Field of 15T. The sample was rotated by 9.3750° before each trace was taken, with the initial trace taken with the field directed along the 110 direction (selected angles shown). The figures are offset along the x-axis for clarity.

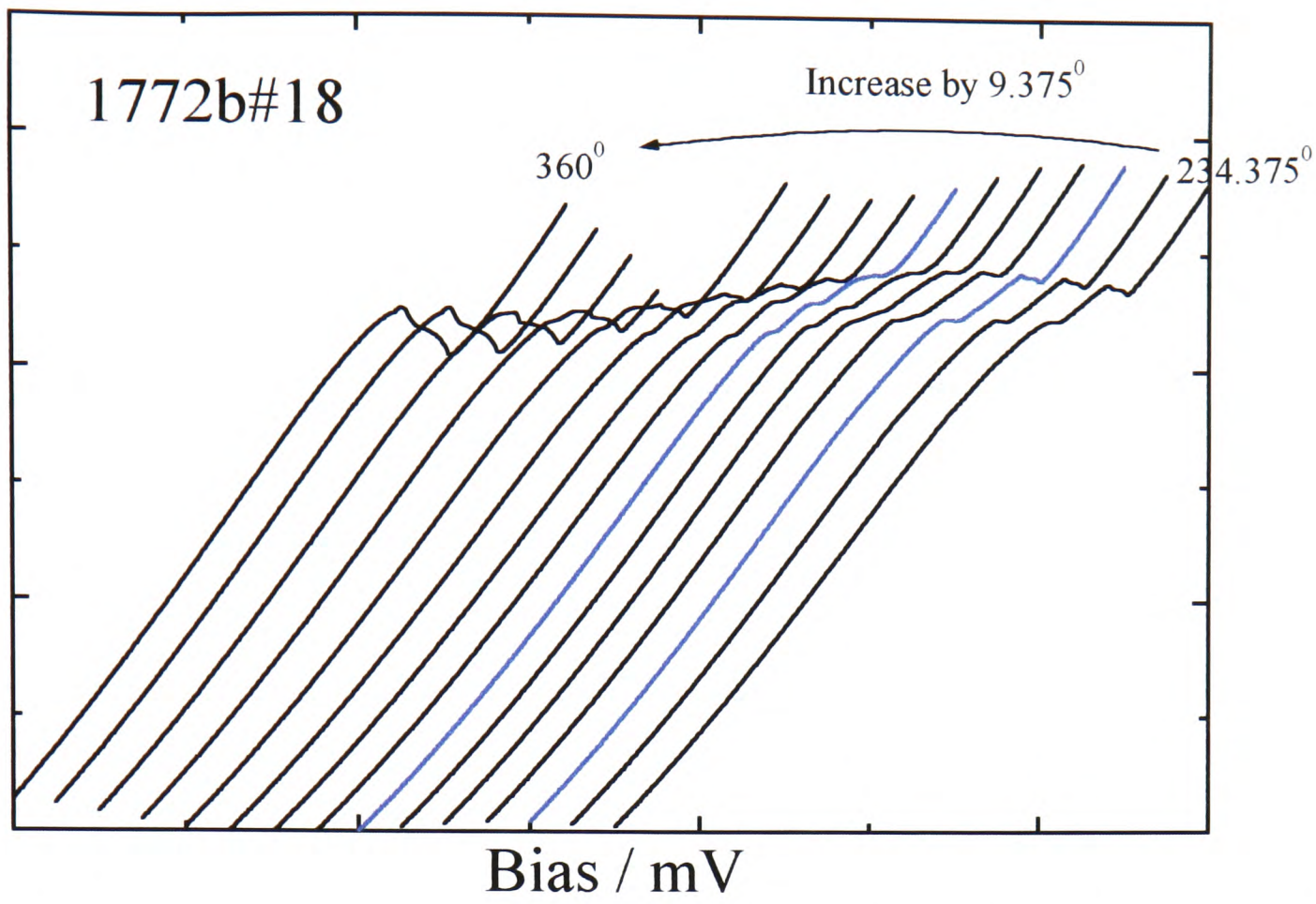


Figure 6.19. As above but with the sample rotated further. Notice that under some orientations, the sharp NDR at 0° is replaced by somewhat weaker multiple NDR features (the blue traces highlight this).

It is worth noting that tunnelling experiments carried out by Marquardt *et al* [22] on InAs/AlSb/GaSb/AlSb/InAs heterostructures with field also in the plane of the interface show that beyond some critical field, a weak shoulder in the IV trace before NDR forms. Through complex **k.p** calculations, they are able to associate the NDR with tunnelling through heavy hole states and the weaker shoulder with tunnelling via light hole states. It is open to speculation if the features observed before NDR here also involve tunnelling through light hole states (as well as heavy hole states). The answer to this can only be resolved through comparison of experimental results with further **k.p** type calculations taking into account the effect of in-plane field.

6.6 Summary

Again, the results here have provided additional confirmation that the vertical transport IV characteristics of the two interface types respond in a very different manner to external stimuli and therefore possibly are the result of a different number of phonons being involved in conduction in each sample type.

Under $B_{||}$, V_p increases as the field is increased in both 'InSb-like' and 'GaAs-like' SHETs. The difference, however, is that at 15T, V_p starts to decrease in the 'InSb-like' samples, whereas in samples with a 'GaAs-like' interface, V_p continues to increase until 50T which was the maximum attainable field. Conduction is found to clearly persist at high fields after the occupied electron and hole dispersions are totally separate in $k_{||}$ space. This is indirect evidence for conduction mediated through inelastic processes and supports the conclusions reached in the previous chapter, i.e. multiple phonon processes occur in samples with both interface types.

Through self-consistent calculations taking into account the effect of in-plane field on the carriers for the first time, conduction in 'InSb-like' samples is shown to be consistent with the mechanism described in 1.5.1, with the peak occurring a phonon energy (30 meV) after the electron and hole dispersions have crossed, V_{30}. Owing to different experimental results at zero field, Khan-Cheema [12] concluded using pressure measurements and calculations that it was the valley that corresponded to V_{30}. What is certain though is that conduction in 'InSb-like' samples is consistent with electron-hole overlap in energy and momentum space (1.5.1) with the fine distinction of the exact NDR peak and valley clouded by inelastic processes. For the 'GaAs-like' samples, to explain the difference between observed and calculated trends in the framework of electron-hole overlap in energy and momentum space aided by inelastic processes would need to a very large phonon cascade. With the results of 4.5.2 showing phonon ladders much larger than the corresponding cascade in 'InSb-like' samples, it seems that this might just be the case.

Finally, with the field rotated, I have shown for the first time that the IV characteristic for each sample is strongly angular dependent. For the 'InSb-like' samples, this data reveals the four fold symmetry in the hole Fermi surface. For the 'GaAs-like' samples, however, complicated NDR effects occur, adding to the mystery behind its resonant conduction. As yet the origin of this effect is unknown. It may simply be due to sample inhomogeneity or be due to electron-heavy hole/electron-light hole coupling that would require detailed **k.p** modelling (the latter of which was ignored in the calculations presented here). This data therefore again suggests a complicated conduction mechanism occurring in 'GaAs-like' samples. Without detailed calculations and further experiments, the debate is still widely open.

6.7 References

[1] F Stern & W E Howard Physical Review 163 p816 1967.

[2] K F Berggren and D J Newson. Semiconductor Science and Technology 1 p327 (1986).

[3] Other in-plane magnetic field studies of InAs/GaSb superlattices by Rundell *et al* predict a semimetal to semiconductor transition due to the increased confinement produced by the field. This is expected to have dramatic effects on the transport properties of the system.. A R Rundell, G P Srivastava and J C Inkson, Physical Review B 55 p5177 (1977).

[4] T Takamasu, N Miura, K Taira, K Funato, H Kawai. Physica B 201 p380 (1994).

[5] E E Mendez, J Nocera and W I Wang. Physical Review B 45 p3910 (1992).

[6] See for example J Singh, Physics of Semiconductors and their Heterostructures, International Edition, McGraw-Hill, Singapore (1993).

[7] R K Hayden, D K Maude, L Eaves, E C Valadares, M Henini, F W Sheard, O H Hughes, J C Portal and L Curry, Physical Review Letters 66 p1749 (1991).

[8] J M Heisz, E Zaremba, Semiconductor Science and Technology 8 p575 (1993).

[9] B Mitrovic, V Milanovic, Z Ikonic. Semiconductor Science and Technology 6 p93-97 (1991).

[10] W Zawadzki Semiconductor Science and Technology B p550 1987.

[11] Condition 5.13 is used throughout. This assumes an exponentially decaying wavefunction far from the interface where the potential profile is flat. This boundary condition does not apply here as the potential varies nearly parabolically. A slight error is therefore introduced, though this is negligible. The difference between the calculated value of Simple Harmonic Oscillator potentials using my algorithm and the true values lead to an error of less than 0.1%.

[12] U M Khan-Cheema, D.Phil. Thesis; Vertical Transport Through an InAs/GaSb Heterojunction at High Pressures and Magnetic Fields, Clarendon Laboratory, Oxford University (1996).

[13] A thorough treatment of magnetoresistance is given by C Kittel in chapter 12 of Quantum Theory of Solids, John Wiley & Sons, Inc. (1986) and by R A Smith, chapter 5, Semiconductors, Cambridge University Press (1964).

[14] G Goldoni and A Fasolino have used a **k.p** Hamiltonian that takes into account the effect of the in-plane magnetic field in this manner to calculate the in-plane dispersions of GaAs/AlAs QWs. Physical Review B 48 p4948 (1993).

[15] See for example J Singh, Physics of Semiconductors and their Heterostructures, International Edition, McGraw-Hill, Singapore (1993).

[16] G Dresselhaus, A F Kip and C Kittel. Physical Review 2 p368 (1955).

[17] U Gennser, V P Kesan, D A Syphers, T P Smith, S S Iyer, E S Yang. Physical Review Letters 67 p3828, (1991).

[18] E L Ivchenko, A Yu Kaminski and U Rossler, Phys. Rev. B 54, 5852 (1996)

[19] E L Ivchenko, A A Toropov and P Voisin, Phys Rev B, in press (1998)

[20] H Im, D.Phil. Thesis; X-band Related Transport in GaAs/AlAs Heterostructures Under Pressure and in Magnetic Fields, Clarendon Laboratory, Oxford University (to be published).

[21] Designed by Andrei Kornilov of the Vereshchagin Institute for High Pressure Physics, Moscow.

[22] R R Marquardt, D A Collings, Y X Liu, D Z-Y Ting and T C McGill – Physical Review B 53 p13624 (1996). Also see Y X Liu *et al.*, Physical Review B 55 p7073 (1997).

7. Concluding Remarks

7.1 Summary

This thesis significantly builds upon the previous work of Khan-Cheema [1] and complementing one another, they collectively constitute a very detailed investigation into the vertical transport properties of the InAs/GaSb SHET. Each experiment time and again has demonstrated that the SHET IV characteristics differs depending on whether the interface is 'InSb-like' or 'GaAs-like'. This is quite clearly seen even under conditions of zero field and ambient pressure as the peak voltage of 'GaAs-like' SHETs at 0.4V is much higher than that of 'InSb-like' SHETs at 0.12V, measured at 77K (PVRs are also different and approximately 1.8 and >2 respectively).

Forward bias IV measurements under pressure reveal more differences in the vertical transport behaviour of the two interface types. The NDR feature is found to disappear with $V_p \to 0$ and $I_p \to 0$ as $\Delta \to 0$ for samples with an 'InSb-like' interface, and the resonant component of the current vanishes before 18 kbar. Self consistent **k.p** band profile calculations have been performed, agreeing very well with previous values of V_c and V_{30} from calculations by Khan-Cheema's decoupled model. This perhaps is unsurprising because at such biases there are no degenerate electrons and holes, so interactions are weak for all in-plane vectors. The results also show that resonant conduction is primarily due to electrons and heavy holes, as light hole states lie below the hole quasi Fermi energy. They are important to perform not only to confirm Khan-Cheema's conclusions, but also to lend faith to the use of decoupled models later when treating the effect of magnetic field parallel and perpendicular to the interface of the SHET.

However, owing to the different pressures at which we performed our pressure runs, our conclusions vary slightly. My data, collected at 4K compared to Khan-Cheema's data at 77K shows that it is V_p and not V_v that follows V_{30} well in the 'InSb-like' samples. The theory thus supports the idea that the peak of the NDR at 4K occurs after the electron and (heavy) hole subbands have crossed one another by approximately a phonon in energy, and the valley after (again through phonon

mediation). As well as specifying the position of the peak and valley to a greater precision than before, the high pressure and low temperature results, presented in chapter 4, provide strong evidence for phonons being involved in the conduction process near the point at which NDR occurs. This last piece of data is very important as it for the first time establishes the long sought after evidence of phonons in the SHET and thereby firmly establishes the resonant conduction mechanism in 'InSb-like' samples described in chapter 1 as due to tunnelling between electrons and holes blurred through the mediation of a few phonons.

The greater challenge has, however, not been explaining resonant conduction in 'InSb-iike' samples, but in the 'GaAs-like' samples. These are found to behave not so predictably with pressure under forward bias. Not only does a noticeable feature exist at 21 kbar where the band overlap is calculated to be in the region of -100 meV, but the NDR also occurs at a much higher bias than expected. The pressure dependence of the peak and valley voltages are consistent with the resonance occurring when E_0 - HH_0 is between 120 and 140 meV. Inelastic process could of course again explain this discrepancy, but to do so in terms of just phonons (of energy ≈30 meV) would require one to postulate up to four or five. In the light of the high pressure, low temperature results with samples with an 'InSb-like' interface where up to 3 phonons were observed close to the NDR region, this certainly seems feasible. Experiments were therefore carried out on these samples under the same conditions. The results were very surprising, revealing *many* features separated by a phonon energy in reverse bias in careful 2nd derivative measurements. Though it is very likely that a similar number of phonons, too weak to be observed, exist in the forward bias, it is difficult to predict if these are the sole inelastic processes responsible for the discrepancy between calculated V_c and V_{120}. What is clear though is that for the first time strong evidence presented here suggests that an extremely efficient cascade of 30 meV phonons does exist and therefore goes a long way in explaining resonant conduction in these sample types too. At the very least, it perhaps unsurprisingly discounts the theory that single phonon events of energy above 100 meV and Auger effects cause such a discrepancy between experiment and theory in such sample types. Moreover, with such numbers of phonons are involved, conduction can be explained

without resorting to questioning the role any interface states play, postulated earlier by Khan-Cheema [1].

$B_\perp$ (chapter 5) measurements have provided additional confirmation that the vertical transport IV characteristic of the two interface types respond in a very different manner to external stimuli. The 'GaAs-like' SHET has an IV trace that is far more difficult to suppress than its 'InSb-like' counterpart. The latter has a region of NDR that disappears at about the magnetic field induced semimetal/semiconductor transition B_c at zero bias. The former, however, exhibits a strong NDR at 40T, whereas its smaller band overlap value suggests it should have disappeared by 50T. Additionally, the data provides strong evidence that the current resonance occurs after the voltage induced semimetal/semiconductor transition. In the quantum limit of one occupied electron and hole spin-split Landau level for example, the two levels pin together at zero bias and any voltage increase should immediately induce the semimetal/semiconductor transition. The experimental IV traces, however, show clear regions of NDR at a finite bias after the quantum limit has been reached.

Beyond about 5T at 1 bar, additional resonances beyond the main NDR resonance are observed. Though these were reported previously [1] as a 'secondary NDR' in the 'InSb-like' samples, detailed measurements performed in the course of this work in the first derivative show that this is not a single 'secondary NDR' feature, but a couple, both of which move up in bias with field but at different rates. The first experiments performed utilising a combination of high pressure and $B_\perp$ reveal the existence of very weak (observable only in the 2nd derivative) features well beyond the main NDR resonance. This entire collection of data has also been analysed using a self-consistent non **k.p** model. The bias position of the high pressure magnetic field induced features is found to be in excellent agreement with the calculated position when $n = i(2eB/h)$ where i is an integer. The modelling therefore strongly suggests that the origin of these features is due to the complete filling of an integer number of Landau levels, at which point the InAs band profile is predicted to undergo a drastic change in shape. Extrapolating this result to 1 bar strongly suggests that the secondary NDR there is also due to the filling of an integer number of Landau levels, with the peak due to the crossing of electron and hole Landau levels by a phonon in

energy, in analogy with the zero field position of the expected NDR peak. However high current densities at such low pressures make any attempt at a quantitative comparison futile. Similar experiments were also performed on samples with 'GaAs-like' samples with the results revealing for the first time the existence of similar 'secondary NDR' features.

Chapter 6 sets out to provide a comprehensive treatment of the vertical transport properties of the SHET under magnetic field parallel to the interface layers ($B_{||}$) in much the same way as chapters 3 to 5 have treated the SHET behaviour in zero field and under $B_{\perp}$. Here again measurements of the IV traces from 'InSb-like' and 'GaAs-like' SHETs also show strong interface dependent differences. The bias at which the main resonance occurs in samples with a 'GaAs-like' interface, for example, increases significantly with increasing $B_{||}$. V_p for the 'InSb-like' SHET, however, increases initially and then starts to decrease as the field is raised. Analysis using complex self-consistent calculations that take into account the coupling of the particle motion along the growth directions and an in-plane direction again leads to the conclusion that V_{30} follows V_p in the 'InSb-like' samples thereby confirming the results at zero field in chapter 4. Unsurprisingly, the 'GaAs-like' samples do not even follow the predicted trend, though of course the evidence for phonons, summarised above, is (again) highly likely to be a reason for the discrepancy. Indeed, the results of the calculations showing the eventual complete separation of the electron and hole dispersion curves with increasing field compared with the lack of any IV feature besides the main NDR again points to the existence of an efficient inelastic conduction path.

Studied under 1st and 2nd derivative using traditional lock-in methods, the 'GaAs-like' samples under $B_{||}$ show very weak features, which to my knowledge have never been observed before, occurring near zero bias and just before the onset of NDR (6.2.2). The origin of these features are as yet unknown and are likely to be the same features that obscure NDR observed in the IV under certain orientations of the in-plane field (Figure 6.6). Such features are not observed in the same experiment performed with 'InSb-like' samples. However, their peak position is found to vary with field so that when plotted in polar coordinates, a clover leaf like (4 fold symmetry) elongated in the [110] direction results. The experiments are consistent with a warped (square)

hold Fermi surface therefore though only future experiments and possibly theory are needed to explain the elongation.

7.2 Future Development

Mentioned in this group initially by Austing [2], the InAs/GaSb single heterojunction was studied in detail by Khan-Cheema, with particularly strong emphasis on its pressure response. This thesis using his work as a foundation, has extended the understanding of the InAs/GaSb SHET especially in magnetic field. In addition, it has confirmed his findings at zero field, presenting a **k.p** algorithm which can be quite easily modified to include the effect of magnetic field [3, 4, 5, 6, 7]. This has for example been used by Liu *et al* [6] to show that the primary interband transport mechanism in InAs/GaSb/AlSb systems arises from the coupling between InAs conduction band states and GaSb light hole states, though weaker shoulders in the IV traces are due to electron-heavy hole coupling that increase with increasing in-plane magnetic field.

Extensions to the work here can immediately be realised by taking advantage of the next generation of pressure cells. An experiment that may yield fruitful insights into the device operation is the behaviour of the SHET in an in-plane field at high pressure. Combined with the results of the corresponding self-consistent calculations (presented here), the high pressure and magnetic field IV dependence can be traced. Additionally, high pressure-in plane field experiments using small spherical pressure cells attached to the end of a suitable rotating insert of may resolve why the NDR actually disappears at some field orientations in 'GaAs-like' samples and may yield more information on why the expected four fold symmetry of the peak voltage position versus angle (section 6.5) is not strictly observed in the 'InSb-like' sample types. The possibility also exists of using cells capable of fitting in the pulse field set-up [8], thus allowing the vertical transport properties of the SHET (and of course of other samples) to be measured at high pressure and very high magnetic fields.

There are many varieties of InAs/GaSb DHET structures whose vertical transport behaviour can be investigated. Samples with a single interface type (i.e. both 'InSb-

like' or both 'GaAs-like') can be used to compare vertical transport through interfaces that are grown with InAs on GaSb and those grown with GaSb on InAs. The effect of mixed interface structures (i.e. 'InSb-like' and 'GaAs-like' in the same sample) on the IV trace can also be studied, and the ability to vary the quantum well width provides an additional experimental variable.

Apart from the SHET and DHET, there exists the possibility of incorporating $In_{1-x}Ga_xSb$ into the structures in order to alter the electrostatics. The $In_{1-x}Ga_xSb$ is capable of acting as a well or barrier for the electrons depending upon the value of x. Also, analysis of the effects of strain on the IV trace is possible because of the lattice mismatch. The prospect of applying similar experimental techniques (and subsequent analysis) to any of these new sample types promises that the InAs/GaSb system will be the subject of many years of rich research in the future.

7.3 References

[1] U M Khan-Cheema, D.Phil. Thesis; Vertical Transport Through an InAs/GaSb Heterojunction at High Pressures and Magnetic Fields, Clarendon Laboratory, Oxford University (1996).

[2] D G Austing, D. Phil. Thesis; The Pressure Dependence of Vertical Transport in Simple Semiconductor Hetrostructures, Clarendon Laboratory, Oxford Univeristy (1992).

[3] T A Vaughan, D.Phil. Thesis; The Magneto-optics of InAs/GaSb Heterostructures, Clarendon Laboratory, Oxford University (1996).

[4] M H Weiler, in Semiconductors and Semimetals, 16 p119 (1981) edited by R K Willardson and A C Beer (Academic, New York).

[5] A **k.p** Hamiltonian for the valence band in the presence of an in-plane magnetic field is described for example by G Goldoni and A Fasolino; Physical Review B 48 p4948 (1993).

[6] A **k.p** Hamiltonian for the valence band in the presence of a magnetic field perpendicular to the interface is given by U Ekenberg and M Altarelli; Physical Review B 32 p3712 (1985).

[7] Y X Liu, R R Marquardt, D Z-Y Ting and T C McGill. Physical Review B 55 p7073 (1997).

[8] Designed by Dr M Eremets of the Troitsk High Pressure Insitute, Moscow (1995).

Appendix A

Parameter	InAs	GaSb
Lattice Constant (Å)	6.0584	6.0954
Band Gap E_g (meV)	418	811
Spin-orbit Splitting Δ_{so}	380	775
γ_1	20.5	14.3
γ_2	9	5.3
γ_3	9	6.5
$E_P = 2m_0P^2$ (eV)	21.11	22.88
Relative Permittivity ε_r	15.15	15.69
m_e^* (m_0)	0.023	0.042
m_{hh}^* (m_0)	0.41	0.33 ($m_{\|\|}^* = 0.1m_0$)
m_{lh}^* (m_0)	0.025	0.05
N_D^{GaSb}		10^{15} cm^{-3}
N_A^{InAs}	10^{15} cm^{-3}	
dE_G^{Γ}/dP	10 meV/kbar	14 meV/kbar

Table A1. Table of variables used in calculations in this thesis.

Appendix B

Deriving the Condition for Confined Γ States

Equations (4.7), (4.8) and (5.13) are derived using a transfer matrix formalism incorporating the differing boundary conditions between the two cases. In order to take into account electron-light hole coupling, the zone centre envelope functions used in chapter 4 as a basis must necessarily be calculated taking into account the rapid decay of, for example, electron wavefunctions in the GaSb layer and similarly of the heavy and light hole wavefunctions' decay in the InAs layer of the SHET. The simpler theory of chapter 5, however, neglects band mixing so it suffices to assume the wavefunctions of all states are zero at the interface. By taking into account the differing boundary conditions for the different cases, this appendix derives the appropriate conditions for deriving the zone centre confined states (and continuum states where necessary). I start by considering the simpler case of assuming the wavefunctions see an infinite barrier at the interface and are therefore zero at this point.

Consider the InAs side of the SHET interface (Figure 1.8). Using the subscript R to denote large positive z (where the band profile is flat) and 0 to denote $z = 0$, the transfer matrix connecting these two points between $z = 0$ and R is T such that,

$$\begin{bmatrix} \psi_R^\Gamma \\ \dfrac{1}{m^*_{z,GaSb}}\dfrac{d\psi_R^\Gamma}{dz} \end{bmatrix} = \tilde{\mathbf{T}} \begin{bmatrix} \psi_0^\Gamma \\ \dfrac{1}{m^*_{z,InAs}}\dfrac{d\psi_0^\Gamma}{dz} \end{bmatrix} \tag{B1}$$

Thus,

$$\psi_R^\Gamma = T_{1,1}\psi_0^\Gamma + T_{1,2}\frac{1}{m^*_{z,InAs}}\frac{d\psi_0^\Gamma}{dz} \tag{B2}$$

and

$$\frac{1}{m^*_{z,GaSb}}\frac{d\psi_R^\Gamma}{dz} = T_{2,1}\psi_0^\Gamma + T_{2,2}\frac{1}{m^*_{z,InAs}}\frac{d\psi_0^\Gamma}{dz} \tag{B3}$$

At large (negative) z away from the interface, the wavefunction will have an exponential form,

$$\psi_R^\Gamma = A\exp(k_f z) \Rightarrow \frac{d\psi_R^\Gamma}{dz} = k_f \psi_R^\Gamma \qquad \textbf{(B4)}$$

Substituting the boundary conditions $\psi_0^\Gamma = 0$ and $\left.\frac{d\psi_0^\Gamma}{dz}\right|_{z=0} = -1$ into equations (B2) and (B3) and using equation (B4), the condition for confinement is easily obtained,

$$T_{2,2} + T_{1,2}\frac{k_f}{m^*_{z,InAs}} = 0 \qquad \textbf{(B5)}$$

The analysis of chapter 4 proceeds by assuming the SHET sits inside a much larger quantum well. The transfer matrix connected the right and left hand sides (denoted by R and L respectively) then is,

$$\begin{bmatrix} \psi_R^\Gamma \\ \dfrac{1}{m^*_{z,GaSb}}\dfrac{d\psi_R^\Gamma}{dz} \end{bmatrix} = \tilde{\mathrm{T}}\begin{bmatrix} \psi_L^\Gamma \\ \dfrac{1}{m^*_{z,InAs}}\dfrac{d\psi_L^\Gamma}{dz} \end{bmatrix} \qquad \textbf{(B6)}$$

Thus,

$$\psi_R^\Gamma = T_{1,1}\psi_L^\Gamma + T_{1,2}\frac{1}{m^*_{z,InAs}}\frac{d\psi_L^\Gamma}{dz} \qquad \textbf{(B7)}$$

and

$$\frac{1}{m^*_{z,GaSb}}\frac{d\psi_R^\Gamma}{dz} = T_{2,1}\psi_L^\Gamma + T_{2,2}\frac{1}{m^*_{z,InAs}}\frac{d\psi_L^\Gamma}{dz} \qquad \textbf{(B8)}$$

Again at large z (now positive) away from the interface, the wavefunction will have an exponential form:

$$\psi_R^\Gamma = A\exp(-k_f z) \Rightarrow \frac{d\psi_R^\Gamma}{dz} = -k_f \psi_R^\Gamma \qquad \textbf{(B9)}$$

where k_f is the value of k at large z. Substituting in (B8):

$$-\frac{1}{m^*_{z,GaSb}}k_f\psi^{\Gamma}_R = T_{2,1}\psi^{\Gamma}_L + T_{2,2}\frac{1}{m^*_{z,InAs}}\frac{d\psi^{\Gamma}_L}{dz} \qquad \textbf{(B10)}$$

Combining this with (B7) one has:

$$T_{1,1}\psi^{\Gamma}_L + T_{1,2}\frac{1}{m^*_{z,InAs}}\frac{d\psi^{\Gamma}_L}{dz} + T_{2,1}\frac{m^*_{z,GaSb}}{k_f}\psi^{\Gamma}_L + T_{2,2}\frac{m^*_{z,GaSb}}{m^*_{z,InAs}}\frac{1}{k_f}\frac{d\psi^{\Gamma}_L}{dz} = 0 \qquad \textbf{(B11)}$$

The confined wavefunction at large $-z$ will similarly have an exponential behaviour:

$$\psi^{\Gamma}_L = B\exp(k_i z) \Rightarrow \frac{d\psi^{\Gamma}_L}{dz} = k_f\psi^{\Gamma}_L \qquad \textbf{(B12)}$$

where k_i is the value of k at large $-z$.

Substituting this into equation (B11) and rearranging, one obtains the necessary condition for a confined state allowing it to penetrate across the interface:

$$\left(T_{2,1} + T_{2,2}\frac{k_i}{m^*_{z,InAs}}\right)\frac{m^*_{z,GaSb}}{k_f} + T_{1,1} + T_{1,2}\frac{k_i}{m^*_{z,InAs}} = 0 \qquad \textbf{(B13)}$$

In calculating the continuum wavefunction states, given the boundary conditions that the wavefunction is zero at the edge of the SHET (Figure 1.8) and that again it penetrates across the interface, one has:

$$\psi^{\Gamma}_L = 0 \qquad \textbf{(B14)}$$

Equation B11 then simplifies to:

$$T_{1,2}\frac{1}{m^*_{z,InAs}}\frac{d\psi^{\Gamma}_L}{dz} + T_{2,2}\frac{m^*_{z,GaSb}}{m^*_{z,InAs}}\frac{1}{k_f}\frac{d\psi^{\Gamma}_L}{dz} = 0 \qquad \textbf{(B15)}$$

After rearranging, the necessary condition for a continuum state is obtained:

$$T_{2,2} + T_{1,2} \frac{k_f}{m^*_{z,InAs}} = 0 \qquad \textbf{(B16)}$$

Appendix C
k.p Matrices

	e	*e*	*hh*	*hh*	*lh*	*lh*	*so*	*so*
$\|iS\uparrow\rangle$	$\frac{\hbar^2 k^2}{2m_0}$							
$\|iS\downarrow\rangle$	0	$\frac{\hbar^2 k^2}{2m_0}$						
$\|3/2,+3/2\rangle$ $\sqrt{1/2}\|X+iY\uparrow\rangle$	$P\hbar k_-$	0	$-\varepsilon_0+\frac{\hbar^2 k^2}{2m_0}$					
$\|3/2,-3/2\rangle$ $\sqrt{1/2}\|X-iY\downarrow\rangle$	0	$P\hbar k_+$	0	$-\varepsilon_0+\frac{\hbar^2 k^2}{2m_0}$				
$\|3/2,+1/2\rangle$ $\sqrt{1/6}\|X+iY\downarrow\rangle-\sqrt{2/3}\|Z\uparrow\rangle$	$-\sqrt{\frac{2}{3}}P\hbar k_z$	$\frac{1}{\sqrt{3}}P\hbar k_-$	0	0	$-\varepsilon_0+\frac{\hbar^2 k^2}{2m_0}$			
$\|3/2,-1/2\rangle$ $-\sqrt{1/6}\|X-iY\uparrow\rangle-\sqrt{2/3}\|Z\downarrow\rangle$	$-\frac{1}{\sqrt{3}}P\hbar k_+$	$-\sqrt{\frac{2}{3}}P\hbar k_z$	0	0	0	$-\varepsilon_0+\frac{\hbar^2 k^2}{2m_0}$		
$\|1/2,+1/2\rangle$ $\sqrt{1/3}\|X+iY\downarrow\rangle+\sqrt{1/3}\|Z\uparrow\rangle$	$\frac{1}{\sqrt{3}}P\hbar k_z$	$\sqrt{\frac{2}{3}}P\hbar k_-$	0	0	0	0	$-\varepsilon_0-\Delta_{so}+\frac{\hbar^2 k^2}{2m_0}$	
$\|1/2,-1/2\rangle$ $-\sqrt{1/3}\|X-iY\uparrow\rangle+\sqrt{1/3}\|Z\downarrow\rangle$	$-\sqrt{\frac{2}{3}}P\hbar k_+$	$\frac{1}{\sqrt{3}}P\hbar k_z$	0	0	0	0	0	$E_{so}+p$

Table C1. The 8-band Kane Hamiltonain relative to the basis functions shown in Table 3.1 with the **k.p** interaction restricted to the Γ_6, Γ_7 and Γ_8 states. The upper triangle is the hermitian conjugate of the lower triangle. Here, ε_0 is the separation of the Γ_6 and Γ_8 states (band gap), and Δ_{so} is the separation between the Γ_8 and Γ_7 states (the spin-orbit split off band and heavy hole band at the zone centre).

	e	*e*	*hh*	*hh*	*lh*	*lh*	*so*	*so*
$\|S\uparrow\rangle$	$E_c+\gamma_c k^2$							
$\|iS\downarrow\rangle$	0	$E_c+\gamma_c k^2$						
$\|3/2,+3/2\rangle$ $\sqrt{1/2}\|X+iY\uparrow\rangle$	$\sqrt{\frac{1}{2}}P'k_-$	0	E_v+p+q					
$\|3/2,-3/2\rangle$ $i\sqrt{1/2}\|X-iY\downarrow\rangle$	0	$\sqrt{\frac{1}{2}}P'k_+$	0	E_v+p+q				
$\|3/2,+1/2\rangle$ $i\sqrt{1/6}\|X+iY\downarrow\rangle-i\sqrt{2/3}\|Z\uparrow\rangle$	$i\sqrt{\frac{2}{3}}P'k_z$	$\sqrt{\frac{2}{3}}P'k_-$	l^*	m	E_v+p-q			
$\|3/2,-1/2\rangle$ $i\sqrt{1/6}\|X-iY\uparrow\rangle+\sqrt{2/3}\|Z\downarrow\rangle$	$\sqrt{\frac{1}{6}}P'k_+$	$i\sqrt{\frac{2}{3}}P'k_z$	m^*	$-l$	0	E_v+p-q		
$\|1/2,+1/2\rangle$ $\sqrt{1/3}\|X+iY\downarrow\rangle+\sqrt{1/3}\|Z\uparrow\rangle$	$\sqrt{\frac{1}{3}}P'k_z$	$i\sqrt{\frac{1}{3}}P'k_-$	$-i\sqrt{\frac{1}{2}}l^*$	$i\sqrt{2}m$	$i\sqrt{2}q$	$i\sqrt{\frac{2}{3}}l$	$E_{so}+p$	
$\|1/2,-1/2\rangle$ $-i\sqrt{1/3}\|X-iY\uparrow\rangle+i\sqrt{1/3}\|Z\downarrow\rangle$	$i\sqrt{\frac{1}{3}}P'k_+$	$\sqrt{\frac{1}{3}}P'k_z$	$i\sqrt{2}m^*$	$i\sqrt{\frac{1}{2}}l$	$-i\sqrt{\frac{3}{2}}l^*$	$i\sqrt{2}q$	0	$E_{so}+p$

Table C2. The 8-band renormalised Kane Hamiltonain matrix used throughout the calculations. The upper triangle is the hermitian conjugate of the lower triangle. Here, the effects of remote band effects inside the Γ_6, Γ_7 and Γ_8 states are included.

$$k_{\pm} = k_x \pm ik_y$$

$$\gamma_c = \frac{\hbar^2}{2m_0}\left[\frac{m_0}{m_c^*} - \frac{2E_P}{3E_g}\right](6\ Band)$$

$$P' = \frac{\hbar}{m}P$$

$$P = \langle S|p_x|X\rangle = \langle S|p_y|Y\rangle = \langle S|p_z|Z\rangle$$

$$p = -\tilde{\gamma}_1\frac{\hbar^2}{2m}\left(k_x^2 + k_y^2 + k_z^2\right)$$

$$q = -\tilde{\gamma}_2\frac{\hbar^2}{2m}\left(k_x^2 + k_y^2 - 2k_z^2\right)$$

$$l = i2\sqrt{3}\tilde{\gamma}_3\frac{\hbar^2}{2m}\left(k_x - ik_y\right)k_z$$

$$m = \sqrt{3}\frac{\hbar^2}{2m}\left(\tilde{\gamma}_2 k_+ k_- - i2\tilde{\gamma}_3 k_x k_y\right)$$

The parameters $\tilde{\gamma}_1, \tilde{\gamma}_2$ and $\tilde{\gamma}_3$ are the modified Luttinger parameters used for the 4×4 valence band Hamiltonian and are related to the Luttinger parameters by

$$\tilde{\gamma}_1 = \gamma_1 - \frac{E_P}{3E_g},\ \tilde{\gamma}_{2(3)} = \gamma_{2(3)} - \frac{E_P}{6E_g}$$

To ensure the hermicity of the Hamiltonian, the 'symmetrized' form was applied using the following substitutions [1, 2]:

$$\gamma\frac{d^2}{dz^2} \rightarrow -\frac{d}{dz}\gamma\frac{d}{dz}, \tag{C1}$$

$$-i\gamma\frac{d}{dz} \rightarrow -\frac{i}{2}\left\{\gamma, \frac{d}{dz}\right\} = -\frac{i}{2}\left(\gamma\frac{d}{dz} + \frac{d}{dz}\gamma\right) \tag{C2}$$

A hermitian operator Q is one such that $\int f^* Q g\, d\tau = \int (fQ)^* g\, d\tau$ and the consequence of this is that its eigenvalues are real (as expected for all observables are real).

Therefore, making use of this property for k_z and k_z^2 one finds:

$$\left\langle \phi_1 \middle| k_z^2 \middle| \phi_2 \right\rangle = \left\langle \phi_1 \middle| \left(-i\frac{\partial^2}{\partial z^2}\right) \middle| \phi_2 \right\rangle = \int \phi_1^* \left\{ i\frac{\partial}{\partial z}\left(i\phi_2'\right)\right\} d\tau$$

$$= -\int \phi_1^* \phi_2''\, d\tau \tag{C3}$$

$$= \int \left(i\phi_1'\right)^* \left(i\phi_2'\right) d\tau$$

$$= \int \phi_1'^* \phi_2' \, d\tau \qquad \textbf{(C4)}$$

Hence we have $\left\langle \phi_1 \middle| k_z^2 \middle| \phi_2 \right\rangle = -\int \phi_1^* \phi_2'' \, d\tau = \int \phi_1'^* \phi_2' \, d\tau$.

This equality therefore justifies the presence of the - sign in (C1). This is usually neglected in the literature as V is constant and therefore, $\left\langle \phi_1 \middle| V \middle| \phi_2 \right\rangle = 0$ so that the change of sign in the off-diagonal element in one lower triangle of the matrix is offset by a change of sign in the other upper triangle. This convenience is inapplicable here where the V varies throughout the junction. It could also be justified by using the following mathematical identity formed by simply rearranging the product integration formula,

$$\int \phi_1 \phi_2'' \, d\tau = \left[\phi_1 \phi_2'\right]_{-\infty}^{\infty} - \int \phi_1' \phi_2' \, d\tau$$

$$\cong -\int \phi_1' \phi_2' \, d\tau$$

because the wavefunctions are normalised and zero at $\pm\infty$.

---

[1] M. Altarelli. Physical Review B 28 p842 (1983).

[2] J Los, A Fasolino and A Catellani. Physical Review B 53 p4630 (1996).